Florian Michael Rott

Photo Initiated Molecular Processes Elucidated by Quantum Chemistry and Theoretical Spectroscopy

Dissertation zur Erlangung des Doktorgrades
der Fakultät für Chemie und Pharmazie
der Ludwig-Maximilians-Universität München

Photo Initiated Molecular Processes Elucidated by Quantum Chemistry and Theoretical Spectroscopy

Florian Michael Rott
aus
München, Deutschland

2022

Erklärung

Diese Dissertation wurde im Sinne von §7 der Promotionsordnung vom 28. November 2011 von Frau Prof. Dr. Regina de Vivie-Riedle betreut.

Eidesstattliche Versicherung

Diese Dissertation wurde eigenständig und ohne unerlaubte Hilfe erarbeitet.

München, 07.03.2022

Florian Rott

Dissertation eingereicht am:	07.03.2022
1. Gutachterin:	Prof. Dr. Regina de Vivie-Riedle
2. Gutachter:	Prof. Dr. Christian Ochsenfeld
Mündliche Prüfung am:	28.04.2022

Für M. V.

"Jetzt ist es vorbei, aber okay
 Ich kann damit leben, es tut halt noch weh
 Jetzt ist es vorbei, bin noch 'n bisschen benebelt
 Aber ich hab's überlebt, hey, danke, das geht schon"

singt NMZS
in *Jetzt ist es vorbei.*

Contents

Processes initiated by the interaction between light and matter are a fundamental step in various chemical, physical and biological phenomena. The present work investigates the photoinduced processes in artificial molecular machines and small molecules with the help of quantum chemical calculations. The research was performed in close collaboration with experimentalists, allowing an in-depth look at the underlying mechanisms of these ultrafast processes.

The first part addresses the relaxation pathways after photoexcitation of the photoswitch hemithioindigo (HTI) and the artificial molecular motors, *motor-1* and *motor-2*. The photochromic compound HTI is a novel photoswitch capable of performing efficient isomerization upon irradiation with non-damaging visible light. Based on time-resolved absorption and emission experiments and supported by high level quantum chemical calculations, a comprehensive reaction model for its photoisomerization, including the effects of different solvents as well as substitutions, is established. The structure of both molecular motors, *motor-1* and *motor-2*, is based on the HTI moiety. By clever design, this switch was turned into a molecular motor, capable of unidirectional rotation. These motors are among the first light-powered molecular motors that operate under ambient and non-damaging conditions. The underlying processes for their multistep rotation was elucidated through multiscale broadband transient absorption measurements and quantum chemical investigations of their excited state potential energy surfaces. From these findings, pathways to improve the rotational speeds and efficiency of light-driven molecular motors in general could be developed.

The second part of this work addresses the theoretical simulation of the ultrafast spectroscopy technique known as attosecond transient absorption spectroscopy (ATAS). Attosecond pulses in the extreme ultraviolet (XUV) or X-ray region provide a powerful tool for investigating ultrafast nuclear and even electron dynamics in atoms, molecules and solids. Due to their high photon energy, they are able to create electron wave packets extremely well localized in time. This makes them an excellent choice for triggering photochemical reaction in a pump-probe scenario. Further, their broad bandwidth provides element, charge and electronic state sensitive insights by probing the inner-valence and core-level states of the excited molecules. To aid the interpretation of the experimental data and provide further insights into these complex interactions between light and matter, a comprehensive framework simulating XUV/X-ray transient absorption spectra is presented. Using *ab initio* non-adiabatic molecular dynamics (NAMD), the ultrafast processes of excited molecules after laser excitation is simulated, enabling the resolution of both the changes in the electronic structure and the nuclear motion over time. Based on this information, the time-dependent XUV/X-ray transient absorption spectra are calculated by applying high-level multi-reference methods, namely restricted active space self-consistend field (RASSCF) and restricted active space perturbation theory (RASPT2). This framework is utilized in the two studies on the molecules vinyl bromide (C_2H_3Br) and trifluoroiodomethane (CF_3I). For both molecules the ultrafast coupled nuclear-electron dynamics after strong-field ionization could be explained in great detail.

List of Publications

This thesis is based on the following five publications listed in chronological order. They are reprinted in the chapters 1 (**1-3**) and 2 (**4**).

1 - R. Wilcken, M. Schildhauer, <u>F. Rott</u>, L. A. Huber, M. Guentner, S. Thumser, K. Hoffmann, S. Oesterling, R. de Vivie-Riedle, E. Riedle and H. Dube, "Complete Mechanism of Hemithioindigo Motor Rotation", *J. Am. Chem. Soc.* **140**, 15, 5311–5318 (2018).
DOI: 10.1021/jacs.8b02349

2 - F.F. Graupner, T. T. Herzog, <u>F. Rott</u>, S. Oesterling, R. de Vivie-Riedle, T. Cordes and W. Zinth, "Photoisomerization of hemithioindigo compounds: Combining solvent- and substituent- effects into an advanced reaction model", *Chem. Phys.* **515**, 614–621 (2018).
DOI: 10.1016/j.chemphys.2018.07.043

3 - M. Schildhauer, <u>F. Rott</u>, S. Thumser, P. Mayer, R. de Vivie-Riedle, and H. Dube, "A Prospective Ultrafast Hemithioindigo Molecular Motor", *ChemPhotoChem* **3**, 6, 365–371 (2019).
DOI: 10.1002/cptc.201900074

4 - <u>F. Rott</u>, M. Reduzzi, T. Schnappinger, Y. Kobayashi, K. F. Chang, H. Timmers, D. M. Neumark, R. de Vivie-Riedle and S. R. Leone, "Ultrafast strong-field dissociation of vinyl bromide: an attosecond transient absorption spectroscopy and non-adiabatic molecular dynamics study", *Struct. Dyn.* **8**, 034104 (2021).
DOI: 10.1063/4.0000102

Additional publications listed in chronological order:

5 - S. Thallmair, D. Keefer, <u>F. Rott</u> and R. de Vivie-Riedle, "Simulating the control of molecular reactions via modulated light fields: from gas phase to solution", *J. Phys. B At. Mol. Opt. Phys.* **50**, 082001 (2017).
DOI: 10.1088/1361-6455/aa6100

6 - J. P. P. Zauleck, M. T. Peschel, <u>F. Rott</u>, S. Thallmair and R. de Vivie-Riedle, "Ultrafast Reactive Quantum Dynamics Coupled to Classical Solvent Dynamics Using an Ehrenfest Approach", *J. Phys. Chem. A* **122**, 2849–2857 (2018).
DOI: 10.1021/acs.jpca.7b10372

The study of the interaction between light and matter is of paramount importance in many disciplines, such as physics, chemistry and biology. As a molecule gets excited by light, either from the sun or by a laser in the lab, its electrons can be promoted from the molecular ground state to electronically excited states or even to the continuum, causing ionization. This initial interaction is followed by a concerted electronic-nuclear motion or, in other words, a photochemical reaction. In nature, this fundamental process can be found in photosynthesis [1, 2], in visual phototransduction - the process that enables our vision [3–7] - and is one of the main reasons for the emergence of radiation damage in our genetic code [8–13]. Photochemical reactions also play an important role in artificial systems, such as photocatalysts [14, 15] and molecular machines, such as photoswitches [16–19] and molecular motors [20–22]. Therefore it is not surprising that a detailed understanding of the underlying mechanism of these reactions is desirable.

After photoexcitation, a single molecule in the gas phase, unable to transfer the excess energy to its surrounding, has two options to return to its ground state (GS): Either directly by emitting a photon, or via radiationless transitions between the different electronic states, smoothly decreasing the electronic energy until the GS is reached. The former is a statistical process, which can happen on the whole potential energy surface (PES), with a certain lifetime depending on the initial and final states. When the multiplicity of said states is different, this process is termed phosphorescence. Otherwise, it is called fluorescence. The latter process, allowing the radiationless transition from one state to another, is mediated by crossings between both involved states. Again, for these crossings a distinction can be made on the basis of the spin states involved. If the spin state changes with the crossings (e.g. from singlet to triplet), one speaks of intersystem crossing (ISC). If it does not, the process is called internal conversion (IC). Especially this process, which mainly happens in the vicinity of conical intersections (CoIns), allows for an ultrafast and very efficient transition between the electronic states [23–25]. CoIns are extraordinary points on the PES where two adiabatic states degenerate, allowing the radiationless transition between them [26]. Elucidating the PES and describing these extraordinary points with theoretical methods can help with the understanding of the relaxation processes after photoexcitation and aid the formulation of mechanisms for these types of reactions.

In the first part of this work, the research on the relaxation pathways after photoexcitation of the photoswitch hemithioindigo (HTI) and the molecular motors, *motor-1* and *motor-2* is presented. The photochromic compound HTI is a promising photoswitch, especially with regard to biological applications [27–30], as it is switchable by non-damaging visible light. Further, it is a very versatile switch, as most of its photophysical properties can be changed significantly by introducing different substituent groups into its structure [28]. Based on time-resolved absorption and emission measurements supported by high-level quantum chemical calculations, a comprehensive reaction model for its photoisomerization, including the effects of different solvents as well as substitutions, is presented in chapter 1.1. The molecular motors, *motor-1* and *motor-2*, presented in chapter 1.2, are designed in the Lab of Prof. Henry Dube, based on the general framework of the photoswitch HTI. The initial design, *motor-1*, is the first light powered molecular motor that can operate under ambient and non-damaging conditions [31]. For its fast and unidirectional rotation, a four-step process involving two thermal and two light-induced steps was proposed [31]. Here, the presented theoretical and experimental investigation sup-

ports the proposed mechanism. From the high-level calculations of the involved excited states, a feasible CoIn could be identified, allowing for ultrafast relaxation in both light-induced steps. The detailed understanding of the complete mechanism of the unidirectional rotation enabled the formulation of three pathways to further increase the rotation speeds and improve efficiency of light-driven molecular motors. The design of *motor-2* [32] incorporated one of these pathways. Reducing one of the thermal barriers, thus removing an isomer from the rotation, resulted in a more efficient three-step process. This is again supported by high-level quantum chemical calculations, identifying a similar CoIn for the photoisomerization. Therefore, the presented study can confirm the validity of removing one metastable isomer in order to improve the efficiency of light-driven molecular motors.

Alongside the ability to initiate photochemical reactions in photoswitches and molecular motors, the interaction of light and matter also opens up the possibility to survey the ultrafast dynamics of these processes with the help of a variety of spectroscopic techniques. To fully time-resolve the dynamic response of a molecule after photoexcitation, very short laser pulses are necessary. The tremendous progress in laser technology over the last decades saw the development of laser sources capable of generating laser pulses covering a wide range of timescales from attosecond to microsecond pulses with energies ranging from the infrared (IR) over the visible (Vis) and ultraviolet (UV) to the X-ray (X-ray) regime [33–41]. This has allowed scientists to not only resolve nuclear dynamics [42, 43], but also the motion of electrons [44, 45] with great detail. Here especially, attosecond transient absorption spectroscopy (ATAS) could be established as a powerful tool capable of resolving coupled non-adiabatic electronic-nuclear dynamics with great spectral and temporal resolution [46–55]. The use of attosecond pulses in the extreme ultraviolet (XUV)/X-ray region not only allowed for the creation of electron wave packets extremely well localized in time, but also enabled element, charge and electronic state sensitive insights by probing the inner-valence and core-level states of the excited molecules. In general, the interpretation of these spectra is quite complicated if inner-valence states (usually M edges) rather than genuine core-level states (K and L edges) are probed. Here, a simulation of the ultrafast dynamics and the spectroscopic process can help in the understanding of these complex interactions between light and matter.

In the second part of this work, a comprehensive framework, for simulating XUV/X-ray transient absorption spectra is introduced (chapter 2.1). Using *ab initio* non-adiabatic molecular dynamics (NAMD), the ultrafast processes of excited molecules after laser excitation can be simulated, making it possible to resolve both the changes in the electronic structure and the nuclear motion over time. Based on this information, the time-dependent XUV/X-ray absorption spectra can be calculated by applying the presented restricted active space self-consistend field (RASSCF)/restricted active space perturbation theory (RASPT2) protocol. Utilizing this framework, two studies uncovering the ultrafast processes after laser excitation in the molecules vinyl bromide (C_2H_3Br) and trifluoroiodomethane (CF_3I) are presented in chapters 2.2 and 2.3.

Artificial Molecular Machines: From Switch to Motor

At the heart of every significant biological process lies a molecular machine performing an often very complex task. In general, molecular machines are molecules that perform a specific task in response to an external stimulus [56], and nature has found fascinating molecules to perform its tasks [57]. One omnipresent example is the light-sensitive receptor protein rhodopsin that plays a vital role in the visual phototransduction cycle enabling our vision. In rhodopsin, the covalently bound 11-*cis*-Retinal and its isomerization to the all-trans-form was identified to be the primary event in the vision cycle [3–7]. Here, the structural change during isomerization after absorption of a photon triggers or switches on a cascade of further reactions, ultimately resulting in an electrical signal that is processed by our brain [58–60]. Having processed the visual signal, the brain might deem what it has seen to be funny and decide to react with a laugh. This reaction will, of course, require the contraction of muscles. The contraction in our muscle cells is made possible by another molecular machine, the motor protein Myosin II [61–65]. In a complex sequence of molecular events called the cross-bridge cycle [66–68], it is able to perform mechanical work using the chemical energy provided by the hydrolysis of adenosine triphosphate (ATP) to adenosine diphosphate (ADP). Following the depletion of ATP, the body needs to replenish its energy reserves, which is again done by the help of a molecular machine, the protein ATP Synthase [69]. Structural ATP Synthase is comprised of two rotary motors F^o, F^1 [70]. The F^1 motor is able to synthesize ATP from ADP and phosphate by utilizing the mechanical torque generated by the rotation of the second motor F^o. Its rotation is powered by the energy of the transmembrane pH gradient [71–74].

Of course, with understanding of how nature's molecular machines operate, scientists started to think about constructing artificial molecular machines to perform specific tasks. One of the first examples of synthetic machines was reported in the early 1980s by Shinkai and Manabe [75]. Using the photoisomerization of azobenzene in combination with crown ethers, they were able to control the transport of ions across liquid membranes. Since these initial steps, numerous advances have been made in this area of research [20, 21, 56, 76–83]. Especially since 2016, when the Nobel Prize in Chemistry was awarded jointly to Jean-Pierre Sauvage, Sir J. Fraser Stoddart and Bernard L. Feringa "for the design and synthesis of molecular machines" [84–86], artificial molecular machines have not only been in the spotlight of the chemistry community, but also the general public. And not without reason, as the possible applications for artificial molecular machines are far-reaching. For example, molecular switches are researched as a medium for optical data-storage [87–90], in altering properties and functions of materials [78, 81] and more recently to trigger reaction cascades in pharmacologic processes [91–95]. Moreover, molecular

motors have been used in drug delivery applications to physically open the lipid bilayer of cellular membranes [96–98].

To further broaden the available building blocks for molecular machines, the search for new molecular switches and motors is an ongoing and growing field of research [99]. Here, especially in regard to possible biological applications, one group of molecules, the HTIs, is very promising [27–30] (see Figure 1.1 for their structure). HTIs are novel photoswitches that are switchable by near UV and visible light. Their photophysical properties can be changed quite significantly by substituting at both carbon rings [28]. This versatility allowed Dube and coworkers to build the first light powered molecular motor (see Figure 1.1 for its structure) that can operate under ambient and non-damaging conditions [31].
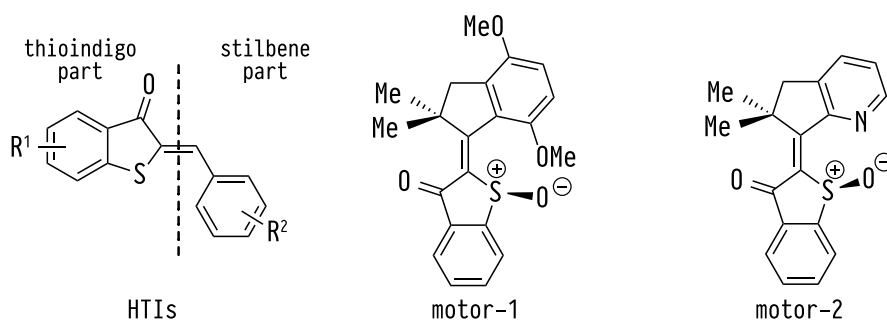

Figure 1.1 – (Left) The HTIs group of molecules are photoswitches that combine a thioindigo and a stilbene fragment. They can be substituted at both carbon rings (R^1, R^2), changing the isomerization dynamics and general photophysical properties. (Middle) Introducing additional stereocenters by oxidizing the sulfur as well as substituting the ring-fused stilbene fragment, results in the molecular motor, *motor-1*. (Right) The second motor, *motor-2*, is built with the same basic thioindigo-stilbene framework in mind, but instead of the methoxy substitution on the stilbene ring, it incorporates nitrogen as a heteroatom into the phenyl ring.

In the following sections, the research on the photoswitch HTI and the two molecular motors, *motor-1* and *motor-2*, based on HTI is presented. Their chemical structures are shown in Figure 1.1. For all three molecules, the relaxation pathways after photoexcitation were elucidated by experimental and theoretical methods. In the case of HTI, a general reaction model for the photoisomerization was developed and the effects of different solvents as well as substitutions are discussed. A thorough investigation into the mechanism of their unidirectional rotation is shown for both motors.

1.1 The Versatility of Hemithioindigo Compounds

Since its first introduction in the early 1900's by Friedländer [100], HTI has been discussed as a molecular switch [101, 102]. HTI combines a thioindigo fragment with a stilbene fragment, and it exists in two different stereoisomers (see Figure 1.2). Upon irradiation with light, it can rotate around the central C=C double bond from the stable Z conformer to the metastable E configuration. Compared to the more commonly utilized photoswitches, stilbenes [103–105] and azobenzenes [18], the HTIs offer a set of distinct photophysical properties making them particularly good candidates for biological applications [28, 29]. First, a high thermal barrier for the *cis/trans* (Z/E) isomerization (typically $>27\,\text{kcal}\,\text{mol}^{-1}$) makes them a very bistable switching system. Second, both directions of the isomerization can be induced by light of different wavelengths ($\lambda_{Z\to E}$ and $\lambda_{E\to Z}$). Third, both absorption wavelengths are redshifted compared to the other mentioned photoswitches, allowing, the use of non-damaging visible light, instead of the usually necessary UV light. Lastly, the photophysical properties can be tuned and changed by introducing different substituent groups to both the stilbene and thioindigo moiety [28].

In the case of the unsubstituted HTI, the reaction pathway and coordinates of the isomerization have been investigated and described very thoroughly by Nenov and coworkers [16].
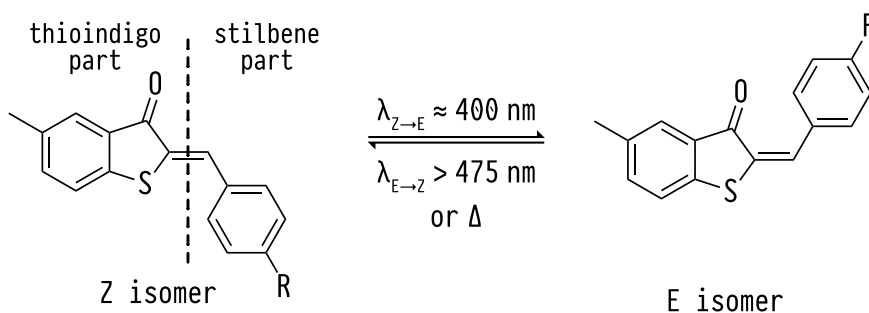
thioindigo part | stilbene part

$\lambda_{Z \to E} \approx 400\,\mathrm{nm}$

$\lambda_{E \to Z} > 475\,\mathrm{nm}$

or Δ

Z isomer — R

E isomer

Figure 1.2 – The light-induced Z/E isomerization of the HTIs, shown by the example of 5-methyl hemithioindigo (5-m-HTI). Thermodynamically, the Z configuration is stable and can be switched to the metastable E configuration upon irradiation with light of $\lambda_{Z \to E} \approx 400\,\mathrm{nm}$. It is also possible to induce the back isomerization with redshifted light of $\lambda_{E \to Z} > 475\,\mathrm{nm}$.

Building upon this work, research shifted to understanding the influences of substituents [106–111], solvents [101, 112, 113] and oxidation state [114] on the photophysical properties. Here, the presented article "Photoisomerization of hemithioindigo compounds: Combining solvent- and substituent- effects into an advanced reaction model" comes in, combining the effects of substituents and solvents, introducing a comprehensive reaction model for the photoisomerization of the HTIs. The presented research opens up new possibilities in the systematic design and tuning of molecular switches. The key points of the article are:

- The Z to E photo-conversion of 5-methyl hemithioindigo (5-m-HTI) in solvents of different polarity in combination with an electron donor or acceptor substituent at the *para* position of the stilbene moiety (see R in Figure 1.2) were measured by ultrafast transient absorption and emission spectroscopy. The solvents were varied starting with the non-polar *n*-hexane, cyclohexane and dodecane, moving to the more polar dichloromethane (DCM) and acetone, and ending with the most polar dimethyl sulfoxide (DMSO). For the three solvents cyclohexane, DCM and DMSO, two additional compounds, 5-m-HTI-OMe and 5-m-HTI-CN, apart from the unsubstituted 5-m-HTI were measured to study the effects of an electron donor substituent ($-$OMe, methoxy group) and an electron accepting one ($-$CN, cyano group).

- Combining the time-resolved absorption and emission measurements allowed for the identification of the different timescales of the relaxation from the excited electronic state to the ground state of the formed photoproduct, the E isomer. Fitting the recorded data sets with multi-exponential functions revealed up to three time constants τ for the complete decay, depending on the solvent and substitution.

- For unsubstituted 5-m-HTI, a strong interaction with the polarity of the solvent was found. The absorption dynamics in the non-polar cyclohexane are modelled well by two time constants, $\tau_1 = 4.5\,\mathrm{ps}$ and $\tau_2 = 58\,\mathrm{ps}$. τ_1 is attributed to a fast initial relaxation from the Franck–Condon (FC) point into an excited state minimum and τ_2 to the further decay pathway of the excited state to the ground state of the E isomer, i.e. the switching of HTI. In polar solvents, e.g., DCM, a third time constant is needed in the analysis of the recorded data set ($\tau_0 = 1.5\,\mathrm{ps}$, $\tau_1 = 32\,\mathrm{ps}$ and $\tau_2 = 216\,\mathrm{ps}$). The new constant τ_0 is attributed to a relaxed structure (RS) that is only stabilized in polar solvents. In general, an increase of the final isomerization time constant τ_3 with the polarity of the solvent is observed, resulting in a maximum lifetime of 590 ps for 5-m-HTI in DMSO.

- For substituted HTIs, it was found that electron donating groups accelerate the isomerization and electron withdrawing groups slow it down. This trend was already discussed by März *et al.* [109], and it is also present in different solvents. Introducing the polar solvent DCM, the final time constant τ_2 for 5-m-HTI-OMe of 12 ps is faster compared to

the 216 ps of the unsubstituted 5-m-HTI, and much slower for 5-m-HTI-CN, where τ_2 is 9000 ps.
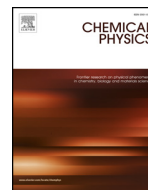
- These experimental observations suggest a transition from the excited state to the ground state via a barrier whose height depends on the solvent and substitution effects. This is supported by the excited state energy profile calculated at the complete active space self-consistend field (CASSCF) level of theory. Here, all critical points on the ground and first excited state PES were optimized. By further analyzing the electronic wavefunction at optimized points, the different effects of solvents and substitutions on the switching speed could be explained by the change in magnitude and direction of the dipole moment throughout the isomerization process. See Fig. 4 of the publication for the complete excited state energy profile and the critical points.

- After excitation to the first excited state S_1, which is of $\pi\pi^*$ character, the system populates a region with significant dipole moment, $\mu_{FC} = 6.5$ D, pointing from the oxygen to the sulfur atom. Here, the electronic structure relaxes and the solvent molecules reorient themselves, leading to an excited state minimum RS, which is still planar but has a stronger dipole moment pointing from the stilbene to the thioindigo moiety. The RS only forms a distinct minimum in polar solvents, resulting in the additional time constant. Now partially rotating around the central C=C bond, the system relaxes into the S_1 Minimum (MinZ), with a similar large dipole moment of $\mu_{MinZ} = 8.9$ D pointing roughly in the same direction. During further rotation, the system passes a region, labeled 'region V' in the paper, where the second excited state S_2, having charge transfer (CT) character ($n\pi^*$), comes energetically close to the S_1 state. This avoided crossing forms a barrier on the relaxation pathway to the ground state of the E isomer. Here the system's wavefunction becomes a mixture of the $\pi\pi^*$ and CT configuration. After passage of the barrier a zwitterionic configuration at about $90°$ rotation is reached. This state can be stabilized in polar solvents, but otherwise is a transition state (TS) connecting two CoIns leading to the ground state. At this TS the dipole moment of $\mu_{TS} = 8.4$ D has flipped, pointing now from the thioindigo to the stilbene moiety. Therefore, at the barrier 'region V' the dipole moment nearly vanishes because, here, the $\pi\pi^*$ and CT states with their opposing dipole moments mix.

- The excited state energy profile leads to the conclusion that the switching speed is dictated by the height of the barrier in 'region V'. But with no significant dipole moment, the barrier itself can not be influenced directly by the polarity of the solvent. The observed influence of solvents can be explained instead by the stabilization of MinZ in polar solvents, consequently changing the effective barrier height and resulting in the increased time constant τ_2 as well as the additional τ_0. Direct influence on the barrier height is only possible by changing its electronic character through the introduction of electron donor or acceptor substituents.

Photoisomerization of hemithioindigo compounds: Combining solvent- and substituent- effects into an advanced reaction model

Franziska F. Graupner[a], Teja T. Herzog[a], Florian Rott[b], Sven Oesterling[b], Regina de Vivie-Riedle[b], Thorben Cordes[a,c,*], Wolfgang Zinth[a,*]

[a] Lehrstuhl für BioMolekulare Optik, Department für Physik and Munich Center for Integrated Protein Science CIPSM, Ludwig-Maximilians-Universität München, Oettingenstraße 67, 80538 München, Germany
[b] Department of Chemistry, Ludwig-Maximilians-Universität München, Butenandt-Str. 5-13, 81377 München, Germany
[c] Physical and Synthetic Biology, Faculty of Biology, Ludwig Maximilians-Universität München, Großhadernerstr. 2-4, 82152 Planegg-Martinsried, Germany

A B S T R A C T

Time resolved absorption and emission experiments are combined with quantum chemical calculations to obtain a quantitative understanding of the light-induced Z to E isomerization of the hemithioindigo photoswitch. Substitution and solvent polarity change the Z to E reaction time by three orders of magnitude from 9 ps for the para-methoxy substituted 5-methyl hemithioindigo in the unpolar cyclohexane to 9 ns for the para-cyano substituted molecule in di-chloromethane. A comparison with quantum chemical calculations reveals the role of the solvent polarity on the reaction speed for distinct substitution patterns of the stilbene moiety. The dipole moments of the different hemithioindigo photoswitches strongly vary on the excited state potential energy surface. Energetic stabilization of the minimum and simultaneous destabilization in the transition region increase the effective reaction barrier for polar solvents, thus strongly decelerating the reaction.

1. Introduction

Photoswitchable molecules have interesting applications ranging from optical data storage, structural switching in smart media, photopharmacology for targeted medical treatments, control of biochemical functions and (artificial) molecular motors [1–5]. For specific applications different classes of photoswitchable molecules are used with adapted chemical properties [6]. A versatile and well-studied class of photochromic molecules is based on hemithioindigo (HTI), a compound introduced originally in the early 1900's and discussed extensively as a molecular switch for more than two decades [7,8]. The HTI molecule features efficient photoswitching by visible and UV-light and thermal stability of its two stereoisomers Z and E (see Scheme 1). HTI is composed of a hemi-thioindigo and a hemi-stilbene moiety that are connected via a central double bond. HTI can undergo photo-isomerization between the stereoisomers Z and E. While the Z-form is thermodynamically favored, a substantial ground state barrier renders the E-isomer metastable for many hours before thermal reconversion to Z takes place at room temperature (see Scheme 1). Depending on the specific substitution pattern of HTI, optical excitation leads to Z/E-photoisomerization on the picosecond time scale with photochemical quantum yields of up to 50% [9–12].

Detailed studies of HTI using systematic chemical substitution revealed a Hammett-like behavior of the photochemical reaction [11,13,14], allowing a directed optimization of the switching speed. This knowledge was utilized in HTI-chromopeptides where HTI operates as a backbone switch to trigger conformational changes in peptide structures [9,15–18] and more recently also for building artificial molecular motors with kHz rotation speeds [3,19]. Ultrafast and reversible switching of light-operated HTI-hairpin peptides could be demonstrated in picosecond infrared experiments [17].

In a previous publication HTI compounds with strongly donating substitutions were studied to obtain photoswitches with highest switching speed [11]. Surprisingly a speed limit was observed. A rise of reaction speed with increasing donor strength of the substitution on the hemi-stilbene moiety was followed by decreasing reaction speed for very strong electron donors. In another more recent study pre-twisting of the HTI-structure was induced by ortho substitutions [12]. In these molecules a strong dependence of reaction speed and reaction pathway – double bond isomerization versus the formation of a twisted intramolecular charge transfer state – on the solvent polarity was observed.

In this paper we lay the ground for a quantitative understanding of the photoinduced reactions of HTI also with respect to solvent environment and substitution. First steps were already taken previously using quantum chemical calculations for non-substituted HTI in

---

Scheme 1. Molecular structure of the studied 5-methyl-HTI compounds with residues R = H, OMe, CN. Photoisomerization from Z → E can be induced by excitation light ≈ 400 nm (hν_1), while the back reaction (not studied here) is exclusively triggered by wavelengths above 475 nm (hν_2).

vacuum [10]. A refinement introduced here allows to treat substituted HTI and the role of the surrounding solvent. For this we combined time-resolved spectroscopy on substituted HTI molecules in different solvents with quantum chemical calculations. The Z to E photo-conversion of 5-methyl hemithioindigo (5-m-HTI) was investigated in solvents of different polarity for different substitution patterns at the stilbene part in para-position by groups of electron donating or withdrawing power. Special emphasis was put on combination of time-resolved absorption and emission measurements to identify the timescale of photoproduct formation, i.e., the transition from the excited electronic state to the electronic ground-state and the product E-photoisomer. A theoretical analysis explains the obtained results within the scope of a previously presented reaction model [10]. The comparison of experiments and theoretical analysis shows that the dipole moment of HTI in the excited electronic state strongly changes during the motion on the potential energy landscape. The influence of the reaction on the polarity of the solvent reflects the modulation of the energetic landscape in the excited electronic state by the stabilization of polar states of HTI. Our study shows the power of combined experimental and theoretical methods to improve the understanding of relevant photochemical processes and facilitates the rational design of photoswitchable compounds with tailored properties.

2. Materials and methods

The methods for time-resolved experiments have been published previously [20]. Here, we provide a brief summary: Steady state spectra were recorded using a spectrophotometer LAMBDA 750 (Perkin Elmer) and a spectrofluorometer Fluorolog 3 (HORIBA). The time resolved fluorescence signal was recorded using a Hamamatsu streak camera (C5680-24C) setup. The excitation pulses were generated from the output of a CPA-system (Clark, MXR-CPA-2001) with pulse duration of about 180 fs at 778 nm. Second harmonic generation (SHG) resulted in excitation pulses centered at 389 nm. Pulse energies ranging from 100 nJ to 500 nJ were employed. Time zero in the emission traces was not determined experimentally. The zero positions of the time axis of Fig. 3 are influenced by the timing between laser system and streak camera and do not coincide with the peak of the excitation pulse. In the fluorescence traces of Fig. 2, time zero was determined as a fitting parameter in the data analysis procedure.

Transient absorption changes were measured with a UV/Vis pump-probe setup according to [20]. Excitation pulses (pump) and white light continuum (probe) were generated from a Ti-sapphire femtosecond laser-amplifier system (Spectra Physics, Spitfire pro) with central wavelength at 800 nm and 90 fs pulse duration. While the excitation light at 400 nm was generated by SHG, the probe pulse was produced by a continuum generation process in CaF_2 [21]. Both pulses were focused onto the sample, under magic angle conditions with typical beam diameters of 150 µm and 50 µm, respectively.

The analysis of the time resolved absorption and fluorescence data

was performed using a sum of exponential functions where the time constants and the amplitudes are determined by a least square fit. In the global analysis, each data set recorded at different probing or emission wavelengths was fitted with one set of time constants for all wavelengths. The fit amplitudes determined as a function of wavelength yield the decay associated spectra.

For all time resolved measurements the sample solution was pumped (by a peristaltic pump) through a fused silica flow-cell (0.5 mm sample layer thickness) with a speed allowing to exchange the irradiated volume between consecutive laser pulses. Throughout the experiments the sample container was illuminated by a cold light source (SCHOTT, KL2500 LCD) equipped with long-pass filter (SCHOTT GG 475, 3 mm thickness) in order to avoid accumulation of the E-isomer.

All solvents used for spectroscopic experiments were obtained from Merck (Darmstadt, Germany) or Sigma Aldrich (Taufkirchen, Germany) in the highest purity available (spectroscopic grade) and used as received. Substitution of the investigated HTI molecules was varied in para-position of the stilbene ring (see Scheme 1). Besides standard 5-m-HTI (R = H, 5-m-HTI-H) we used an electron donating (5-m-HTI-OMe) and electron withdrawing (5-m-HTI-Br, 5-m-HTI-CN) substitution. The HTI derivatives were synthesized by the lab of Karola Rück-Braun according to published methods [7,22–25] and were already used and described in previous publications [13].

If not otherwise stated all quantum chemical calculations were performed using the program package Molpro2012 [26] and the 6-31G* basis set. The geometry of the Franck Condon point (FC) was optimized at the DFT level of theory using Gaussina09 [27] and the hybrid functional B3LYP. The geometries of the planar relaxed structure (RS), the minimum of the S_1 state (MinZ) and the S_0 transition state (TS(S_0)*) were optimized using the complete active space SCF (CASSCF) method. For RS and MinZ an active space (AS) of 12 electrons and 11 orbitals was used (AS(12,11)) including the central carbon-carbon double bond, the sulfur lone pair as well as two sets of bonding and antibonding π orbitals on the stilbene part and the thioindigo part. The TS(S_0)* geometry was optimized with an AS(2,2). All dipole moments were calculated on the single state CASPT2 (SS-CASPT2) level of theory as implemented in Molpro2012 (RS2), based on CASSCF AS(2,2) wavefunctions of the optimized geometries. All shown electrostatic potentials (ESP) are also based on these CASSCF wavefunctions.

3. Results

3.1. Stationary spectroscopy

A first qualitative overview on the influence of the solvent on HTI properties was obtained from stationary absorption and fluorescence spectroscopy. The spectra of 5-m-HTI-H in different solvents are shown in Fig. 1. For the non-polar solvent cyclohexane we find an absorption spectrum (Fig. 1A) with vibronic progression and a major peak at 436 nm. When 5-m-HTI-H is dissolved in a more polar solvent the absorption spectrum broadens, loses vibronic structure and shifts weakly to longer wavelengths. For 5-m-HTI-H in DMSO the absorption peaks at 443 nm. A stronger effect of the solvent is seen in the emission (Fig. 1B). The fluorescence spectrum in cyclohexane peaks at 461 nm and exhibits a weak Stokes shift of 1244 cm^{-1}. For more polar solvents one observes broadening and a strong red shift of the emission spectra. As one example one finds for 5-m-HTI-H in DMSO λ_{fl} = 529 nm and a corresponding Stokes shift of 3670 cm^{-1}. For substituted 5-m-HTI-H similar trends regarding the emission peaks are found (for details see Supplementary material SM-Fig. 1). The observations point to an emitting state with a dipole moment increasing upon substitution from OMe via H to CN. The dipole moment leads to a stabilization of this state in polar solvents causing the increase of the emission wavelength.
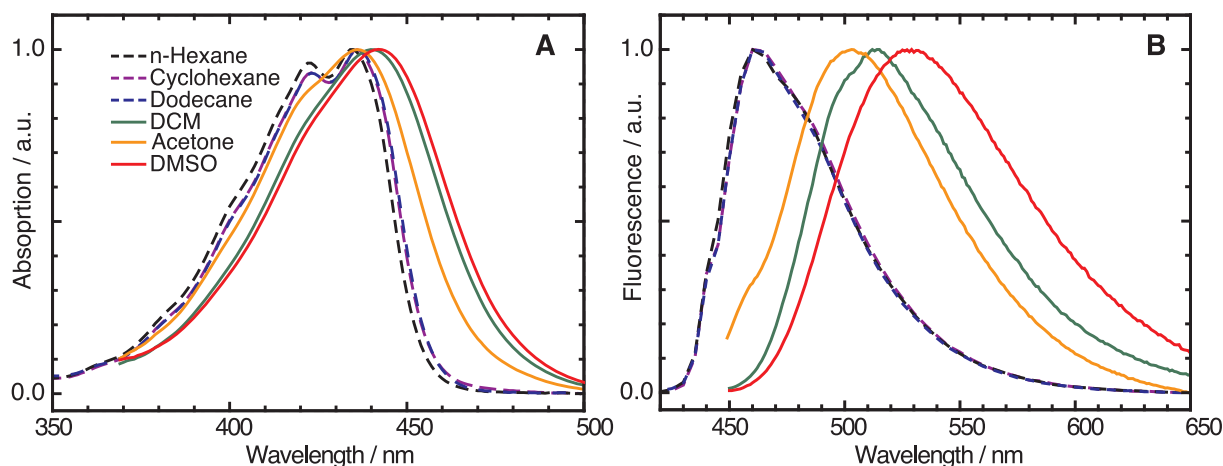
Fig. 1. Normalized spectra of 5-m-HTI-H in different solvents. A) Absorption spectra. B) Stationary fluorescence emission upon photo-excitation at 398 nm. Absorption and emission spectra of other substituted HTI are shown as Supplementary Material (SM-Figs. 1 and 2).

3.2. Time resolved experiments on the Z to E isomerization

Fig. 2 gives an example for the influence of the solvent polarity on the reaction dynamics. The results from time-resolved experiments for un-substituted 5-m-HTI-H in the non-polar solvent cyclohexane are shown on the left part, those for the more polar solvent dichloromethane (DCM) on the right. In the upper part **A** we compare transient absorption and emission data. From these it is evident that both techniques monitor similar processes: The excited state decay (as seen by fluorescence transients, Fig. 2A) correlates with the decay of the induced absorption (as seen by transient absorption experiments, Fig. 2A) thus monitor excited state dynamics. Both techniques show a non mono-exponential excited state decay and that the reaction is faster in the non-polar solvent.

The central part **B** of Fig. 2 presents an overview of the transient absorption data $\Delta A(\lambda_{pr}, t_D)$ recorded at different probing wavelengths λ_{pr} as a function of delay time t_D. The results of a global analysis of these data by multi-exponential functions, are given in the lower part. For the non-polar solvent cyclohexane the absorption data are well modelled by two exponentials with time constants $\tau_1 = 4.5$ ps and $\tau_2 = 58$ ps. The related decay associated spectra (DAS) are shown in the lower part **C** of Fig. 2. The fast kinetic component reflects some changes in excited state absorption and in stimulated emission (around 580 nm) which are likely related to a motion out of the Franck-Condon range. The dominating component with a time constant of $\tau_2 = 58$ ps, reflects the final decay of the excited state absorption and the recovery of the essential part of the ground state absorption. This interpretation is supported by the time-resolved fluorescence with a time constant $\tau_{fl} = 60$ ps which is in agreement with τ_2 from the absorption experiment. The offset seen at late delay times represents the absorption shift due to the formation of 5-m-HTI-H molecules in the E-form. The analysis of the emission data yields the longer time constant $\tau_{fl} = 60$ ps nearly identical to τ_2 from the absorption experiment. This experiment supports the interpretation that the decay of the fluorescence emission, i.e. the transition from the excited electronic state to the ground state occurs simultaneously with the dominant absorption change observed in the transient absorption experiment. Modeling the absorption data of the 5-m-HTI-H in the polar solvent requires three kinetic components. For 5-m-HTI-H in DCM time constants of $\tau_0 = 1.5$ ps, $\tau_1 = 32$ ps and $\tau_2 = 216$ ps are found. Again the longest time constant in absorption also appears as the final decay time in the emission data and represents the transition away from the excited electronic state to the ground state. These data shown here are in good qualitative agreement with recent results from other HTI molecules with similar substitutions [11,13].

Additional information on the solvent dependence of 5-m-HTI-H is

obtained from a set of time-resolved emission experiments (see Fig. 3) which supply the time constants of the decay of the excited state. The results are summarized in Table 1, where the time constants $\tau_{fl} = \tau_2$ representing excited state decay (i.e. the isomerization) are given for the different solvents. The time constants depend strongly on the polarity of the solvent represented by the dipole moment μ_{sol} or the dielectric constant ε. Short lifetimes in the 50 ps range are found for $\mu_{sol} < 0.1$ D. We find longer decay times between 200 and 600 ps in polar solvents $\mu_{sol} > 1.5$ D. In contrast, only a weak viscosity dependence is found for the excited state decay. As one example, the chemically related *n*-hexane and cyclohexane have a 3-fold differing viscosity, but the fluorescence lifetimes τ_{fl} of 5-m-HTI-H varies only by a factor of ~1.33 (see Table 1).

Additional time-resolved absorption and emission experiments were performed for substituted 5-m-HTI-OMe (electron donor substitution) and 5-m-HTI-CN (electron acceptor substitution) in the solvents cyclohexane, DCM and DMSO. The time constants of the excited state decay, i.e. τ_{fl} (which are equivalent to τ_2), are summarized in Table 2. The corresponding emission data is shown in SM-Fig. 3. The following general features are observed: (i) For the electron donating substituent methoxy group, R = OMe the decay of the excited electronic state is always much faster (e. g. $\tau_{fl} = 12$ ps in DCM) than for un-substituted 5-m-HTI-H (e. g. 216 ps in DCM). For the electron withdrawing substituent, R = CN, a much slower decay ($\tau_{fl} = 9000$ ps) is observed. (ii) In comparison between different solvents, a lower solvent polarity favors faster excited state decay.

3.3. Quantum chemical treatment of the excited state of HTI

The experimental observations indicate that the transition from the excited state to the ground-states is controlled by a barrier whose height depends on the substituents and the polarity of the solvent. We calculated the optimized structures of the critical points in the ground (S_0) and first excited $\pi\pi^*$ state (S_1), which leads to the energy profile of the isomerization shown in Fig. 4. By inspection of the electronic wavefunction we can predict how this profile will be influenced during the reaction by polar solvents. The main barrier (marked as region V in green) for the isomerization from the Z-isomer to the E-isomer arises from an avoided crossing between the initial $\pi\pi^*$ configuration, and a charge transfer state $S_2(CT)$. The CT character is stabilized during the isomerization. The rotation around the central double bond lifts the π bond and both electrons switch to the remaining p-orbital of the thioindigo fragment.

The important geometries on the excited state with $\pi\pi^*$ character are the Franck-Condon point FC*, the relaxed structure RS and the
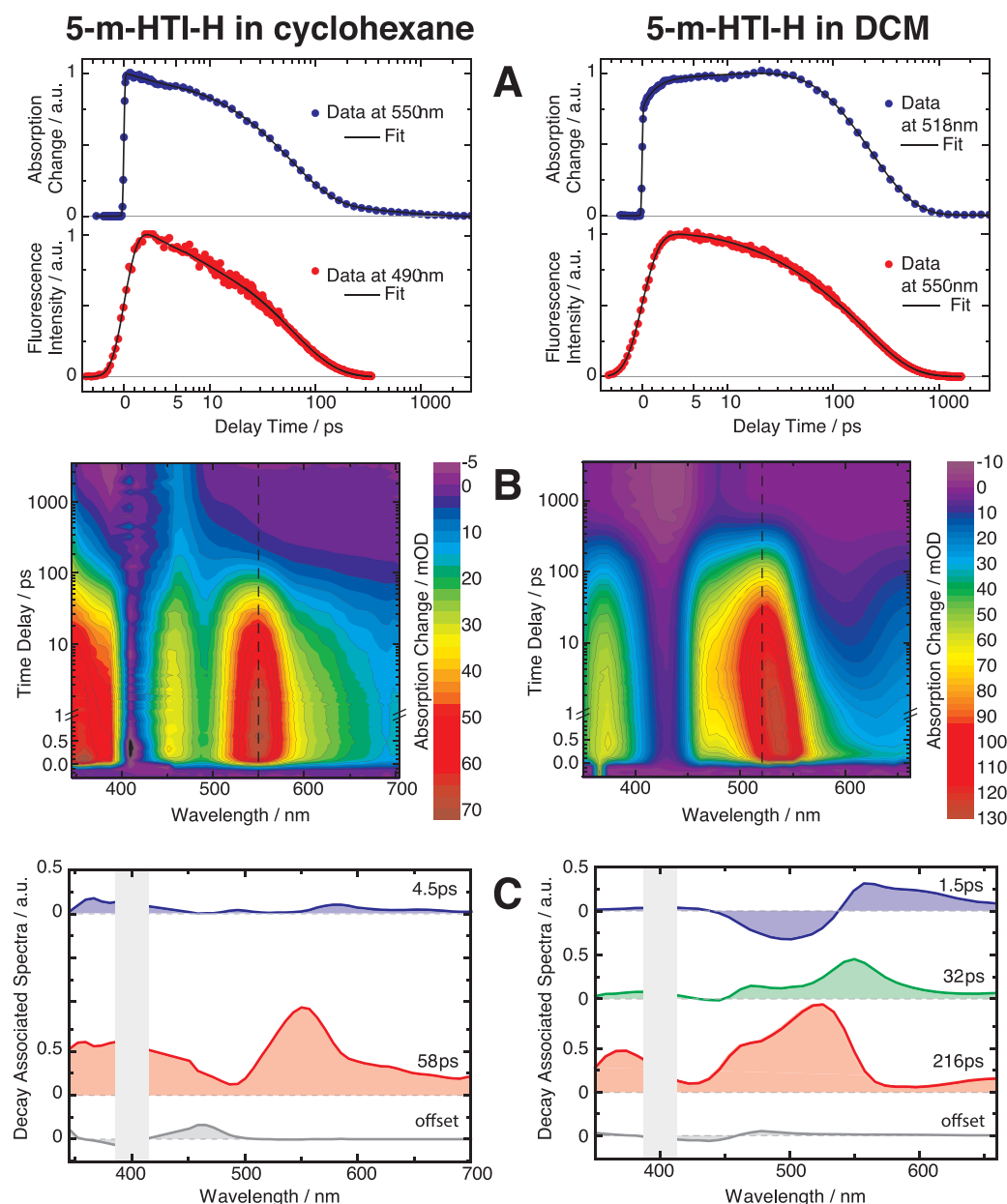
Fig. 2. Absorption and emission dynamics for 5-m-HTI-H in the non-polar solvent cyclohexane (left panels) and the polar solvent DCM (right panels). A) Transient absorption change (blue points) at the peak of the excited state absorption (see dashed lines in B) and fluorescence signal (red points) at the emission maximum. Solid lines: Multiexponential model functions describing absorption and emission curves with one set of lifetimes for each solvent. B) 2D-display of the absorption changes (color coded) at different wavelengths and delay times. C) Decay associated spectra (DAS) obtained upon a multiexponential modeling of the absorption data with the indicated time constants. Grey bars cover absorption data influenced by stray light from excitation pulses. (For interpretation of the references to colour in this figure legend, the reader is referred to the web version of this article.)

minimum MinZ. In the region V of the barrier the adiabatic wave-function becomes a mixture of both the $\pi\pi^*$ and the CT ($n\pi^*$) configuration. Further rotation will lead to the zwitterionic configuration at 90°, which can be stabilized in polar solvents and becomes otherwise a transition state (TS) connecting two conical intersections (CoIn) with the ground state [10] symbolized as one CoIn in Fig. 4. It was not feasible to optimize this TS in the excited state, therefore we used the geometry of the S_0 transition state $(TS(S_0)^*)$ as closest reference point. It is the TS of the isomerization in the electronic ground state. A measure for the change in electron distribution along the reaction profile is the dipole moment and the ESP. Both are calculated for the critical points and are shown in Fig. 4 (top) and in Table 3.

Comparison of the dipole moments shows, that their direction

nearly flips between the $\pi\pi^*$ state and the CT state. A small component of the dipole moment remains pointing from the oxygen atom to the sulfur atom throughout the isomerization. The larger components point along the central double bond. For the $\pi\pi^*$ configuration this part points from the stilbene moiety to the thioindigo fragment and for the CT configuration in the reversed direction. Due to the mixture of electronic character in the region V of the barrier the dipole moment nearly vanishes in this area. The calculated ESP supports this finding.

4. Discussion

Previous experiments on substituted HTI in polar solvents revealed a pronounced substitution dependence which was explained by a
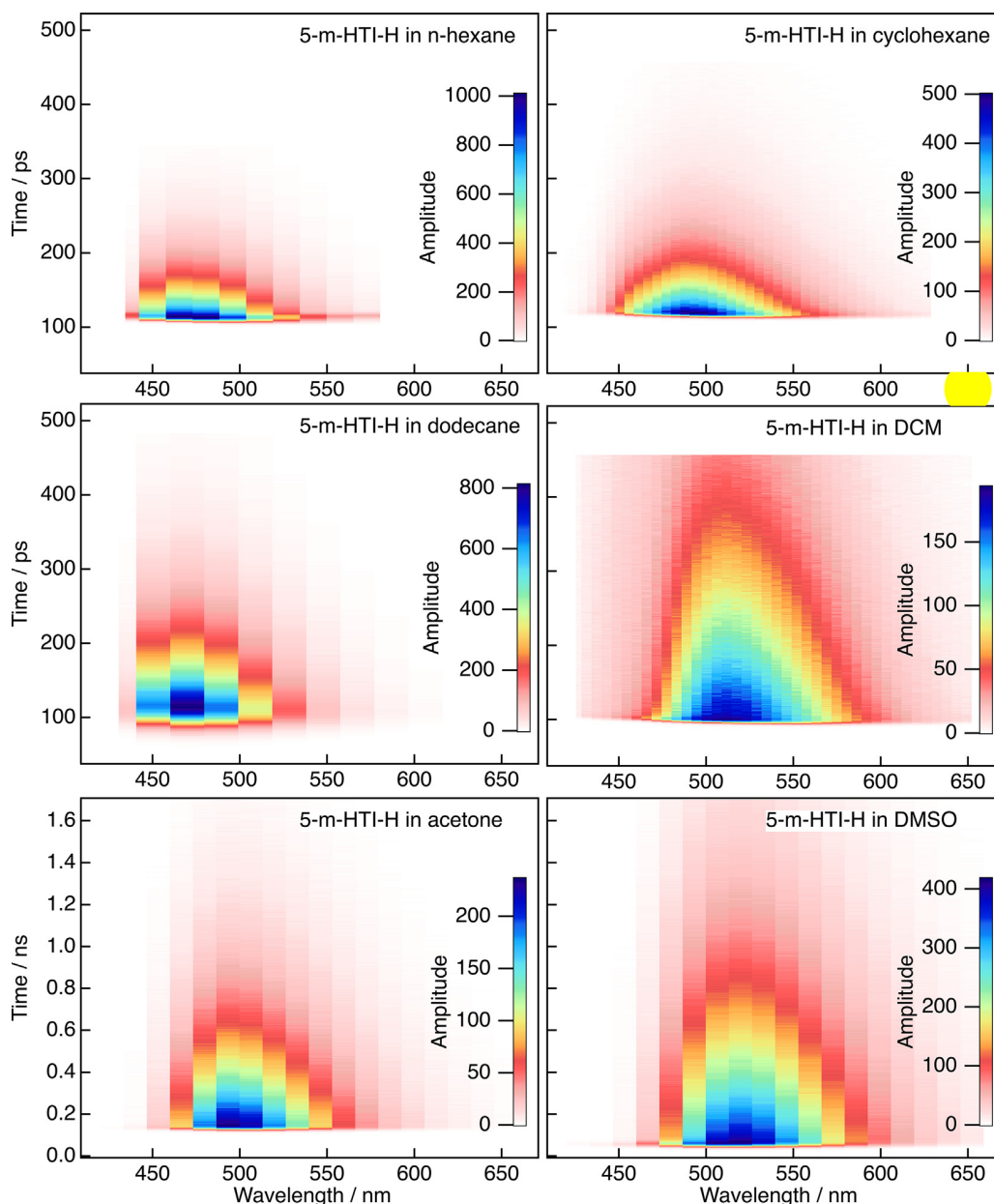
Fig. 3. Time-resolved emission data (color coded) for the unsubstituted 5-m-HTI-H in different solvents. The time constants τ_{fl} range from 45 ps to 590 ps (see Table 1). Spectral resolution of the recorded data was 10 nm. The pixels along the wavelength axis were suitably binned to obtain amplitudes (counts/pixel) allowing a reasonable quality of the fitting process. (For interpretation of the references to colour in this figure legend, the reader is referred to the web version of this article.)

Table 1

Results of the time resolved fluorescence measurements of un-substituted 5-m-HTI-H in different aprotic solvents. τ_{fl} refers to the lifetime of the major fluorescence component representing the decay of the excited electronic state (data see Fig. 3). Solvent parameters dipole moment μ_{sol} and viscosity η (at 25 °C) are taken from [31] and dipole moments indicated by * from [32].

	n-Hexane	Cyclohexane	Dodecane	DCM	Acetone	DMSO
τ_{fl} [ps]	45	60	70	216	360	590
μ_{sol} [D]	0.09*	0.00*	0.00*	1.60	2.88	3.96
ε_r	1.89	2.02	2.01	8.93	21.01	47.24
η[mPa s^{-1}]	0.30	0.89	1.38	0.413	0.306	1.99

Table 2

Results of the time resolved fluorescence measurements of 5-m-HTI with para substituted hemi stilbene in different aprotic solvents. For each combination the reaction limiting time constant τ_{fl} is shown which refers to the decay of the major fluorescence component. This time constant is qualitatively reproduced in the time resolved absorption experiments. The corresponding fluorescence data are shown in Fig. 3 and SM-Figs. 3 and absorption data in SM-Figs. 4.

		Solvent		
		Cyclohexane	DCM	DMSO
para-substitution	–OMe	9 ps	12 ps	25 ps
	–H	60 ps	216 ps	590 ps
	–CN	180 ps	9000 ps	6000 ps

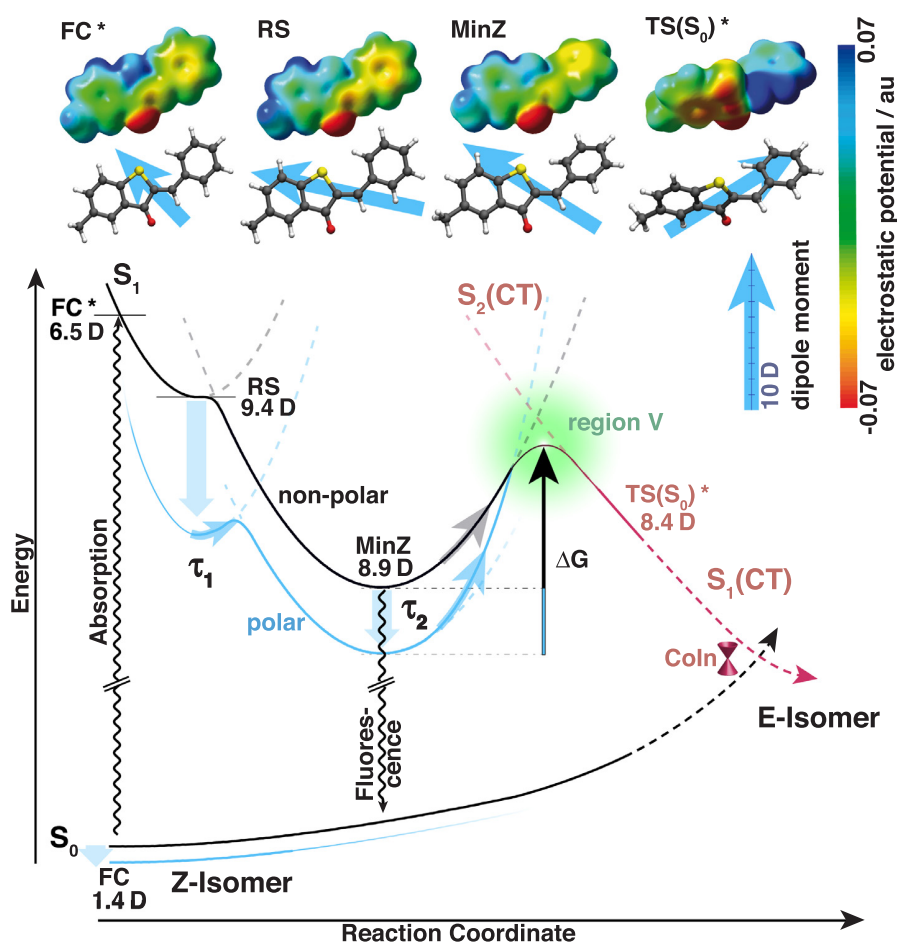**Fig. 4.** Reaction model with molecular dipole moments at important areas of the excited state potential surface. The upper part shows the electronic potential isosurface at an electron density of 5-m-HTI-H. The corresponding molecular structures are shown underneath together with the dipole moments drawn to scale and centered at the molecular center of mass. The reaction scheme in black illustrates the results of quantum chemical computations of un-substituted 5-m-HTI-H in vacuum. The blue potential surface rationalizes the deformation of the potential surfaces by the influence of a polar solvent. (For interpretation of the references to colour in this figure legend, the reader is referred to the web version of this article.)

Table 3

Molecular dipole moments μ^D and angle δ towards the central C=C double bond of the HTI compounds for different substitutions and for characteristic regions on the excited state surface. Between MinZ and TS(S_0)* the projection of the dipole moment onto the central double bond ($\mu^D \cos(\delta)$) changes sign. See Fig. 4.

		Transient states									
		FC		FC*		RS		MinZ		TS(S_0)*	
Substitution	OMe	3.1 D	72°	7.0 D	3°	9.7 D	36°	8.9 D	41°	10.3 D	154°
	H	1.4 D	59°	6.5 D	46°	9.4 D	26°	8.9 D	31°	8.4 D	148°
	CN	6.0 D	27°	11.5 D	71°	14.7 D	2°	14.3 D	6°	4.7 D	144°

qualitative reaction model [15,16]. The Franck Condon State FC* populated by light absorption relaxes quickly ($\tau_0 \approx 1$ ps) by reorientation and redistribution of the polar solvent molecules and by a first rearrangement of the structure of HTI. In this process a relaxed state RS is formed in polar solvents. In a subsequent reaction (τ_1) the system evolves to the excited state minimum MinZ by changing the electronic structure and slightly twisting around the central double bond. From MinZ the reaction proceeds over a barrier V where the isomerization reaction to the E isomer or the back reaction to the ground state of the isomer Z occurs. The observed substituent effects on the lifetime τ_2 can be explained by tuning the height of the effective barrier V, either by changing the energy of MinZ and/or by changing the electronic character at the barrier. This was already predicted on the basis of detailed quantum chemical calculations on HTI [10]. We now extend this study to obtain a consistent picture of the reactions of native and substituted HTI in different solvents. We make use of the fact that the dipole moment is a quantitative measure to monitor the changes in charge distribution upon electronic excitation and during the isomerization of

HTI. The temporal change in charge distribution, together with the polarity of the solvent tune the energetics and finally determine the reaction dynamics.

When HTI is optically excited, it starts from a ground state with low dipole moment $\mu_{Z,S0} = 1.4$ D to the Franck Condon state FC* which has a significant dipole moment of $\mu_{FC^*} = 6.5$ D. This fast induced dipole moment is oriented with an angle $\delta = 46°$ towards the central double bond (see Fig. 4 and Table 3) thus pointing from the oxygen to the sulfur. Rearrangement of the electronic structure and reorganization lead to a relaxed state RS which is still essentially planar, but has a stronger dipole moment forming a small angle ($\delta = 26°$), i.e., the dipole moment points from the stilbene to the thioindigo part. The lifetime of this relaxed state is visible in the polar solvents via the intermediate time constant τ_1. In non-polar solvents this state does not form a distinct minimum on the potential energy surface. Accordingly the experiments for HTI compounds in non-polar solvents do not show a related time constant τ_1 in the reaction dynamics. Partial rotation around the central double bond combined with a pyramidalization leads to the minimum

MinZ. The molecule still has a large dipole moment (μ_{MinZ} = 8.9 D) in roughly the same direction. From this long-lived state the dominant part of the fluorescence emission originates. With a further rotation around the central double bond the system passes the region V where the second excited state S_2(CT) comes energetically close to the S_1 state. Beyond this region the transition state TS(S_0)* is reached at approximately 90° rotation, where the dipole moment has flipped. It has an angle $\delta \approx 148°$ and points from the thioindigo to the stilbene part. The charge distribution reflects the zwitterionic character at this geometry (Fig. 4).

This charge migration during the photoinduced isomerization of the HTI molecule can explain most of the experimentally observed solvent dependence. When 5-m-HTI-H is in a non-polar solvent the changes in dipole moment of the solute do not lead to significant stabilization of the respective states. There should be only a weak shift of the fluorescence emission and a small reaction barrier should lead to a fast S_1-decay. After light absorption, the reaction will proceed with a fast motion away from the Franck Condon state FC* towards the excited state MinZ. The weak stabilization of MinZ for small dielectric constants of the medium results in a small Stokes-shift of the fluorescence emission (see Fig. 1). Subsequently the reaction proceeds via the barrier V with a small height ΔG passing thereafter the transition state TS (S_0)* from where the CoIns to the groundstate can be reached. Thus the poor stabilization of MinZ results in a fast reaction.

In polar media energetic stabilization may become important. The red-shift of emission spectra of 5-m-HTI-H directly demonstrates a significant stabilization of the fluorescing state MinZ. The stabilization due to the solvent occurs with delay times related to electronic and reorientational response of the solvent with respect to the change in charge distribution during the isomerization and is indicated as the blue energy profile in Fig. 4. The degree of stabilization of the critical points depends on their dipole moment and the dielectric constant of the solvent (see Table 3) [28–30]. This stabilization can explain the appearance of an additional transient component during the excited state reaction of 5-m-HTI-H in polar solvents when the region corresponding to state RS is stabilized due to its higher dipole moment and becomes a local minimum. Another consequence of a strong stabilization appears at MinZ. Due to the large dipole moment μ_{MinZ} = 8.9 D the energy of MinZ is strongly stabilized in the polar solvents. As already mentioned the dipole moment nearly vanished in the region V (Fig. 4), which is thus not stabilized. Since the subsequent reaction is controlled by the effective barrier the overall reaction is decelerated.

For substituted 5-m-HTI the combined action of substitution and solvent polarity are described within the same model. The Stokes shift increases with polarity and the reaction slows down. Comparing the molecular dipole moments of the excited state intermediates (Table 3) one finds that for all substitutions the dipole moments flip their directions between MinZ and TS(S_0)* by large angles. Therefore one can expect that the dipole moment in the region of the barrier is vanishing. Thus stabilization of MinZ by polar solvents slows down of the photoreaction. A direct confirmation comes from the electron accepting substitution CN where the largest dipole moment of MinZ was calculated and where the longest time constants were found in polar solvents.

5. Conclusions

In conclusion, the presented experimental and theoretical investigations lead to a consistent picture of the photoisomerization reaction of HTI-compounds in different solvents. The changes in reaction dynamics which range from few picoseconds to the nanoseconds, can be well explained with quantum chemical modeling. Upon optical excitation the different HTI-molecules proceed on the excited state potential energy surface via regions with strongly changing dipole moments. Thus the potential energy surface in the excited electronic state is strongly affected by solvent polarity and by substitution. Note that

stabilization due to the solvent typically occurs with a time delay reflecting the response time of the solvent to the changes in charge distribution during the isomerization. Most important is the stabilization of the excited state minimum where the dipole moment of the HTI-compounds varies with substitution. Combined with a small or vanishing dipole moment in the range of the energetic barrier this leads to the strong changes in the reaction time constants. The presented reaction model gives important insights into the behavior of molecular switches in different environments and opens new strategies for the design and the systematic tuning of molecular switches.

Appendix A. Supplementary data

Supplementary data associated with this article can be found, in the online version, at https://doi.org/10.1016/j.chemphys.2018.07.043.

References

[1] L.A. Huber, K. Hoffmann, S. Thumser, N. Böcher, P. Mayer, H. Dube, Direct observation of hemithioindigo-motor unidirectionality, Angew. Chem. Int. Ed. 56 (2017) 14536–14539, https://doi.org/10.1002/anie.201708178.

[2] C. Petermayer, S. Thumser, F. Kink, P. Mayer, H. Dube, Hemiindigo: highly bistable photoswitching at the biooptical window, J. Am. Chem. Soc. 139 (2017) 15060–15067, https://doi.org/10.1021/jacs.7b07531.

[3] R. Wilcken, M. Schildhauer, F. Rott, L.A. Huber, M. Guentner, S. Thumser, K. Hoffmann, S. Oesterling, R. de Vivie-Riedle, E. Riedle, H. Dube, Complete mechanism of hemithioindigo motor rotation, J. Am. Chem. Soc. 140 (2018) 5311–5318, https://doi.org/10.1021/jacs.8b02349.

[4] J. Broichhagen, T. Podewin, H. Meyer-Berg, Y. von Ohlen, N.R. Johnston, B.J. Jones, S.R. Bloom, G.A. Rutter, A. Hoffmann-Röder, D.J. Hodson, D. Trauner, Optical control of insulin secretion using an incretin switch, Angew. Chem. Int. Ed. 54 (2015) 15565–15569, https://doi.org/10.1002/anie.201506384.

[5] T. Podewin, J. Broichhagen, C. Frost, D. Groneberg, J. Ast, H. Meyer-Berg, N.H.F. Fine, A. Friebe, M. Zacharias, D.J. Hodson, D. Trauner, A. Hoffmann-Röder, Optical control of a receptor-linked guanylyl cyclase using a photoswitchable peptidic hormone, Chem. Sci. 8 (2017) 4644–4653, https://doi.org/10.1039/C6SC05044A.

[6] C. Brieke, F. Rohrbach, A. Gottschalk, G. Mayer, A. Heckel, Light-controlled tools, Angew. Chem. Int. Ed. 51 (2012) 8446–8476, https://doi.org/10.1002/anie.201202134.

[7] T. Yamaguchi, T. Seki, T. Tamaki, K. Ichimura, Photochromism of hemithioindigo derivatives. I. Preparation and photochromic properties in organic solvents, Bull. Chem. Soc. Jpn. 65 (1992) 649–656, https://doi.org/10.1246/bcsj.65.649.

[8] T. Seki, T. Tamaki, T. Yamaguchi, K. Ichimura, Photochromism of hemithioindigo derivatives. II. Photochromic behaviors in bilayer membranes and related systems, Bull. Chem. Soc. Jpn. 65 (1992) 657–663, https://doi.org/10.1246/bcsj.65.657.

[9] T. Cordes, D. Weinrich, S. Kempa, K. Riesselmann, S. Herre, C. Hoppmann, K. Rück-Braun, W. Zinth, Hemithioindigo-based photoswitches as ultrafast light trigger in chromopeptides, Chem. Phys. Lett. 428 (2006) 167–173, https://doi.org/10.1016/j.cplett.2006.07.043.

[10] A. Nenov, T. Cordes, T.T. Herzog, W. Zinth, R. de Vivie-Riedle, Molecular driving forces for Z/E isomerization mediated by heteroatoms: the example hemithioindigo, J. Phys. Chem. A 114 (2010) 13016–13030, https://doi.org/10.1021/jp107899g.

[11] B. Maerz, S. Wiedbrauk, S. Oesterling, E. Samoylova, A. Nenov, P. Mayer, R. de Vivie-Riedle, W. Zinth, H. Dube, Making fast photoswitches faster-using hammett analysis to understand the limit of donor-acceptor approaches for faster hemithioindigo photoswitches, Chem. - Eur. J. 20 (2014) 13984–13992, https://doi.org/10.1002/chem.201403661.

[12] S. Wiedbrauk, B. Maerz, E. Samoylova, A. Reiner, F. Trommer, P. Mayer, W. Zinth, H. Dube, Twisted hemithioindigo photoswitches: solvent polarity determines the type of light-induced rotations, J. Am. Chem. Soc. 138 (2016) 12219–12227, https://doi.org/10.1021/jacs.6b05981.

[13] T. Cordes, T. Schadendorf, B. Priewisch, K. Ruck-Braun, W. Zinth, The Hammett

relationship and reactions in the excited electronic state: hemithioindigo Z/E-photoisomerization, J. Phys. Chem. A 112 (2008) 581–588, https://doi.org/10.1021/jp077472l.

[14] T. Cordes, T. Schadendorf, K. Rück-Braun, W. Zinth, Chemical control of Hemithioindigo-photoisomerization – Substituent-effects on different molecular parts, Chem. Phys. Lett. 455 (2008) 197–201, https://doi.org/10.1016/j.cplett.2008.02.096.

[15] T. Cordes, B. Heinz, N. Regner, C. Hoppmann, T.E. Schrader, W. Summerer, K. Rück-Braun, W. Zinth, Photochemical Z → E isomerization of a hemithioindigo/hemistilbene ω-amino acid, ChemPhysChem. 8 (2007) 1713–1721.

[16] T. Cordes, C. Elsner, T.T. Herzog, C. Hoppmann, T. Schadendorf, W. Summerer, K. Rück-Braun, W. Zinth, Ultrafast hemithioindigo-based peptide-switches, Chem. Phys. 358 (2009) 103–110, https://doi.org/10.1016/j.chemphys.2008.12.027.

[17] N. Regner, T.T. Herzog, K. Haiser, C. Hoppmann, M. Beyermann, J. Sauermann, M. Engelhard, T. Cordes, K. Rück-Braun, W. Zinth, Light-switchable hemithioindigo–hemistilbene-containing peptides: ultrafast spectroscopy of the Z → E isomerization of the chromophore and the structural dynamics of the peptide moiety, J. Phys. Chem. B 116 (2012) 4181–4191, https://doi.org/10.1021/jp300982a.

[18] S. Kitzig, M. Thilemann, T. Cordes, K. Rück-Braun, Light-switchable peptides with a hemithioindigo unit: peptide design, photochromism, and optical spectroscopy, ChemPhysChem. 17 (n.d.) 1252–1263. doi:10.1002/cphc.201501050.

[19] M. Guentner, M. Schildhauer, S. Thumser, P. Mayer, D. Stephenson, P.J. Mayer, H. Dube, Sunlight-powered kHz rotation of a hemithioindigo-based molecular motor, Nat. Commun. 6 (2015) 8406, https://doi.org/10.1038/ncomms9406.

[20] F.J. Lederer, F.F. Graupner, B. Maerz, M. Braun, W. Zinth, Excimer formation in 9,10-dichloroanthracene – solutions and crystals, Chem. Phys. 428 (2014) 82–89, https://doi.org/10.1016/j.chemphys.2013.11.005.

[21] R. Huber, H. Satzger, W. Zinth, J. Wachtveitl, Noncollinear optical parametric amplifiers with output parameters improved by the application of a white light continuum generated in CaF2, Opt. Commun. 194 (2001) 443–448.

[22] K. Eggers, T.M. Fyles, P.J. Montoya-Pelaez, Synthesis and characterization of photoswitchable lipids containing hemithioindigo chromophores, J. Org. Chem. 66 (2001) 2966–2977, https://doi.org/10.1021/jo0056848.

[23] W. Steinle, K. Rück-Braun, Synthesis and characterization of novel bifunctional hemithioindigo chromophores, Org. Lett. 5 (2003) 141–144, https://doi.org/10.1021/ol027102+.

[24] T. Lougheed, V. Borisenko, T. Hennig, K. Rück-Braun, G.A. Woolley, Photomodulation of ionic current through hemithioindigo-modified gramicidin channels, Org. Biomol. Chem. 2 (2004) 2798–2801, https://doi.org/10.1039/B408485C.

[25] T. Schadendorf, C. Hoppmann, K. Rück-Braun, Synthesis of rigid photoswitchable hemithioindigo ω-amino acids, Tetrahedron Lett. 48 (2007) 9044–9047, https://doi.org/10.1016/j.tetlet.2007.10.110.

[26] H.-J. Werner, P.J. Knowles, G. Knizia, F.R. Manby, M. Schütz, P. Celani, T. Korona, R. Lindh, A. Mitrushenkov, G. Rauhut, K.R. Shamasundar, T.B. Adler, R.D. Amos, A. Bernhardsson, A. Berning, D.L. Cooper, M.J.O. Deegan, A.J. Dobbyn, F. Eckert, E. Goll, C. Hampel, A. Hesselmann, G. Hetzer, T. Hrenar, G. Jansen, C. Köppl, Y. Liu, A.W. Lloyd, R.A. Mata, A.J. May, S.J. McNicholas, W. Meyer, M.E. Mura, A. Nicklass, D.P. O'Neill, P. Palmieri, D. Peng, K. Pflüger, R. Pitzer, M. Reiher, T. Shiozaki, H. Stoll, A.J. Stone, R. Tarroni, T. Thorsteinsson, M. Wang, MOLPRO, version 2012.1, a package of ab initio programs, Cardiff, UK, 2012.

[27] M.J. Frisch, G.W. Trucks, H.B. Schlegel, G.E. Scuseria, M.A. Robb, J.R. Cheeseman, G. Scalmani, V. Barone, B. Mennucci, G.A. Petersson, H. Nakatsuji, M. Caricato, X. Li, H.P. Hratchian, A.F. Izmaylov, J. Bloino, G. Zheng, J.L. Sonnenberg, M. Hada, M. Ehara, K. Toyota, R. Fukuda, J. Hasegawa, M. Ishida, T. Nakajima, Y. Honda, O. Kitao, H. Nakai, T. Vreven, J.A. Montgomery Jr., J.E. Peralta, F. Ogliaro, M. Bearpark, J.J. Heyd, E. Brothers, K.N. Kudin, V.N. Staroverov, R. Kobayashi, J. Normand, K. Raghavachari, A. Rendell, J.C. Burant, S.S. Iyengar, J. Tomasi, M. Cossi, N. Rega, J.M. Millam, M. Klene, J.E. Knox, J.B. Cross, V. Bakken, C. Adamo, J. Jaramillo, R. Gomperts, R.E. Stratmann, O. Yazyev, A.J. Austin, R. Cammi, C. Pomelli, J.W. Ochterski, R.L. Martin, K. Morokuma, V.G. Zakrzewski, G.A. Voth, P. Salvador, J.J. Dannenberg, S. Dapprich, A.D. Daniels, Ö. Farkas, J.B. Foresman, J.V. Ortiz, J. Cioslowski, D.J. Fox, Gaussian 09 Revision D.01, n.d.

[28] E. Lippert, Dipolmoment und Elektronenstruktur von angeregten Molekülen, Z Naturforschg10a. (n.d.) 541–545.

[29] N. Mataga, Y. Kaifu, M. Koizumi, The solvent effect on fluorescence spectrum, change of solute-solvent interaction during the lifetime of excited solute molecule, Bull. Chem. Soc. Jpn. 28 (1955) 690–691, https://doi.org/10.1246/bcsj.28.690.

[30] N. Mataga, Y. Kaifu, M. Koizumi, Solvent effects upon fluorescence spectra and the dipole moments of excited molecules, Bull. Chem. Soc. Jpn. 29 (1956) 465–470, https://doi.org/10.1246/bcsj.29.465.

[31] D.R. Lide, CRC Handb. Chem. Phys. 76th ed., CRC Press, London, 1995, p. 2576.

[32] Y. Marcus, Prop. Solvents, 1st ed., Wiley, Chichester, New York, 1998, p. 254.

1.2 Hemithioindigo Based Molecular Motors

Building upon the versatility of the HTI platform, Dube and coworkers synthesized *motor-1* [31], a molecular motor capable of fast unidirectional rotation at ambient conditions upon irradiation with visible light. Starting from HTI, the introduction of additional stereocenters by oxidizing the sulfur and ring-fusing the stilbene fragment confined the rotation around the central C=C to one direction and suppressed unwanted back-movements. Further substitution of the stilbene resulted in the four isomers **A-1**, **B-1**, **C-1** and **D-1** shown in Figure 1.3. From the ground state energy profile and low temperature time resolved nuclear magnetic resonance (NMR) spectroscopy, a reaction pathway for the rotation, consisting of four steps, two thermal and two light-induced, was proposed [31]. But, due to its very fast rotation, direct experimental access to all four intermediate states was only possible by significantly increasing the sterical hindrance and operating the motor at very low temperatures ($-105\,^\circ$C) [115]. However, the light-induced processes on the excited state PES are still unknown, so that critical insights into the mechanism of the rotation are missing. The following section 1.2.1 presents the theoretical and experimental investigation on the complete unidirectional rotation of the molecular motor, *motor-1*. It uncovers the complete mechanism of the rotation, the relevant reaction coordinates, as well as the critical points on the excited PES. Based on these findings, three possible pathways to improve the efficiency as well as the rotation speeds of light-driven motors are derived. These improvements were utilized in the design of *motor-2* [32], the second molecular motor built upon the HTI framework. Its unidirectional, three-step rotation pathway is presented in section 1.2.2.
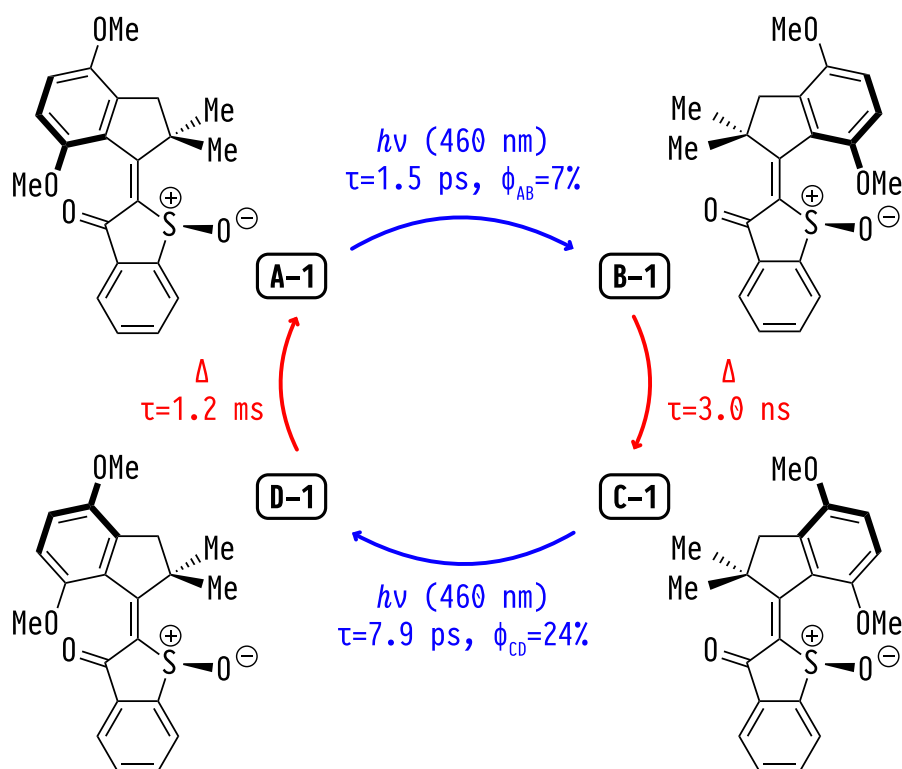
Figure 1.3 – The four isomers **A-1**, **B-1**, **C-1** and **D-1** of the HTI based molecular motor, *motor-1*. The complete pathway of the rotation consists of two thermal steps (Δ), shown in red, and two light ($h\nu$) induced ones, shown in blue. Further, the time constants τ for all four steps and the quantum yields ϕ for the two light-induced steps are shown.

1.2.1 The Complete Mechanism of the Hemithioindigo Motor Rotation

To gain insights into the complete light-driven mechanism, the rotation of *motor-1* was scrutinized by a combination of multiscale broadband transient absorption measurements, covering time scales from fs to ns, with a high-level theoretical description of the involved excited states.

Further, the absorption measurements allowed the extraction of the time constants τ for all four steps and the quantum yields ϕ for the two light-induced ones. The article "Complete Mechanism of Hemithioindigo Motor Rotation" was published in the *Journal of the American Chemical Society*. The key statements of this study on the rotation mechanism of *motor-1* are:

- Calculations at the coupled-cluster, including singles and doubles (CCSD) and time-dependent density functional theory (TDDFT) levels of theory revealed that upon irradiation with 460 nm light pulses, both isomers **A-1** and **C-1** transition to the first excited state S_1, which is of $n\pi^*$ character. Here, the n orbital denotes the oxygen lone-pair of the carbonyl group and the π^* orbital the central C=C double bond. The first two triplet states, T_1 and T_2, of $\pi\pi^*$ and $n\pi^*$ character, respectively, are located energetically close to S_1, indicating a possible interaction down the reaction pathway.

- With the help of extensive CCSD and TDDFT benchmark calculations as well as previous research on HTI [16, 17, 109], a suitable active space (AS) for the CASSCF calculations of twelve electrons in eleven orbitals [AS(12,11)] was chosen. The complete AS with all included orbitals is reprinted in appendix D.1.

- The calculated ground and excited state energy profiles at the CASSCF level of theory are in very good agreement with the observed experimental behavior, supporting the four-step process shown in Figure 1.3 as the mechanism of the unidirectional rotation.

- Starting at the thermodynamically stable isomer **A-1**, excitation leads to population of the S_1 state, where the reaction pathway can split into two possible branches: (1) Rotating around the central C=C double bond an S_1 minimum is reached. Further rotation to about 90° leads to a CoIn, where the system is able to cross over to the S_2 state and subsequently to the ground state of the **B-1** isomer. Because all critical points on this reaction pathway lie energetically below the FC region, the system possesses enough energy to reach the isomer **B-1**, completing the first 180° of rotation. From the transient absorption measurements, a time constant of 1.5 ps and a quantum yield of 7 % are extracted for this relaxation. (2) In the vicinity of the FC point, the system also has the possibility to cross over to the T_2 state via ISC by tilting of the stilbene moiety. After crossing to the T_1 state and further rotation, a T_1 minimum is reached at about 90°. From here, only a relaxation back to the ground state of **A-1** by ISC was found. For this unproductive pathway a time constant of 100 ns and a quantum yield of 8 % were determined.

- For the following thermal step from the metastable isomer **B-1** to the thermodynamically stable one, **C-1**, a small barrier of 0.25 eV and a time constant of 3.0 ns at 22 °C was found.

- Excitation of the **C-1** isomer also leads to population of the first excited state S_1. Similarly to the first light-induced step, two relaxation pathways are possible. (1) Staying on the S_1 potential surface, a minimum is reached by rotating around the C=C bond. Afterwards a CoIn with the S_2 state can be reached, allowing the system to relax to the ground state of the **D-1** isomer. For this pathway, a time constant of 7.9 ps and a significantly higher quantum yield of 24 % is derived from the transient absorption measurements. (2) In the FC region, the triplet pathway is accessible via ISC to the T_1 state. Subsequent relaxation into a T_1 minimum at about 280° of torsion only leads the system back to the ground state of **C-1**. The transient absorption measurements did not show any formation of this loss channel.

- The final step from **D-1** back to **A-1** is subject to a slightly higher barrier of 0.57 eV. The time constant of 1.2 ms is significantly longer compared to the first thermal step from **B-1** to **C-1**. But with isomer **A-1** being the thermodynamically stable one, this step completely converts, completing the full rotation.

- The maximum rotation rate of *motor-1* can be determined by the highest barrier of the complete multistep process. Here the 0.57 eV of the final thermal step results in a maximum

rate of about 1 kHz at ambient temperatures. However, a rate model calculation including the photoreactions forming the thermodynamically metastable states **B-1** and **D-1**, revealed the constant population of isomer **D-1** as rate limiting and not the thermal step from **D-1** to **A-1** itself. Therefore, the realistic maximum rotation rate decreases to about 0.01 Hz to 1 Hz at 20 °C.

- Three pathways to improve the rotation speeds of light-driven motors are derived. First, enhance the quantum yields of the photoreactions. Second, lower the barriers of the thermal steps, thus effectively removing the metastable isomers from the reaction pathway. Third, enhance the extinction coefficients and absorption range to increase the probability of a photon absorption.

Hereafter, the article "Complete Mechanism of Hemithioindigo Motor Rotation" published in the *Journal of the American Chemical Society* is reprinted with permission from *J. Am. Chem. Soc.* **140**, 15, 5311–5318 (2018). Copyright 2018 American Chemical Society. Parts of the supporting information of this article are reprinted in the appendix D.1. The complete supporting information is available at: https://pubs.acs.org/doi/abs/10.1021/jacs.8b02349.

# Complete Mechanism of Hemithioindigo Motor Rotation

Roland Wilcken,[†] Monika Schildhauer,[‡] Florian Rott,[§] Ludwig Alexander Huber,[‡] Manuel Guentner,[‡] Stefan Thumser,[‡] Kerstin Hoffmann,[‡] Sven Oesterling,[§] Regina de Vivie-Riedle,[§] Eberhard Riedle,[†] and Henry Dube*,[‡]

[†]Lehrstuhl für BioMolekulare Optik, Ludwig-Maximilians-Universität München, Oettingenstrasse 67, D-80538 München, Germany
[‡]Department für Chemie and Munich Center for Integrated Protein Science CIPSM and [§]Department für Chemie, Ludwig-Maximilians-Universität München, Butenandtstrasse 5-13, D-81377 München, Germany

S *Supporting Information*

ABSTRACT: Hemithioindigo-based molecular motors are powered by nondamaging visible light and provide very fast directional rotations at ambient conditions. Their ground state energy profile has been probed in detail, but the crucial excited state processes are completely unknown so far. In addition, very fast processes in the ground state are also still elusive to date and thus knowledge of the whole operational mechanism remains to a large extent in the dark. In this work we elucidate the complete light-driven rotation mechanism by a combination of multiscale broadband transient absorption measurements covering a time scale from fs to ms in conjunction with a high level theoretical description of the excited state. In addition to a full description of the excited state dynamics in the various time regimes, we also provide the first experimental evidence for the elusive fourth intermediate ground state of the original HTI motor. The fate of this intermediate also is followed directly proving complete unidirectionality for both 180° rotation steps. At the same time, we uncover the hitherto unknown involvement of an unproductive triplet state pathway, which slightly diminishes the quantum yield of the *E* to *Z* photoisomerization. A rate model analysis shows that increasing the speed of motor rotation is most effectively done by increasing the photoisomerization quantum yields instead of barrier reduction for the thermal ratcheting steps. Our findings are of crucial importance for improved future designs of any light-driven molecular motor in general to yield better efficiencies and applicability.
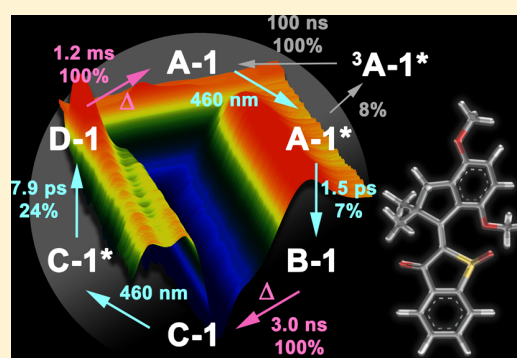
INTRODUCTION

Molecular motors[1] are archetypical molecular machines[2−6] as they allow conversion of energy input into directional mechanical motions and ultimately into mechanical work at the nano scale.[7−12] Nowadays a variety of molecular motor designs are available,[1,13−25] the most efficient of which use light energy to power unidirectional intramolecular rotations of a rotor part relative to a stator part.[13,17,18,21,22] We have recently reported on a new molecular motor **1** (Figure 1) based on the hemithioindigo (HTI) chromophore, which is driven by nondamaging visible light and achieves complete unidirectionality with very high rotation speeds (up to 1 kHz at ambient temperature under ideal conditions).[18] Because of its fast rotation, direct experimental access to all intermediate states of **1** in the electronic ground state could not be achieved. Only after introduction of significantly increased steric hindrance it was possible to observe all four ground state intermediates populated during rotation in a related HTI motor derivative at very low temperatures (−105 °C).[26] Despite this progress, a characterization of the ultrafast kinetics in the electronically excited state has not been available for this type of molecular motor. Excited state measurements are so far only available for Feringa-type molecular motors.[27−32] For very fast ground state

molecular motor processes measured with sufficient time resolution, see refs 33 and 34, and for time-resolved measurements of different molecular machines, see for example refs 35−38. This leaves the crucial light-powered movements of the new HTI motors completely in the dark.

In the present work, we provide a comprehensive mechanistic picture for the unidirectional rotation of HTI motor **1** using a variety of spectroscopic techniques. We extensively use time-resolved absorption spectroscopy with a multiscale broadband setup[39,40] as well as a thorough theoretical description of both the ground[41] and the excited state. For comparable theoretical modeling of the excited state of light-driven molecular motors see refs 42−48. Our work gives unprecedented insights into the intricate details of unidirectional HTI motor motion and delivers a quantitative picture of the whole operational mechanism. From these findings, clear recommendations can be made for improved molecular motors with higher efficiencies and rotation speeds, which stress the importance of increasing the photoisomerization quantum yield over the reduction of thermal barriers. Our
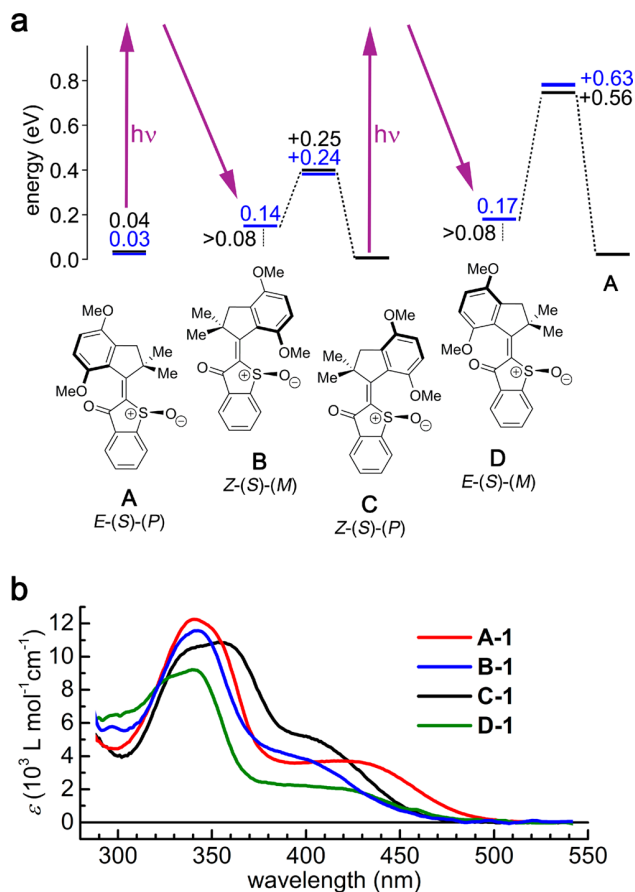
Figure 1. (a) Comparison of the theoretical (blue) and experimentally determined (black) ground state energy profile of HTI molecular motor **1**. Only the (*S*)-enantiomers are shown for clarity. The energy barrier of the thermal helix-inversion leading to conversion from isomer **B** to **C** and the completeness of this step as well as the corresponding conversion of **D** to **A** at ambient temperature are measured for the first time in this work. (b) Molar absorption coefficients of all four isomers **A**–**D** of HTI motor **1**. The spectra of the **B** and **D** isomers are extracted from the transient absorption measurements.

conclusions can be generalized to any light-driven molecular motor system and are therefore of crucial importance for a broad variety of molecular machines and nanosystems.

■ **EXPERIMENTAL SECTION**

In order to follow the processes from the femtosecond (fs) to millisecond (ms) time scale, a multiscale broadband transient absorption setup is used. The setup is based on a 1 kHz Ti:sapphire amplifier system (CPA2001, Clark MXR), which is electronically synchronized with a wavelength tunable nanosecond (ns)-laser (NT242 SHG/SFG, EKSPLA) operating also at 1 kHz. This allows the gapless recording of the initial photoinduced (isomerization) dynamics as well as the subsequent thermal dynamics of the photoproducts. The probe pulse, generated by supercontinuum generation in a CaF$_2$ plate, ranges from 285 to 720 nm[39] and is recorded by a double CCD-frame camera system with single-shot spectral referencing for high sensitivity and fidelity. To follow the ultrafast photoinduced processes, the sample is excited with fs-pulses varying between 350 and 460 nm. These are generated by frequency conversion in a noncollinear optical parametric amplifier (NOPA) with subsequent frequency doubling.[49] This allows us to study the temporal evolution with a time resolution of <50 fs up to a delay of 2 ns. For the slower and/or thermal induced dynamics, the same

sample is pumped with the ns-pulse and probed with the same supercontinuum. Delays up to 700 μs with an instrumental response function of 2.5 ns are possible.[40,50] This time range is further extended by chopping down the ns-laser to a repetition rate of 50 Hz and then probing the same excited volume multiple times. Delays of up to 18 ms are achieved with this setup.

Data evaluation was done by analysis of the temporal dynamics and by reconstruction of the species spectra. The disentanglement of the kinetics from the overlapping species is done by fitting the data with a set of exponential functions at a single wavelength or by global analysis.[51,52] The spectra of the individual species are reconstructed by a quantitative spectral analysis. This is done by subtraction of the well-known ground state bleach (GSB) signal making use of its unique spectral features. For the species present at this delay time its spectrum is determined and the scaling of the GSB gives its current concentration. Comparison with the total number of excited molecules via reconstruction at early delays allows the quantum yield for this species to be retrieved. In this way we could deduce the reaction times, the species spectra, the quantum yield for the photoisomerization steps, and follow the thermal steps from time-resolved data. For more details on the experimental setup and conditions as well as on the data evaluation, we refer the reader to the Supporting Information.

■ **RESULTS**

Ground State Energy Profile and Absorption Spectra. The ground state energy profile of HTI motor **1** has been analyzed previously both theoretically as well as experimentally (see Figure 1a for a comparison of the theoretically predicted and experimentally assessed ground-state energy profile of **1**).[18] Four energetically different stable states are found, i.e., isomer **A** (with *E*-(*S*)-(*P*)/*E*-(*R*)-(*M*) configuration), **B** (*Z*-(*S*)-(*M*)/*Z*-(*R*)-(*P*)), **C** (*Z*-(*S*)-(*P*)/*Z*-(*R*)-(*M*)), and **D** (*E*-(*S*)-(*M*)/*E*-(*R*)-(*P*)). Isomer **C** is the thermodynamically most stable state followed by isomer **A**, both of which can be isolated and studied separately. The rate limiting step for the complete unidirectional 360° rotation is found to be the thermal helix inversion from **D** to **A**. This thermal step could directly be followed by low-temperature NMR spectroscopy establishing an associated energy barrier of 0.57 eV for this process. The complementary helix inversion from **B** to **C** is significantly faster and could therefore not be observed up to now. In this work we provide a comprehensive and quantitative picture of the dynamic processes of the HTI motor function including the so far elusive fast thermal helix inversion step from **B** to **C**.

The optical spectra of the four isomers **A**–**D** (see Figure 1b) differ sufficiently to allow optical detection of the various conversion processes. The spectrum of stable isomers **A** and **C** can be directly measured. The spectra for **B** and **D** were extracted from the transient measurements (see below).

Excited State Energy Profile. To shed light on the excited state processes, we calculated distinctive points along the rotation pathways on both the singlet and triplet potential for motor **1** using the complete active space SCF (CASSCF) method with the 6-31G* basis set. Because of the size of motor **1** it is not feasible to include all π-orbitals in the active space of the CASSCF calculations. Using benchmark calculations at the time-dependent density functional theory (TDDFT) and coupled clusters singles and doubles (CCSD) level of theory as well as previous research on the related HTI chromophore[53] we comprised an active space of 12 electrons and 11 orbitals (see Figure S25). It includes the central CC double bond (π_5), the CO double bond (π_2), two sets of bonding and antibonding orbitals on the stilbene part (π_3, π_4), and one set on the thioindigo part (π_1) as well as the oxygen lone-pair (n_1) of the CO double bond.

Article

The pathways in the excited state were followed starting from either **A-1** or **C-1** to uncover the whole 360° motion. The obtained energy profiles are shown in Figure 2 (see also Table S1 for the underlying data and Tables S3–S20 for the exact geometries of the shown points).
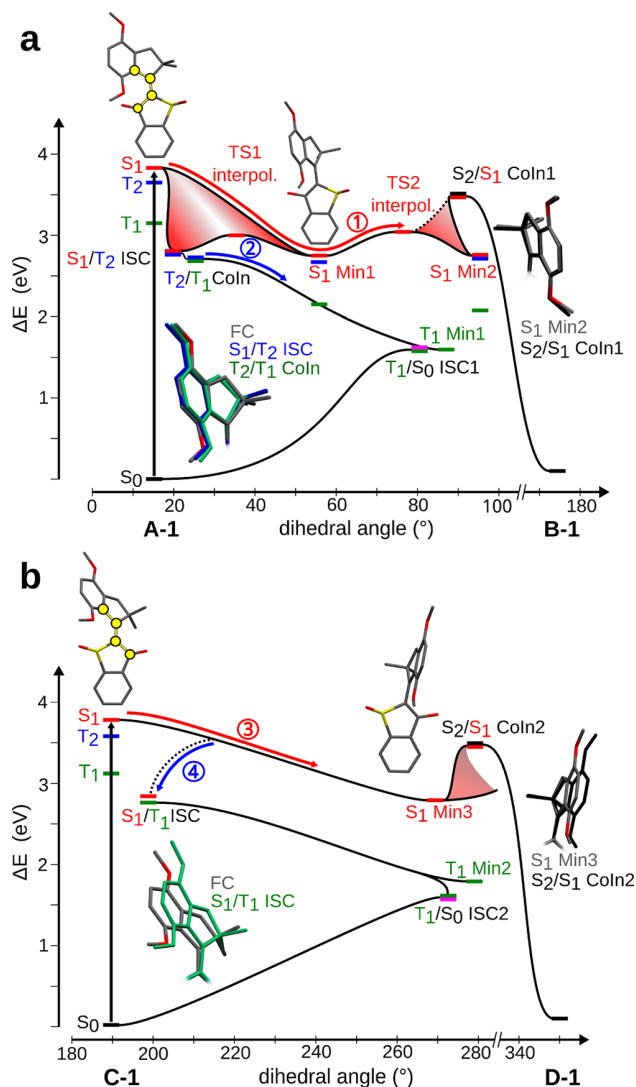

Figure 2. Calculated reaction paths for photoexcited **A-1** (a) and **C-1** (b). The ΔE values (in eV) of the optimized structures relative to the ground state energy of **A-1** (a) or **C-1** (b) are plotted against the dihedral angle (in degrees) of the central CC double bond (highlighted as yellow circles on the FC geometries). Important second coordinates are indicated by the red surfaces. Furthermore, structural differences at the S_1/T_2 ISC (blue), the S_1/T_1 ISC (green) and the T_2/T_1 CoIn (green) compared to their respective FC point (gray) are shown. Likewise, the differences at the S_2/S_1 CoIns (black) compared to the S_1 Min2 and S_1 Min3 (both gray) are shown as well.

Starting from **A-1** with a torsional angle of 16.3° around the central double bond, excitation leads to population of the S_1 state ($n\pi^*$). Here the reaction pathway can split into two branches (labeled 1 and 2 in Figure 2a). As a first step on the singlet branch 1, the system relaxes into a S_1 minimum (S_1 Min1) accompanied by elongation of the central CC double bond as well as a rotation to 56° torsion around it. Further double bond rotation to a 90° torsion angle allows the molecule

to reach a conical intersection (CoIn1) after passing a transition state (TS2 interpol.). CoIn1 allows the system to cross to the S_2 state and subsequently relax to the ground state potential surface of **B-1** isomer to complete the first double-bond isomerization.

From the transition state (TS2 interpol.), the molecule can also reach a second minimum on the S_1 potential (S_1 Min2). The S_1 Min2 is characterized by a dihedral angle of 91.1° around the central double bond. Interpolating between the geometries of both S_1 minima revealed an upper limit for TS2, which energetically lies below the CoIn1 (see TS2 interpol. in Figure 2a). From the S_1 Min2, the molecule can also reach CoIn1 and subsequently the ground state **B-1** isomer. As both the TS2 and the CoIn1 energetically lie below the FC point, the molecule therefore possesses enough energy to reach the ground state of **B-1** after excitation of **A-1**.

The second pathway, labeled 2, starts in the vicinity of the FC point where it is possible for the system to reach the T_2 state ($n\pi^*$) via intersystem crossing (ISC). This intersection is characterized by elongation of the central CC double bond as well as a sideway tilt of the stilbene part as depicted in Figure 2a. It seems plausible that the system reaches the ISC directly from the FC point, but a back rotation from the S_1 Min1 could also be possible. Interpolating between the geometries of the S_1/T_2 ISC point and the S_1 Min1 revealed an upper limit for the barrier (TS1 interpol. in Figure 2a), which lies energetically below the FC point. Thus, both ISC possibilities mentioned are feasible for reaching the triplet state after the optical excitation. Once crossed into the T_2 state, an energetically close lying CoIn (T_2/T_1 CoIn) with the T_1 state ($\pi\pi^*$) can be reached by a downward tilt of the stilbene part. Now, a relaxation into the T_1 minimum (T_1 Min1) can follow, which is accompanied by rotation around the central double bond as well as further tilting of the stilbene part. However, all ISC points found with S_0 lead the system back to the ground state of **A-1** and are therefore unproductive in terms of isomerization.

The calculated excited state pathways for the second part of the directional 360° rotation are depicted in Figure 2b. Starting from **C-1** with 189.0° torsion around the central double bond excitation also leads to population of the S_1 state ($n\pi^*$). Again, we find two different possible pathways (see 3 and 4 in Figure 2b). The S_1 state relaxes into the minimum S_1 Min3 in pathway 3 by elongation of the central double bond and a rotation around this bond to an angle of 270°. Rotating even further, the system can reach CoIn2 at 277.4° with the S_2 state. Although the CoIn2 lies energetically higher than the S_1 Min3, it still is below the FC region, which allows the system to cross to the S_2 state and subsequently relax to the ground state of the **D-1** isomer. The triplet pathway 4 is accessible via an ISC between the S_1 and T_1 state ($\pi\pi^*$) somewhat further away from the FC at a dihedral angle of 195.8°. Subsequent relaxation into the T_1 Min2 is accompanied by a further rotation around the central double bond to 280° torsion. Again all found ISC points with S_0 lead the system back to the ground state of **C-1**, making the triplet pathway again a competing loss channel for the motor rotation.

Time-Resolved Absorption Measurements. Time-resolved absorption spectroscopy was used to probe the ultrafast dynamics of the electronically excited states and the follow up photoproducts after excitation of the pure **A** and **C** isomers of motor **1**. The measured transient absorption data are shown in Figure 3 for both photoisomerizations starting either from pure
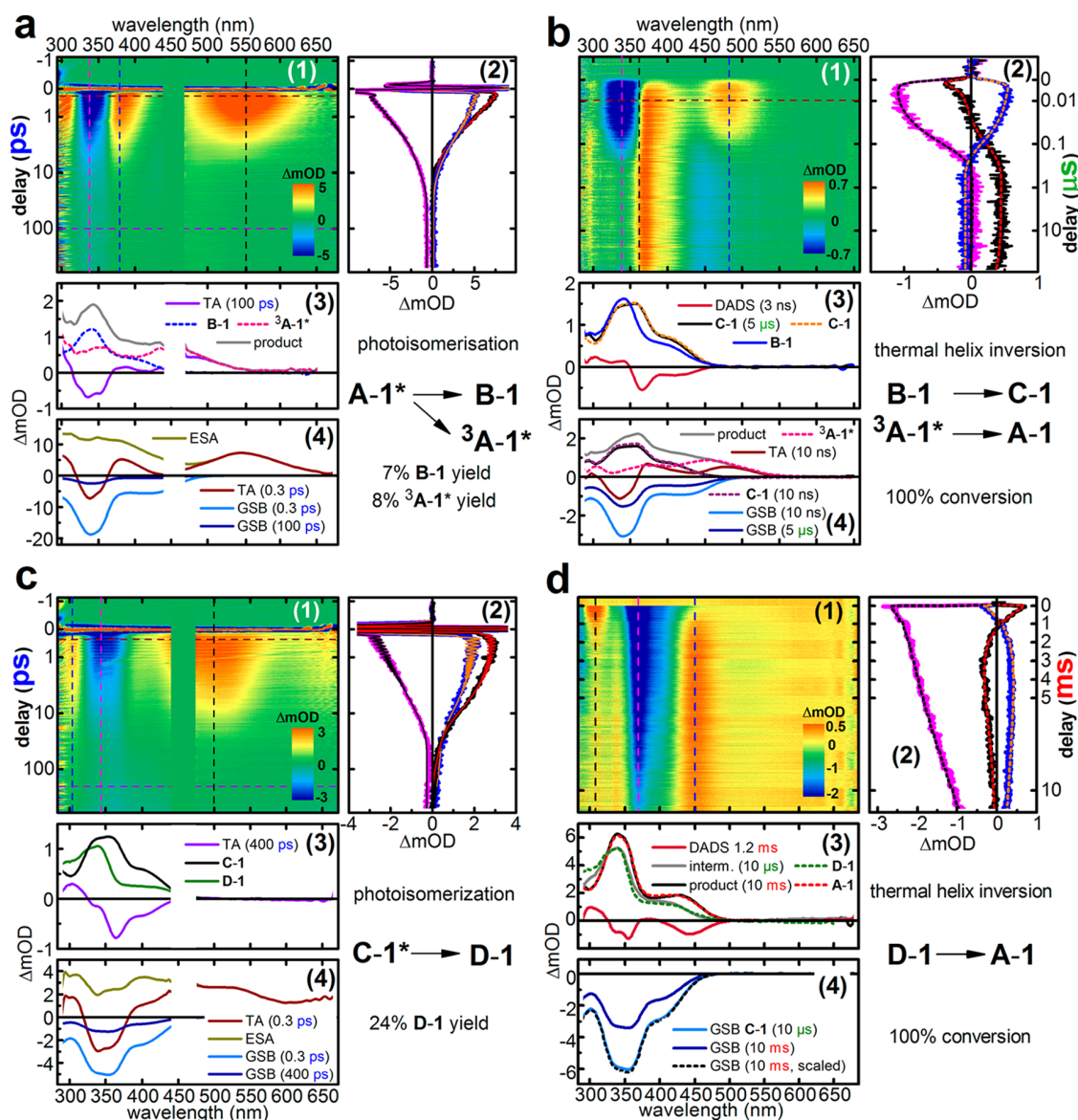
Figure 3. Time-resolved absorption spectra of motor **1** after optical excitation in CH₂Cl₂ at 22 °C. (a) 1. Transient spectra after 460 nm excitation of **A-1** on the fs/ps time scale. 2. Kinetic fits for the dynamics of different species at selected wavelengths (indicated in color code in inset a-1). 3. Reconstruction of the absorption spectrum of intermediate species **B-1** and ³**A-1*** populated after the decay of **A-1***. 4. Spectral reconstruction at early delay times and comparison of the GSB bleach contribution at later delay time to receive the isomerization quantum yield. (b) 1. Transient spectra obtained during thermal decay of **B-1** and ³**A-1*** on the ns/µs time scale. 2. Fitted kinetic data of the **B-1** and ³**A-1*** decay. 3. Reconstruction of the absorption spectrum of the **B-1** decay product, which is identical to the spectrum of **C-1**. 4. A 50% GSB bleach recovery is observed during the ³**A-1*** decay while the **C-1** signal stays constant. (c) 1. Transient spectra obtained after 460 nm excitation of **C-1**. 2. Kinetic fits for the decay dynamics of different species at selected wavelengths (indicated in color code in inset c-1) on the fs/ps time scale. 3. Reconstruction of the absorption spectrum of the intermediate species **D-1** populated after decay of photoexcited **C-1***. 4. **C-1** GSB comparison for the quantum yield determination. (d) 1. Transient absorption spectra obtained during thermal decay of **D-1** on the ms time scale after 350 nm excitation of **C-1**. 2. Fitted kinetic data of the **D-1** decay. 3. Reconstruction of the absorption spectrum of the **D-1** decay product, which is identical to the spectrum of **A-1**. 4. The **C-1** GSB stays constant over 10 ms (scaled by the flow out dynamics of the flow cell, which reduces the signal strength by 55%).

A-1 or pure **C-1** and for the respective thermal conversions of isomers **B-1** and **D-1**.

After exciting **A-1** at 22 °C in CH₂Cl₂ solution with 460 nm light pulses, a very strong excited state absorption (ESA, red colors in Figure 3a) is observed similar to other HTI photoswitches (Figure 3a).[54−60] At the same time the GSB is clearly visible at around 350 nm (compare blue spectrum in Figure 1b) while still overlapped by the ESA. We observe the decay of the ESA with a time constant of 1.5 ps leading to

longer lived absorption features and 85% recovery of the GSB. Spectral analysis of the remaining absorption reveals an unusual long wavelength wing up to 550 nm, which is not found in the absorption of isomers **A**−**D** (compare Figure 1b). As described in the following, the product absorption found here is the sum of **B-1** intermediate and **A-1** triplet (³**A-1***), which are generated simultaneously and can only be disentangled by their different dynamics on longer time scales.

On the ns time scale (Figure 3b) we observe a change in this product absorption with a time constant of 3 ns, while the GSB remains unchanged. Spectral analysis of the corresponding decay-associated difference spectra (DADS) allows us to extract the absorption spectrum of the responsible decaying species (see Supporting Information for details). Very similar features compared to the **C-1** isomer are found in this absorption; especially, the faint shoulder at longer wavelengths indicates the presence of a *Z* configured double bond. This spectral feature is also reproduced in the calculated absorption of **B-1**.[18] Therefore, the species populated 1.5 ps after excitation of **A-1** and decaying thermally with a time constant of 3 ns can be assigned to the hitherto elusive **B-1** intermediate.

Subsequently, an even slower decay of the residual red-shifted absorption band is observed with a time constant of 100 ns while about 50% of the residual GSB recovers. Therefore, this decay only leads to restoration of the initial **A-1** absorption and represents an unproductive pathway (**A-1** to **A-1** conversion) that does not allow double-bond isomerization. The QM calculations reveal a possible intersystem crossing in the excited state of **A-1** before the double-bond isomerization reaches 90° rotation. Therefore, the strongly red-shifted band can be assigned to the T_1 (^{3}**A-1***) excited state of **A-1**.

After the ^{3}**A-1*** state has decayed completely back to the S_0 state the remaining and very long-lived product absorption is identical to the **C-1** absorption (see Figure 3b). Thus, the above-described 3 ns decay of **B-1** exclusively leads to formation of **C-1** (no GSB recovery during this process). Because the absorptions of the ^{3}**A-1*** excited state and **C-1** overlap, the final product can only be identified after completion of the slow decay of ^{3}**A-1***.

Excitation of **C-1** with 460 nm light leads again to a very strong ESA covering the entire probe wavelength range (285–700 nm, Figure 3c). Decay of the ESA proceeds with a time constant of 7.9 ps leading to a new long-lived absorption and 76% recovery of the GSB. A full spectral reconstruction of the corresponding species at later delay times delivers a fourth absorption spectrum different from the **A-1**, **B-1**, and **C-1** spectra. Therefore, this absorption spectrum can be assigned to **D-1**. Very similar features compared to the **A-1** isomer are found in this absorption spectrum, especially the plateau at longer wavelengths indicates the presence of an *E* configured double bond. This plateau is also reproduced in the calculated absorption of **D-1**.[18]

On the ns/μs time scale no changes in the spectral signals of **D-1** were observed. An additional time-resolved absorption measurement was conducted at the ms time scale to monitor the slow thermal decay of the **D-1** isomer at 22 °C (Figure 3d). This process has been measured before at low temperatures using NMR spectroscopy. The decay of **D-1** proceeds with a time constant of 1.2 ms and leads to a complete conversion into only the **A-1** isomer. In this way not only the previously determined energy barrier of 0.57 eV can be confirmed; at the same time, the completeness of this step is now demonstrated at ambient temperature directly. These results raise the upper limit for the energy difference between **D-1** and **A-1** isomers to 0.08 eV (see Figure 1).

In summary, the photoisomerization of **A-1** to **B-1** proceeds in 1.5 ps with a quantum yield of $\phi_{A/B} = 7\%$ while the de-excitation of an unproductive triplet state ($\phi_{A/A(T1)} = 8\%$) occurs with a time constant of 100 ns. The thermal helix inversion proceeds exclusively from **B-1** to **C-1** and takes place with a time constant of 3 ns at 22 °C, which corresponds to a

free activation enthalpy of ~0.25 eV. This value is in very good agreement with the theoretical description predicting 0.24 eV. The analogous photoisomerization of **C-1** to **D-1** proceeds in 7.9 ps with a considerably higher quantum yield of $\phi_{C/D} = 24\%$ and without obvious formation of a triplet state. The 1.2 ms thermal decay of **D-1** to **A-1** was followed by a time-resolved absorption measurement at 22 °C and confirmed the previously determined activation energy of 0.57 eV as well as the completeness of this process at ambient temperature. All measured time constants and quantum yields are summarized in Figure 4.
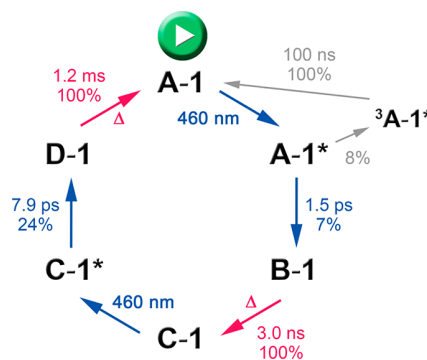

Figure 4. Comprehensive mechanism of HTI-motor **1** operation under irradiation conditions at ambient temperature. All measurements were conducted at 22 °C in CH_2Cl_2 as solvent. Processes involving excited states are shown in blue or gray arrows; thermal processes in the ground state are shown with red arrows.

■ DISCUSSION

We have followed the excited state dynamics of the HTI motor **1** as well as the fast helix inversion steps in the ground state at ambient temperature using time-resolved absorption measurements that span time scales from fs to ms. The experimentally observed behavior as well as quantified thermodynamic and kinetic data are in very good agreement with the theoretical description for both the ground state as well as the excited state. It is therefore now possible to derive a comprehensive mechanistic view of all crucial processes governing the unidirectional rotation, which adheres to a four-step motor model with two fast photoisomerization equilibria and two slower thermal steps breaking microscopic reversibility. Figure 4 shows the full mechanistic picture for motor **1**.

Starting from stable state **A**, a first photoreaction takes place, which populates a second thermally unstable state **B** by photoisomerization of the double bond and concomitant helicity inversion within 1.5 ps after a pulsed excitation. Of all optically excited molecules a fraction of 7% is indeed converted. For a more complete conversion multiple excitation is needed. Thermal decay of the second state leads to a further helicity inversion and proceeds only in one (forward) direction driven by sufficient energy difference to the next more stable (third) state **C** in 3.0 ns. This time of 3.0 ns is the relaxation time of all molecules that have been transferred into state **B**. At this point microscopic reversibility is broken, and from the third state a second independent photoreaction takes place leading to a fourth, thermally unstable, state **D** in 7.9 ps after optical excitation. The yield of 24% for the third step is quite sizable. Its thermal decay again proceeds only in one direction and completely reforms the first state **A** in 1.2 ms.

We have additionally observed the intermediate population of a nonproductive triplet excited state ^{3}**A***, which is populated with a yield of 8% after photoexcitation of the **A** isomer. As the photoisomerization of **A** to **B** proceeds similarly efficient, this unwanted side pathway seems to significantly diminish the efficiency of the motor operation. However, employing a simple rate model (see Supporting Information for details), it becomes clear that it is much more important to diminish the high quantum yield of the unproductive internal conversions **A*** to **A** (85%) and **C*** to **C** (76%) in favor of the desired forward reactions **A*** to **B** and **C*** to **D**. Actually, the presence of the triplet state does not lead to a significant reduction in performance; much more important is the intrinsically low quantum yield for the forward reactions.

With the measurements performed at 22 °C we have now unambiguously established complete unidirectionality of light-powered HTI motor **1** rotation at ambient temperature. By determining the highest kinetic barrier in this multistep process, the theoretically maximal rotation speed at a given temperature can be estimated. The highest barrier is found for the thermal **D** to **A** conversion with a value of 0.57 eV, which is in very good agreement with the previously measured barrier at low temperatures (0.56 eV). This gives a theoretical maximum speed for the rotation of approximately 1 kHz at ambient temperatures. However, to establish the rotation speed of a photon-driven molecular motor under realistic irradiation conditions the whole process needs to be taken into consideration, especially the photoreactions leading to thermally instable states **B** and **D**. Only if the photoreactions are able to keep the motor in the thermally limiting step (isomer **D** in this case) is it possible to achieve the theoretically maximal rotation rate.

To obtain the irradiation conditions needed for maximum rotation speed we have set up a rate model similar to published models[42,48] and solved it numerically (see details in the Supporting Information). For motor **1**, we obtain light intensities of about 1000 W/cm^2 to constantly populate rate-limiting state **D**. This would amount to 10 W light even on a diameter focus in the sample as small as 1 mm. Similar values are obtained for any light-driven motor, for which quantum yields of the photoreactions are available in the literature.[28,29] Surprisingly, under typical irradiation conditions the light-driven population of state **D** becomes rate-limiting rather than the thermal step, which reduces the maximum rotation rate of motor **1** to about 0.01−1 Hz at 20 °C. One reason for this astonishing result lies in the low quantum yields of the photoreactions achieved so far in synthetic motors. It becomes clear that fast directional motions cannot be driven by such extremely high light intensities for simple practical and chromophore stability reasons.

On the basis of these results, we propose three options to improve rotation speeds of light-driven motors: (1) enhance the quantum yields of the photoreactions, preferably only in the forward direction of the motion, (2) lower the barriers for thermal (helix inversion) steps in the ground state to effectively remove thermally instable intermediates (**B** and **D** in our case) before they can absorb photons and reenter the photoequilibria (the latter can also be done by heating), and (3) enhance extinction coefficients and absorption range to increase the probability of photon absorption.

Apart from molecular design, another interesting option is the utilization of pulsed excitation with high intensity light sources delivering the required amount of photons in only a short time interval, which prevents the excitation of the intermediates. With a proper setup, directional rotation speeds in the high kHz range might be possible to realize. Nevertheless, highly light-stable chromophores are certainly required for this approach to be successful.

■ CONCLUSIONS

In this work we have studied the complete mechanism of the unidirectional HTI motor rotation both in the ground as well as the excited state using time-resolved absorption spectroscopy as the main experimental tool in conjunction with a thorough, high-level theoretical assessment. We cover an experimental time scale from fs to ms to elucidate both, the details of the ultrafast excited state processes as well as fast ground state processes under the same ambient conditions. This detailed analysis gives unprecedented insights into the working mechanism of photodriven molecular machines and delivers quantitative data on key properties such as speed, degree of unidirectionality, quantum yield of individual processes, and overall efficiencies of the light-powered motions. We found that HTI motor **1** fully adheres to a four-step directional rotation mechanism consisting of two photoisomerization steps each followed by a ratcheting thermal helix inversion. In this work, elusive ground state intermediate **B-1** has been experimentally proven for the first time, and its fate has been monitored directly. In doing so we deliver unambiguous evidence for complete unidirectionality of both thermal helix inversion processes. We also provide experimental and theoretical evidence for the formation of an unproductive triplet state intermediate of the **A-1** isomer. However, a rate model for the directional rotation cycle taking into account all measured quantum yields clearly shows that rather than suppressing the triplet state suppression of the internal conversion of **A-1*** to **A-1** is of prime importance to increase the rotation speed and efficiency. With these findings we have uncovered and quantified the complete HTI motor rotation mechanism and deliver unprecedented insight into the different factors determining efficiency and speed of these intriguing molecular machines. With the herein presented results, future design of photodriven molecular motors is greatly facilitated and can be conducted in a much more conscious way.

■ ASSOCIATED CONTENT

ⓢ Supporting Information

The Supporting Information is available free of charge on the ACS Publications website at DOI: 10.1021/jacs.8b02349.

> Details of transient absorption measurements on femto- to millisecond time scales, extinction coefficients of all ground state intermediates, rate model of the motor rotation cycle and frequency calculations, details of the theoretical description of the motor excited state including optimized geometries of critical points (PDF)

■ AUTHOR INFORMATION

Corresponding Author

*heduch@cup.uni-muenchen.de

ORCID ⓘ

Regina de Vivie-Riedle: 0000-0002-7877-5979
Henry Dube: 0000-0002-5055-9924

Author Contributions

R.W., M.S., and F.R. contributed equally to the creation of this work.

Notes

The authors declare no competing financial interest.

REFERENCES

(1) Kassem, S.; van Leeuwen, T.; Lubbe, A. S.; Wilson, M. R.; Feringa, B. L.; Leigh, D. A. *Chem. Soc. Rev.* **2017**, *46*, 2592−2621.

(2) Erbas-Cakmak, S.; Leigh, D. A.; McTernan, C. T.; Nussbaumer, A. L. *Chem. Rev.* **2015**, *115*, 10081−10206.

(3) Kay, E. R.; Leigh, D. A. *Angew. Chem., Int. Ed.* **2015**, *54*, 10080−10088.

(4) Leigh, D. A. *Angew. Chem., Int. Ed.* **2016**, *55*, 14506−14508.

(5) Kay, E. R.; Leigh, D. A.; Zerbetto, F. *Angew. Chem., Int. Ed.* **2007**, *46*, 72−191.

(6) Kassem, S.; Lee, A. T. L.; Leigh, D. A.; Marcos, V.; Palmer, L. I.; Pisano, S. *Nature* **2017**, *549*, 374−378.

(7) Eelkema, R.; Pollard, M. M.; Vicario, J.; Katsonis, N.; Ramon, B. S.; Bastiaansen, C. W.; Broer, D. J.; Feringa, B. L. *Nature* **2006**, *440*, 163.

(8) Li, Q.; Fuks, G.; Moulin, E.; Maaloum, M.; Rawiso, M.; Kulic, I.; Foy, J. T.; Giuseppone, N. *Nat. Nanotechnol.* **2015**, *10*, 161−165.

(9) Foy, J. T.; Li, Q.; Goujon, A.; Colard-Itte, J.-R.; Fuks, G.; Moulin, E.; Schiffmann, O.; Dattler, D.; Funeriu, D. P.; Giuseppone, N. *Nat. Nanotechnol.* **2017**, *12*, 540−545.

(10) Garcia-Lopez, V.; Chen, F.; Nilewski, L. G.; Duret, G.; Aliyan, A.; Kolomeisky, A. B.; Robinson, J. T.; Wang, G.; Pal, R.; Tour, J. M. *Nature* **2017**, *548*, 567−572.

(11) Chen, J.; Leung, F. K.; Stuart, M. C. A.; Kajitani, T.; Fukushima, T.; van der Giessen, E.; Feringa, B. L. *Nat. Chem.* **2017**, *10*, 132−138.

(12) Orlova, T.; Lancia, F.; Loussert, C.; Iamsaard, S.; Katsonis, N.; Brasselet, E. *Nat. Nanotechnol.* **2018**, DOI: 10.1038/s41565-017-0059-x.

(13) Koumura, N.; Zijlstra, R. W. J.; van Delden, R. A.; Harada, N.; Feringa, B. L. *Nature* **1999**, *401*, 152−155.

(14) Hernandez, J. V.; Kay, E. R.; Leigh, D. A. *Science* **2004**, *306*, 1532−1537.

(15) Fletcher, S. P.; Dumur, F.; Pollard, M. M.; Feringa, B. L. *Science* **2005**, *310*, 80−82.

(16) Haberhauer, G. *Angew. Chem., Int. Ed.* **2011**, *50*, 6415−6418.

(17) Greb, L.; Lehn, J. M. *J. Am. Chem. Soc.* **2014**, *136*, 13114−13117.

(18) Guentner, M.; Schildhauer, M.; Thumser, S.; Mayer, P.; Stephenson, D.; Mayer, P. J.; Dube, H. *Nat. Commun.* **2015**, *6*, 8406.

(19) Barrell, M. J.; Campana, A. G.; von Delius, M.; Geertsema, E. M.; Leigh, D. A. *Angew. Chem., Int. Ed.* **2011**, *50*, 285−290.

(20) Wilson, M. R.; Sola, J.; Carlone, A.; Goldup, S. M.; Lebrasseur, N.; Leigh, D. A. *Nature* **2016**, *534*, 235−240.

(21) Kistemaker, H. A.; Stacko, P.; Visser, J.; Feringa, B. L. *Nat. Chem.* **2015**, *7*, 890−896.

(22) Ruangsupapichat, N.; Pollard, M. M.; Harutyunyan, S. R.; Feringa, B. L. *Nat. Chem.* **2011**, *3*, 53−60.

(23) Tierney, H. L.; Murphy, C. J.; Jewell, A. D.; Baber, A. E.; Iski, E. V.; Khodaverdian, H. Y.; McGuire, A. F.; Klebanov, N.; Sykes, E. C. H. *Nat. Nanotechnol.* **2011**, *6*, 625−629.

(24) Perera, U. G. E.; Ample, F.; Kersell, H.; Zhang, Y.; Vives, G.; Echeverria, J.; Grisolia, M.; Rapenne, G.; Joachim, C.; Hla, S.-W. *Nat. Nanotechnol.* **2013**, *8*, 46−51.

(25) Erbas-Cakmak, S.; Fielden, S. D. P.; Karaca, U.; Leigh, D. A.; McTernan, C. T.; Tetlow, D. J.; Wilson, M. R. *Science* **2017**, *358*, 340−343.

(26) Huber, L. A.; Hoffmann, K.; Thumser, S.; Böcher, N.; Mayer, P.; Dube, H. *Angew. Chem., Int. Ed.* **2017**, *56*, 14536−14539.

(27) Augulis, R. n.; Klok, M.; Feringa, B. L.; Loosdrecht, P. H. M. v. *Phys. Status Solidi C* **2009**, *6*, 181−184.

(28) Conyard, J.; Addison, K.; Heisler, I. A.; Cnossen, A.; Browne, W. R.; Feringa, B. L.; Meech, S. R. *Nat. Chem.* **2012**, *4*, 547−551.

(29) Conyard, J.; Cnossen, A.; Browne, W. R.; Feringa, B. L.; Meech, S. R. *J. Am. Chem. Soc.* **2014**, *136*, 9692−9700.

(30) Conyard, J.; Stacko, P.; Chen, J.; McDonagh, S.; Hall, C. R.; Laptenok, S. P.; Browne, W. R.; Feringa, B. L.; Meech, S. R. *J. Phys. Chem. A* **2017**, *121*, 2138−2150.

(31) Amirjalayer, S.; Cnossen, A.; Browne, W. R.; Feringa, B. L.; Buma, W. J.; Woutersen, S. *J. Phys. Chem. A* **2016**, *120*, 8606−8612.

(32) Pang, X.; Cui, X.; Hu, D.; Jiang, C.; Zhao, D.; Lan, Z.; Li, F. *J. Phys. Chem. A* **2017**, *121*, 1240−1249.

(33) Klok, M.; Boyle, N.; Pryce, M. T.; Meetsma, A.; Browne, W. R.; Feringa, B. L. *J. Am. Chem. Soc.* **2008**, *130*, 10484−10485.

(34) Kulago, A. A.; Mes, E. M.; Klok, M.; Meetsma, A.; Brouwer, A. M.; Feringa, B. L. *J. Org. Chem.* **2010**, *75*, 666−679.

(35) Panman, M. R.; Bodis, P.; Shaw, D. J.; Bakker, B. H.; Newton, A. C.; Kay, E. R.; Brouwer, A. M.; Buma, W. J.; Leigh, D. A.; Woutersen, S. *Science* **2010**, *328*, 1255−1258.

(36) Panman, M. R.; Bakker, B. H.; den Uyl, D.; Kay, E. R.; Leigh, D. A.; Buma, W. J.; Brouwer, A. M.; Geenevasen, J. A.; Woutersen, S. *Nat. Chem.* **2013**, *5*, 929−934.

(37) Jewell, A. D.; Tierney, H. L.; Baber, A. E.; Iski, E. V.; Laha, M. M.; Sykes, E. C. *J. Phys.: Condens. Matter* **2010**, *22*, 264006.

(38) Sun, J.; Wu, Y.; Liu, Z.; Cao, D.; Wang, Y.; Cheng, C.; Chen, D.; Wasielewski, M. R.; Stoddart, J. F. *J. Phys. Chem. A* **2015**, *119*, 6317−6325.

(39) Megerle, U.; Pugliesi, I.; Schriever, C.; Sailer, C. F.; Riedle, E. *Appl. Phys. B: Lasers Opt.* **2009**, *96*, 215−231.

(40) Riedle, E.; Wenninger, M. *Chemical Photocatalysis*; De Gruyter: Berlin, 2013; pp 319−375.

(41) Oruganti, B.; Wang, J.; Durbeej, B. *Int. J. Quantum Chem.* **2018**, *118*, e25405.

(42) Kazaryan, A.; Kistemaker, J. C. M.; Schäfer, L. V.; Browne, W. R.; Feringa, B. L.; Filatov, M. *J. Phys. Chem. A* **2010**, *114*, 5058−5067.

(43) Kazaryan, A.; Lan, Z.; Schafer, L. V.; Thiel, W.; Filatov, M. *J. Chem. Theory Comput.* **2011**, *7*, 2189−2199.

(44) Filatov, M.; Olivucci, M. *J. Org. Chem.* **2014**, *79*, 3587−600.

(45) Nikiforov, A.; Gamez, J. A.; Thiel, W.; Filatov, M. *J. Phys. Chem. Lett.* **2016**, *7*, 105−110.

(46) Garcia-Iriepa, C.; Marazzi, M.; Zapata, F.; Valentini, A.; Sampedro, D.; Frutos, L. M. *J. Phys. Chem. Lett.* **2013**, *4*, 1389−1396.

(47) Maafi, M.; Brown, R. G. *J. Photochem. Photobiol., A* **2007**, *187*, 319−324.

(48) Klok, M.; Browne, W. R.; Feringa, B. L. *Phys. Chem. Chem. Phys.* **2009**, *11*, 9124−9131.

(49) Riedle, E.; Beutter, M.; Lochbrunner, S.; Piel, J.; Schenkl, S.; Spörlein, S.; Zinth, W. *Appl. Phys. B: Lasers Opt.* **2000**, *71*, 457−465.

(50) Sailer, C. F.; Riedle, E. *Pure Appl. Chem.* **2013**, *85*, 1487−1498.

(51) Fita, P.; Luzina, E.; Dziembowska, T.; Radzewicz, C.; Grabowska, A. *J. Chem. Phys.* **2006**, *125*, 184508.

(52) Ruckebusch, C.; Sliwa, M.; Pernot, P.; de Juan, A.; Tauler, R. *J. Photochem. Photobiol., C* **2012**, *13*, 1−27.

(53) Nenov, A.; Cordes, T.; Herzog, T. T.; Zinth, W.; de Vivie-Riedle, R. *J. Phys. Chem. A* **2010**, *114*, 13016−13030.

(54) Cordes, T.; Weinrich, D.; Kempa, S.; Riesselmann, K.; Herre, S.; Hoppmann, C.; Rück-Braun, K.; Zinth, W. *Chem. Phys. Lett.* **2006**, *428*, 167−173.

(55) Cordes, T.; Schadendorf, T.; Priewisch, B.; Rück-Braun, K.; Zinth, W. *J. Phys. Chem. A* **2008**, *112*, 581−588.

Article

(56) Cordes, T.; Schadendorf, T.; Lipp, M.; Rück-Braun, K.; Zinth, W. *Springer Ser. Chem. Phys.* **2009**, *92*, 319−321.

(57) Cordes, T.; Elsner, C.; Herzog, T. T.; Hoppmann, C.; Schadendorf, T.; Summerer, W.; Rück-Braun, K.; Zinth, W. *Chem. Phys.* **2009**, *358*, 103−110.

(58) Maerz, B.; Wiedbrauk, S.; Oesterling, S.; Samoylova, E.; Nenov, A.; Mayer, P.; de Vivie-Riedle, R.; Zinth, W.; Dube, H. *Chem. - Eur. J.* **2014**, *20*, 13984−13992.

(59) Wiedbrauk, S.; Maerz, B.; Samoylova, E.; Reiner, A.; Trommer, F.; Mayer, P.; Zinth, W.; Dube, H. *J. Am. Chem. Soc.* **2016**, *138*, 12219−12227.

(60) Wiedbrauk, S.; Maerz, B.; Samoylova, E.; Mayer, P.; Zinth, W.; Dube, H. *J. Phys. Chem. Lett.* **2017**, *8*, 1585−1592.

1.2.2 A Prospective Ultrafast Hemithioindigo Molecular Motor

The research on *motor-1* resulted in three possible pathways to improve the efficiency and rotation speeds of light-driven molecular motors: (1) Enhance the quantum yields of the photo isomerization. (2) Remove one of the metastable isomers from the reaction pathway by lowering the barrier of its thermal step. (3) Increase the probability of a photon absorption by increasing the extinction coefficients and absorption range of the chromophore. With the design of *motor-2*, the lab of Prof. Henry Dube followed the second pathway in improving upon the initial design of *motor-1* [32]. Introducing a nitrogen heteroatom into the stilbene ring, instead of methoxy substitution of said ring, removed one of the metastable isomers, turning the four-step process into the three-step rotation shown in Figure 1.4.
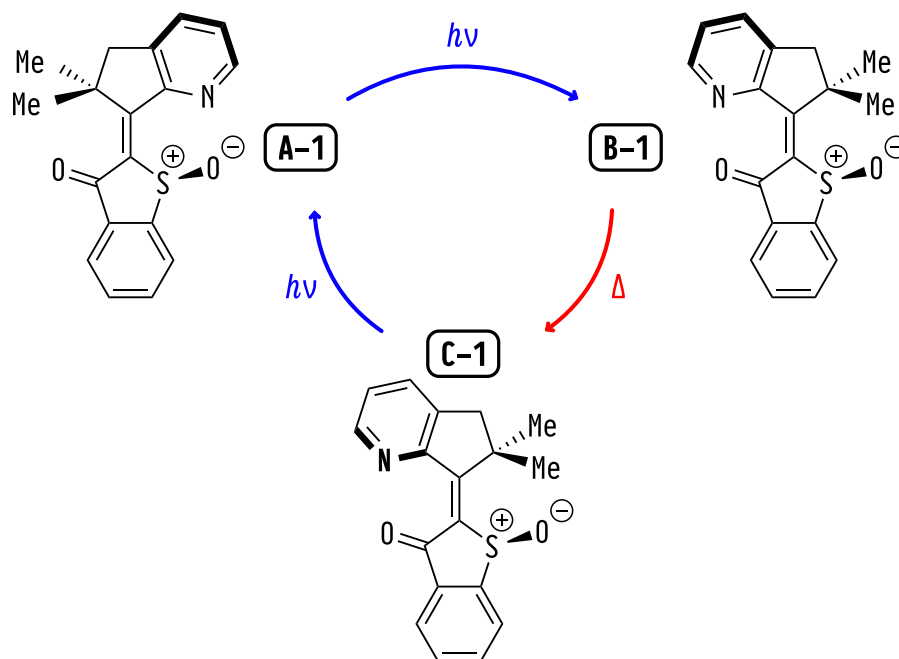
Figure 1.4 – The three isomers **A-1**, **B-1** and **C-1** of the HTI based molecular motor, *motor-2*. The complete pathway of the rotation consists of one thermal (Δ) and two light ($h\nu$) induced steps.

The following article "A Prospective Ultrafast Hemithioindigo Molecular Motor" presents the mechanism of the three-step rotation, elucidated by ambient and low temperature absorption and NMR spectroscopy as well as quantum chemical calculations at the CASSCF level of theory. The key statements of the article are:

- Supported by TDDFT benchmark calculations, the same AS as for *motor-1* one could be utilized within the CASSCF calculations. The obtained excited state energy profiles of both photo isomerization revealed a similar picture to the mechanism of *motor-1*, corroborating the unidirectional rotation by the three-step process shown in Figure 1.4.

- Starting at the thermodynamically most stable isomer **A-1**, excitation leads to population of the first excited state, S_1. Subsequently, the system reaches an S_1 minimum by elongation of the C=C bond and a slight rotation around it. After rotating further and passing a TS, a second minimum on the excited state PES is reached. Here, a CoIn is accessible, where the system is able to cross over to the S_2 state and subsequently relax to the ground state of the **B-1** isomer. As all critical points on the pathway lie energetically below the FC region, the motor possesses enough energy to carry out the first part of the rotation.

- The thermal step from the metastable **B-1** to the stable **C-1** isomer is subject to a very small barrier between $2.2 \, \text{kcal} \, \text{mol}^{-1}$ to $2.9 \, \text{kcal} \, \text{mol}^{-1}$, resulting in a rapid conversion at ambient conditions.

- After the thermal step, excitation of the **C-1** isomer again leads to population of the S_1 state. Similar to the first step, two minima, connected by a TS, exist on the S_1 excited state PES. At the second minimum, an S_1/S_2 CoIn is accessible, allowing the system to relax to the ground state of the **A-1** isomer. All critical points lie energetically below the FC point, so the system is able to complete the full 360° rotation.

- The findings confirm *motor-2* as a suitable molecular motor for ultrafast rotation upon irradiation with visible light. This allows for the removal of one of the thermal steps, thereby improve the efficiency of *motor-2* and molecular motors in general.

- Additionally, the influence of protonation on the mechanism was investigated. Both isomers retain their photoswitching capabilities and the rotation is not hampered, but the protonation changes the overall stability of the three isomers. After protonation the isomer **C-1** is the thermodynamically most stable one. This drastic change provides first evidence for the influence of outside stimuli other than light on the HTI motor framework, opening up further possibilities in the control of molecular motors.

Hereafter, the article "A Prospective Ultrafast Hemithioindigo Molecular Motor" published in *ChemPhotoChem* is reprinted with permission from *ChemPhotoChem* **3**, 6, 365–371 (2019). Copyright 2019 John Wiley and Sons. The relevant parts of the supporting information for this article are reprinted in the appendix D.2. The complete supporting information is available under: https://doi.org/10.1002/cptc.201900074.

A Prospective Ultrafast Hemithioindigo Molecular Motor

Monika Schildhauer,[a, b] Florian Rott,[a] Stefan Thumser,[a, b] Peter Mayer,[a, b] Regina de Vivie-Riedle,[a] and Henry Dube*[a, b]

The maximum speed of light-driven molecular motors is an important key-property governing not only their overall performances but also many advanced functions. Currently, special emphasis lies on increasing the rate of unidirectional rotations to surpass natural systems and harness the full potential of artificial motors. Herein, we report a new molecular setup for a prospective light-powered three-step motor based on the hemithioindigo chromophore. Comprehensive quantum chemical treatment predicts a very low energy barrier for the only thermal ratcheting step in the unidirectional 360° rotation. Thus an ultrafast motion in the THz range could be possible with this motor at high light intensities and consequently a precise control of rotation speeds solely by light intensity variations could potentially be achieved. Experimental analyses using X-ray crystallography and solution spectroscopy deliver first insights into the working mechanism and show that visible-light photoswitching is feasible in both stable switching states. Additionally, significant alterations of the ground-state energies can be induced by pH changes without hampering photoswitching capabilities.

1. Introduction

Artificial molecular motors provide unidirectional movement upon external energy input[1] and are quintessential tools for the construction of advanced synthetic nanomachinery.[2] Their development has led to a number of systems with different types of directional motions or energy supplies.[3] Light powered rotary motors[3a,b,j–p] enable straight forward address-ability, well defined motions, and waste-free fueling while at the same time promise extremely fast rotation speeds because of the typically ultrashort nature of photoreactions.[3n,4] As their rotation mechanism usually includes considerably slower thermal ratcheting steps in the ground state, these steps need to be accelerated in order to realize the full potential of such

light-driven molecular motors.[5] Consequently many efforts have been made in reducing ground-state barriers and currently MHz-rotation speeds are theoretically possible if the excited state steps are assumed not to be rate limiting.[6] In this work we present a hemithioindigo (HTI)[7] molecular motor setup (1), which is predicted from the theoretical description to enable a theoretical maximum of up to THz-rotation speeds under the same assumption. Its synthesis, conformational analysis, as well as physical and photophysical properties are described and augmented by quantum chemical calculations. By introducing a heterocyclic pyridine moiety as rotor fragment this HTI offers additional opportunities for sensing, pH sensitive motor operation, tuning of photo/physical properties, or integration into supramolecular architectures. As a showcase the influences of pH changes on the properties of 1 are also described in this work.

2. Results and Discussion

2.1. Synthesis

Prospective HTI motor 1 was synthesized according to Figure 1a, starting from the described pyridine 2[8] and (phenylthio)acetic acid 3. Pyridine 2 was converted into the twofold-methylated ketone 4 following an established synthesis protocol for related indanones.[3l] Likewise generation of benzothiophenone 5 from 3 has been described earlier.[9] The condensation reaction between ketone 4 and benzothiophenone 5 to HTI 6 proceeds smoothly in 80% yield at −78°C in the presence of BCl_3 as Lewis acid. The resulting HTI 6 was oxidized to the final product 1 using H_2O_2 in 61% yield. Crystals suitable for x-ray structural analysis were obtained for the synthetic intermediate N-oxide 8, HTI 6 in the Z isomeric form and the final product 1, also as Z isomer. As can be seen from the crystal structure analysis, HTI 6 assumes a completely planar structure in the Z isomeric form. The distance between the N and the S atoms is 2.7 Å and thus well below the sum of the van der Waals radii hinting at the presence of a positive N—S interaction, a variant of chalcogen bonding.[10] In the crystal structure of oxidized HTI 1 a significant helical twisted around the photoisomerizable central double bond is observed. The corresponding dihedral angle dSC(8)C(11)C(13) is 12.4° (Figure 1b). In this case the stable sulfoxide stereo center dictates the sense of the helicity and thus diastereomerically pure configurations (either Z-(S)-(P) or Z-(R)-(M)) are observed in the racemic crystal. The observed helicity in Z-1, with respect to the position of the sulfoxide oxygen atom, is similar to the helicity

[a] M. Schildhauer, F. Rott, S. Thumser, Dr. P. Mayer, Prof. Dr. R. de Vivie-Riedle, Dr. H. Dube
Department für Chemie
Ludwig-Maximilians-Universität München
D-81377 Munich (Germany)
E-mail: heducb@cup.uni-muenchen.de
[b] M. Schildhauer, S. Thumser, Dr. P. Mayer, Dr. H. Dube
Munich Center for Integrated Protein Science CIPSM
Ludwig-Maximilians-Universität München
D-81377 Munich (Germany)

Figure 1. Synthesis of prospective HTI motor **1** with its thioindigo fragment as stator and its stilbene fragment as rotor. a) Conditions: i) 1) NaH, glyme, 0 °C, 10 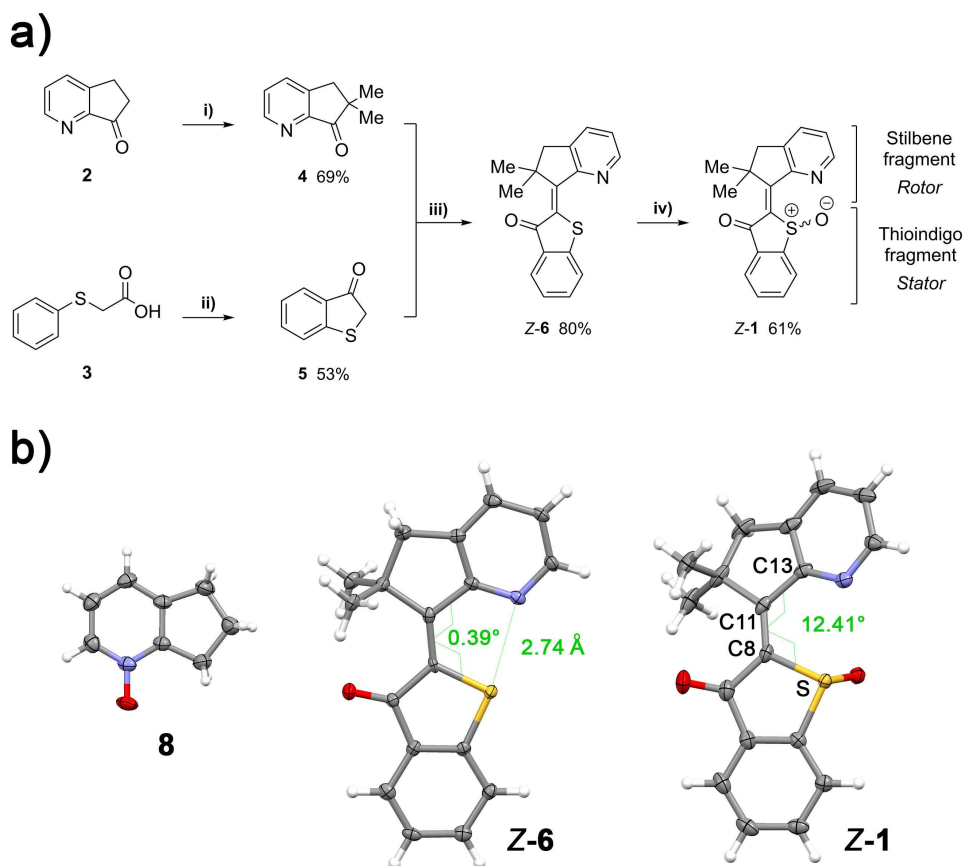min; 2) MeI, 0–23 °C, 18 h; ii) 1) SOCl₂, reflux, 2 h; 2) AlCl₃, dichloroethane, 0–23 °C, 1. h; iii) BCl₃, BF₃·OEt₂, CH₂Cl₂, −78 °C, 20 min; iv) H₂O₂, AcOH, CH₂Cl₂, 24 h. b) Structures of synthetic intermediates **8**, Z-**6**, and of HTI Z-**1** in the crystalline state proving their identities.

of the already established HTI motors in their stable Z configuration.[3l,3m,3o]

2.2. Theoretical Description

The ground state energy profile of HTI **1** was scrutinized on different levels of theory, i.e. B3LYP/6-311G(d,p) PCM(CH₂Cl₂), B3LYP/6-311G(d,p), and MPW1K/6-311G(d,p) (Figure 2). For convenience only structures with (S) configured sulfoxide were taken into account. Different to the original HTI molecular motors only three instead of four stable minimum structures (with Z-(S)-(P) = isomer **A**, E-(S)-(M) = isomer **B**, and E-(S)-(P) = isomer **C** configurations, respectively) were found for HTI **1** regardless of the theoretical method used. The **A** isomer was found to be the thermodynamic minimum structure with lowest energy in all cases. The next stable structure is the **C** isomer, which is however 4.1–5.1 kcal/mol higher in energy compared to **A**. The third and least stable structure is the **B** isomer, which is 6.2–7.2 kcal/mol higher in energy than **A**. Both isomers **B** and **C** possess an E configured double bond but opposite helicity. The energy barrier for thermal helix inversion starting from **B** to reach the **C** structure was found to be very small with only 2.2–2.9 kcal/mol. Therefore, this step would

proceed in ps at ambient temperatures reaching similar speeds as have been established for photoisomerization reactions of HTI photoswitches and motors. Apparently the limited sterical hindrance of the pyridine moiety and the presence of a lone pair close to the thioindigo fragment causes this favorably low barrier – a feature that is of great interest in the design of efficient molecular motors.[5a,b,d] A fourth stable state with Z configuration and a helicity opposite to isomer **A** was not found in the calculations despite extensive conformational searching. All initial structures with such helicity unequivocally led to the **A** isomer after optimization. It must therefore be concluded that such a configuration is not a minimum state in **1** but instead leads directly to the **A** isomer in an energetically down-hill process and not back to **C**.

To further investigate the light induced rotation of this prospective molecular motor distinctive points along the rotation pathway in the excited state were calculated (for related theoretical descriptions of molecular motor excited states see for example[11]) using the complete active space SCF (CASSCF) method with the 6-31G(d) basis set. It is not possible to include all π-orbitals in the active space of the CASSCF calculation as a result of the size of HTI **1**. Using results from excited state calculations of the original HTI motor[3m] as well as benchmark calculations at the time-dependent density function
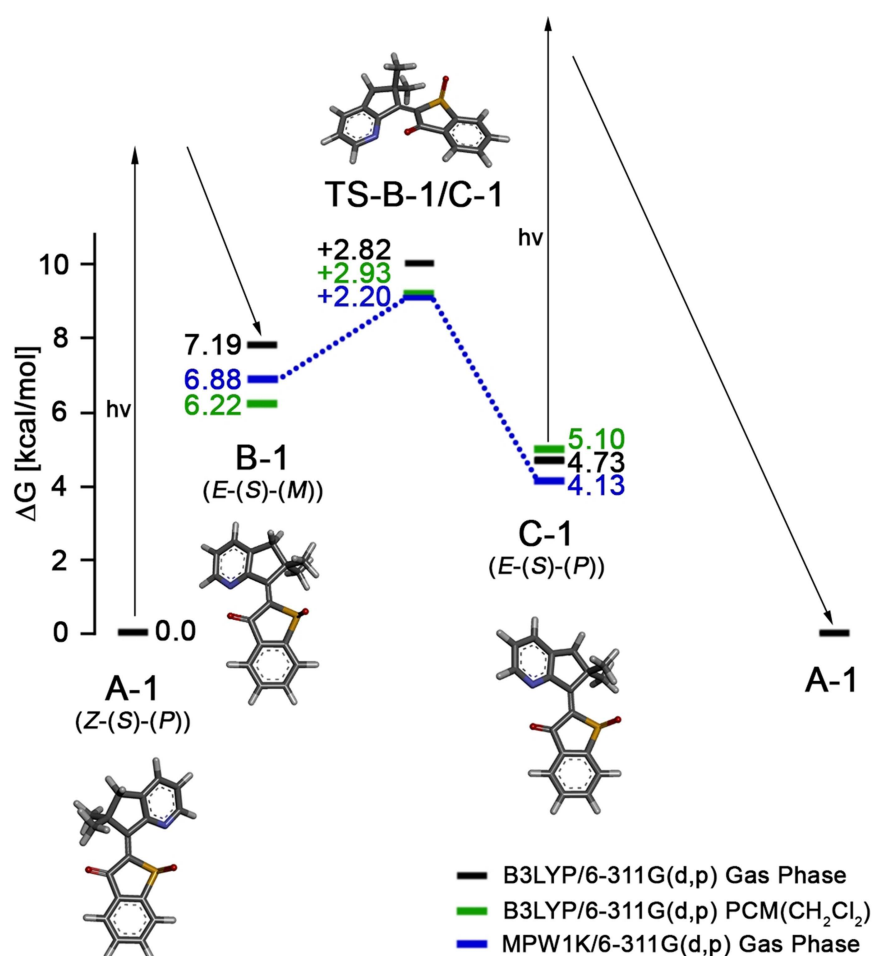
Figure 2. Ground state energy profile of motor **1** calculated at the B3LYP/6-311G(d,p) PCM(CH$_2$Cl$_2$) (green), B3LYP/6-311G(d,p) (black) and MPW1K/6-311G(d,p) (blue) levels of theory. Energies are given in kcal/mol. The (*S*)-enantiomeric form of motor **1** has been used in the theoretical description. All optimized structures were confirmed to be stationary points by frequency analysis. Illustrative structures (MPW1K/6-311G(d,p)) are given as stick representations for every stationary point.

level of theory (TDDFT), an active space of 12 electrons and 11 orbitals was composed (see Figure SI 39) for **1**. The active space was composed of the central CC double bond (π_5), the CO double bond (π_2), two sets of bonding and antibonding orbitals on the stilbene fragment (π_3, π_4) and one set on the thioindigo fragment (π_1) as well as the oxygen lone-pair (n_1) of the CO double bond. Starting from either **A** or **C**, the excited state pathways were followed to describe the entire 360° motion. The obtained energy profiles are shown in Figure 3 (see also Table SI 5 for the underlying data and Table SI 7–SI 17 for the exact geometries of the shown points).

Starting from isomer **A** with a torsional angle of 190.8° around the central CC double bond, excitation leads to population of the S$_1$ state (nπ*). As a first step the system relaxes into a S$_1$ minimum (S$_1$ Min1) accompanied by elongation of the CC double bond to 1.422 Å and a rotation to 196.5° torsion around it. Further double bond rotation to 275° allows for the molecule to reach a conical intersection (Coln1) after passing through a transition state (TS1 interpol., see pathway 1 in Figure 3a). Coln1 describes the crossing between

the S$_2$ and S$_1$ states. At this rotation angle of 275° the S$_2$ state has significant ground-state character of isomer **B**. Following this character along the reaction coordinate the system directly relaxes to the ground state of isomer **B** at 345°, thus completing the first double-bond photoisomerization. From the transition state (TS1 interpol.) the molecule can also reach a second minimum on the S$_1$ potential (S$_1$ Min2). The second minimum is characterized by a dihedral angle of 275.2° around the central double bond. Linear interpolation between the geometries of both minima revealed an upper limit for TS1 which lies energetically below the Coln1 (see TS1 interpol in Fig. 3a). From the S$_1$ Min2, Coln1 can also be reached by the molecule, followed by the ground state of **B**. As a result of the fact that both TS1 and Coln1 lie below the FC point energetically, the molecule has sufficient initial energy to reach the ground state of **B** after excitation of **A**.

The calculated excited state pathway for the second part of the directional 360° rotation is depicted in Figure 3b. Starting from **C-1** with 13.8° torsion around the central double-bond excitation also leads to population of the S$_1$ state (nπ*). Again,
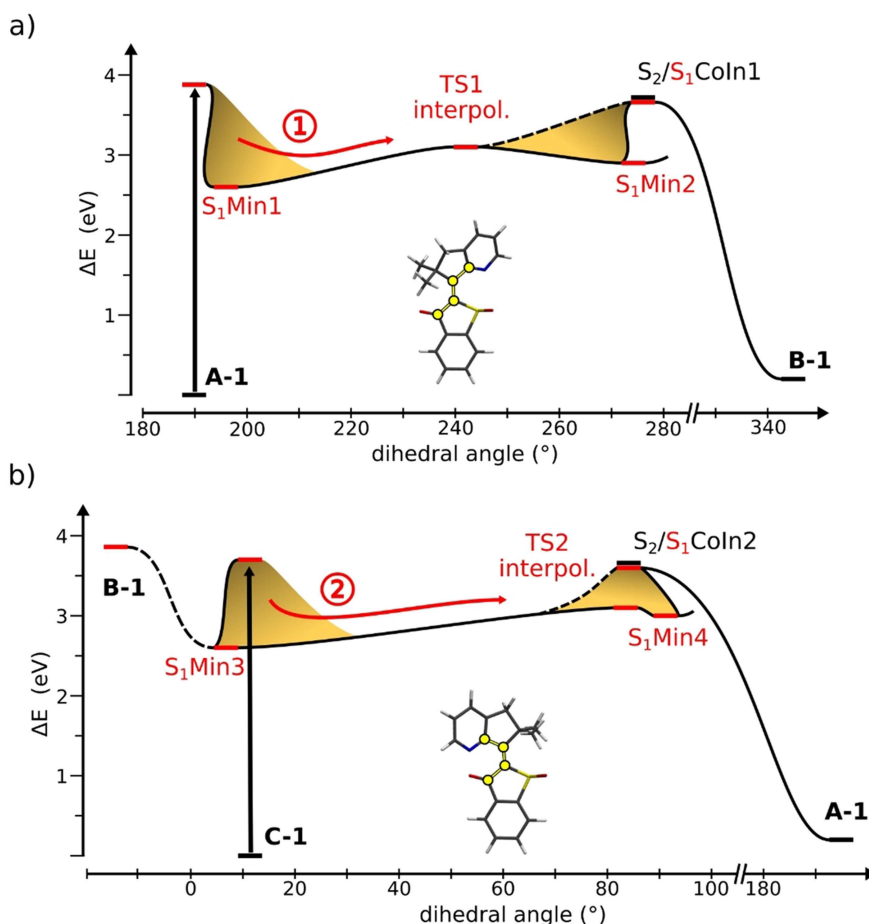
Figure 3. Calculated reaction paths of photoexcited isomer a) **A** and b) **C** (b) of HTI **1** are described. The ΔE values [eV] of the optimized structures relative to the ground state energy of **A** (a) or **C** (b) are plotted against the dihedral angle [°] of the central CC double bond (highlighted as yellow circles on the FC geometries). Important second coordinates are represented by yellow slopes.

the system relaxes into a minimum S_1 Min3 by elongation of the central double bond to 1.414 Å and a rotation around this bond to 7.8°. As the excited state potential rises in energy in the rotation direction towards isomer **B** and no further minimum was found along this pathway (see dashed line in Figure 3b) an undesired back rotation in the "wrong" direction is unlikely. Further forward rotation to 84° enables the molecule to reach a conical intersection (CoIn2) before passing a transition state (TS2 interpol.). Similar to the first photochemical step, CoIn2 allows the system to cross to the S_2 state, which again directly correlates with the ground-state of isomer **A**. Relaxation to the ground-state minimum at 190° completes the second double bond photoisomerization. From the TS2 the systems can also reach a second minimum S_1 Min4, which is characterized by a dihedral angle of 275.2° around the central double bond. Linear interpolation between the geometries of both minima revealed an upper limit for TS2 which lies energetically below the CoIn2 (see TS2 interpol in Figure 3b). From the S_1 Min4 the molecule can also reach CoIn2 and subsequently the ground state of **A**. Both the TS2 and CoIn2 lie energetically below the FC point, so the molecule has sufficient

initial energy to reach the ground state of **A** after excitation of **C**.

Based on the calculated energy schemes predictions about the photoisomerization process and its directionality can be made. Starting from isomer **A** the first 180° of the double-bond rotation are expected to emulate exactly the behavior of the original HTI motor.[3l,n] Photoirradiation leads to isomerization of the central double bond from the *Z* to the *E* configuration and at the same time an inversion of the helicity around this bond. As a result isomer **B** is populated in this first step. The intrinsic directionality of this motion is dictated by the preferred initial helicity of **A**. Previous theoretical assessments of different prospective molecular motor structures have emphasized that even slightly pronounced helicity in the ground state is enough to predetermine the direction of double-bond photoisomerizations.[12] This finding is confirmed in our theoretical description of the excited state of **A**. The **B** isomer is then expected to convert to the significantly more stable **C** isomer in a thermally activated process. Because of the very low barrier for the **B** to **C** helix inversion this process should be extremely rapid. The undesired thermal back conversion to **A** should be prevented by the much higher associated energy barrier
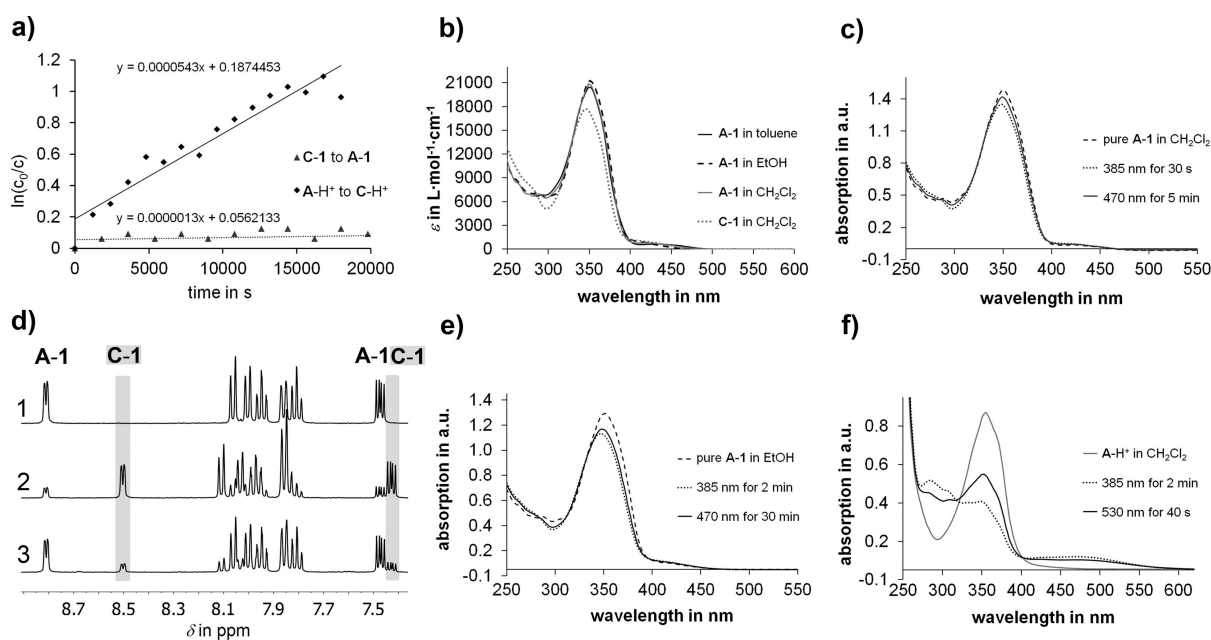
Figure 4. Photo/physical properties of HTI **1** in solution. a) First order kinetic analysis of the thermal **C-1** to **A-1** isomerization in CH$_2$Cl$_2$ (triangles) and of the thermal **A-H**$^+$ to **C-H**$^+$ isomerization (squares). b) Molar absorption of HTI **1** in toluene (isomer **A**, solid black), CH$_2$Cl$_2$ (isomer **A-1**, solid grey; isomer **C-1**, dotted grey), and EtOH (isomer **A-1**, dashed black). c) UV/Vis absorption changes of **A-1** in CH$_2$Cl$_2$ induced by irradiation with 385 nm (dotted black) and 470 nm light (solid black). d) Changes in the ^{1}H NMR spectrum of **A-1** in EtOD (spectrum 1) induced by irradiation with 385 nm (spectrum 2) and 470 nm light (spectrum 3). Newly appearing isomer **C** is highlighted in grey. e) UV/Vis absorption changes of **A-1** (dashed black) in EtOH induced by irradiation with 385 nm (dotted black) and 470 nm light (solid black). f) UV/Vis absorption changes of protonated **A-1** (solid grey) in CH$_2$Cl$_2$ induced by irradiation with 385 nm (dotted grey) and 530 nm light (solid black).

expected for such *E* to *Z* double-bond isomerization. Owing to the large energy difference between **B** and **C** (more than at least 1.1 kcal/mol) no population of **B** should remain at ambient temperatures and thus the photochemical back reaction from **B** to **A** is prevented at this point. Furthermore, the establishment of a true photo-equilibrium, in which also **B** absorbs and enters the backwards photoreaction to **C**, would effectively be prevented since thermal **B** to **C** conversion rapidly reduces the concentration of **B** isomers present in solution.

From **C** a different photoisomerization can be established, the directionality of which should again be dictated by the initial helicity in **C**.[12] Again this preferred trajectory is also predicted by our theoretical description of the excited state of **C**. However, the expected photoproduct with *Z* configured double bond and inverted helicity compared to **C** cannot be populated in this case. Instead it is expected from the calculations that such high-energy conformation (which would be the product of the **C** photoreaction) should directly stabilize its energy by further rotation resulting in direct population of the starting isomer **A**. Based on this theoretical assessment HTI **1** is a strong candidate for a novel three-step motor, operating with only one distinct thermal ratcheting step during a full 360° rotation. Its directionality is dictated by the configuration of the stable sulfoxide stereo center, which in turn predefines helicity in the molecule and thus the sense of rotation. The repulsive interactions of the two lone pairs on the sulfoxide and the nitrogen atom are most probably responsible for the

elimination of a stable minimum in the *Z* isomeric configuration opening up a direct photoreaction pathway from **C** to **A**.

2.3. Physical and Photophysical Properties

Based on the theoretical assessment, obtaining direct experimental proof of the light powered unidirectional rotation of HTI **1** is currently out of reach even with more advanced analytical methods. However, some aspects of the energy profile could be scrutinized and exact values or upper and lower limits for minimum energies and energy barriers were established.

The **C** isomer of HTI **1** was found to be thermally labile preventing straightforward isolation and separate analysis. Therefore, **C**-isomer-enriched solutions were generated prior to the studies by irradiation of **A** isomer at suitable wavelengths. When a 82:18 mixture of **C**:**A** in toluene-*d*$_8$ was heated at 40°C, during 5 h full conversion to pure **A** was detected. First-order kinetic analysis gave a free activation energy of $\Delta G^* = 23.8$ kcal/mol for this process (Figure 4a). In CD$_2$Cl$_2$ the corresponding barrier is significantly higher with 25.7 kcal/mol. The result shows that thermal *E* to *Z* isomerization in **1** encounters significant energy barriers - much higher than the calculated barrier for thermal helix inversion. Since no residual **C** isomer is seen at 40°C a lower limit for the energy difference between **C** and **A** can be calculated by assuming that 5% of residual **C** would not be detectable in the NMR experiment and using the

Gibbs-Helmholtz equation. This is a conservative estimate as typically signals of species with 1 to 2% abundance can be detected by ^{1}H NMR. The corresponding energy difference is 1.0 kcal/mol in the present case.

The photochemistry of HTI **1** was scrutinized at ambient and low temperatures using mainly absorption and NMR spectroscopy as analytical tools. The absorptions of isomers **A** and **C** are not significantly different with a strong band centered at around 350 nm and a second much weaker band at around 430 nm (Figure 4b). Different to the original HTI motor absorption of the *E* isomeric **C** is shifted to slightly shorter wavelengths compared to the *Z* configured **A**. Overall photochromism is very small for HTI **1**, which in fact is a great advantage for a molecular motor as both isomers **A** and **C** now have similar chances to catch supplied photons. Irradiation of pure **A** in different solvents at ambient temperature leads to immediate increase of only **C** signals (see Figure 4c for absorption spectra and the Supporting Information for corresponding ^{1}H NMR spectra in CD$_2$Cl$_2$). At 385 nm up to 87% of **C** can be accumulated but also with visible light more than 70% **C** can be obtained at wavelengths up to 450 nm. Likewise also at low temperatures down to −105 °C no intermediates were observed upon in situ irradiation of **A** in the NMR spectrometer and only **C** is seen as newly formed product (see Supporting Information). After switching off the light and waiting for 5 min at −80 or 7 min at −105 °C as well as after annealing to 23 °C and recooling to −80 or −105 °C no further spectral changes were observed in the ^{1}H NMR spectra showing the absence of thermally labile intermediates (see Supporting Information). This behavior is expected because of the very low calculated energy barrier for thermal conversion of **B** to **C**. Based on the experimental results an upper limit for this energy barrier can be given, again under the conservative assumption that 5% of a species cannot be distinguished in the ^{1}H NMR spectrum. This barrier then cannot be higher than 11.0 kcal/mol in this case (which would lead to a half life of 40 s at −105 °C). If a solution enriched in **C** is irradiated at longer wavelengths (usually >450 nm) the **A** isomer is reformed as can be seen by recovery of its absorption or ^{1}H NMR spectrum (see Figure 4c for CH$_2$Cl$_2$ and 4d-e for EtOH solution as well as the Supporting Information). It could thus be shown that both isomers **A** and **C** undergo productive photoisomerizations in solutions of different polarity using UV or visible light irradiation.

2.4. Influences of Protonation

Protonation of **A** leads to pronounced signal shifts in the ^{1}H NMR spectrum but much less pronounced spectral changes in the absorption (see Figure 4f and the Supporting Information for details). However, upon irradiation and accumulation of **C** the absorption is changed significantly, with the maximum at 350 nm declining and two new bands at around 300 nm and 460 nm growing in (Figure 4f). Irradiation of a CH$_2$Cl$_2$ solution of protonated **A**-H$^+$ at ambient and low temperatures resulted in formation of a new absorption that was assigned to protonated **C**. Up to 68% **C**-H$^+$ was obtained after 385 nm

irradiation as judged by ^{1}H NMR spectroscopy (see Supporting Information). Conversely, irradiation of a solution enriched in **C**-H$^+$ with 530 nm light leads to partial recovery of the **A**-H$^+$ absorption (Figure 4f). This experiment shows that also both isomers **C**-H$^+$ and **A**-H$^+$ are undergoing productive photochemistry and can be interconverted under continuous illumination. Leaving a CD$_2$Cl$_2$ solution enriched in **C**-H$^+$ over prolonged time in the dark leads to full conversion to **C**-H$^+$ establishing that **C**-H$^+$ is now the thermodynamically most stable state – in stark contrast to unprotonated HTI **1**. The corresponding first order kinetic analysis delivered an energy barrier of 23.9 kcal/mol for the thermal double bond isomerization showing the accelerating influence of protonation on this process (Figure 4a). Taken together, protonation leads to significant changes in the ground state minima energies and the spectral characteristics of HTI **1** while general photoisomerization capabilities are not hampered and viable photoswitching is still observed for both stable switching states. The observed pH sensitivity of **1** thus provides first evidences for responsiveness towards different outside stimuli other than light that are promising for regulating its molecular machine properties.[13]

3. Conclusion and Outlook

In summary, we present a new asymmetric HTI photoswitch bearing a pyridine moiety in close proximity to the photoisomerizable double bond. According to quantum chemical calculations of the ground and the excited state this molecular setup should behave as ultrafast light-driven three step motor under illumination conditions at ambient temperatures. It would therefore be possible to omit one thermal ratcheting step in the ground state facilitating efficiency of the whole directional motion. Using crystallographic structural analysis together with solution experiments the calculated ground state energy profile could be assessed with exact values or upper and lower limits for certain minimum and maximum energies. Protonation of the HTI leads to considerable changes in isomer stabilities while at the same time photoswitching capabilities remain, which shows pH responsiveness of this system opening up a further level of control for the operation of this prospective molecular motor. In the future this molecular setup will form the basis for very fast molecular motors capable of sensing changes in their microenvironment and reacting to them with altered performances.

Conflict of Interest

The authors declare no conflict of interest.

[1] a) S. Kassem, T. van Leeuwen, A. S. Lubbe, M. R. Wilson, B. L. Feringa, D. A. Leigh, *Chem. Soc. Rev.* **2017**, *46*, 2592–2621; b) D. Roke, S. J. Wezenberg, B. L. Feringa, *Proc. Natl. Acad. Sci. U.S.A.* **2018**, *115*, 9423–9431.

[2] a) E. R. Kay, D. A. Leigh, F. Zerbetto, *Angew. Chem. Int. Ed.* **2007**, *46*, 72–191; b) E. R. Kay, D. A. Leigh, *Angew. Chem. Int. Ed.* **2015**, *54*, 10080–10088; c) D. A. Leigh, *Angew. Chem. Int. Ed.* **2016**, *55*, 14506–14508; d) S. Erbas-Cakmak, D. A. Leigh, C. T. McTernan, A. L. Nussbaumer, *Chem. Rev.* **2015**, *115*, 10081–10206; e) M. Baroncini, L. Casimiro, C. de Vet, J. Groppi, S. Silvi, A. Credi, *ChemistryOpen* **2018**, *7*, 169–179.

[3] a) N. Koumura, R. W. J. Zijlstra, R. A. van Delden, B. L. Feringa, *Nature* **1999**, *401*, 152–155; b) H. A. Kistemaker, P. Stacko, J. Visser, B. L. Feringa, *Nat. Chem.* **2015**, *7*, 890–896; c) J. V. Hernandez, E. R. Kay, D. A. Leigh, *Science* **2004**, *306*, 1532–1537; d) M. J. Barrell, A. G. Campana, M. von Delius, E. M. Geertsema, D. A. Leigh, *Angew. Chem. Int. Ed.* **2011**, *50*, 285–290; e) M. R. Wilson, J. Sola, A. Carlone, S. M. Goldup, N. Lebrasseur, D. A. Leigh, *Nature* **2016**, *534*, 235–240; f) S. Erbas-Cakmak, S. D. P. Fielden, U. Karaca, D. A. Leigh, C. T. McTernan, D. J. Tetlow, M. R. Wilson, *Science* **2017**, *358*, 340–343; g) S. P. Fletcher, F. Dumur, M. M. Pollard, B. L. Feringa, *Science* **2005**, *310*, 80–82; h) N. Ruangsupapichat, M. M. Pollard, S. R. Harutyunyan, B. L. Feringa, *Nat. Chem.* **2010**, *3*, 53–60; i) T. Kudernac, N. Ruangsupapichat, M. Parschau, B. Macia, N. Katsonis, S. R. Harutyunyan, K. H. Ernst, B. L. Feringa, *Nature* **2011**, *479*, 208–211; j) L. Greb, J. M. Lehn, *J. Am. Chem. Soc.* **2014**, *136*, 13114–13117; k) L. Greb, A. Eichhofer, J. M. Lehn, *Angew. Chem. Int. Ed.* **2015**, *54*, 14345–14348; l) M. Guentner, M. Schildhauer, S. Thumser, P. Mayer, D. Stephenson, P. J. Mayer, H. Dube, *Nat. Commun.* **2015**, *6*, 8406; m) L. A. Huber, K. Hoffmann, S. Thumser, N. Böcher, P. Mayer, H. Dube, *Angew. Chem. Int. Ed.* **2017**, *56*, 14536–14539; n) R. Wilcken, M. Schildhauer, F. Rott, L. A. Huber, M. Guentner, S. Thumser, K. Hoffmann, S. Oesterling, R. de Vivie-Riedle, E. Riedle, H. Dube, *J. Am. Chem. Soc.* **2018**, *140*, 5311–5318; o) E. Uhl, S. Thumser, P. Mayer, H. Dube, *Angew. Chem. Int. Ed.* **2018**, *57*, 11064–11068; p) A. Gerwien, P. Mayer, H. Dube, *J. Am. Chem. Soc.* **2018**; q) H. L. Tierney, C. J. Murphy, A. D. Jewell, A. E. Baber, E. V. Iski, H. Y. Khodaverdian, A. F. McGuire, N. Klebanov, E. C. H. Sykes, *Nat. Nanotechnol.* **2011**, *6*, 625–629; r) U. G. E. Perera, F. Ample, H. Kersell, Y. Zhang, G. Vives, J. Echeverria, M. Grisolia, G. Rapenne, C. Joachim, S.-W. Hla, *Nat. Nanotechnol.* **2013**, *8*, 46–51.

[4] a) J. Conyard, K. Addison, I. A. Heisler, A. Cnossen, W. R. Browne, B. L. Feringa, S. R. Meech, *Nat. Chem.* **2012**, *4*, 547–551; b) J. Conyard, P. Stacko, J. Chen, S. McDonagh, C. R. Hall, S. P. Laptenok, W. R. Browne,

B. L. Feringa, S. R. Meech, *J. Phys. Chem. A* **2017**, *121*, 2138–2150; c) S. Amirjalayer, A. Cnossen, W. R. Browne, B. L. Feringa, W. J. Buma, S. Woutersen, *J. Phys. Chem. A* **2016**, *120*, 8606–8612.

[5] a) B. Oruganti, B. Durbeej, *J Mol Model* **2016**, *22*, 219; b) B. Oruganti, J. Wang, B. Durbeej, *ChemPhysChem* **2016**, *17*, 3399–3408; c) B. Oruganti, J. Wang, B. Durbeej, *Int. J. Quantum Chem.* **2018**, *118*, e25405; d) M. M. Pollard, M. Klok, D. Pijper, B. L. Feringa, *Adv. Funct. Mater.* **2007**, *17*, 718–729.

[6] M. Klok, N. Boyle, M. T. Pryce, A. Meetsma, W. R. Browne, B. L. Feringa, *J. Am. Chem. Soc.* **2008**, *130*, 10484–10485.

[7] a) P. Friedländer, *Chem. Ber.* **1906**, *39*, 1060–1066; b) V. A. Izmail'skii, M. A. Mostoslavskii, *Ukr. Khem. Zh.* **1961**, *27*, 234–237; c) S. Kitzig, M. Thilemann, T. Cordes, K. Ruck-Braun, *ChemPhysChem* **2016**, *17*, 1252–1263; d) S. Wiedbrauk, H. Dube, *Tetrahedron Lett.* **2015**, *56*, 4266–4274; e) C. Petermayer, H. Dube, *Acc. Chem. Res.* **2018**, *51*, 1153–1163; f) K. Eggers, T. M. Fyles, P. J. Montoya-Pelaez, *J. Org. Chem.* **2001**, *66*, 2966–2977; g) K. Tanaka, K. Kohayakawa, S. Iwata, T. Irie, *J. Org. Chem.* **2008**, *73*, 3768–3774; h) S. Wiedbrauk, T. Bartelmann, S. Thumser, P. Mayer, H. Dube, *Nat. Commun.* **2018**, *9*, 1456; i) A. Gerwien, T. Reinhardt, P. Mayer, H. Dube, *Org. Lett.* **2018**, *1*, 232–235; j) A. Gerwien, M. Schildhauer, S. Thumser, P. Mayer, H. Dube, *Nature Commun.* **2018**, *9*; k) A. Nenov, T. Cordes, T. T. Herzog, W. Zinth, R. de Vivie-Riedle, *J. Phys. Chem. A* **2010**, *114*, 13016–13030; l) T. Cordes, T. Schadendorf, K. Rück-Braun, W. Zinth, *Chem. Phys. Lett.* **2008**, *455*, 197–201; m) J. E. Zweig, T. R. Newhouse, *J. Am. Chem. Soc.* **2017**, *139*, 10956–10959.

[8] C. S. Pereira, S. Salgado, F. Rizzo-Aguiar, X. Garcia-Mera, J. E. Rodríguez-Borges, *Synlett* **2013**, *24*, 837–838.

[9] a) K. v. Auwers, *Ber. Dtsch. Chem. Ges. B* **1920**, *53B*, 2285–2299; b) C. E. Dalgliesh, F. G. Mann, *J. Chem. Soc.* **1945**, 893–909.

[10] a) S. Tsuzuki, N. Sato, *J. Phys. Chem. B* **2013**, *117*, 6849–6855; b) W. Wang, B. Ji, Y. Zhang, *J. Phys. Chem. A* **2009**, *113*, 8132–8135; c) R. M. Minyaev, V. I. Minkin, *Can. J. Chem.* **1998**, *76*, 776–788; d) D. J. Pascoe, K. B. Ling, S. L. Cockroft, *J. Am. Chem. Soc.* **2017**, *139*, 15160–15167.

[11] a) C. Garcia-Iriepa, M. Marazzi, F. Zapata, A. Valentini, D. Sampedro, L. M. Frutos, *J. Phys. Chem. Lett.* **2013**, *4*, 1389–1396; b) B. Oruganti, J. Wang, B. Durbeej, *Org. Lett.* **2017**, *19*, 4818–4821; c) J. Wang, B. Durbeej, *ChemistryOpen* **2018**, *7*, 583–589.

[12] G. Marchand, J. Eng, I. Schapiro, A. Valentini, L. M. Frutos, E. Pieri, M. Olivucci, J. Leonard, E. Gindensperger, *J. Phys. Chem. Lett.* **2015**, *6*, 599–604.

[13] a) S. J. Wezenberg, K. Y. Chen, B. L. Feringa, *Angew. Chem. Int. Ed.* **2015**, *54*, 11457–11461; b) T. van Leeuwen, W. Danowski, S. F. Pizzolato, P. Stacko, S. J. Wezenberg, B. L. Feringa, *Chem. Eur. J.* **2018**, *24*, 81–84; c) A. Faulkner, T. van Leeuwen, B. L. Feringa, S. J. Wezenberg, *J. Am. Chem. Soc.* **2016**.

Simulation of Transient XUV/X-ray Absorption Spectrograms

In the previous chapter, we have seen how light-induced reactions can allow molecules to switch between two distinct states and even perform unidirectional rotation. Apart from initiating photochemical reactions, the interaction between light and matter can further offer the ability to survey the ultrafast dynamics of these processes with a variety of spectroscopic techniques. With the help of very short laser pulses, the dynamic response of a laser excited molecule can be followed on its intrinsic timescale from picoseconds to attoseconds. This approach was pioneered by the groundbreaking work of Ahmed H. Zewail, on the ultrafast dissociation of iodine cyanide (ICN) [116] and sodium iodide (NaI) [117], which later earned him the 1999 Nobel Prize in Chemistry [118]. Since then, the field of ultrafast spectroscopy has experienced tremendous growth. Relentless technological progress has seen the development of laser sources capable of generating laser pulses covering a wide range of timescales, from attosecond to microsecond pulses, with energies ranging from the IR up to the X-ray regime [33–41]. In addition, the continuous development of ever more sophisticated spectroscopic techniques, going beyond the classical pump−probe scenario, has increased the amount of information recoverable from these experiments [119, 120]. This has allowed scientists to not only resolve nuclear dynamics [42, 43], but also the motion of electrons [44, 45] with great detail.

Ever since their first demonstration via high-harmonic generation (HHG) [121], attosecond pulses in the XUV region have been applied to investigate ultrafast process in atoms, molecules and solids, with great success. Their high photon energy, capable of easily removing a valence electron, allows the creation of electron wave packets extremely well localized in time. This makes them an ideal triggering tool in a general pump-probe scenario. Additionally, their broad bandwith enables probing of the inner-valence and core-level states, providing insights about charge, elementary composition and electronic state of the system at hand. Building on these properties, ATAS in particular could be established as a powerful tool capable of resolving coupled non-adiabatic electronic-nuclear dynamics with great spectral and temporal resolution [46–55]. However, the analysis and interpretation of these spectra can be quite complicated, due to multiplet effects, if inner-valence states (usually M edges) rather than genuine core-level states (K and L edges) are probed. These challenges occurred for both studies on vinyl bromide (C_2H_3Br) and trifluoroiodomethane (CF_3I) presented in this work. Additionally, both studies exposed the molecules to a strong-field pump pulse to initiate the ultrafast dynamics. This non-resonant excitation process makes identifying the populated excited states difficult, further complicating the interpretation of the recorded data. Here, a simulation of both the ultrafast dynamics and the corresponding XUV/X-ray absorption spectrum is vital to the understanding of this complex interaction between light and matter.

The following section 2.1, introduces a protocol to simulate ATAS and, in sections 2.2 and 2.3, it is shown how employing this protocol can help to explain the ultrafast processes after laser excitation in vinyl bromide (C_2H_3Br) and trifluoroiodomethane (CF_3I).

2.1 Theoretical Framework

In treating ultrafast spectroscopy experiments in a theoretical framework, one can break them down into three steps summarized in Figure 2.1: (1) The perturbation of the system of interest, by a pump pulse, triggering an ultrafast process. (2) The following dynamic response. (3) The spectroscopic observation of the perturbed system via the probe pulse. All three steps present unique challenges and need to be addressed adequately by the theoretical framework. A good summary, especially of the last two steps, their challenges and state-of-the-art treatment, is also given in a recent review by Conti, Cerullo, Nenov and Garavelli [122].
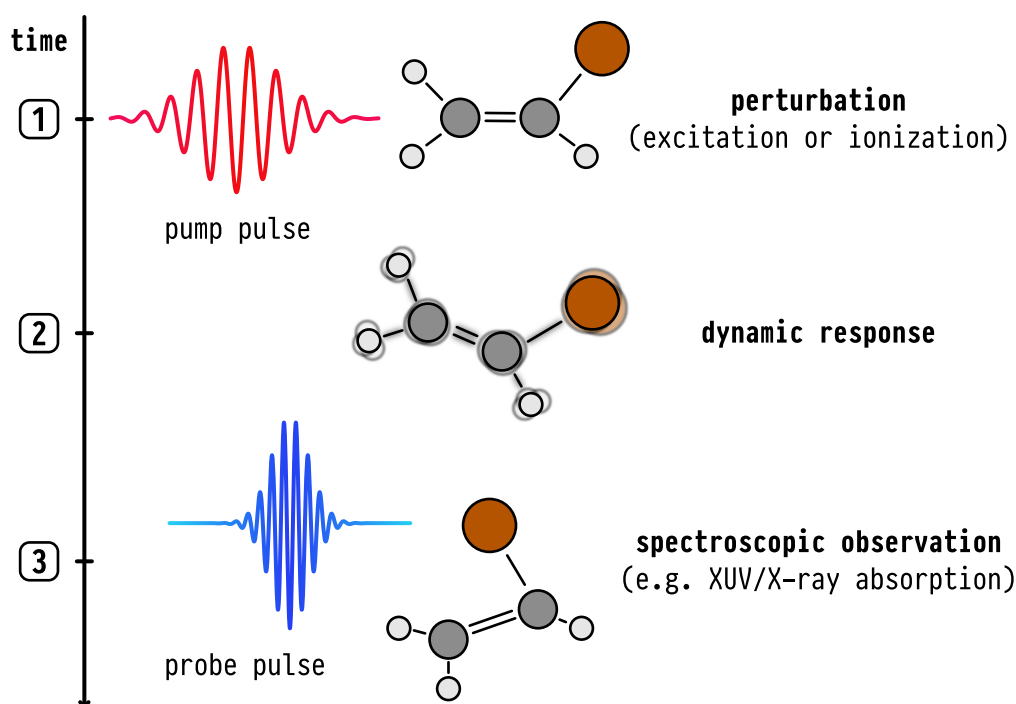
Figure 2.1 – Illustration of the three main steps of a pump-probe experiment. (1) The system (here vinyl bromide) is perturbed by the pump pulse. Depending on the available energy and intensity of the pump laser pulse, this can lead to excitation or even ionization of the molecule. (2) Subsequently, the system dynamically responds to this perturbation of the electronic wavefunction. (3) In the last step the changing system is spectroscopically observed with the delayed probe pulse. The employed spectroscopic technique again depends on the available energy and intensity of the probe laser light.

Starting at the beginning, one has to describe the interaction of the molecule with the electric field of the pump laser pulse. Depending on the available energy, the system can be electronically excited and even ionized [123]. Here, highly nonlinear phenomena including above-threshold ionization (ATI), tunneling ionization and HHG play an important role [124] and make the simulations of this initial laser interaction quite challenging. Two promising approaches in simulating photoexcitation and ionization are of note. First, there is the recently extended R-matrix with time dependence (RMT) ansatz [125–129], which is implemented in the program suites UKRMOL/RMT [128, 129] and QUANTEMOL [130]. Second, the time-dependent B-spline algebraic diagrammatic construction (TD B-spline ADC) method developed by a collaboration of Averbukh, Ruberti and Decleva [131–135]. Both methods have already been successfully utilized in the calculation of photo excitation and ionization of atoms and small molecules [133, 135–139]. These are, however, by no means the only options. For a good summary of the available approaches, see the reviews of Ishikawa and Sato [140] and Armstrong *et al.* [141]. The

simulation of photoexcitation and ionization is not part of the present work as these processes were alternatively approximated by an instantaneous excitation or ionization of the molecule.

Following the initial interaction with the pump pulse, the perturbed system undergoes ultrafast processes that need to be simulated adequately. In order to describe this dynamic response, one has to solve the time-dependent Schrödinger equation (TDSE). Depending on the system at hand, this is most commonly done either fully quantum mechanically via quantum dynamics (QD) or in a semiclassical fashion. The biggest hurdle in using QD simulations lies in the "curse of dimensionality", as the calculation time and storage requirements scale exponentially with the number of included nuclear degrees of freedom. Thus, it is necessary to identify and treat only the degrees of freedom most significant to the observed dynamic response and neglect the rest. This, of course, can be quite challenging and there is ongoing research to help with the selection of suitable coordinates [142–148]. For the present framework the dynamic response of the system is described by *ab initio* NAMD simulations, which have successfully been used in varying cases in chemistry and material science [149, 150]. Within NAMD, the nuclei of the system are approximated by classical bodies obeying Newton's laws of motion. To propagate the system, the necessary forces acting on the nuclei are calculated from the gradient of the electronic wavefunction accessible by solving the time-independent Schrödinger equation (TISE). All NAMD simulation performed in this work were done with the open source program package SURFACE HOPPING INCLUDING ARBITRARY COUPLINGS (SHARC) [151–153], developed by the group of Leticia González. For a general introduction to SHARC and the underlying theory please refer to the review by Mai, Marquetand and González [152] and the dissertation of Thomas Schnappinger [154].

In the final step, the perturbed system is spectroscopically observed by the delayed probe pulse. Here, depending on the available energy and intensity of the probe laser, different spectroscopic processes are utilized. Within this work XUV/X-ray absorption spectroscopy provided the relevant element- and site-specific insights into the electronic and nuclear structure of the system. However, the simulation of the inner-valence- and core-excited states, accessible by the XUV/X-ray light, presents some unique challenges, although at first glance, there are many similarities to the calculation of valence-excited states. In general, (valence-)excited states are calculated by diagonalization of the Hamiltonian matrix. Commonly this is done by iterative diagonalization schemes, like the Davidson algorithm [155], that solve for the lowest-energy states (eigenvalues) of the spectrum first. This complicates the calculation of core-excited states, as they occur at very high energies (usually $>100\,\text{eV}$) above numerous valence-excited states. This results in a huge Hamiltonian matrix, which makes the diagonalization computationally very expensive. A direct, exact diagonalization of only the core-space is not possible due to the off-diagonal coupling between the valence- and core-states as illustrated in Figure 2.2. But, in general, these couplings are very small, as the core orbitals are strongly localized in space and the valence- and core-excited states are well separated in energy. Thus, in a good approximation, these couplings can be discarded, which decouples the valence- and core-space from each other and allows for a direct calculation of just the core-excited states. This so-called core-valence separation (CVS) approximation of the electronic Hamiltonian matrix was first introduced by Cederbaum, Domcke, Schirmer and Barth [156, 157] and has since been applied to most of the major density functional theory (DFT) as well as wave function based electronic structure theories. Here, Stener and coworkers [158] proposed an implementation for TDDFT, which later was coined restricted excitation window time dependent density functional theory (REW-TDDFT) [159], that has successfully been utilized in a number of different cases [160–164]. More recently, Dreuw and coworkers have contributed significantly to the adaption of the algebraic diagrammatic construction (ADC) scheme of the polarization propagator in the calculation of core-excited states by implementing the CVS approximation for different orders of ADC [ADC(2), ADC(2)-x and ADC(3)] [165–169]. In the same manner, Coriani and coworkers successfully implemented the approximation for the family of coupled cluster (CC) approaches [170–174]. Within the present work, the CVS approximation is utilized in an ansatz based on the RASSCF method. This ansatz was first proposed by Josefsson and coworkers [175] to calculate the *L* edge spectra of

transition metal complexes, and due to the versatility of RASSCF, it has since been applied by many groups in a multitude of cases [176–191]. Once again, these are by far not the only possibilities in calculating core-excited states and a good overview of the available DFT and wave function based methods is given by Zhang and coworkers [192] and, more recently, in the reviews by Norman and Dreuw [193], Lundberg and Delcey [194] and Rankine and Penfold [195]. For the sake of completeness, it must also be mentioned, that extensive research has been devoted to the development of real-time (RT) methods for the calculation of core-excited states. The progress in this area is summarized in the reviews of Norman and Dreuw [193] and also Li and coworkers [196].
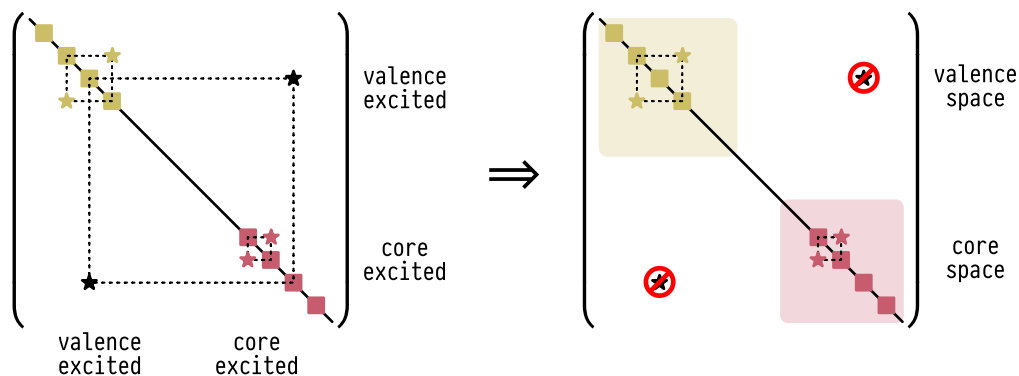

Figure 2.2 – Structure of the shifted electronic Hamiltonian matrix $M_{ij} = \langle \Psi_i | (\mathbf{H} - E) | \Psi_j \rangle$. The excited states are illustrated as squares. The valence-excited states are shown in yellow and the core-excited states in red. The stars on the off-diagonals represent the couplings between the states. The couplings between states of the two spaces (valence and core) are shown in black. Generally, they are quite small, but render an exact direct diagonalization of just the core-excited space difficult. Within the CVS approximation these couplings are neglected, thus decoupling the spaces from each other, allowing the direct diagonalization of just the core-space.

In the following, the theoretical framework to simulate attosecond transient absorption spectra is introduced. Section 2.1.1 first describes the RASSCF/RASPT2 protocol to calculate valence- and core-excited states, and section 2.1.2 summarizes the procedure necessary to generate a transient spectrogram from the information of an NAMD simulation.

2.1.1 RASSCF/RASPT2 Protocol for Valence- and Core-excited States

The algorithm for the calculation of core excitations and subsequently the XUV/X-ray absorption spectrum with the RASSCF method is mainly based on the works of Josefsson and coworkers [175] and Wang, Odelius and Prendergast [182]. As all calculations for the research on C_2H_3Br and CF_3I were performed with the OpenMolcas [197, 198] program package, the mentioned routines and keywords in the following framework are specific to OpenMolcas, but the general procedure can also be performed in other electronic-structure program packages, such as Molpro [199, 200] or PySCF [201–203].

The algorithm utilizes the RASSCF method [204, 205], where both the valence space of the system, and the excitation processes of the core electrons can be described in the same theoretical framework. RASSCF is an extension to general CASSCF, where the AS is further partitioned into three sub spaces RAS1, RAS2 and RAS3, with additional constraints applied to their occupation. In general, they are systematically labeled RAS($n, l, m; i, j, k$), where, i, j and k are the number of orbitals in the RAS1, RAS2, and RAS3 sub spaces, respectively, n is the total number of electrons in all active spaces, l the maximum number of holes allowed in the RAS1, and m the maximum number of electrons allowed in RAS3. For the RAS2, all possible configurations are allowed, making it analogous to the AS within CASSCF. This further partitioning of the orbital space makes the restricted active space (RAS) formalism conceptionally a very intuitive and elegant method in describing the core-excitation process. This is summarized and illustrated in Figure 2.3. Including the relevant valence orbitals (occupied as well as virtual) in the RAS2
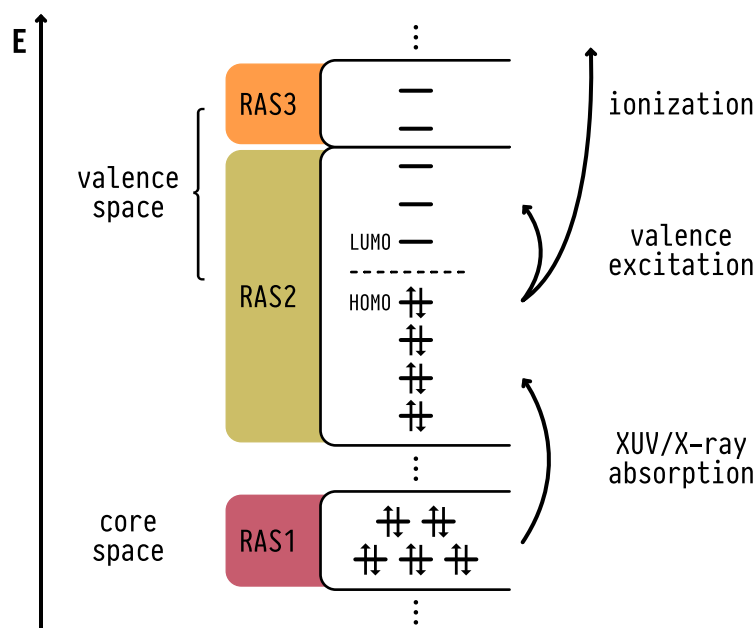
Figure 2.3 – Diagram of the relevant excitations for a XUV/X-ray absorption spectrum (XAS) and how they are represented in the RASSCF ansatz. The combination of the RAS3 and RAS2 depicted in orange and green allows for a high quality description of valence-excited states, as well as possible ionic states. Including the relevant core orbitals into the RAS1, shown in red, and allowing for one hole, makes the calculation of core-excitations possible.

subspace allows for a high quality description of valence excited as well as possible ionized states. Here, similarly to general CASSCF, the maximum feasible number of orbitals and electrons is limited by the necessity of the full configuration interaction (FCI) calculation within this subspace. But including some of the relevant, or even further orbitals, in the RAS3 subspace and limiting the possible excitations to it makes it possible to increase the total size of the valence space without drastically increasing the computational cost. However, the relocation of orbitals from the RAS2 to the RAS3 subspace needs to be done with caution, as it might change the description of the valence-excited states. Here, a good grasp on the system at hand as well as further benchmark calculations are advisable. It is, however, also possible to not use the RAS3 subspace at all. The necessary core orbitals accessible by the probe pulse are included in the RAS1 and, by only allowing for one hole in this subspace, the calculation of core-excited states is possible. In the following, a procedure built on top of this partitioning scheme, the general RASSCF/RASPT2 protocol to calculate the valence- and core-excited states starting from an initial Hartee-Fock (HF) calculation is presented. This protocol is summarized in Figure 2.4 with all corresponding input files listed in appendix A. To perform the protocol one goes through the following steps:

(1) In the first step, an applicable AS for the valence space of the system at hand needs to be set up. Here, it is common to start from a set of HF orbitals and perform an initial CASSCF calculation, with the relevant orbitals in the AS (Both corresponding input files are listed in Listing A.1 and A.2). As already mentioned, the selection of the active orbitals is vital for a correct description of the system and its excited states. Although there are general guidelines on how to best choose an AS [206, 207], it is always necessary to benchmark and verify the size, as well as the selection of orbitals. If the system is subject to relativistic effects, these can be treated within OPENMOLCAS in a two-step approach, both based on the Douglas–Kroll Hamiltonian (DKH) [208, 209]. Here, the relativistic effects are partitioned into two parts: the scalar relativistic effects and spin-orbit coupling (SOC). The scalar part is accounted for by using the relativistic atomic natural orbital (ANO-RCC) basis set [210–214], which is constructed using the DKH. At the time of writing OPENMOLCAS sets further necessary configuration parameters automatically when using
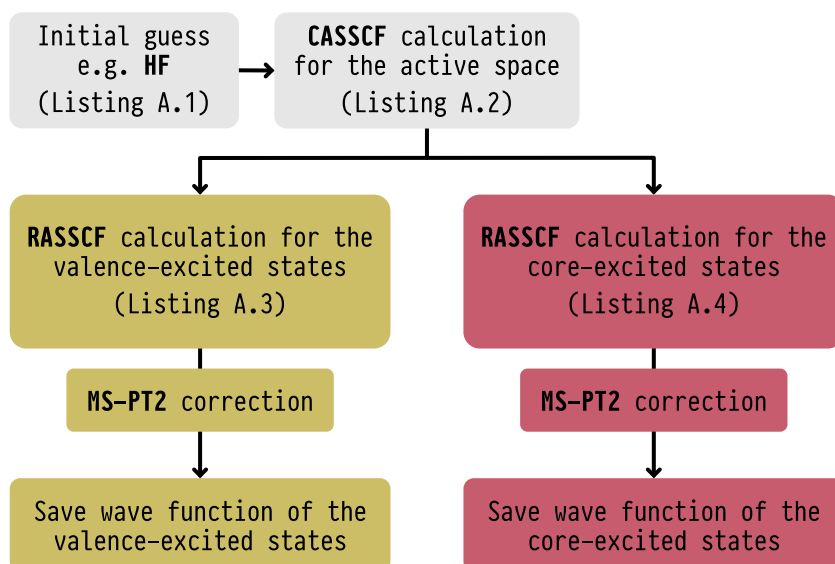
Figure 2.4 – Flowchart illustrating the RASSCF/RASPT2 protocol for the calculation of valence- and core-excited states within the same framework. The corresponding input files for OPENMOLCAS are listed in appendix A.

this basis set. The treatment of the SOC will be handled in the second part of the protocol, as it is not included in a RASSCF calculation.

(2) The converged CASSCF wave function can now serve as the initial guess for all following RASSCF calculations. Its original AS is included in the RAS2 subspace, and it is decided whether to include further (virtual-)orbitals in the RAS3 subspace or not use it at all. Then the relevant core-orbitals are added to the RAS1 subspace, completing the description of the three subspaces. To suppress unwanted orbital rotations with the valence space and aid convergence in the RASSCF calculation itself, the core orbitals are kept frozen to their shape from the initial HF wave function. From here, the setup of the calculation differs slightly, depending on whether the valence- or core-excited states are to be calculated.

   (a) For the valence-excited states, no further configuration is necessary, and they are calculated by a default RASSCF calculation as listed in Listing A.3.

   (b) For the core-excited states, as already mentioned, the CVS approximation needs to be used in order to make their calculation possible. Within OPENMOLCAS this is done by applying the core-hole projection operator onto the RASSCF wave function [215], forcing a hole in a specified RAS subspace. The corresponding keyword is HEXS, which is set to the RAS subspace where the maximum occupation should be eliminated. The complete input file for this calculation is listed in Listing A.4.

(3) Both converged RASSCF calculations can be followed by a perturbative inclusion of the dynamic electron correlation within a multi-state complete active space perturbation theory (CASPT2) (MS-CASPT2) [216] or extended multi-state CASPT2 (XMS-CASPT2) [217, 218] calculation. Here, the setup for valence- and core-excited states is again identical (See Listing A.3 and Listing A.4). It should be mentioned that the CASPT2 calculation of the core-excited states is especially prone to intruder states, and a benchmark for sensible values for the ionization-potential electron-affinity (IPEA) [219] and imaginary shift [220] is advisable. For example, in the case of vinyl bromide, an IPEA shift of 0.25 hartree and an additional imaginary shift of 0.2 hartree were necessary. Of course, it is possible to skip this step, e.g. if the CASPT2 calculations are computationally infeasible. In this case, one would directly continue with the converged RASSCF calculations to the last step of the protocol.

(4) With the RASSCF/RASPT2 calculations converged, we arrive at two wave functions describing the valence- and core-excited states. Finally, it is necessary to save both wave functions as an OPENMOLCAS `JOBIPH` binary file, as these are utilized in the following steps, in the calculation of the excitations energies and oscillator strengths. If a MS-CASPT2 or XMS-CASPT2 calculation was performed, the wave function will be saved to a ".JobMix" file. For a RASSCF calculation it is saved to a ".JobIph" file.

The presented algorithm based on RASSCF, and the subsequent treatment of the dynamic correlation within CASPT2 allows for a high quality description of valence- as well as core-excited wave functions in the same framework. In the following section, the protocol to generate a transient absorption spectrum (TAS) from these wave functions is introduced.

2.1.2 Transient XUV/X-ray Absorption Spectrogram
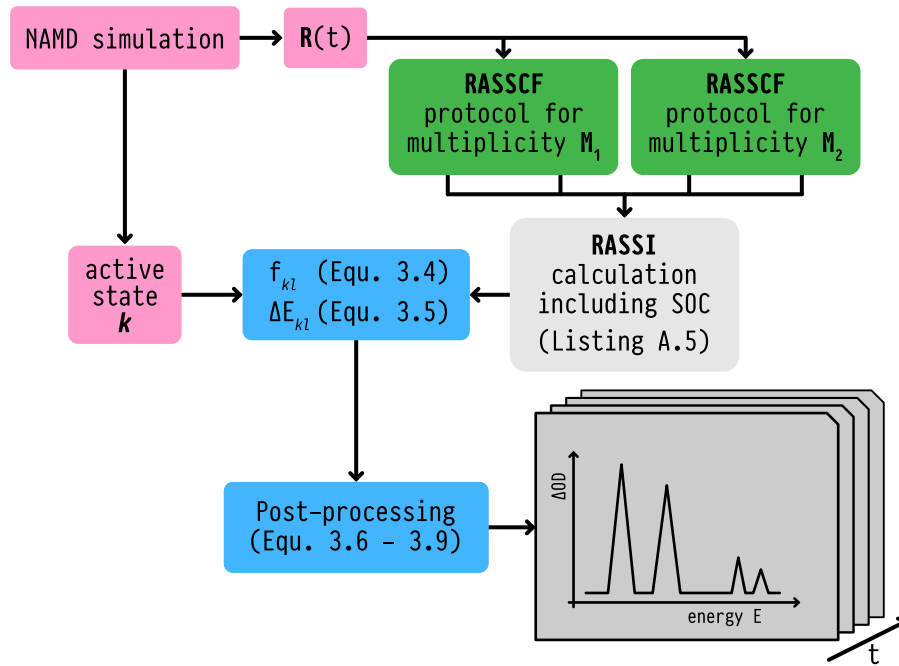
Figure 2.5 – Flowchart illustrating the complete protocol for calculating a time resolved absorption spectrum based on the geometry $R(t)$ and the active states k from the NAMD simulation. The corresponding input files for OPENMOLCAS are listed in appendix A.

Combining the just introduced RASSCF/RASPT2 ansatz with information that is available from *ab initio* NAMD allows the simulation of a transient XUV/X-ray absorption spectrogram. The complete procedure is summarized in the flowchart depicted in Figure 2.5 and the relevant input file is supplied in appendix A. We start at top left of Figure 2.5 with an NAMD simulation of the perturbed system. Here the nuclei of the system are approximated by classical bodies and propagated following Newton's equation of motion:

$$M_A \frac{\partial^2 \mathbf{R}_A(t)}{\partial t^2} = -\frac{\partial E_{el}^k(t)}{\partial \mathbf{R}_A},$$
(2.1)

with M_A the atomic mass of nuclei A and $E_{el}^k(t)$ the electronic energy of the current active state k which is calculated by solving the TISE of the system at the current geometry. So at every time step t the geometry defined by the nuclear coordinates $\mathbf{R}(t)$ and the currently active electronic state k can be extracted from the trajectory and further processed in the simulation of the spectrum. Subsequently, the valence- as well as the core-excited states of the system with multiplicity M_1 (e.g. singlet) are calculated by the above introduced protocol. As already mentioned, relativistic effects are treated within the Douglas–Kroll (DK) transformation of the

relativistic Hamiltonian in two steps. Scalar relativistic effects were already included in the RASSCF calculation of the valence- and core-excited states by utilizing an ANO-RCC basis set. To include the SOC effects, both of these calculations also have to be performed for the multiplicity M_2 (e.g. triplet), resulting in a total of four wave functions for each geometry. In the next step these so called 'spin-free (SF) states' are used as the basis in the restricted active space state interaction (RASSI) method [221–223], where the interactions between all states including the SOC are treated with the use of the atomic mean field integrals (AMFI) [224]. Here it is important to mention that, since the valence- and core-excited states are obtained from different calculations, their wave functions are not necessarily orthogonal. This problem was already mentioned by Wang, Odelius and Prendergast [182], and they suggested using a correction to the overall Hamiltonian already introduced by Malmqvist, Roos and Schimmelpfennig [223] in their original implementation for the SOC treatment in the RASSI method. For this correction all Hamilton matrix elements H_{kl} are shifted by

$$\Delta H_{kl} = \frac{1}{2}\big(\Delta E_k + \Delta E_l\big)S_{kl}, \tag{2.2}$$

with ΔE_k and ΔE_l denoting the energy shifts of the kth and lth states and S_{kl} the corresponding overlap matrix elements. This can be achieved by the keyword `HDIAG` in the `RASSI` module of OPENMOLCAS and supplying the energies of all calculated states in the input file (see Listing A.5 for the general structure of such a calculation). From the RASSI calculation, one arrives at a set of spin-orbit (SO) states $\psi_i^{SO\text{-}RASSI}$, that can be represented in the basis of the supplied SF states $\psi_j^{SF\text{-}RASSI}$ by the linear combination

$$\psi_i^{SO\text{-}RASSI} = \sum_j c_{ij}\psi_j^{SF\text{-}RASSI}. \tag{2.3}$$

After the RASSI calculation, the active state k from the NAMD simulation can now be used to identify the matching valence-excited SO state from the RASSCF/RASPT2 calculations. Depending on the computational setup and level of theory of the dynamics simulation, this can be more or less involved and, in general, it also depends on the system and the complexity of the observed dynamical processes. For example, in the case of neutral vinyl bromide, it was done by comparing the scalar product between the dipole moments vectors of the active state k and the different valence-excited SF states. But, for the cationic species, it was sufficient to just use the same state number/index. Finally, for both cases, the valence-excited SO state with the largest contribution of the matched SF state was selected in the further calculation of the spectrum. To help with the understanding of the connections between the different states, the illustration in Figure A.2 in the appendix A shows how the different states, starting with the original RASSCF states, are intertwined. With the correct valence-excited SO state identified, two values, the oscillator strengths f and the excitation energies ΔE, are then used in the generation of the spectrum at the current time step t. In the following, we will focus on the core-valence transition $k \rightarrow l$, with the initial state k, the ground state or any other valence-excited state of the system and the final state l, a core-excited state with one hole in the core space. For this transition the oscillator strength f$_{kl}$ is calculated within the `RASSI` module following the equation

$$\text{f}_{kl} = \frac{2}{3}\frac{m_e}{\hbar^2 e^2}(E_l - E_k)\sum_{x,y,z}\left\langle\psi_l^{SO\text{-}RASSI}\big(\mathbf{r};\mathbf{R}(t)\big)\Big|\hat{\mu}_{x,y,z}\Big|\psi_k^{SO\text{-}RASSI}\big(\mathbf{r};\mathbf{R}(t)\big)\right\rangle^2, \tag{2.4}$$

with m_e denoting the electron mass, $\hbar$ the reduced Planck constant, e the elementary charge, E_l and E_k the energies of both states, $\psi_l^{SO\text{-}RASSI}\big(\mathbf{r};\mathbf{R}(t)\big)$ the wave function of the final state l, $\psi_k^{SO\text{-}RASSI}\big(\mathbf{r};\mathbf{R}(t)\big)$ the wave function of the initial state k and $\hat{\mu}$ the dipole moment operator. Further the excitation energy of the transition is given by the difference

$$\Delta E_{kl} = E_k - E_l. \tag{2.5}$$

To go beyond a simple delta-peak spectrum of f_{kl} over ΔE_{kl}, some post-processing is necessary. Figure 2.6 illustrates the different steps and connects the following equations to actual plots, based on the dataset of vinyl bromide. Generally, calculated peaks are broadened by either a Gaussian function, a Lorentz function, or a convolution of both functions, a Voigt profile. All three functions are shown in appendix B. Using the example of the Gaussian function, the peak of quantities ΔE_{kl} and f_{kl} can be broadened by the function

$$G_{kl}(E; \Delta E_{kl}, \sigma, t) = f_{kl} \cdot \frac{1}{\sigma\sqrt{2\pi}} \exp\left(\frac{-\left(E - \Delta E_{kl}\right)^2}{2\sigma^2}\right), \tag{2.6}$$

with the standard deviation σ which in turn can be calculated from the full width at half maximum (FWHM) Γ, commonly used in spectroscopy, by

$$\sigma = \frac{\text{FWHM}}{2\sqrt{2\ln 2}} = \frac{\Gamma}{2\sqrt{2\ln 2}}. \tag{2.7}$$

The complete spectrum $G_k(E; t)$ (shown in (2) of Figure 2.6) for the given initial state k is obtained by the summation over all l relevant broadened signals $G_{kl}(E; \Delta E_{kl}, \sigma, t)$ and subsequent normalization:

$$G_k(E; t) = \frac{1}{N} \sum_l G_{kl}(E; \Delta E_{kl}, \sigma). \tag{2.8}$$

To simulate the complete spectrum $G(E; t)$ for one timestep t (shown in (3) of Figure 2.6) all spectra $G_k(E; t)$ of the M calculated trajectories are summed up:

$$G(E; t) = \frac{1}{M} \sum^M G_k(E; t). \tag{2.9}$$

If one wants to include additional contributions to this spectrum, e.g., from different species of the system like singly or double ionized molecules, they can be added here. This can be done by performing a similar NAMD simulation of the additional species and subsequent calculation of the core excitations and finally the corresponding spectrum $G(E; t)$. It is also possible to just approximate further contributions, as it was done in the case of vinyl bromide (see plot (4) of Figure 2.6). Here, the experimentally observable ground state bleach was approximated by subtracting the static ground state spectrum of neutral vinyl bromide calculated at $t = 0$ fs. In the final step the complete procedure is repeated for all time steps t of all the M trajectories and one arrives at the transient spectrum $G(E, t)$ shown in (5) of Figure 2.6, based on the NAMD simulation of the system at hand.

In the following sections, the application of the complete procedure on the two systems C_2H_3Br and CF_3I in order to study their ultrafast dynamics after laser excitation is presented.

2.2 The Ultrafast Strong-Field Dissociation of Vinyl Bromide

The article "Ultrafast strong-field dissociation of vinyl bromide: an attosecond transient absorption spectroscopy and non-adiabatic molecular dynamics study" published in *Structural Dynamics* shows the strength of the combined experimental and theoretical approach, demonstrating it for the ultrafast dissociation of vinyl bromide. The key statements of the article are:

- The strong-field initiated ultrafast dynamics of vinyl bromide has been studied by ATAS. Probing the Br M edge with XUV laser light allows for an assessment of the competing processes in neutral and ionized vinyl bromide.

- The rich transient absorption spectrogram shown in FIG. 3 of the publication was recorded for an energy range between 64.0 eV to 72.0 eV with a time resolution of 2.3 fs. The ground state bleaching signals at 71.0 eV and 71.9 eV appears as a doublet, due to the
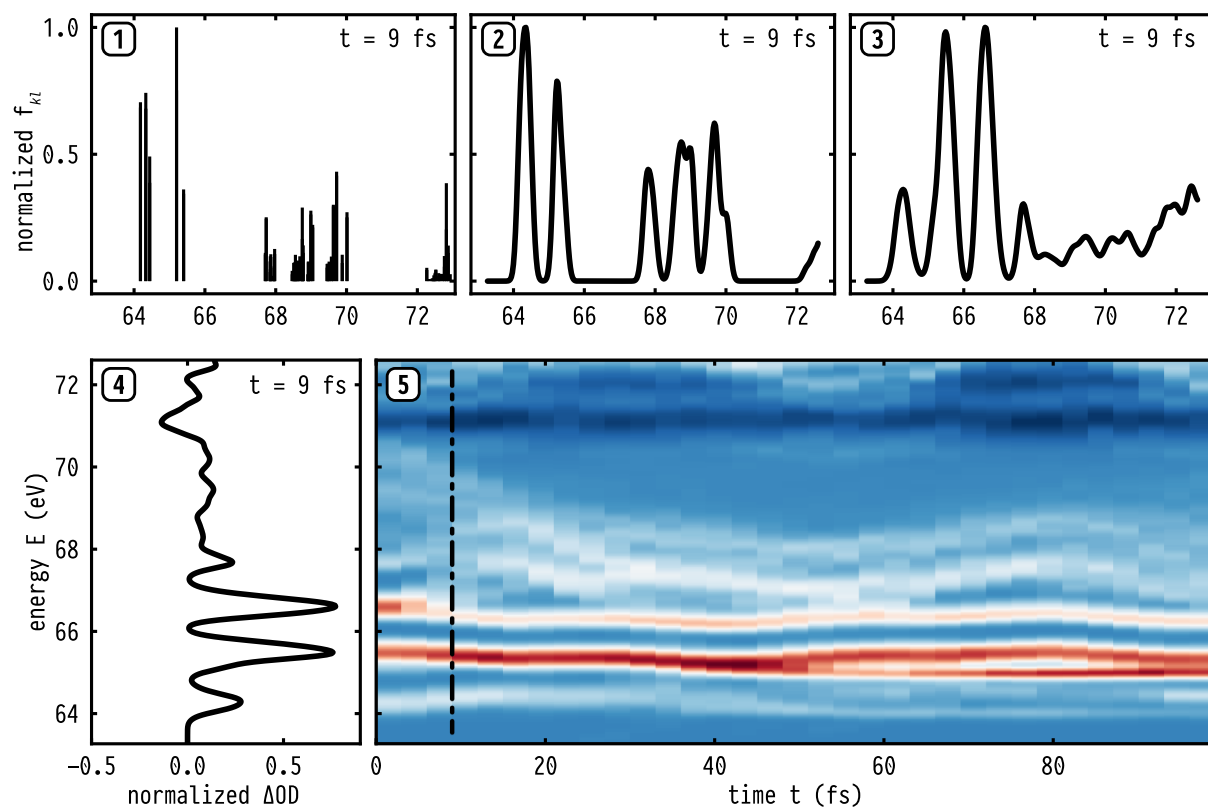
Figure 2.6 – Illustration of the post-processing steps necessary to turn a single core excitation spectrum into a final ATAS spectrum, exemplified by the calculations of the ultrafast dissociation of cationic vinyl bromide. (1) Stemplot of f_{kl} over ΔE_{kl} for all l transitions of a specific active state k of one trajectory at time step $t = 9\,$fs. (2) The complete broadened spectrum $G_k(E;t)$ comprised of all the l Gaussian broadened peaks $G_{kl}(E;\Delta E_{kl},\sigma,t)$ (see Equations 2.6 and 2.8). Here specifically, a value of $\sigma = 0.1\,$eV was used. (3) The broadened spectra $G_k(E;t)$ of all calculated trajectories and relevant active states k for the time step $t = 9\,$fs are summed up, resulting in the spectrum $G(E;t)$ (see Equation 2.9). (4) Additional contributions to the complete spectrum, like signals stemming from further species of vinyl bromide, can be added. Here, an approximation of the experimentally observable ground state bleach was included by subtracting the static ground state spectrum of neutral vinyl bromide calculated at $t = 0\,$fs. (5) Repeating these steps for all time steps t results in this complete transient spectrum $G(E,t)$ based on the NAMD simulation of the system. Here, the dotted black line indicates the spectrum shown in subplot (4).

spin-orbit splitting of the $3d_{5/2}$ and $3d_{3/2}$ states in Br. This spin-orbit splitting is also present in the main doublet at $65.5\,$eV and $66.4\,$eV and further weaker signals up to $70\,$eV, which have been attributed to ionic states of vinyl bromide [225]. All signals show a pronounced oscillation, corresponding to different vibrational eigenmodes of vinyl bromide. Additional sharp atomic Br lines at $64.4\,$eV and $65.0\,$eV, at temporal delays $>100\,$fs, indicate an ultrafast dissociation of either the neutral molecule, the ion or both. A previous unreported signal in the region of $64.0\,$eV to $65.0\,$eV shows a different more complex behavior compared to the vibrational features. A magnified view of this energy range is shown in FIG. 4 of the publication. After an initial upshift to about $64.4\,$eV, the signal bifurcates after around $30\,$fs. Afterwards the main branch shifts down in energy to $64.1\,$eV, reaching the value of the atomic Br $M_{4,5}$ transition. As this transition $Br(P_{1/2}) \to Br(D_{5/2})$ is dipole forbidden in the atomic limit, but not in the molecular context, this signal vanishes for longer time scales $>80\,$fs. This coincides with the birth and rise of the allowed atomic Br transitions $Br(P_{3/2}) \to Br(D_{5/2})$ and $Br(P_{1/2}) \to Br(D_{3/2})$ at $64.4\,$eV and $65.0\,$eV respectively. The observed behavior in the region of $64.0\,$eV to $65.0\,$eV clearly indicates an ultrafast dissociation process.

- For these complex spectral features, several possibilities were discussed. A previous study on vinyl bromide [225] predicted a signal in this energy range to stem from the second excited state (D_3) of the cation following Koopmans' theorem. But ATAS experiments on methyl bromide [51] attributed a similar signal to a neutral excited state, populated by a multi-photon process. Both possibilities are also supported by applying Koopmans' theorem, as for the neutral vinyl bromide, one would expect a signal of an electronically excited $\pi\pi^*$ state in the same energy range.

- To untangle the involvement of neutral and cationic vinyl bromide, the dynamics of both species after strong field excitation are investigated by NAMD simulations. The geometry and state information from the NAMD simulations were then utilized in the RASPT2 ansatz to calculate the transient XUV/X-ray absorption spectra for both species. The detailed, state-resolved analysis of the calculated trajectories and related spectral features of the simulated spectra allowed for a rigorous and quantitative comparison with the experimental data. This enabled attribution of all spectral features of the transient XUV/X-ray absorption spectra to the corresponding species of vinyl bromide.

- For neutral vinyl bromide, the multi-photon process that results in the excitation to the bright $\pi\pi^*$ state was approximated by a one-photon process within the NAMD simulation. For the analysis of the excited state dynamics, 189 trajectories were taken into account. After excitation, neutral vinyl bromide exclusively shows ultrafast dissociation of the C−Br bond, with on average a doubling of the initial bond length after about 50 fs. In general, the simulated XAS matches the energy range of the experiment very well (see FIG. 6 of the publication for the simulated spectrum). Further, as predicted by Koopmans' theorem there are prominent signals in the range between 64.0 eV to 65.0 eV. Within the first 20 fs all signals shift to lower energies, and two sharp features, a stronger one at 64.3 eV and a weaker one at 65 eV, appear. After about 40 fs simulation time, both signals remain constant in energy, with the energetically lower one becoming increasingly prominent. With all trajectories dissociated at this point in time, the signals are the spin-allowed transitions of atomic bromide. But compared to the experimentally recorded spectrum, it is clear that the signal from the neutral species alone cannot explain the observed patterns in the energy range between 64.0 eV to 65.0 eV.

- With the used pump pulse, the first three cationic states, D_1, D_2 and D_3 are accessible, so 50 trajectories were started in each. For the analysis of the dynamics of the three cationic states, 11, 26 and 45 trajectories were taken into account. Compared to the purely dissociative dynamics of the neutral species, the cationic species showed more complex behaviour depending on the initial state. The transient XAS, shown in FIG. 8 of the publication, was simulated based on all analyzed trajectories. To attribute the spectral features to the different observed dynamics, XAS spectra for the corresponding subset of trajectories alone were also simulated (see FIG. S21 - S26 in the appendix D.3).

- For the trajectories started in the D_1 and D_2 states, only bound state vibrational dynamics were observed. In both cases, the C=C double bond and the C−Br bond showed oscillation periods between 20 fs to 75 fs corresponding to the electronic character of both cationic states. Comparing with the neutral spectrum, we again see the ground state bleach in the region between 71.0 eV to 72.5 eV, but, here, its intensity distribution is modulated by contributions from the D_1 signal. Further, the D_1 state shows a clear doublet at 66.7 eV and 67.7 eV stemming from the spin-orbit splitting. Both peaks oscillate with a period matching the observed oscillation of the C−Br bond of the D_1 trajectories. The most intense features of the spectrum, a doublet at 65.5 eV and 66.5 eV can be assigned to the D_2 state. It also shows a modulation of the signal that matches the observed oscillation periods of the C=C and C−Br bond vibrations of the D_2 trajectories. In summary, the signals stemming from the D_1 and D_2 states show a clear oscillation, but neither of them can reproduce the splitting of the intense 65.5 eV peak nor the weak band at 64 eV.

- The spectrum of all trajectories started in the D_3 state, again shows the distinct doublet now at $64.3\,\text{eV}$ and $65.2\,\text{eV}$ (FIG. S23 in appendix D.3). But, in contrast to the oscillating features, both signals become constant after about half an oscillation period at about $40\,\text{fs}$ and subsequently split up into four constant contributions at $64.0\,\text{eV}$, $64.5\,\text{eV}$, $65.0\,\text{eV}$ and $65.5\,\text{eV}$. This can be explained by the three different $C-Br$ bond dynamics observed in the trajectories: purely vibrational, slow dissociative and fast dissociative. The vibrational bound state dynamics show the prominent doublet peak at $64.3\,\text{eV}$ and $65.2\,\text{eV}$, oscillating with the period of the $C-Br$ bond. For the fast dissociating trajectories, the same doublet occurs, but, after the initial first half of the oscillation period, both peaks remain constant in energy at $64.0\,\text{eV}$ and $65.0\,\text{eV}$. This is further accompanied by a significant change in the intensities of both peaks. The peak at $65.0\,\text{eV}$ strongly increases in intensity, while the energetically lower peak fades. This change stems from the bromide becoming more and more "atom-like" with increasing distance to the vinyl cation. Here from the two spin-allowed transitions $Br(P_{3/2}) \rightarrow Br(D_{5/2})$ and $Br(P_{1/2}) \rightarrow Br(D_{3/2})$, only the higher one $Br(P_{1/2}) \rightarrow Br(D_{3/2})$ survives in the atomic limit. Finally, for the slow dissociative trajectories, a mixture of both distinct spectral features of the fast dissociative and purely vibrational ones is observed.

- In summary, the prominent features in the energy range between $64\,\text{eV}$ to $66\,\text{eV}$ originate from overlapping contributions of the cationic vinyl bromide. It is composed of the spectral features of the non-dissociative dynamics in the D_2 and D_3 states, and the spin-orbit excited atomic Br generated in the dissociation in the D_3.

The article "Ultrafast strong-field dissociation of vinyl bromide: an attosecond transient absorption spectroscopy and non-adiabatic molecular dynamics study" was published in *Structural Dynamics* under the terms of the Creative Commons Attribution 4.0 International License (CC BY 4.0, URL: https://creativecommons.org/licenses/by/4.0/). In the following it is reprinted unaltered from *Struct. Dyn.* **8**, 034104 (2021). Copyright 2021 Author(s). The supporting information for this article is reprinted unaltered in the appendix D.3.

Ultrafast strong-field dissociation of vinyl bromide: An attosecond transient absorption spectroscopy and non-adiabatic molecular dynamics study

View Online   Export Citation   CrossMark

Florian Rott,[1] Maurizio Reduzzi,[2] (iD) Thomas Schnappinger,[1] (iD) Yuki Kobayashi,[2] (iD) Kristina F. Chang,[2]
Henry Timmers,[2] Daniel M. Neumark,[2,3] (iD) Regina de Vivie-Riedle,[1,a)] (iD) and Stephen R. Leone[2,3,4,a)] (iD)

AFFILIATIONS

[1]Department of Chemistry, LMU Munich, 81377 Munich, Germany
[2]Department of Chemistry, University of California, Berkeley, California 94720, USA
[3]Chemical Sciences Division, Lawrence Berkeley National Laboratory, Berkeley, California 94720, USA
[4]Department of Physics, University of California, Berkeley, California 94720, USA

[a)]Authors to whom correspondence should be addressed: regina.de_vivie@cup.uni-muenchen.de and srl@berkeley.edu

ABSTRACT

Attosecond extreme ultraviolet (XUV) and soft x-ray sources provide powerful new tools for studying ultrafast molecular dynamics with atomic, state, and charge specificity. In this report, we employ attosecond transient absorption spectroscopy (ATAS) to follow strong-field-initiated dynamics in vinyl bromide. Probing the Br M edge allows one to assess the competing processes in neutral and ionized molecular species. Using *ab initio* non-adiabatic molecular dynamics, we simulate the neutral and cationic dynamics resulting from the interaction of the molecule with the strong field. Based on the dynamics results, the corresponding time-dependent XUV transient absorption spectra are calculated by applying high-level multi-reference methods. The state-resolved analysis obtained through the simulated dynamics and related spectral contributions enables a detailed and quantitative comparison with the experimental data. The main outcome of the interaction with the strong field is unambiguously the population of the first three cationic states, D_1, D_2, and D_3. The first two show exclusively vibrational dynamics while the D_3 state is characterized by an ultrafast dissociation of the molecule via C–Br bond rupture within 100 fs in 50% of the analyzed trajectories. The combination of the three simulated ionic transient absorption spectra is in excellent agreement with the experimental results. This work establishes ATAS in combination with high-level multi-reference simulations as a spectroscopic technique capable of resolving coupled non-adiabatic electronic-nuclear dynamics in photoexcited molecules with sub-femtosecond resolution.

I. INTRODUCTION

Since the demonstration of attosecond pulses, in the extreme ultraviolet (XUV) region of the electromagnetic spectrum (10–124 eV), via high-order harmonic generation (HHG), these pulses have been exploited for time-resolved investigations of ultrafast photo-initiated processes in atoms, molecules, and solids. Due to the high associated photon energy, capable of easily removing a valence electron from the sample under consideration, attosecond pulses allow one to create electron wave packets extremely well localized in time. This property, which makes them very sharp photo-triggering tools in a "pump-probe" scenario, is at the basis of the early attosecond streaking technique.[1] Originally devised as a temporal characterization methodology for the attosecond pulses themselves,[2] "streaking" has

been exploited as a genuine spectroscopic tool, allowing for the determination of attosecond delays in photoemission both in atomic[3,4] and solid-state[5,6] systems. With the same spirit, attosecond pulses have been used in the last decade to create electron wave packets in highly excited cationic states of molecules, leading to the discovery of effects such as electron localization in diatomic molecules[7] and, later, of purely electronic charge migration in biomolecules.[8] On the other hand, the broad bandwidth of attosecond pulses makes them particularly valuable probing tools, because of the element, charge, and electronic state sensitivity gained by accessing the inner valence (in the XUV) and the core level states (in the soft x-ray region, and, possibly in the future, in the hard x ray) of elements. Along these lines, after the seminal work of Goulielmakis *et al.*,[9] attosecond XUV pulses have

been exploited to take snapshots of ultrafast processes in atoms,[10,11] molecules,[12,13] and solid-state materials,[14–17] triggered by the strong-field interaction of the sample with an ultrashort few-cycle pulse. While this scheme is very convenient from the implementation viewpoint [carrier-envelope phase (CEP) stable few-cycle pulses are ideal drivers for the generation of isolated attosecond pulses, and thus, a replica for excitation purposes can be easily derived] and grants exquisite temporal localization of the initially prepared excited wave packet due to the extremely short pulses employed, there are two main bottlenecks historically ascribed to this methodology, limiting the range of applications—on the one hand, the non-resonant and non-perturbative nature of the excitation process; on the other, the complications in data interpretation due to multiplet effects in probing inner valence states (usually M edges) rather than genuine core level states (K and L edges). Some of the main recent directions in attoscience and, in general, of table-top ultrafast soft x-ray spectroscopy solve these methodological issues, moving toward single photon excitation schemes (from strong field to weak field)[18,19] and core level probing (from 800-nm-driven XUV HHG to soft x-ray ponderomotively scaled HHG).[20–22] Because of the great spectroscopic interest in the water window spectral region (containing the K absorption edges of carbon, nitrogen and oxygen as well as the L edges of calcium, scandium, titanium, and vanadium) for chemistry, biology, and materials science, these developments are crucial for the future of the field and hold promise to elucidate photoinduced processes of paramount importance, such as UV radiation damage of DNA and light-induced phase transitions from each individual atom's perspective. Still, the above-mentioned difficulties can be greatly diminished by an appropriate theoretical ansatz.

For the complete treatment of such time-resolved spectroscopy experiments in a theoretical framework, three different problem sets need to be addressed. As a first step, one has to describe the interaction of the system with the strong near infrared (NIR) field. Although it is possible[23–25] to simulate the strong-field ionizations and excitations, it is not the focus of this work and we assume an instantaneous ionization or excitation. Second, one has to adequately describe the ultrafast processes the system undergoes after irradiation with the strong few-femtosecond NIR pump pulse. In our work, this is done by performing *ab initio* non-adiabatic molecular dynamics (NAMD) for the relevant electronic states. This makes it possible to resolve both the changes in the electronic structure and the nuclear motion over time. The third problem set is the simulation of the time-resolved XUV absorption spectrogram. In order to tackle this task, we use the restricted active space self-consistent field (RASSCF) theory followed by a perturbative inclusion of the dynamic electron correlation (RASPT2) to calculate the XUV absorption along each trajectory.

Besides the high-quality description of the absorption itself, the RASPT2 technique also allows one to decompose the entire spectrogram into its state-specific components. The RASPT2 ansatz to calculate the XAS spectra was first proposed by Josefsson and co-workers[26] to calculate the L-edge spectra of transition metal complexes. Due to the versatility of the RASSCF, it was used by many groups in varying cases,[27–42] but, in general, there are a variety of methods reported in the literature to calculate x-ray absorption (XAS) or XUV absorption spectra. First, simulations were done with the static exchange (STEX) approximation.[43–46] Later, Stener and co-workers[47] proposed an ansatz based on the restricted excitation window time dependent

density functional theory (REW-TDDFT), which was successfully utilized in a number of different cases.[20,48–51] More recently, the core-valence separation (CVS) approximation[52] was used in conjunction with coupled-cluster (CC) theory.[53–57] Also, Hait and co-workers successfully utilized the Restricted Open-Shell Kohn–Sham (ROXS) theory[58,59] in the prediction of core-level spectra.[60,61] A good overview of the various methods is given by Zhang and co-workers[62] and, more recently, in the reviews by Norman and Dreuw[63] and Lundberg and Delcey.[64]

Here, we propose a joint experimental and theoretical approach and apply it to follow the strong-field-initiated dynamics of vinyl bromide (C_2H_3Br), exposed to a few-cycle NIR field. The ultrafast photophysics of vinyl bromide, similar to other substituted ethylenes, has been historically studied in connection to photoactivated cis/trans-isomerization.[65] In vinyl halides, in particular, the halogen substituent (F, Cl, Br, I) introduces conical intersections between the $\pi\pi^*$ state and $n\pi^*/n\sigma^*$ states, leading to efficient ultrafast photodissociation of the halogen–carbon bond.[66] We employ attosecond transient absorption spectroscopy (ATAS) to simultaneously follow neutral and cationic states dynamics of the molecule after the interaction with the strong NIR field by probing the Br M edge. The experiment leverages a previous investigation,[67] performed at coarser tens-of-femtoseconds temporal resolution, highlighting the great amount of information and detail accessed by attosecond spectroscopies. That work assigned features based on conventional intuition known at the time; in hindsight from the new theoretical work here, numerous assignments of the features in the earlier experimental spectra are reassessed.

II. METHODS

The output of a carrier-envelope phase (CEP) stable Ti:sapphire system ($\lambda = 800$ nm), delivering 27 fs pulses with an energy of 2 mJ per pulse at 1 kHz, is spectrally broadened in a Ne-filled stretched hollow-core fiber. The pulses are then compressed using both a set of broadband chirped mirrors and a 1-mm-thick ammonium dihydrogen phosphide (ADP) crystal,[68] yielding a compressed pulse duration of sub-4 fs. The pulses are then divided into a pump and probe arm using a 50:50 beam splitter. The employed ATAS pump-probe scheme is depicted in Fig. 1. The XUV-probe pulse is generated via HHG by focusing the few-cycle NIR pulses into a 3-mm-long gas cell backed with 30 Torr of Ar. Isolated attosecond pulses, covering the energy range between 55 and 73 eV, are obtained by the amplitude gating technique,[69] as shown in Fig. 1. The residual NIR light is filtered out of the probe arm with a 200-nm-thick Al filter. According to previous streaking measurements,[68] the XUV pulse duration is estimated to be 170 as. A toroidal mirror is used to focus the radiation into a static gas cell (3 mm interaction length) filled with 10 Torr of C_2H_3Br (Sigma-Aldrich) at room temperature (298 K).

The NIR-pump pulse travels through a piezoelectric delay stage and is collinearly recombined with the XUV-probe with a hole mirror placed before the focusing toroidal mirror. On target, the intensity of the NIR-pump pulse, $I = 2 \times 10^{14}$ W cm^{-2}, is high enough to trigger various competing processes, both in the neutral molecule (via frustrated tunnel ionization and multiphoton excitation) and in its cation (via strong-field ionization). The NIR-pump pulse is finally removed from the beam path after the interaction gas cell using a second 200-nm-thick Al filter. The XUV radiation transmitted through the interaction gas cell is analyzed with a home-built spectrograph, consisting
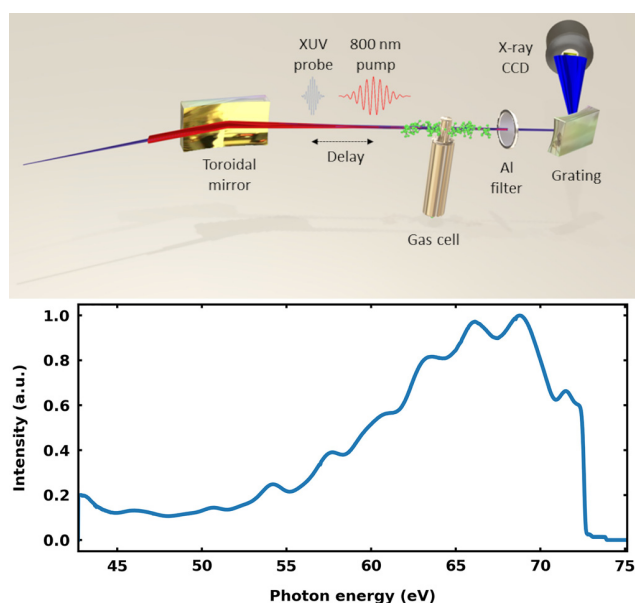
FIG. 1. (Top) Schematic of the employed ATAS setup. After being delayed by a piezo-driven stage and collinearly recombined (not shown), the 800 nm fs pump and XUV attosecond (as) probe pulses are focused with a toroidal mirror into a static absorption gas cell, filled with vinyl bromide. The transmitted XUV light, after removal of the copropagating 800 nm radiation by an aluminum filter, is spectrally dispersed with a grating and imaged with a CCD camera. (Bottom) The XUV spectrum of the generated attosecond probe pulses. The sharp decrease at 72.7 eV is due to the employed aluminum filter.

of a dispersive, gold-coated, aberration-corrected concave XUV grating (Hitachi) and a back-illuminated x-ray-sensitive cooled CCD camera (Princeton Instruments). The energy resolving power of the spectrograph is estimated to be $E/dE = 1000$ from previous experiments,[11] yielding a resolution of 70 meV at 70 eV photon energy. A beam shutter is programmed to block the NIR pump arm in order to reference the C_2H_3Br XUV absorption spectrum with and without the NIR pump pulse and measure the differential optical density, defined as the natural logarithm of the ratio between the spectra when the pump is on and off.

III. COMPUTATIONAL DETAILS

A. *Ab initio* level of theory

The electronic states of vinyl bromide were computed using the state-average complete active space self-consistent field method[70,71] including five states in the state-averaging procedure (SA5-CASSCF). All calculations were carried out with the OpenMolcas[72,73] program package using a modified ATZP basis set (m-ATZP). For more details about the modification and the validation of its use, see the supplementary material Sec. II B.[108] An active space (AS) including eight electrons in seven orbitals [AS(8,7)] was employed. It includes the carbon–carbon double bond (π_1, π_3^*) (Fig. 2), the carbon–bromine single bond (σ_1, σ_2^*) as well as both remaining bromine $4p$ orbitals. One nonbonding orbital is part of a second π orbital (π_2); the other one forms the lone-pair n_1. To stabilize the active space, we also had to include one additional virtual orbital (π_4^*), which has significant
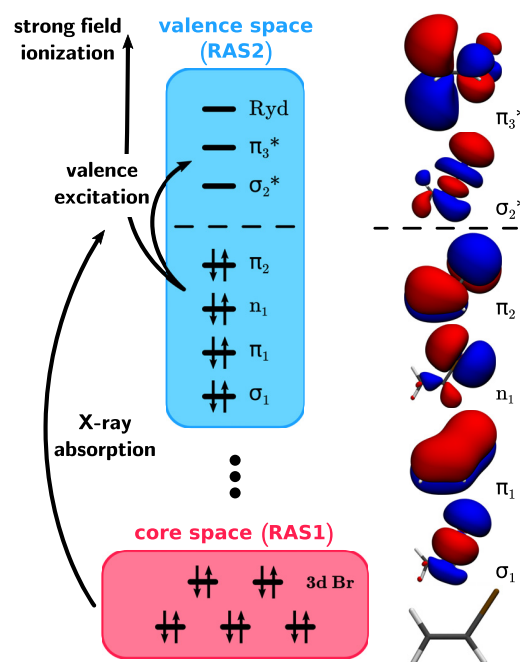
FIG. 2. Diagram of the relevant excitations for an x-ray/XUV absorption spectrum. The RAS2 depicted in blue allows us to describe the valence excited states as well as cationic states after the interaction with the strong field. The RAS1 includes all five $3d$ bromine core orbitals and is shown in red. The combination of both RASs allows us to treat the x-ray/XUV absorption and simulate the XAS. The orbitals are shown with an isovalue of 0.02 and oriented according to the geometry at the bottom.

Rydberg (Ryd.) contributions. The complete AS is shown in Fig. S7 in the Supporting Information, and the main parts of it, except for the π_4^*/Ryd. orbital, are also in Fig. 2. An overview of the excited states of both neutral and cationic vinyl bromide, their vertical excitation energies, and electronic character is given in Table I. The states are ordered

TABLE I. Excited state electronic character and vertical excitation energies ΔE of neutral and cationic vinyl bromide. The excitation energy is given in units of eV relative to the neutral ground state (S_0) at the Frank–Condon point. For the character of the cationic vinyl bromide, the orbitals that are partially occupied are listed.

	Neutral			Cationic	
State	Character	ΔE (eV)	State	Character	ΔE (eV)
T_1	$\pi_2 \rightarrow \pi_3^*$	4.08	D_1	π_2	8.81
T_2	$\pi_2 \rightarrow \sigma_2^*$	6.26	D_2	n_1	9.72
T_3	$n_1 \rightarrow \sigma_2^*$	6.61	D_3	π_1	11.28
S_1	$\pi_2 \rightarrow \sigma_2^*$	6.67	D_4	σ_1	12.94
S_2	$\pi_2 \rightarrow \pi_3^*$	7.34	D_5	n_1, π_2, π_3^*	14.26
S_3	$n_1 \rightarrow \sigma_2^*$	7.50			
T_4	$n_1 \rightarrow \pi_3^*$	7.53			
S_4	$n_1 \rightarrow \pi_3^*$	7.77			
T_5	$\pi_2 \rightarrow \pi_4^*$	8.16			

with increasing energy and are labeled according to their adiabatic state number at the Frank–Condon (FC) point.

B. Dynamics simulation

The NAMD of vinyl bromide were simulated using the surface hopping including arbitrary couplings (SHARC) program package.[74–76] A set of 400 initial conditions (geometries and velocities) were generated based on a Wigner distribution[77,78] at 0 K computed from harmonic vibrational frequencies in the optimized ground state minimum. The underlying optimization and frequency calculations were performed at the closed-shell coupled-cluster level of theory, including singles, doubles, and perturbative contributions of triples using the aug-cc-pVTZ basis set[79–83] [CCSD(T)/aug-cc-pVTZ]. For the neutral species, a subset of 300 trajectories was randomly chosen and propagated starting in the bright $\pi\pi^*$ state (at the FC point S_2). To relate to the excitation process, the initialization for the neutral species was done in the diagonal representation, where the spin-mixed, fully adiabatic states were obtained by diagonalizing the electronic Hamiltonian matrix, which itself is built up from five singlet and triplet states for the neutral species. In addition, all relevant spin–orbit interactions are included in the Hamiltonian matrix. To ensure excitation only to the bright $\pi\pi^*$ state, the transition dipole moment for each initial geometry is calculated as the selection criterion. For the cation, the trajectories were set up in the molecular Coulomb Hamiltonian (MCH) representation, where the states are represented in the basis of the eigenfunctions of the molecular Coulomb Hamiltonian, consisting of five doublet and quartet states. Sets of 50 randomly chosen trajectories were started each in the D_1, D_2, and D_3 ionic states. In both cases, the propagation itself was performed in the diagonal representation. The necessary energies, gradients, spin–orbit and non-adiabatic couplings (SOC, NAC) were calculated on-the-fly at the SA5-CASSCF level of theory using the Molcas/OpenMolcas interface included in SHARC. The non-adiabatic transitions were treated within Tully's fewest switch trajectory surface hopping (TSH) algorithm[84] as implemented in SHARC.[76] The integration of the nuclear motion is done using the Velocity-Verlet algorithm with a maximal simulation time of 100 fs using a time step of 0.5 fs. The subsequent analysis of the trajectories of both species is done in the MCH representation.

C. Simulation of x ray/XUV absorption spectra

The following describes, first, the general procedure how we calculated the static x-ray/XUV absorption spectrum (further abbreviated as only XAS) based on the RASPT2 ansatz and second, how we used the NAMD simulation to generate the transient XAS of vinyl bromide.

The algorithm for the calculation of the XAS is mainly based on the works of Josefsson and co-workers[26] and Wang, Odelius, and Prendergast.[42] Here, both the valence space of vinyl bromide and the excitation processes of the core electrons are described in the same theoretical framework of the restricted active space self-consistent field (RASSCF) method.[85,86] RASSCF is an extension to the general CASSCF approach, where the active space is further partitioned into three subspaces RAS1, RAS2, and RAS3, with additional constraints applied to their occupation. In general, they can be systematically labeled RAS($n, l, m; i, j, k$), where, i, j, and k are the number of orbitals in the RAS1, RAS2, and RAS3 subspaces, respectively, n is the total

number of electrons in the active spaces, l the maximum number of holes allowed in the RAS1, and m the maximum number of electrons allowed in RAS3. For the RAS2, all possible configurations are allowed, making it analogous to the AS within CASSCF. For vinyl bromide, the RAS2 was built up similarly to the AS utilized in the NAMD. It also included the carbon–carbon double bond (π_1, π_3^*), the carbon–bromine single bond (σ_1, σ_2^*) as well as both remaining bromine $4p$ orbitals (π_2, n_1) and one additional virtual orbital with significant Rydberg contributions. For the RAS1, we included all five $3d$ orbitals of bromine and allowed for one hole. To enhance convergence within the RASSCF and to suppress unwanted orbital rotation with the valence space, the core orbitals were kept frozen to their shape from the Hartree–Fock calculation. The RAS3 was not utilized, thus resulting in RAS(18, 1, 0; 5, 7, 0) for neutral and RAS(17, 1, 0; 5, 7, 0) for cationic vinyl bromide. The diagram in Fig. 2 summarizes all relevant excitations and orbitals involved for the computational setup. As bromine is already subject to spin–orbit effects,[87] relativistic effects were included and treated in two steps, both based on the Douglas–Kroll Hamiltonian.[88,89] In the first step, within each spin symmetry the states were optimized in a state-averaged RASSCF procedure carried out with the relativistic atomic natural orbital basis (ANO-RCC),[90–94] contracted to ATZP quality (ANO-RCC-ATZP). This is followed by a perturbative inclusion (PT2) of the dynamic electron correlation within the multistate RASPT2 method,[95–99] where the default ionization-potential electron-affinity (IPEA) shift[100] of 0.25 Hartree was used. An additional imaginary shift[101] of 0.2 Hartree was applied to reduce problems with intruder states. In the second step, these "spin-free" states were used as a basis in the restricted active space state interaction (RASSI) method,[102–104] where the spin–orbit coupling (SOC) was treated with the use of the atomic mean-field spin–orbit integrals (AMFI).[105]

For the simulation of the transient XAS discussed further below, we utilized the geometric information from the on-the-fly trajectories. For every 3 fs snapshot, the XAS spectrum is calculated. Note that the multi-configurational wave function from the dynamics simulation could not be reused as it did not include all orbitals necessary for the proper description of the XAS spectrum. The spectrum requires a new active space including the five bromine $3d$ core-orbitals and the extended ANO-RCC-ATZP basis set.

For each single XAS calculation, seven singlet and eight triplet valence excited states for the neutral and five-doublet and three-quartet valence excited states for the cationic species are calculated. Additional 40 core excited states for both species, and all four multiplicities, were calculated by enforcing one hole in RAS1. This results in a total of 95 states for the neutral and 88 states for the cationic species. The interaction between all these states, including SOC, was treated within in the RASSI method. Note that since the valence and core excited states are obtained from different calculations, their corresponding wave functions are not inevitably orthogonal. This was already mentioned by Wang, Odelius, and Prendergast.[42] Following their proposed procedure, we applied the original correction to the overall Hamiltonian as introduced in Ref. 104. The next step is to match the valence states from the XAS calculation with the valence states from the trajectory calculations to obtain the transient XAS spectrum for the active state. In the case of the neutral vinyl bromide, we used the dipole moment vector of the active state of the trajectory for the matching. For the cationic case, we found it to be sufficient to

use the state number (index) of the active state. The oscillator strengths that are related to the matched valence excited state were then used to simulate the transient XAS. The vertical transition energies were obtained from the spin–orbit RASSI states (SO-RASSI) and no energy shift was applied. An overall Gaussian convolution with $\sigma = 0.1$ eV was applied to broaden the calculated spectrum. For each time step, the convoluted spectra were averaged over all geometries and then normalized to the maximum of all calculated time steps. Furthermore, the XAS of the S_0 ground state at time $t = 0$ fs was subtracted to simulate the ground state bleach in the energy range upwards of 70.0 eV. A flow chart of the complete procedure as well as example Molcas inputs for the necessary calculations can be found in the supplementary material Sec. II G.[108]

IV. RESULTS AND DISCUSSION

A. Spectroscopic assignments of the transient absorption spectra

The transient absorption spectrogram, recorded by collecting the differential optical density at different pump-probe delays with 2.3 fs step size, is shown in Fig. 3. Further details on data processing are provided in Sec. I A of the supplementary material.[108] The spectral range of the attosecond XUV-probe pulse covers the pre-edge region of the $M_{4,5}$ edge of Br (located at 75.3 eV), corresponding to the excitation of a Br $3d$ electron. The applied NIR pump pulse launches multiple strong-field-initiated dynamics in vinyl bromide. The main process triggered is strong-field ionization, but neutral valence excited-state vinyl bromide can also be formed by a multiphoton process. As shown by closely related studies on methyl iodide,[12] methyl bromide,[13] and vinyl bromide,[67] both processes can occur under these conditions, leading to a rich transient absorption spectrum.

The bleaching signals at 71.0 and 71.9 eV are due to the depletion of the ground state of the molecule after the interaction with the strong NIR field. They appear as a doublet, as is the case for features discussed below, due to the 0.9 eV spin–orbit splitting of $3d_{5/2}$ and $3d_{3/2}$ states in Br.[106] The main doublet appearing at 65.5 and 66.4 eV as well as the weaker signals up to 70 eV has been assigned to ionic states including

FIG. 3. XUV transient absorption spectrogram of C_2H_3Br exposed to strong-field interaction with a sub-4 fs NIR pulse centered at $\lambda = 800$ nm, with a peak intensity of $I = 2 \times 10^{14}$ W cm^{-2}. The transient is recorded by collecting the differential optical density at different pump-probe delays, with a step size of 2.3 fs. For negative delays, the XUV pulse arrives first, and for positive delays the NIR pulse arrives first.

also the dication.[67] Following the previous assignment, the main doublet corresponds to the excitation of the $3d$ Br electron of the ionic vinyl bromide in the D_2 state (for details of the nomenclature see Table I). At long temporal delays ($t > 100$ fs), sharp atomic Br lines at 64.4 and 65.0 eV indicate an ultrafast dissociation of the molecule or ion.

Pronounced, periodic, delay-dependent spectral modulations of the absorption are visible both in the ground state bleaching and cationic state signals. In both cases, they reflect vibrational wavepacket motion, as already pointed out in a number of closely related investigations.[12,13] The delay-dependent spectral first-moment of the absorption signal in the range 70.3–71.5 eV reveals a clear oscillation (see Sec. I B of the supplementary material[108]) with a period of 52.5 fs. The corresponding frequency of 635 cm^{-1} agrees well with the C–Br eigenmode ν_3 in the ground electronic state of neutral C_2H_3Br (see Table S7 in the supplementary material[108] and Ref. 107). Given the initial phase of $\phi_0 = -\pi$ (cosine-like wave), the wavepacket is likely to be launched by a bond softening mechanism, as detailed by Wei et al.[12] This fine mapping in the energy domain of the vibrational wavepacket motion is one of the unique aspects of ATAS.

A more prominent example of this resolving capability is provided by the dynamics of the cationic D_2 state. The spectral first-moment of the signal in the range 65.2–65.7 eV is in this case composed of the sum of two dephased sinusoidals (see Sec. I B of the supplementary material[108]) with frequencies of 480 and 1220 cm^{-1}, corresponding to the ν_3 (C–Br, stretching) and ν_7 (CCH, bending) eigenmodes, respectively (see Table S7 in the supplementary material[108]). The activation of the ν_3 and ν_7 modes in the ionization process to the D_2 state of cationic vinyl bromide has already been observed and understood in terms of the displacive nature of the vertical Franck–Condon excitation.[107] Indeed, the equilibrium geometry of the D_2 cationic state features two main differences compared to the neutral ground state: an increase in C–Br bond length (by 0.06 Å) and in CCH angle (by 9.10%) (see Table S9 in the supplementary material[108]). In comparison with a spectral domain spectroscopy method, here, ATAS allows one to completely map in space and time this multidimensional motion, giving access to the phase of the different contributions, relative to the instant and to each other.

In the energy region of 64.0 and 65.0 eV, a previously not reported short-lived ($t < 100$ fs) feature centered at 64.3 eV at $t = 0$ fs is observed. A zoom of the transient absorption spectrogram showing this new feature can be found in Fig. 4. It is immediately evident that, compared to the oscillatory nature of the vibrational coherences explained above, the temporal behavior of the feature is more complicated. After an initial energy upshift of the absorption feature, from 64.30 to 64.45 eV within the first 25 fs, the signal bifurcates around $t = 30$ fs. The main branch downshifts in energy by 0.35 eV in the following 10 fs, reaching the asymptotic value of the atomic Br $M_{4,5}$ transition[106] $P_{1/2} \rightarrow D_{5/2}$ at 64.1 eV at $t = 40$ fs. It is important to note that the $1/2$ to $5/2$ transition is strictly dipole forbidden in the atomic limit due to spin–orbit selection rules, but, in the molecule, because of spin–orbit coupling among electrons, the restriction is removed. In fact, the signal at 64.1 eV vanishes within the following 40 fs, in concomitance with the birth and rise to asymptotic intensity of the allowed atomic Br transitions $P_{3/2} \rightarrow D_{5/2}$ (at 64.4 eV) and $P_{1/2} \rightarrow D_{3/2}$ (at 65.0 eV). The transient behavior, combined with the delayed rise of the atomic Br dissociation products, clearly indicates that we
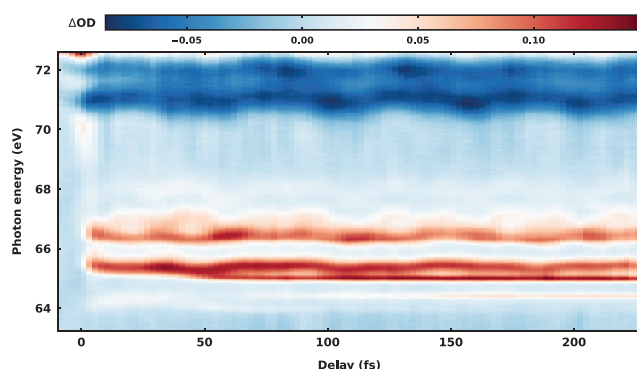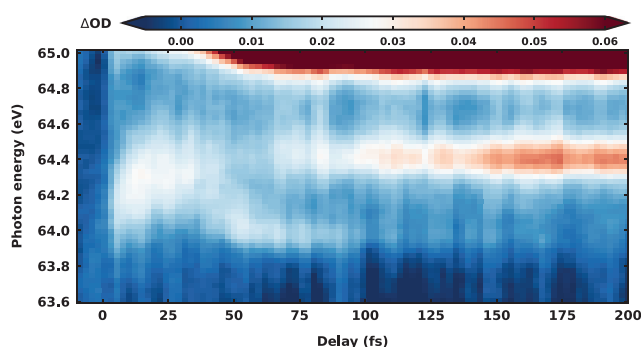
FIG. 4. Zoom of the transient absorption spectrogram showing the new feature in the energy range between 64.0 and 65.0 eV.

are observing an ultrafast dissociation process. The observation appears in close connection to the recently investigated ATAS of methyl bromide.[13] There, the feature was assigned to a neutral excited state populated by multiphoton process and the bifurcation was attributed to the non-adiabatic passage through a conical intersection. In the case of vinyl bromide, it is not straightforward to distinguish in the spectroscopic data whether this signal originates from an ionic or neutral dissociation process. In the critical range between 64.1 and 65.0 eV, the previous investigation[67] of vinyl bromide predicted the appearance of a signal due to the second-excited cationic state (D_3) according to Koopman's theorem, which could, however, not be resolved at that time. Applying the same simple Koopman's picture on neutral vinyl bromide, a signal in the same range is expected, which could be assigned to an electronically excited $\pi\pi^*$ state of the neutral.

In fact, the first UV absorption band of the molecule is composed of a very broad (>0.5 eV) feature centered around 6.5 eV;[107] this is in range with the distance between the signal under consideration and the ground state bleach doublet. In the present strong-field pump scenario, such an excited state could be reached in principle via a four-photon-process. Noteworthy, an ultrafast C–Br bond-rupture channel of the neutral has been inferred from 193 nm photodissociation studies.[65] In order to disentangle between the two possibilities, neutral vs ion as well as to explain the complete transient absorption spectrogram, we simulated the transient XAS spectra for neutral and ionic vinyl bromide.

B. Excited state dynamics of the neutral vinyl bromide

In order to initiate the neutral dynamics, we approximate the multiphoton process as a one-photon excitation. We start 300 trajectories in the bright excited state (for more details see Sec. III B). Using the default selection criteria provided by SHARC, 189 trajectories were taken into account for the analysis of the excited state dynamics and calculation of the XAS spectrum. The initial and final populated adiabatic states are summarized in Table II.

The excitation to the bright $\pi\pi^*$ state corresponds to an initial population of 38% in the S_2 state and 34% in the S_3 state. Since Br is a heavy atom, where spin–orbit effects arise, we also see a slightly smaller initial population of 16% in the T_3 state. After excitation, all trajectories show non-adiabatic as well as spin–orbit transitions within the simulation time of 100 fs. The overall change in

TABLE II. Population of the ten calculated neutral states at the start and end point of the simulation. All percentages are given with respect to the total number of analyzed trajectories.

State	Start	End	State	Start	End
S_0	0%	8%	T_1	0%	18%
S_1	4%	8%	T_2	0%	18%
S_2	38%	5%	T_3	2%	16%
S_3	34%	2%	T_4	16%	11%
S_4	3%	2%	T_5	3%	12%

population for all states is shown in Fig. S9 in the supplementary material.[108] In the first 20 fs, population is mainly transferred from the three initial states into the triplet states T_2 to T_5. After this initial period of 20 fs, also, the population of the S_0 and T_1 states increases, where T_1 is populated faster. Over the next 80 fs, the general trend of population transfer to the triplet states stays the same. Only the population of the S_0 state increases to about 8%. At the end of the simulation, most of the population (about 75%) can be found in one of the triplet states. The remaining 25% is distributed over all five singlet states. In each multiplicity, the first two states (S_0, S_1, T_1, T_2) are populated the most.

No matter in what electronic state the trajectories end up, their final geometries show a quite uniform picture. For elucidation, the temporal evolution of both the C=C double bond and the C–Br bond is shown in Fig. 5. All analyzed trajectories are of dissociative nature, showing on average a doubling of the initial C–Br bond length after about 50 fs. No oscillation in the C–Br bond and only a very weak one in the C=C double bond are observed. The fragments reveal that only homolytic dissociation occurs. Two types of electronic configuration are present, which differ only in the position of the unpaired electron in the vinyl radical. In the case of the S_{0-2} and T_{1-3} states, the unpaired electron resides in the 2p orbital of carbon that was part of the former σ C–Br bond ($H_2C = C^\bullet H$). For states $S_{3,4}$ and $T_{4,5}$, the electron is in the π_2 orbital of the C=C bond, with the carbon 2p orbital now being doubly occupied ($H_2C {}^\bullet\!- CH$). For both channels,
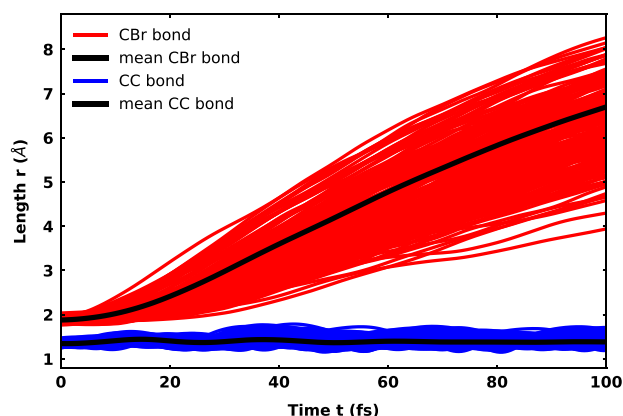

FIG. 5. Temporal evolution of the CC double bond and the CBr bond for the 189 analyzed trajectories of neutral vinyl bromide.

the electron on the Br radical sits in one of the three now degenerate $3p$ orbitals.

Combining the data from the analyzed trajectories with our RASPT2 ansatz, we simulated the transient XAS of neutral vinyl bromide. The resulting time-resolved spectrum is plotted in Fig. 6. First one has to note that the simulated spectrum matches the experimental energy range quite well, keeping in mind that we did not apply a shift to the excitation energies. The energetic position of the ground state bleach at 71.0–72.5 eV matches very well. The temporal modulation is missing, since we simply subtracted the XAS of the S_0 ground state at time $t = 0$ fs as mentioned in Sec. III C. In the range of 64.0–65.0 eV, prominent features occur that are predicted by Koopman's theorem. All of them are shifting approximately 1 eV toward lower energies within the first 20 fs. Thereafter, two sharp features, a stronger one at 64.3 eV and a significantly weaker one at 65 eV, appear. After another 10–20 fs, all signals remain constant in energy and the feature at low energy becomes more and more pronounced. Since nearly all trajectories are dissociated at this point in time, these two remaining constant signals are the spin-allowed transitions of atomic bromine. From both transitions, the lower lying $Br(P_{3/2}) \rightarrow Br(D_{5/2})$ is more dominant. Comparison to the experimental spectrum reveals that the signals from the neutral species alone cannot explain the experimentally observed pattern in this energy range. Thus, signal contributions from the ionic species are required in this region as well as evidently also in the higher energy part above 65.5 eV.

C. Dynamics of the cationic vinyl bromide

Next, we examined the excited state dynamics of cationic vinyl bromide. As discussed in the previous work,[67] the first three ionic states (D_1, D_2, and D_3) are accessible with the pump pulse used. Accordingly, we started 150 trajectories equally distributed in each of these states. For the analysis, 82 out of the 150 calculated trajectories were taken into account, using the same selection criteria as for the neutral case. The 82 trajectories break down to 11 that started in the D_1 state, 26 in the D_2 state, and 45 in the D_3 state. The overall change in population for all 82 trajectories is shown in Fig. S17 in the supplementary material.[108] All three states are bound states, with, however,

decreasing dissociation energies, reflecting the increasing weakening of the C=C double bond with ionization energy. Contrary to the neutral case, their dynamics differ depending on the initial state and will be discussed individually in the following.

1. Starting from the D_1 state

The electronic character of the D_1 state is characterized by an ionization from the π_2 orbital (see Figs. 2 and S7). The complete population remains in the D_1 state for the entire simulation time. There is no interaction with either the other doublet or quartet states (see Fig. S11). None of the analyzed trajectories dissociate. This is in good agreement with the result of a relaxed scan along the C–Br bond that predicts a barrier of about 1.5 eV for the dissociation (see Fig. S28 and the computational details Sec. V B in the supplementary material1[108]). We observe an oscillation of the C=C bond with a period of about $T = 25$ fs and of the C–Br bond with a period of $T = 50$ fs (see Fig. S12). The launching of both oscillations is reasonable, since the affected π_2 orbital has contributions from both the C=C double bond as well as one of the bromine $4p$ orbitals.

2. Starting from the D_2 state

For the D_2 state, the electron hole is generated in the n_1 lone-pair orbital of the bromine. Again, most of the population remains in the initial state D_2, with only a small part, less than 5%, being transferred into the D_1 state. As for the D_1 state, there is no further interaction with the other electronic states (see Fig. S13) and none of the analyzed trajectories dissociate. The barrier toward direct dissociation is about 1 eV (see relaxed scan Fig. S28). Since ionization from orbital n_1 mainly affects the C–Br bond, a pronounced oscillation along this bond with a period of about $T = 75$ fs (see Fig. S14) is observed. The bond elongates from the initial 1.9 to roughly 2.08 Å. Only a weak oscillation, with a period of about $T = 20$ fs, that dampens over the simulation time, is present in the C=C bond. This bond is hardly affected and its bond length shortens only marginally to about 1.31 Å. In summary, the first two ionic states exclusively show bound state vibrational dynamics.

3. Starting from the D_3 state

For the D_3 state, the hole is created in the C=C bonding π_1 orbital (see Figs. 2 and S7), which has contributions from the C=C double bond and the bromine $4p$ orbital. The C=C double bond as well as the C–Br bond are now strongly weakened. Accordingly, the relaxed scan (see Fig. S28) predicts a small barrier of only 0.2 eV for a direct dissociation. The temporal evolution of the D_3 population (see Fig. S15) shows a slow but steady decay due to population transfer to the D_2 and D_1 state after the first 20 fs. There is also a slight intermediate interaction with the D_4 state between 20 and 60 fs, but again, there is no further significant interaction with the remaining electronic states. After 100 fs, more than 80% of the population is still in the D_3 and about 10% in each of the D_2 and D_1 states. In the barrier region, transitions to the D_4 state via conical intersections are possible (see Sec. V of the supplementary material[108] for the optimized structure). After the barrier, the D_3 and D_4 state switch character. For the new character, the σ_1 orbital of the C–Br bond is only singly occupied leading to a repulsive potential correlating with the dissociation channel of the D_1
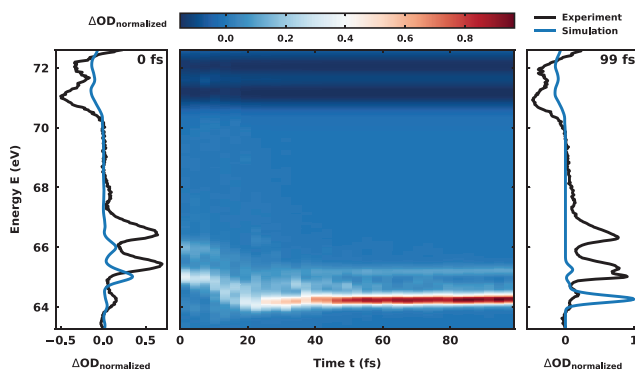

FIG. 6. Simulated transient XAS of the neutral trajectories starting in the bright $\pi\pi^*$ state. On the left and right, the spectrum for time $t = 0$ and $t = 99$ fs, respectively, is shown in blue overlaid with the experimental transient absorption spectogram in black at delays $d = 6.8$ and $d = 107.6$ fs.

or D_2 state. Judging from the small barrier compared to both other cationic states, one would expect most of the trajectories to dissociate. And indeed, the dynamics starting in the D_3 state reveal a more complex situation regarding the temporal evolution of the C–Br bond (see Fig. 7). Three types of dynamics were recognized, the pure vibrational (green), the slow dissociative (yellow), and the fast dissociative (red). The classification was done with regard to the length of the C–Br bond at the end of the simulation. Trajectories with a bond length longer than 3.5 Å were classified as fast. The range 3.5–2.2 Å was classified as slow and trajectories with shorter bond length as vibrational. The final distribution regarding these three types of dynamics is listed in Table III. About half of the analyzed trajectories dissociate within the simulation time of 100 fs, with the other half showing purely vibrational dynamics. For all trajectories, the C=C bond shows oscillation with a period of about $T = 25$ fs. The purely vibrational trajectories indicate a slow oscillation with about $T = 100$ fs in the C–Br bond. All of them stay in the D_3 state, not being able to overcome the barrier. For the fast dissociating trajectories, at about 40 fs and a C–Br bond length of about 2.59 Å, we can see a clear separation from the rest of the trajectories. In the case of the slow dissociating trajectories, the separation happens later at 60 fs at a bond length of about 2.37 Å.

In general, the dissociation in the D_3 state is considerably slower compared to the neutral vinyl bromide, where we observed the onset of dissociation after 50 fs. For the cationic states, the bond cleaves heterolytically, leaving a neutral bromine radical and a vinyl cation. For the dissociation channel of all three states, D_1, D_2, or D_3, the unpaired electron is located in one of the three now degenerate Br $3p$ orbitals.

Again using the described ansatz in Sec. III C and the data from the 82 analyzed trajectories, we simulated the complete transient XAS for the cationic states, which are depicted in Fig. 8. Comparing it to the experimental spectrum in Fig. 3, the overall resemblance in the measured energy range is strikingly good. To assign the different features of the spectrum, we additionally simulated the XAS only for a subset of the trajectories depending on their starting state, D_1 (Fig. S21), D_2 (Fig. S22), and D_3 (Fig. S23). In the case of the D_3, it is

TABLE III. Observed dynamics of the 82 analyzed trajectories for cationic vinyl bromide. In the table heading, Dissociation is abbreviated as Diss.

Initial state	Vibrational	Slow Diss.	Fast Diss.
D_1	11	0	0
D_2	26	0	0
D_3	21	8	16

further separated according to the bound and dissociative dynamics (Figs. S24–S26).

In the following, we discuss the significant features of the spectrum in the context of the corresponding dynamical processes of vinyl bromide. Starting from the top, we observe the same ground state bleach as for the neutral states, but this time the intensity distribution is modulated by contributions from the D_1 signal. The signals in the energy range 67–69 eV can be attributed to the D_1 state. Although it is difficult to see the peaks in the complete spectrum, Fig. S21 clearly shows the pronounced doublet signal at 66.7 and 67.7 eV, the former with a higher, about twice, intensity compared to the latter. This doublet arises from the already mentioned spin–orbit splitting of the $3d_{5/2}$ and $3d_{3/2}$ orbitals of Br. Both signals oscillate with a period of about $T = 50$ fs, which is in good agreement with the observed oscillation of the C–Br bond in the trajectories. In correspondence to the shortening of the C–Br bond during the oscillation, the signals shift to higher energies, reaching a maximum of about 67.7 and 68.7 eV in a half period. This shift can be explained by the electronic character of the D_1 state. It has a hole in the π_2 orbital, which has anti-bonding character with respect to the C–Br bond. Hence, shortening the bond destabilizes the π_2 orbital and results in higher XUV excitation energies.

The next features at 65.5 and 66.5 eV in Fig. 8 are the most intense ones of the spectrum and can be attributed mainly to the D_2 state by comparison to the D_2 XAS (see Fig. S22). Here, the bromine-induced doublet structure shows most clearly and the energetically higher signal is less intense. The slight modulations with periods of
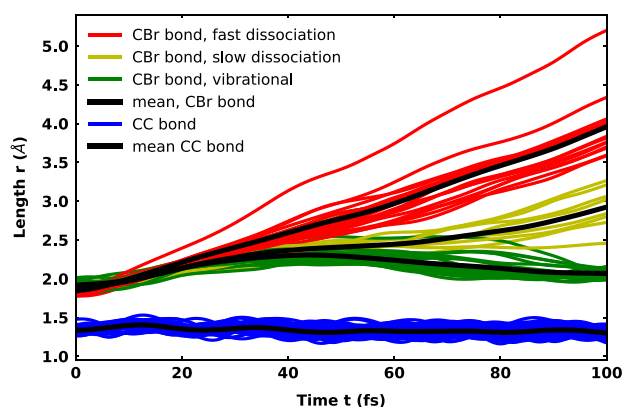

FIG. 7. Temporal evolution of the C=C double bond and the C–Br bond for the 45 analyzed trajectories that started in the D_3 state of the cationic vinyl bromide. For the C–Br bond, the corresponding trajectories are color coded according to their observed behavior. Only vibrational trajectories are shown in green, slow dissociating ones in yellow, and (fast) dissociating trajectories in red. The average of the C–Br bond length was only calculated for the subset of the trajectories.

FIG. 8. Simulated transient XAS of the cationic trajectories starting in the D_1, D_2, and D_3 states. On the left and right, the spectrum for time $t = 0$ and $t = 99$ fs, respectively, is shown in blue overlaid with the experimental transient absorption spectrogram in black at delays $d = 6.8$ and $d = 107.6$ fs. Additional overlay plots at times 24, 48, and 72 fs as well as separated XAS of the different starting states and different observed dynamics are depicted in the supplementary material, Sec. IV.

about $T = 80$ and $T = 25$ fs can be assigned to the C–Br and C=C bond vibrations in the D_2 trajectories. With the elongation of the C–Br bond the doublet shifts toward lower energies. The elongation stabilizes the n_1 lone-pair orbital and thus the D_2 state, resulting in lower core excitation energies. This shift of about 0.3 eV is considerably smaller compared to the 1 eV of the D_1 signal. Summarizing, the signals from both the D_1 and D_2 states show clear oscillations, but neither reproduce the characteristic splitting of the intense 65.5 eV peak at about 50 fs nor the weak band around 64 eV. These features must come from the D_3 state.

The combined XAS for all D_3 trajectories is shown in Fig. S23. The weak signals between 66 and 70 eV correspond to the core excitation into the σ^* orbital of the C–Br bond. Again, the spectrum is dominated by the distinct doublet, now at 64.3 and 65.2 eV. In contrast to the previously discussed oscillating features, these signal traces become constant after about half an oscillation period at 40 fs and split up into four contributions at 64.0, 64.5, 65.0, and 65.5 eV with different intensities. They can be assigned to the various processes observed in the D_3 trajectories.

The XAS for the purely vibrational bound state dynamics (see Fig. S24) shows weak signals between 66 and 70 eV and the prominent doublet peak at 64.3 and 65.2 eV, both oscillating with the period of the C–Br bond. The phase shift originates from the different final orbitals that are excited to. Bond elongation stabilizes the σ^* orbital resulting in a down-shift of the weak signal. Simultaneously, the singly occupied π_1 orbital is destabilized leading to an up-shift of the doublet signal.

For the XAS of the fast dissociating trajectories (see Fig. S26), the same doublet splitting at 64.3 and 65.2 eV occurs. After the initial first half of the oscillation period, the signal changes drastically. Both peaks become constant at an energy of 64.0 and 65.0 eV, and a strong increase in intensity for the energetically higher signal at 65.0 eV is observed while the other one is fading. This change in intensity and shape reflects the transition from the "molecular" bromine to the atomic bromine. With increasing distance between the bromine and the vinyl cation, the Br character becomes progressively more atom-like. From the two spin-allowed transitions $Br(P_{3/2}) \rightarrow Br(D_{5/2})$ and $Br(P_{1/2}) \rightarrow Br(D_{3/2})$, dominantly the higher lying transition $Br(P_{1/2}) \rightarrow Br(D_{3/2})$ survives. Thus, in the cationic dissociation, spin–orbit excited $Br(P_{1/2})$ atoms are mostly generated, which is in excellent agreement with the experiment.

From the discussion of the XAS from the bound and the fast dissociating D_3 trajectories, one would expect to see a mixture of their distinct signals in the XAS of the slow dissociating ones. Indeed, in the first 50 fs, Fig. S25 only shows the oscillating signals of the bound trajectories. In the time between 50 and 80 fs, the signals from the dissociating trajectories start to overlap converting into the constant signals of the atomic bromine at 64.0 and 65.0 eV.

In summary, the prominent features between 64 and 66 eV of the total XAS (Fig. 8) originate from overlapping signals of the cationic vinyl bromide. The signal is composed of spectral features of the non-dissociative dynamics in the D_2 and D_3 states and of the spin–orbit excited atomic Br generated in the dissociation of D_3. This assignment relies on the fact that in vinyl bromide, the dynamics in the neutral states can be well distinguished from the dynamics in the cationic states, which can also be resolved in the XAS spectrum. In the accessible neutral state, a $\pi\pi^*$ excitation is immediately followed by a

transition from the $\pi\pi^*$ to the $n\sigma^*$ configuration initiating barrierless dissociation. In contrast, for the cationic case, the hole is generated in different orbitals for the different states. The first two cationic states are bound due to being well separated in energy from dissociation channels. However, for D_3 a slow transfer of the hole from the π into the σ orbital weakens the C–Br bond and leads to dissociation.

V. CONCLUSION

We introduced a joint experimental and theoretical approach to follow in real-time the electronic structure change in molecules via attosecond transient absorption spectroscopy. It is then applied to study the ultrafast dynamics of vinyl bromide, after strong-field excitation from a few-cycle pulse centered at 800 nm. The remarkable agreement between the experimental and the calculated ATAS traces proves the high fidelity of the RASPT2 ansatz in combination with NAMD. Thus, it is possible to remove one of the two main bottlenecks historically ascribed to the employed methodology: the difficulty in data interpretation due to multiplet effects in probing inner valence rather than genuine core level states. Based on the NAMD trajectories, we calculated the state-specific XAS spectra and their temporal evolution. This allows for detailed insights into the electronic-state-resolved dynamics. In particular, we were able to clearly assign the experimentally observed spectrum to the dynamics of the first three electronic states of the cation, D_1, D_2, and D_3. The first two states remain bound, allowing us to time-resolve the ensuing multidimensional vibrational dynamics with high sensitivity. The second excited cationic state D_3, instead, presents richer dynamics. In addition to the pure vibrational motion, fast and slow dissociation channels also appear, leading to ultrafast rupture of the halogen–carbon bond in 50% of the calculated trajectories. No significant ultrafast relaxation channel from D_2 to D_1 has been observed, which is different from the very recent results on strong-field ionized ethylene.[22] Each of the above-mentioned channels has a clear fingerprint in the ATAS spectrum, and they are unambiguously assigned thanks to the theoretical comparison. Extensions of the described methodology are imaginable both on the experimental and theoretical side. The combination of attosecond absorption and charged-particle-based spectroscopies (angle-integrated, via time-of-flight, or even angle-resolved, via velocity-map-imaging spectroscopy) would allow for an even greater insight into the different relaxation and fragmentation channels, providing a multidimensional space of correlated observables. In order to circumvent the issue of the non-resonant and non-perturbative nature, one could explicitly simulate the interaction of the molecule with the strong NIR field. A suitable approach would be the recently developed R-matrix ansatz[23,24] or the B-Spline Restricted Correlation Space - Algebraic Diagrammatic Construction approach.[25] Overall, the platform here presented can be readily applied to single-photon-excitation studies and to the soft x-ray spectral region, where the presence of carbon, nitrogen, and oxygen edges allows for molecular ultrafast studies with unprecedented time resolution.

AUTHORS' CONTRIBUTIONS

ACKNOWLEDGMENTS

Structural Dynamics	ARTICLE	scitation.org/journal/sdy

DATA AVAILABILITY

The data that support the findings of this study are available from the corresponding author upon reasonable request.

REFERENCES

[1]M. Hentschel, R. Kienberger, C. Spielmann, G. A. Reider, N. Milosevic, T. Brabec, P. Corkum, U. Heinzmann, M. Drescher, and F. Krausz, "Attosecond metrology," Nature 414, 509–513 (2001).

[2]J. Itatani, F. Quéré, G. L. Yudin, M. Y. Ivanov, F. Krausz, and P. B. Corkum, "Attosecond streak camera," Phys. Rev. Lett. 88, 173903 (2002).

[3]M. Schultze, M. Fieß, N. Karpowicz, J. Gagnon, M. Korbman, M. Hofstetter, S. Neppl, A. L. Cavalieri, Y. Komninos, T. Mercouris, C. A. Nicolaides, R. Pazourek, S. Nagele, J. Feist, J. Burgdörfer, A. M. Azzeer, R. Ernstorfer, R. Kienberger, U. Kleineberg, E. Goulielmakis, F. Krausz, and V. S. Yakovlev, "Delay in photoemission," Science 328, 1658–1662 (2010).

[4]M. Ossiander, F. Siegrist, V. Shirvanyan, R. Pazourek, A. Sommer, T. Latka, A. Guggenmos, S. Nagele, J. Feist, J. Burgdörfer, R. Kienberger, and M. Schultze, "Attosecond correlation dynamics," Nat. Phys. 13, 280–285 (2017).

[5]A. L. Cavalieri, N. Müller, T. Uphues, V. S. Yakovlev, A. Baltuška, B. Horvath, B. Schmidt, L. Blümel, R. Holzwarth, S. Hendel, M. Drescher, U. Kleineberg, P. M. Echenique, R. Kienberger, F. Krausz, and U. Heinzmann, "Attosecond spectroscopy in condensed matter," Nature 449, 1029–1032 (2007).

[6]L. Seiffert, Q. Liu, S. Zherebtsov, A. Trabattoni, P. Rupp, M. C. Castrovilli, M. Galli, F. Submann, K. Wintersperger, J. Stierle, G. Sansone, L. Poletto, F. Frassetto, I. Halfpap, V. Mondes, C. Graf, E. Ruhl, F. Krausz, M. Nisoli, T. Fennel, F. Calegari, and M. F. Kling, "Attosecond chronoscopy of electron scattering in dielectric nanoparticles," Nat. Phys. 13, 766–770 (2017).

[7]G. Sansone, F. Kelkensberg, J. F. Pérez-Torres, F. Morales, M. F. Kling, W. Siu, O. Ghafur, P. Johnsson, M. Swoboda, E. Benedetti, F. Ferrari, F. Lépine, J. L. Sanz-Vicario, S. Zherebtsov, I. Znakovskaya, A. Lhuillier, M. Y. Ivanov, M. Nisoli, F. Martín, and M. J. Vrakking, "Electron localization following attosecond molecular photoionization," Nature 465, 763–766 (2010).

[8]F. Calegari, D. Ayuso, A. Trabattoni, L. Belshaw, S. De Camillis, S. Anumula, F. Frassetto, L. Poletto, A. Palacios, P. Decleva, J. B. Greenwood, F. Martín, and M. Nisoli, "Ultrafast electron dynamics in phenylalanine initiated by attosecond pulses," Science 346, 336–339 (2014).

[9]E. Goulielmakis, Z. H. Loh, A. Wirth, R. Santra, N. Rohringer, V. S. Yakovlev, S. Zherebtsov, T. Pfeifer, A. M. Azzeer, M. F. Kling, S. R. Leone, and F. Krausz, "Real-time observation of valence electron motion," Nature 466, 739–743 (2010).

[10]M. Sabbar, H. Timmers, Y. J. Chen, A. K. Pymer, Z. H. Loh, S. G. Sayres, S. Pabst, R. Santra, and S. R. Leone, "State-resolved attosecond reversible and irreversible dynamics in strong optical fields," Nat. Phys. 13, 472–478 (2017).

[11]Y. Kobayashi, M. Reduzzi, K. F. Chang, H. Timmers, D. M. Neumark, and S. R. Leone, "Selectivity of electronic coherence and attosecond ionization delays in strong-field double ionization," Phys. Rev. Lett. 120, 233201 (2018).

[12]Z. Wei, J. Li, L. Wang, S. T. See, M. H. Jhon, Y. Zhang, F. Shi, M. Yang, and Z. H. Loh, "Elucidating the origins of multimode vibrational coherences of polyatomic molecules induced by intense laser fields," Nat. Commun. 8, 1–7 (2017).

[13]H. Timmers, X. Zhu, Z. Li, Y. Kobayashi, M. Sabbar, M. Hollstein, M. Reduzzi, T. J. Martínez, D. M. Neumark, and S. R. Leone, "Disentangling conical intersection and coherent molecular dynamics in methyl bromide with attosecond transient absorption spectroscopy," Nat. Commun. 10, 1–8 (2019).

[14]M. Schultze, K. Ramasesha, C. D. Pemmaraju, S. A. Sato, D. Whitmore, A. Gandman, J. S. Prell, L. J. Borja, D. Prendergast, K. Yabana, D. M. Neumark, and S. R. Leone, "Attosecond band-gap dynamics in silicon," Science 346, 1348–1352 (2014).

[15]M. Lucchini, S. A. Sato, A. Ludwig, J. Herrmann, M. Volkov, L. Kasmi, Y. Shinohara, K. Yabana, L. Gallmann, and U. Keller, "Attosecond dynamical Franz–Keldysh effect in polycrystalline diamond," Science 353, 916–919 (2016).

[16]A. Moulet, J. B. Bertrand, T. Klostermann, A. Guggenmos, N. Karpowicz, and E. Goulielmakis, "Soft x-ray excitonics," Science 357, 1134–1138 (2017).

[17]F. Schlaepfer, M. Lucchini, S. A. Sato, M. Volkov, L. Kasmi, N. Hartmann, A. Rubio, L. Gallmann, and U. Keller, "Attosecond optical-field-enhanced carrier injection into the GaAs conduction band," Nat. Phys. 14, 560–564 (2018).

[18]Y. Kobayashi, K. F. Chang, T. Zeng, D. M. Neumark, and S. R. Leone, "Direct mapping of curve-crossing dynamics in IBr by attosecond transient absorption spectroscopy," Science 364, 79–83 (2019).

[19]K. F. Chang, M. Reduzzi, H. Wang, S. M. Poullain, Y. Kobayashi, L. Barreau, D. Prendergast, D. M. Neumark, and S. R. Leone, "Revealing electronic state-switching at conical intersections in alkyl iodides by ultrafast XUV transient absorption spectroscopy," Nat. Commun. 11, 1–7 (2020).

[20]A. R. Attar, A. Bhattacherjee, C. D. Pemmaraju, K. Schnorr, K. D. Closser, D. Prendergast, and S. R. Leone, "Femtosecond x-ray spectroscopy of an electro-cyclic ring-opening reaction," Science 356, 54–59 (2017).

[21]Y. Pertot, C. Schmidt, M. Matthews, A. Chauvet, M. Huppert, V. Svoboda, A. Von Conta, A. Tehlar, D. Baykusheva, J. P. Wolf, and H. J. Wörner, "Time-resolved x-ray absorption spectroscopy with a water window high-harmonic source," Science 355, 264–267 (2017).

[22]K. S. Zinchenko, F. Ardana-Lamas, I. Seidu, S. P. Neville, J. van der Veen, V. U. Lanfaloni, M. S. Schuurman, and H. J. Wörner, "Sub-7-femtosecond conical-intersection dynamics probed at the carbon K-edge," Science 371, 489–494 (2021).

[23]A. C. Brown, G. S. J. Armstrong, J. Benda, D. D. A. Clarke, J. Wragg, K. R. Hamilton, Z. Mašín, J. D. Gorfinkiel, and H. W. van der Hart, "RMT: R-matrix with time-dependence. solving the semi-relativistic, time-dependent Schrödinger equation for general, multielectron atoms and molecules in intense, ultrashort, arbitrarily polarized laser pulses," Comput. Phys. Commun. 250, 107062 (2020).

[24]Z. Mašín, J. Benda, J. D. Gorfinkiel, A. G. Harvey, and J. Tennyson, "UKRmol: A suite for modelling electronic processes in molecules interacting with electrons, positrons and photons using the R-matrix method," Copmut. Phys. Commun. 249, 107092 (2020).

[25]M. Ruberti, "Restricted correlation space B-spline ADC approach to molecular ionization: Theory and applications to total photoionization cross-sections," J. Chem. Theory Comput. 15, 3635–3653 (2019).

[26]I. Josefsson, K. Kunnus, S. Schreck, A. Föhlisch, F. de Groot, P. Wernet, and M. Odelius, "Ab initio calculations of x-ray spectra: Atomic multiplet and molecular orbital effects in a multiconfigurational SCF approach to the L-edge spectra of transition metal complexes," J. Phys. Chem. Lett. 3, 3565–3570 (2012).

[27]R. Klooster, R. Broer, and M. Filatov, "Calculation of x-ray photoelectron spectra with the use of the normalized elimination of the small component method," Chem. Phys. 395, 122–127 (2012).

[28]P. Wernet, K. Kunnus, S. Schreck, W. Quevedo, R. Kurian, S. Techert, F. M. F. de Groot, M. Odelius, and A. Föhlisch, "Dissecting local atomic and inter-molecular interactions of transition-metal ions in solution with selective x-ray spectroscopy," J. Phys. Chem. Lett. 3, 3448–3453 (2012).

[29]S. I. Bokarev, M. Dantz, E. Suljoti, O. Kühn, and E. F. Aziz, "State-dependent electron delocalization dynamics at the solute-solvent interface: Soft-x-ray absorption spectroscopy and ab initio calculations," Phys. Rev. Lett. 111, 083002 (2013).

[30]E. Suljoti, R. Garcia-Diez, S. I. Bokarev, K. M. Lange, R. Schoch, B. Dierker, M. Dantz, K. Yamamoto, N. Engel, K. Atak, O. Kühn, M. Bauer, J.-E. Rubensson, and E. F. Aziz, "Direct observation of molecular orbital mixing in a solvated organometallic complex," Angew. Chem., Int. Ed. 52, 9841–9844 (2013).

[31]K. Atak, S. I. Bokarev, M. Gotz, R. Golnak, K. M. Lange, N. Engel, M. Dantz, E. Suljoti, O. Kühn, and E. F. Aziz, "Nature of the chemical bond of aqueous

Fe2+ probed by soft x-ray spectroscopies and *ab initio* calculations," J. Phys. Chem. B **117**, 12613–12618 (2013).

[32]K. Kunnus, I. Josefsson, S. Schreck, W. Quevedo, P. S. Miedema, S. Techert, F. M. F. de Groot, M. Odelius, P. Wernet, and A. Föhlisch, "From ligand fields to molecular orbitals: Probing the local valence electronic structure of Ni(2+) in aqueous solution with resonant inelastic x-ray scattering," J. Phys. Chem. B **117**, 16512–16521 (2013).

[33]N. Engel, S. I. Bokarev, E. Suljoti, R. Garcia-Diez, K. M. Lange, K. Atak, R. Golnak, A. Kothe, M. Dantz, O. Kühn, and E. F. Aziz, "Chemical bonding in aqueous ferrocyanide: Experimental and theoretical x-ray spectroscopic study," J. Phys. Chem. B **118**, 1555–1563 (2014).

[34]D. Maganas, P. Kristiansen, L.-C. Duda, A. Knop-Gericke, S. DeBeer, R. Schlögl, and F. Neese, "Combined experimental and *ab initio* multireference configuration interaction study of the resonant inelastic x-ray scattering spectrum of CO_2," J. Phys. Chem. C **118**, 20163–20175 (2014).

[35]R. V. Pinjari, M. G. Delcey, M. Guo, M. Odelius, and M. Lundberg, "Restricted active space calculations of L-edge x-ray absorption spectra: From molecular orbitals to multiplet states," J. Chem. Phys. **141**, 124116 (2014).

[36]S. I. Bokarev, M. Khan, M. K. Abdel-Latif, J. Xiao, R. Hilal, S. G. Aziz, E. F. Aziz, and O. Kühn, "Unraveling the electronic structure of photocatalytic manganese complexes by L-edge x-ray spectroscopy," J. Phys. Chem. C **119**, 19192–19200 (2015).

[37]G. Grell, S. I. Bokarev, B. Winter, R. Seidel, E. F. Aziz, S. G. Aziz, and O. Kühn, "Multi-reference approach to the calculation of photoelectron spectra including spin–orbit coupling," J. Chem. Phys. **143**, 074104 (2015).

[38]L. Weinhardt, E. Ertan, M. Iannuzzi, M. Weigand, O. Fuchs, M. Bär, M. Blum, J. D. Denlinger, W. Yang, E. Umbach, M. Odelius, and C. Heske, "Probing hydrogen bonding orbitals: Resonant inelastic soft x-ray scattering of aqueous NH_3," Phys. Chem. Chem. Phys. **17**, 27145–27153 (2015).

[39]M. Guo, L. K. Sørensen, M. G. Delcey, R. V. Pinjari, and M. Lundberg, "Simulations of iron K pre-edge x-ray absorption spectra using the restricted active space method," Phys. Chem. Chem. Phys. **18**, 3250–3259 (2016).

[40]M. Preuße, S. I. Bokarev, S. G. Aziz, and O. Kühn, "Towards an *ab initio* theory for metal L-edge soft x-ray spectroscopy of molecular aggregates," Struct. Dyn. **3**, 062601 (2016).

[41]M. Guo, E. Källman, R. V. Pinjari, R. Carvalho Couto, L. K. Sørensen, R. Lindh, K. Pierloot, and M. Lundberg, "Fingerprinting electronic structure of heme iron by *ab initio* modeling of metal L-edge x-ray absorption spectra," J. Chem. Theory Comput. **15**, 477–489 (2019).

[42]H. Wang, M. Odelius, and D. Prendergast, "A combined multi-reference pump-probe simulation method with application to XUV signatures of ultra-fast methyl iodide photodissociation," J. Chem. Phys. **151**, 124106 (2019).

[43]H. Ågren, V. Carravetta, O. Vahtras, and L. G. M. Pettersson, "Direct, atomic orbital, static exchange calculations of photoabsorption spectra of large molecules and clusters," Chem. Phys. Lett. **222**, 75–81 (1994).

[44]H. Ågren, V. Carravetta, L. G. M. Pettersson, and O. Vahtras, "Static exchange and cluster modeling of core electron shakeup spectra of surface adsorbates: CO/Cu(100)," Phys. Rev. B: Condens. Matter Mater. Phys. **53**, 16074–16085 (1996).

[45]V. Carravetta, L. Yang, O. Vahtras, H. Ågren, and L. G. M. Pettersson, "*Ab-initio* static exchange calculations of shake-up spectra of molecules and surface adsorbates," J. Phys. IV **7**, C2–519–C2–520 (1997).

[46]V. Carravetta, O. Plashkevych, and H. Ågren, "A screened static-exchange potential for core electron excitations," Chem. Phys. **263**, 231–242 (2001).

[47]M. Stener, G. Fronzoni, and M. de Simone, "Time dependent density functional theory of core electrons excitations," Chem. Phys. Lett. **373**, 115–123 (2003).

[48]N. A. Besley and A. Noble, "Time-dependent density functional theory study of the x-ray absorption spectroscopy of acetylene, ethylene, and benzene on Si(100)," J. Phys. Chem. C **111**, 3333–3340 (2007).

[49]S. DeBeer George, T. Petrenko, and F. Neese, "Time-dependent density functional calculations of ligand K-edge x-ray absorption spectra," Inorg. Chim. Acta **361**, 965–972 (2008).

[50]Y. Zhang, J. D. Biggs, D. Healion, N. Govind, and S. Mukamel, "Core and valence excitations in resonant x-ray spectroscopy using restricted excitation window time-dependent density functional theory," J. Chem. Phys. **137**, 194306 (2012).

[51]F. Lackner, A. S. Chatterley, C. D. Pemmaraju, K. D. Closser, D. Prendergast, D. M. Neumark, S. R. Leone, and O. Gessner, "Direct observation of ring-opening dynamics in strong-field ionized selenophene using femtosecond inner-shell absorption spectroscopy," J. Chem. Phys. **145**, 234313 (2016).

[52]L. S. Cederbaum, W. Domcke, and J. Schirmer, "Many-body theory of core holes," Phys. Rev. A **22**, 206–222 (1980).

[53]S. Coriani and H. Koch, "Communication: X-ray absorption spectra and core-ionization potentials within a core-valence separated coupled cluster framework," J. Chem. Phys. **143**, 181103 (2015).

[54]T. J. A. Wolf, R. H. Myhre, J. P. Cryan, S. Coriani, R. J. Squibb, A. Battistoni, N. Berrah, C. Bostedt, P. Bucksbaum, G. Coslovich, R. Feifel, K. J. Gaffney, J. Grilj, T. J. Martinez, S. Miyabe, S. P. Moeller, M. Mucke, A. Natan, R. Obaid, T. Osipov, O. Plekan, S. Wang, H. Koch, and M. Gühr, "Probing ultrafast $\pi\pi*/n\pi*$ internal conversion in organic chromophores via K-edge resonant absorption," Nat. Commun. **8**, 29 (2017).

[55]M. L. Vidal, X. Feng, E. Epifanovsky, A. I. Krylov, and S. Coriani, "New and efficient equation-of-motion coupled-cluster framework for core-excited and core-ionized states," J. Chem. Theory Comput. **15**, 3117–3133 (2019).

[56]B. N. C. Tenorio, T. Moitra, M. A. C. Nascimento, A. B. Rocha, and S. Coriani, "Molecular inner-shell photoabsorption/photoionization cross sections at core-valence-separated coupled cluster level: Theory and examples," J. Chem. Phys. **150**, 224104 (2019).

[57]R. Faber and S. Coriani, "Core–valence-separated coupled-cluster-singles-and-doubles complex-polarization-propagator approach to x-ray spectroscopies," Phys. Chem. Chem. Phys. **22**, 2642–2647 (2020).

[58]M. Filatov and S. Shaik, "A spin-restricted ensemble-referenced Kohn–Sham method and its application to diradicaloid situations," Chem. Phys. Lett. **304**, 429–437 (1999).

[59]T. Kowalczyk, T. Tsuchimochi, P.-T. Chen, L. Top, and T. Van Voorhis, "Excitation energies and stokes shifts from a restricted open-shell Kohn–Sham approach," J. Chem. Phys. **138**, 164101 (2013).

[60]D. Hait, E. A. Haugen, Z. Yang, K. J. Oosterbaan, S. R. Leone, and M. Head-Gordon, "Accurate prediction of core-level spectra of radicals at density functional theory cost via square gradient minimization and recoupling of mixed configurations," J. Chem. Phys. **153**, 134108 (2020).

[61]D. Hait and M. Head-Gordon, "Highly accurate prediction of core spectra of molecules at density functional theory cost: Attaining sub-electronvolt error from a restricted open-shell Kohn–Sham approach," J. Chem. Phys. Lett. **11**, 775–786 (2020).

[62]Y. Zhang, W. Hua, K. Bennett, and S. Mukamel, "Nonlinear spectroscopy of core and valence excitations using short x-ray pulses: Simulation challenges," in *Density-Functional Methods for Excited States. Topics in Current Chemistry*, edited by N. Ferré, M. Filatov, and M. Huix-Rotllant (Springer International Publishing, Cham, 2016), Vol 368.

[63]P. Norman and A. Dreuw, "Simulating x-ray spectroscopies and calculating core-excited states of molecules," Chem. Rev. **118**, 7208–7248 (2018).

[64]M. Lundberg and M. G. Delcey, "Multiconfigurational approach to x-ray spectroscopy of transition metal complexes," in *Transition Metals in Coordination Environments: Computational Chemistry and Catalysis Viewpoints*, edited by E. Broclawik, T. Borowski, and M. Radoń (Springer International Publishing, Cham, 2019), Vol 29. .

[65]H. Katayanagi, N. Yonekuira, and T. Suzuki, "C–Br bond rupture in 193 nm photodissociation of vinyl bromide," Chem. Phys. **231**, 345–353 (1998).

[66]P. Zou, K. E. Strecker, J. Ramirez-Serrano, L. E. Jusinski, C. A. Taatjes, and D. L. Osborn, "Ultraviolet photodissociation of vinyl iodide: Understanding the halogen dependence of photodissociation mechanisms in vinyl halides," Phys. Chem. Chem. Phys. **10**, 713–728 (2008).

[67]M.-F. Lin, D. M. Neumark, O. Gessner, and S. R. Leone, "Ionization and dissociation dynamics of vinyl bromide probed by femtosecond extreme ultraviolet transient absorption spectroscopy," J. Chem. Phys. **140**, 064311 (2014).

[68]H. Timmers, Y. Kobayashi, K. F. Chang, M. Reduzzi, D. M. Neumark, and S. R. Leone, "Generating high-contrast, near single-cycle waveforms with third-order dispersion compensation," Opt. Lett. **42**, 811 (2017).

[69]E. Goulielmakis, M. Schultze, M. Hofstetter, V. S. Yakovlev, J. Gagnon, M. Uiberacker, A. L. Aquila, E. M. Gullikson, D. T. Attwood, R. Kienberger, F. Krausz, and U. Kleineberg, "Single-cycle nonlinear optics," Science **320**, 1614–1617 (2008).

[70]B. O. Roos, "The complete active space self-consistent field method and its applications in electronic structure calculations," in *Ab initio* Methods in

Quantum Chemistry Part 2, *Advances in Chemical Physics* Vol. 41, edited by K. P. Lawley (John Wiley & Sons, Inc., Hoboken, NJ, USA, 1987), pp. 399–445.

[71]B. O. Roos, P. R. Taylor, and P. E. M. Sigbahn, "A complete active space SCF method (CASSCF) using a density matrix formulated super-CI approach," Chem. Phys. **48**, 157–173 (1980).

[72]I. Fdez Galván, M. Vacher, A. Alavi, C. Angeli, F. Aquilante, J. Autschbach, J. J. Bao, S. I. Bokarev, N. A. Bogdanov, R. K. Carlson, L. F. Chibotaru, J. Creutzberg, N. Dattani, M. G. Delcey, S. S. Dong, A. Dreuw, L. Freitag, L. M. Frutos, L. Gagliardi, F. Gendron, A. Giussani, L. González, G. Grell, M. Guo, C. E. Hoyer, M. Johansson, S. Keller, S. Knecht, G. Kovačević, E. Källman, G. L. Manni, M. Lundberg, Y. Ma, S. Mai, J. P. Malhado, P. Å. Malmqvist, P. Marquetand, S. A. Mewes, J. Norell, M. Olivucci, M. Oppel, Q. M. Phung, K. Pierloot, F. Plasser, M. Reiher, A. M. Sand, I. Schapiro, P. Sharma, C. J. Stein, L. K. Sørensen, D. G. Truhlar, M. Ugandi, L. Ungur, A. Valentini, S. Vancoillie, V. Veryazov, O. Weser, T. A. Wesołowski, P.-O. Widmark, S. Wouters, A. Zech, J. P. Zobel, and R. Lindh, "Openmolcas: From source code to insight," J. Chem. Theory Comput. **15**, 5925–5964 (2019).

[73]F. Aquilante, J. Autschbach, A. Baiardi, S. Battaglia, V. A. Borin, L. F. Chibotaru, I. Conti, L. De Vico, M. Delcey, I. Fdez Galván, N. Ferré, L. Freitag, M. Garavelli, X. Gong, S. Knecht, E. D. Larsson, R. Lindh, M. Lundberg, P. Å. Malmqvist, A. Nenov, J. Norell, M. Odelius, M. Olivucci, T. B. Pedersen, L. Pedraza-González, Q. M. Phung, K. Pierloot, M. Reiher, I. Schapiro, J. Segarra-Martí, F. Segatta, L. Seijo, S. Sen, D.-C. Sergentu, C. J. Stein, L. Ungur, M. Vacher, A. Valentini, and V. Veryazov, "Modern quantum chemistry with [Open]Molas," J. Chem. Phys. **152**, 214117 (2020).

[74]S. Mai, M. Richter, M. Heindl, M. F. S. J. Menger, A. Atkins, M. Ruckenbauer, F. Plasser, L. M. Ibele, S. Kropf, M. Oppel, P. Marquetand, and L. González, "SHARC2.1: Surface hopping including arbitrary couplings—Program package for non-adiabatic dynamics," sharc-md.org (2019).

[75]M. Richter, P. Marquetand, J. González-Vázquez, I. Sola, and L. González, "SHARC: *Ab initio* molecular dynamics with surface hopping in the adiabatic representation including arbitrary couplings," J. Chem. Theory Comput. **7**, 1253–1258 (2011).

[76]S. Mai, P. Marquetand, and L. González, "Nonadiabatic dynamics: The SHARC approach," Wiley Interdiscip. Rev.: Comput. Mol. Sci. **8**, e1370 (2018).

[77]J. P. Dahl and M. Springborg, "The Morse oscillator in position space, momentum space, and phase space," J. Chem. Phys. **88**, 4535–4547 (1988).

[78]R. Schinke, *Photodissociation Dynamics: Spectroscopy and Fragmentation of Small Polyatomic Molecules* (Cambridge University Press, 1995).

[79]A. K. Wilson, T. van Mourik, and T. H. Dunning, "Gaussian basis sets for use in correlated molecular calculations. VI. Sextuple zeta correlation consistent basis sets for boron through neon," J. Mol. Struct.: THEOCHEM **388**, 339–349 (1996).

[80]K. A. Peterson, D. E. Woon, and T. H. Dunning, "Benchmark calculations with correlated molecular wave functions. IV. The classical barrier height of the H + H2 → H2 + H reaction," J. Chem. Phys. **100**, 7410–7415 (1994).

[81]D. E. Woon and T. H. Dunning, "Gaussian basis sets for use in correlated molecular calculations. III. The atoms aluminum through argon," J. Chem. Phys. **98**, 1358–1371 (1993).

[82]R. A. Kendall, T. H. Dunning, and R. J. Harrison, "Electron affinities of the first-row atoms revisited. Systematic basis sets and wave functions," J. Chem. Phys. **96**, 6796–6806 (1992).

[83]T. H. Dunning, "Gaussian basis sets for use in correlated molecular calculations. I. The atoms boron through neon and hydrogen," J. Chem. Phys. **90**, 1007–1023 (1989).

[84]J. C. Tully, "Molecular dynamics with electronic transitions," J. Chem. Phys. **93**, 1061–1071 (1990).

[85]B. O. Roos, "The complete active space SCF method in a Fock-matrix-based super-CI formulation," Int. J. Quantum Chem. **18**, 175–189 (2009).

[86]P. A. Malmqvist, A. Rendell, and B. O. Roos, "The restricted active space self-consistent-field method, implemented with a split graph unitary group approach," J. Phys. Chem. **94**, 5477–5482 (1990).

[87]B. A. Hess, R. J. Buenker, and P. Chandra, "Toward the variational treatment of spin–orbit and other relativistic effects for heavy atoms and molecules," Int. J. Quantum Chem. **29**, 737–753 (1986).

[88]M. Douglas and N. M. Kroll, "Quantum electrodynamical corrections to the fine structure of helium," Ann. Phys. **82**, 89–155 (1974).

[89]B. A. Hess, "Relativistic electronic-structure calculations employing a two-component no-pair formalism with external-field projection operators," Phys. Rev. A **33**, 3742–3748 (1986).

[90]B. O. Roos, R. Lindh, P.-A. Malmqvist, V. Veryazov, P.-O. Widmark, and A. C. Borin, "New relativistic atomic natural orbital basis sets for lanthanide atoms with applications to the Ce diatom and LuF₃," J. Phys. Chem. A **112**, 11431–11435 (2008).

[91]B. O. Roos, R. Lindh, P.-Å. Malmqvist, V. Veryazov, and P.-O. Widmark, "New relativistic ANO basis sets for actinide atoms," Chem. Phys. Lett. **409**, 295–299 (2005).

[92]B. O. Roos, R. Lindh, P.-Å. Malmqvist, V. Veryazov, and P.-O. Widmark, "New relativistic ANO basis sets for transition metal atoms," J. Phys. Chem. A **109**, 6575–6579 (2005).

[93]B. O. Roos, R. Lindh, P.-Å. Malmqvist, V. Veryazov, and P.-O. Widmark, "Main group atoms and dimers studied with a new relativistic ANO basis set," J. Phys. Chem. A **108**, 2851–2858 (2004).

[94]B. O. Roos, V. Veryazov, and P.-O. Widmark, "Relativistic atomic natural orbital type basis sets for the alkaline and alkaline-earth atoms applied to the ground-state potentials for the corresponding dimers," Theor. Chem. Acc. **111**, 345–351 (2004).

[95]K. Andersson, P. A. Malmqvist, B. O. Roos, A. J. Sadlej, and K. Wolinski, "Second-order perturbation theory with a CASSCF reference function," J. Phys. Chem. **94**, 5483–5488 (1990).

[96]K. Andersson, P. Malmqvist, and B. O. Roos, "Second-order perturbation theory with a complete active space self-consistent field reference function," J. Chem. Phys. **96**, 1218–1226 (1992).

[97]J. Finley, P.-Å. Malmqvist, B. O. Roos, and L. Serrano-Andrés, "The multi-state CASPT2 method," Chem. Phys. Lett. **288**, 299–306 (1998).

[98]P.-Å. Malmqvist, K. Pierloot, A. R. M. Shahi, C. J. Cramer, and L. Gagliardi, "The restricted active space followed by second-order perturbation theory method: Theory and application to the study of CuO₂ and Cu₂O₂ systems," J. Chem. Phys. **128**, 204109 (2008).

[99]V. Sauri, L. Serrano-Andrés, A. R. M. Shahi, L. Gagliardi, S. Vancoillie, and K. Pierloot, "Multiconfigurational second-order perturbation theory restricted active space (RASPT2) method for electronic excited states: A benchmark study," J. Chem. Theory Comput. **7**, 153–168 (2011).

[100]G. Ghigo, B. O. Roos, and P.-Å. Malmqvist, "A modified definition of the zeroth-order Hamiltonian in multiconfigurational perturbation theory (CASPT2)," Chem. Phys. Lett. **396**, 142–149 (2004).

[101]N. Forsberg and P.-Å. Malmqvist, "Multiconfiguration perturbation theory with imaginary level shift," Chem. Phys. Lett. **274**, 196–204 (1997).

[102]P.-Å. Malmqvist, "Calculation of transition density matrices by nonunitary orbital transformations," Int. J. Quantum Chem. **30**, 479–494 (1986).

[103]P.-Å. Malmqvist and B. O. Roos, "The CASSCF state interaction method," Chem. Phys. Lett. **155**, 189–194 (1989).

[104]P. Å. Malmqvist, B. O. Roos, and B. Schimmelpfennig, "The restricted active space (RAS) state interaction approach with spin–orbit coupling," Chem. Phys. Lett. **357**, 230–240 (2002).

[105]B. Schimmelpfennig, L. Maron, U. Wahlgren, C. Teichteil, H. Fagerli, and O. Gropen, "On the efficiency of an effective Hamiltonian in spin–orbit CI calculations," Chem. Phys. Lett. **286**, 261–266 (1998).

[106]M. Mazzoni and M. Pettini, "Inner shell transitions of Br I in the EUV," Phys. Lett. A **85**, 331–333 (1981).

[107]A. Hoxha, R. Locht, B. Leyh, D. Dehareng, K. Hottmann, H. W. Jochims, and H. Baumgärtel, "The photoabsorption and constant ionic state spectroscopy of vinylbromide," Chem. Phys. **260**, 237–247 (2000).

[108]See supplementary material at https://www.scitation.org/doi/suppl/10.1063/4.0000102 for details on the post-processing and evaluation of the experimental data and the computational details especially the validation of the chosen computational setup of the NAMD simulations. Also shown are additional figures to support the results of the analyzed trajectories as well as the simulated transient absorption spectra as mentioned in the text. Further, the geometries of the optimized conical intersection as well as exited state minima are listed.

2.3 The Ultrafast Charge Transfer in Ionized Trifluoroiodomethane

In a similar fashion to the previous section, the RASSCF/RASPT2 ansatz was utilized to analyse the ultrafast charge transfer dynamics of the halomethane trifluoroiodomethane (CF_3I). The group of Prof. Hans Jakob Wörner at the ETH Zürich probed the dynamics of strong-field ionized CF_3I with a novel experimental scheme that combines ATAS on the $N_{4,5}$ edge of iodine, with strong-field-ionization mass spectrometry. In this way, they are able to take advantage of the sub-femtosecond time resolution of ATAS and its site specificity, while also supporting the electronic-state assignment with the measured fragmentation patterns. The result of this ATAS measurement is shown in Figure 2.7.
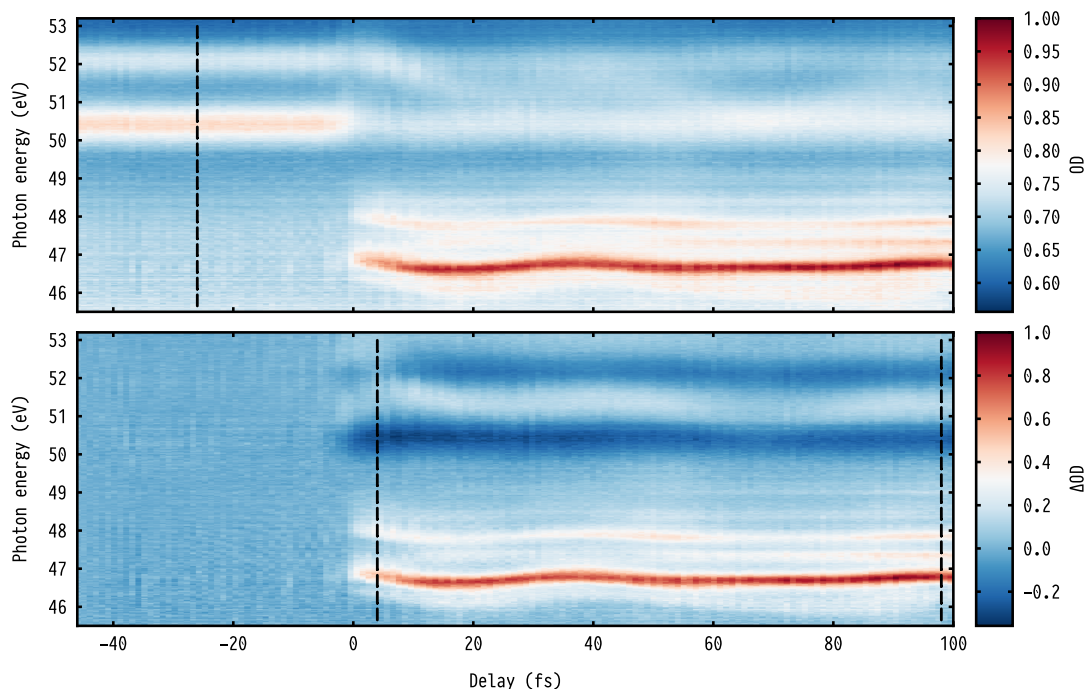

Figure 2.7 – Attosecond XUV absorption spectrum of CF_3I, exposed to a strong-field pump pulse. For negative delays, the XUV pulse arrives first, and for positive delays the pump pulse arrives first. The absolute optical density (OD) is plotted in the top part of the figure, whereas the differential optical density ΔOD is shown on the bottom. The black dotted lines at $-26.0\,\text{fs}$, $4.0\,\text{fs}$ and $98.0\,\text{fs}$ delay indicate cuts of the recorded data, that are discussed in the spectroscopic assignments of the different features.

Within the experiment, trifluoroiodomethane is exposed to a pump pulse with intensities larger than $300\,\text{TW}\,\text{cm}^{-2}$. At these intensities, CF_3I is known to undergo strong-field ionization of the highest occupied molecular orbital (HOMO), HOMO-1 and HOMO-2 orbitals, populating the excites states $\tilde{X}$, $\tilde{A}$ and $\tilde{B}$ of the cation, respectively. From the time-of-flight mass spectrum, it is known that the following dissociation of CF_3I^+ mainly produces the fragments CF_3^+ and I^+. This is in accordance with an previous study by Downie and coworkers [226]. With the help of MS-CASPT2 calculations (see Appendix C.3 for more details), a comprehensive picture of the different excited states, their electronic character and corresponding dissociation channels could be obtained, as shown in Figure 2.8 and Table 2.1.

For the first state, $\tilde{X}$, the strong-field ionization creates a valence hole on the iodine, as the electron is removed from either of the I lone-pair orbitals lp_1 or lp_2. Due to SOC, it is split up into $\tilde{X}$ ($^2E_{3/2}$) and $\tilde{X}$ ($^2E_{1/2}$). In the dissociation limit, the SO splitting is lifted, and CF_3I^+ fragments into a CF_3^+ cation and an $I^\bullet$ radical. The third state, $\tilde{A}$ ($^2A_1$), an ionization from the C–I bonding σ_4 orbital, also fragments into a CF_3^+ cation and an $I^\bullet$ radical, but here the radical is in the spin excited $^2P_{1/2}$ state. The next three states $\tilde{B}$, $\tilde{C}$ and $\tilde{D}$, all have the hole on the fluorine part of the molecule, as the strong-field pulse removes an electron from the F lone-pair
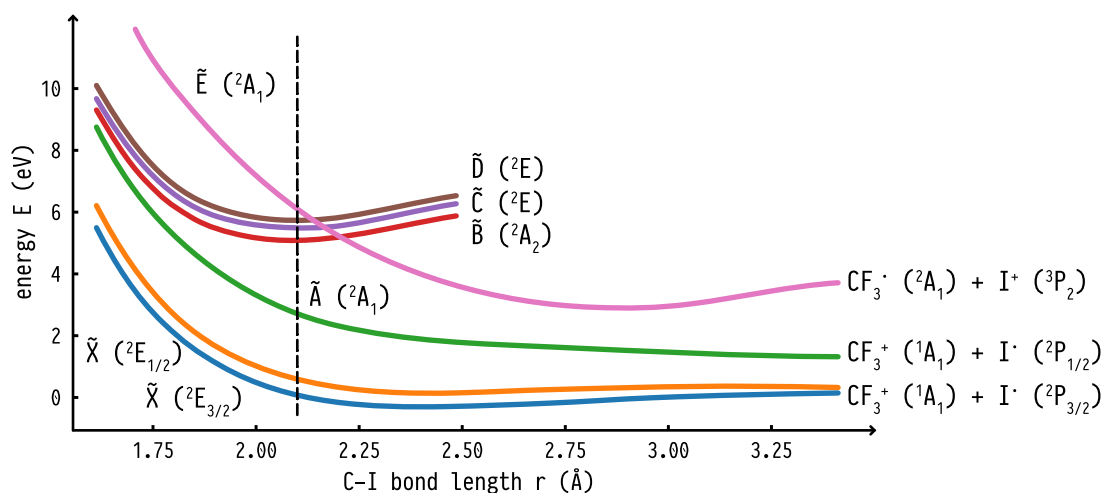
Figure 2.8 – Illustration of the PESs of cationic CF_3I, based a relaxed scan of the $C-I$ bond performed at the MS-CASPT2 level of theory. The states are color-coded corresponding to their electronic character at the FC region indicated by the black dotted line.

orbitals lp_3, lp_4 and lp_5, respectively. Finally, the last state, $\tilde{E}$ ($^2A_1$), again shows an I centered hole, as the electron is removed from the orbitals lp_1 or lp_2. It crosses the three "fluorine hole" states in the vicinity of the FC region, ultimately fragmenting into a $CF_3^{\bullet}$ radical and an I^+ cation in the $^3P_2$ GS. The passage of this CoIn, and the coinciding CT, is attributed to the most exceptional feature in the recorded spectrum, the delayed appearance of the absorption signal at 47.3 eV. Unlike the other features at lower and higher energies, it only rises after a delay of about 10 fs. This could be supported by simulating the corresponding XAS spectra of the involved states.

In the following, first the computational setup necessary to simulate the XAS spectra of neutral and cationic CF_3I with the RASSCF/RASPT2 protocol is presented. Afterwards, the main features of the recorded spectra are spectroscopically assigned with the help of the simulated spectra of both species. Finally, compelling evidence for the ultrafast charge transfer dynamics is presented.

Table 2.1 – Excited state electronic character and vertical excitation energies ΔE of cationic trifluoroiodomethane. The excitation energy is given in units of eV relative to the neutral ground state at the FC point and is calculated at the MS-CASPT2 level of theory, including SO effects. For the electronic character, the partially occupied orbitals of the dominant CI vector are listed. The experimental ionization energies are taken from the work of Yates and coworkers [227]

State	Character	Ionization energies (eV)	
		ΔE	Exp. [227]
$\tilde{X}$ ($^2E_{3/2}$)	lp_1	10.54	10.45
$\tilde{X}$ ($^2E_{1/2}$)	lp_2	11.12	11.18
$\tilde{A}$ ($^2A_1$)	σ_4	13.30	13.25
$\tilde{B}$ ($^2A_2$)	lp_3	15.22	15.56
$\tilde{C}$ (^2E)	lp_4	15.92	16.32
$\tilde{D}$ (^2E)	lp_5	16.27	17.28
$\tilde{E}$ ($^2A_1$)	$lp_{1,2}, \sigma_5^*$	16.80	19.25

2.3.1 Computational Setup

In order to sufficiently describe the valence space of trifluoroiodomethane and subsequently simulate the ATAS, a suitable AS needs to be set up. This was done by comparing to experimental

ionization energies, as well as calculated charge distributions, as reported by Yates and coworkers [227]. The complete selection process is described in more detail in appendix C.2. Initial benchmarks showed that a large AS of 24 electrons in 16 orbitals was necessary to correctly describe the valence space of CF_3I. It was comprised of the carbon-iodine bond (σ_4, σ_5^*), both iodine lone-pair orbitals lp_1 and lp_2, as well as the three carbon-fluorine bonds (σ_1, σ_6^*, σ_2, σ_7^* and σ_3, σ_8^*). Additionally, all six of the fluorine lone-pair orbitals (lp_3, lp_4, lp_5, lp_6, lp_7 and lp_8) needed to be included, as, otherwise, it was not possible to correctly describe the excited state order of the cation. The complete AS and all orbitals are shown in Figure 2.9. An overview of the relevant excited states, their vertical excitation energies, and electronic character is given in Table 2.1. The states are listed with increasing energy and are labeled according to their order in the FC region. Based on this AS, the necessary RAS subspaces for the calculation of the core-excited states were set up. As the experiment probed at the $N_{4,5}$ edge of iodine, its five $4d$ orbitals were included in the RAS1. In order to reduce the computational costs, the original AS(24,16) was split between the RAS2 and RAS3 subspaces. The three virtual orbitals of the carbon-fluorine bonds (σ_6^*, σ_7^* and σ_8^*) made up the RAS3 and a single excitation into them was allowed. The remaining 13 orbitals were include in the RAS2 subspace, resulting in the RAS(34, 1, 1; 5, 13, 3) illustrated in Figure 2.9. The relocation of the three virtual orbitals into the RAS3 was thoroughly tested, which is again described in more detail in appendix C.2. With the splitting of the AS, the calculations necessary for one spectrum could be performed within about three days. For calculations including the complete AS in the RAS2 a total time of over three months was estimated, which was considered impractical. For all calculations the ANO-RCC [210–214] basis set contracted to VDZP quality (ANO-RCC-VDZP) was utilized, as any larger basis set would not be feasible.

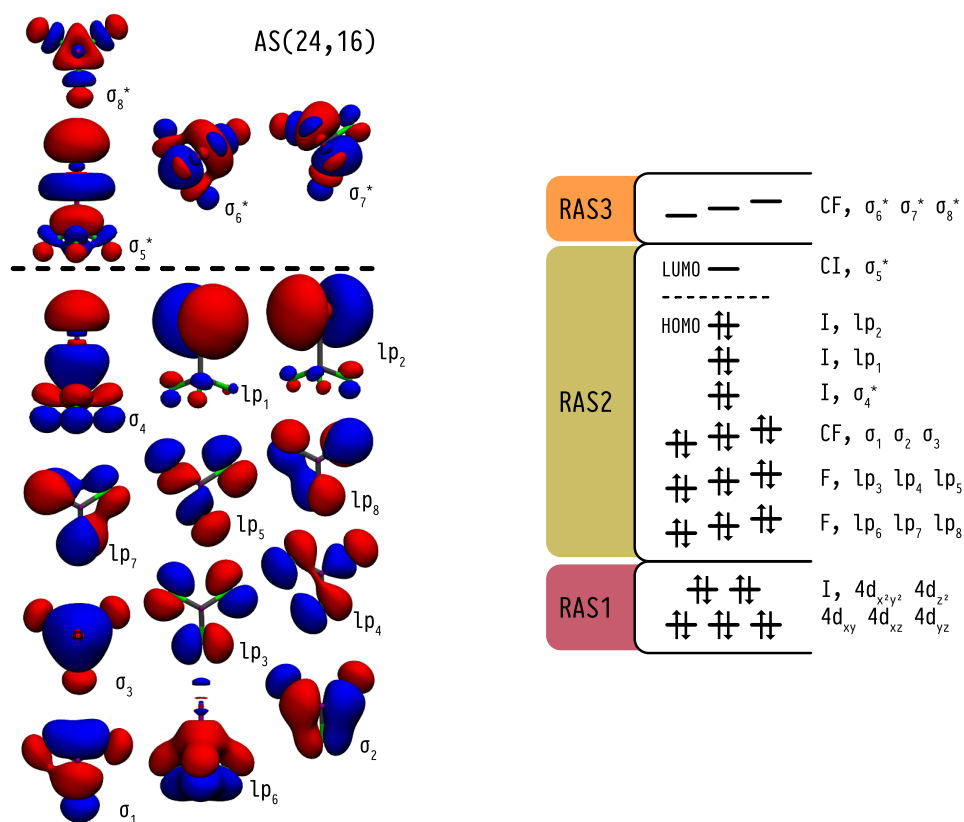**Figure 2.9** – (Left) Molecular orbitals included in the AS(24,16) of trifluoroiodomethane. All orbitals are rendered with an isovalue of 0.04. Orbitals σ_4, σ_5^*, lp_1, lp_2 and lp_6 are shown in a side view, whereas the rest are shown from the top, along the C–I bond. (Right) Diagram of the RAS subspaces of the RAS(34, 1, 1; 5, 13, 3), utilized in the simulation of the XAS of CF_3I.

2.3.2 Spectroscopic Assignments of the Transient Absorption Spectra

To completely disentangle the contributions of the different species to the XAS, we started with the simulation of the static GS spectrum of neutral CF_3I at the FC geometry. In the experimental signal shown in Figure 2.10, two distinct doublets at 50.4 eV and 52.1 eV and 55.4 eV and 57.1 eV, in both cases with a splitting of 1.70 eV, are visible. By applying only a small shift of 1.30 eV to the excitation energies, the simulated spectrum matches the experimental one very well. The first doublet at 50.4 eV and 52.1 eV can be attributed to an excitation from the I $4d$ orbitals into the σ_5^* anti-bonding orbital of the C−I bond. The splitting of 1.70 eV arises from the SO splitting of the $4d_{5/2}$ and $4d_{5/2}$ orbitals of I. Similarly, the second doublet at 56.1 eV and 57.7 eV can be attributed to an excitation into the anti-bonding orbitals σ_6^*, σ_7^* and σ_8^* of the C−F bond. However, compared to the experiment, this doublet is shifted about 0.7 eV to higher energies. This can be explained by the moderate size of the basis set ANO-RCC-VDZP, which may not be able to fully describe the σ_6^*, σ_7^* and σ_8^* orbitals, especially if these orbitals are subject to Rydberg-type contributions. Overall, the simulated steady-state spectrum from the GS matches the experimental one very well, as the intensity distribution of the two doublets is spot-on and only a moderate shift of the excitation energies needed to be applied.
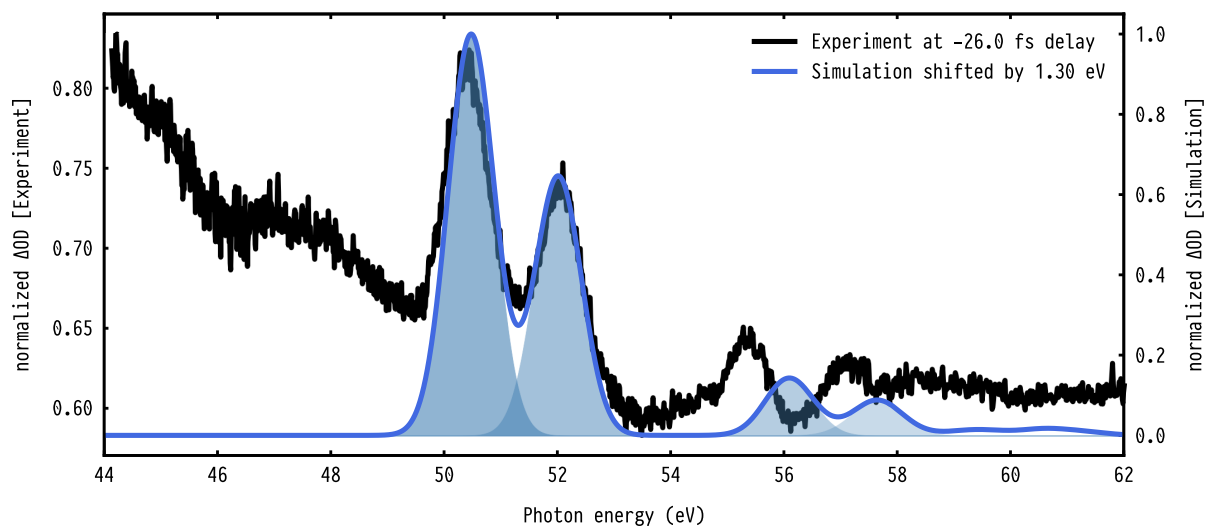

Figure 2.10 – Simulated ground state spectrum of neutral CF_3I shown in blue. It is shifted by 1.30 eV, to match the experimental signal at negative delay of −26.0 fs shown in black. The calculated peaks were broadened by applying a Gaussian with $\sigma = 0.4$ eV.

In a similar fashion, the XAS spectra for the cation were calculated. In Figure 2.11, the simulated spectrum of cationic CF_3I^+ is compared to the experimental one at a delay of 4.0 fs. The simulated spectrum is calculated as the sum of the first four excited states $\tilde{X}$ ($^2E_{3/2}$, $^2E_{1/2}$), $\tilde{A}$ and $\tilde{B}$. Additionally, the spectrum of neutral CF_3I, shown in Figure 2.10, was subtracted to approximate the GS bleach present in the experiment. Applying a shift of 1.30 eV to all excitation energies, the simulated spectrum again matches the experimental one very well. The three features visible between 46.0 eV to 49.0 eV can be attributed to the $\tilde{X}$ and $\tilde{A}$ states. The signal of the $\tilde{B}$ state, a doublet at 50.4 eV and 52.1 eV, energetically overlaps with the GS bleach. And similar to the GS, the doublet can be attributed to an excitation from the I $4d$ orbitals into the σ_5^* anti bonding orbital of the C−I bond. This is consistent with the electronic character of the $\tilde{B}$ state in the FC region. Here, the hole is located on the fluorine part of the molecule, and thus should not affect the iodine too much. Although both signals are overlapping, we are convinced that the $\tilde{B}$ state is populated, as a positiv signal at 52.0 eV, compensating the GS bleach, is visible. Overall the features of the experimental spectrum can be simulated very well with the contribution from the first four excited states.

To further investigate the influence of the different dissociation channels on the spectrum, an anologous spectrum was calculated based on the geometry at the end of the relaxed scan.
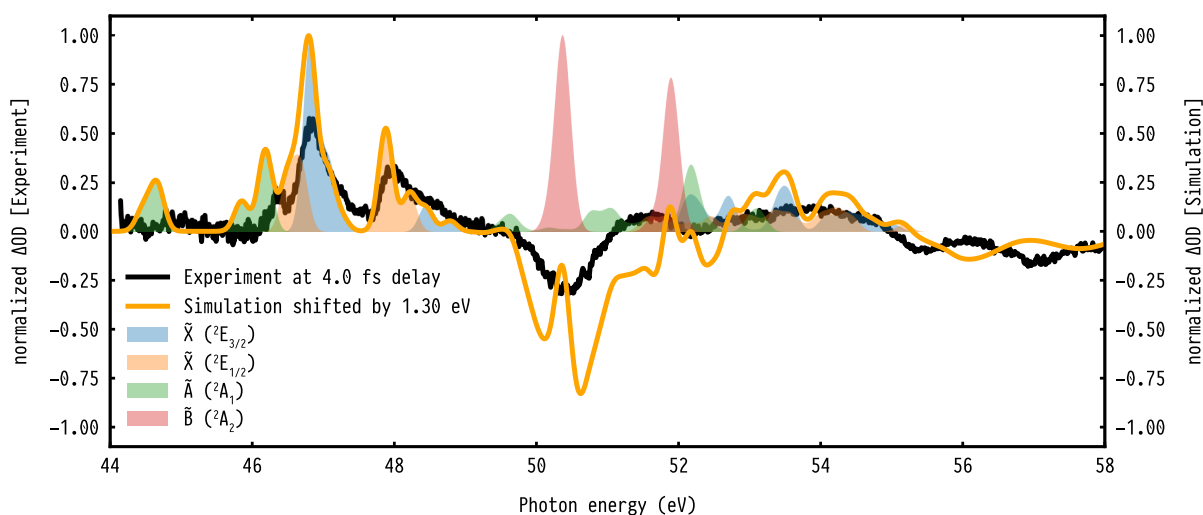
Figure 2.11 – The simulated excited state spectrum of cationic CF_3I is shown in orange, shifted by $1.30\,eV$. It is calculated as the sum of the individual spectra for the first four states $\tilde{X}$ ($^2E_{3/2}$, $^2E_{1/2}$), $\tilde{A}$ and $\tilde{B}$. The separate contribution of the different states is indicated in blue, orange, green and red, respectively. Additionally, the GS spectrum of CF_3I was subtracted, to approximate the GS bleach present in the experiment. The calculated peaks for the cationic states were broadened by applying a Gaussian with $\sigma = 0.1\,eV$. The experimental signal is shown in black for a delay of $4.0\,fs$.

This spectrum was compared to an experimental one at $98.0\,fs$. To determine which of the excited states are subject to dissociation, a QD simulation based on the MS-CASPT2 PESs was performed. The simulation setup is described in more detail in appendix C.5. The $C-I$ bond remains bound in the first two states $\tilde{X}$ ($^2E_{3/2}$) and $\tilde{X}$ ($^2E_{1/2}$) of the cation. Therefore, one would not expect to see contributions of the $I^\bullet$ radical in the $^3P_{3/2}$ GS to the signal at later delays. However, as dissociation occurred within the simulation time in both states $\tilde{A}$ and $\tilde{B}$, we still expect to see contributions of both the spin excited $I^\bullet$ ($^3P_{1/2}$) radical and the ground state I^+ ($^3P_2$) cation. Based on these considerations, the spectra of the $\tilde{X}$ ($^2E_{3/2}$, $^2E_{1/2}$) states at the FC region were combined with the spectra of the $\tilde{A}$ and $\tilde{B}$ state calculated at the final geometry of the relaxed scan, resulting in the simulated spectrum shown in Figure 2.12. Additionally, the spectra of $I^\bullet$ radical and I^+ cation, produced by the dissociation, were included. With the applied shift of $1.3\,eV$ and $0.70\,eV$ for the molecular and atomic species, respectively, the features of the experimental spectrum can be simulated very well. This corroborates the capabilities of the RASSCF/RASPT2 ansatz and the chosen AS in correctly describing the XAS of neutral and cationic CF_3I.

2.3.3 The Ultrafast Charge Transfer

To assess whether the delayed feature at $47.3\,eV$ in the experimental spectrum can be attributed to CT dynamics mediated by the CoIn between the states $\tilde{B}$ ($^2A_2$) and $\tilde{E}$ ($^2A_1$), the TAS of the $\tilde{B}$ state along the relaxed scan was calculated. It is plotted over the corresponding $C-I$ bond length in Figure 2.13. For bond lengths between $1.80\,Å$ and $2.20\,Å$, a doublet with a splitting of about $1.7\,eV$ is visible above $50\,eV$. With increasing bond length, the doublet red-shifts to about $49.9\,eV$ and $51.4\,eV$. In this region of the PES, the hole is located on the fluorine part of the molecule and the doublet can be attributed to an excitation from the $I\,4d$ orbitals into the σ_5^* anti-bonding orbital of the $C-I$ bond. As already mentioned, this feature is similar to the observed doublet in the GS spectrum. The signal changes drastically in the region of the CoIn at about $2.20\,Å$. This coincides with a change of electronic character, as the hole is now located on the iodine, with either the σ_4 bonding orbital of the $C-I$ bond or one of the I lone-pair orbitals lp_1 and lp_2 partially occupied. Here, three distinct features at $47.0\,eV$, $47.3\,eV$ and $48.5\,eV$ appear abruptly. These features can all be attributed to excitations from the $I\,4d$ orbitals into the σ_5^* orbital. Their signals remain constant until $2.55\,Å$, where a second region of strong coupling,

namely an avoided crossing, is reached. Here, a mixture of spectroscopic signatures of the $\tilde{A}$ and $\tilde{D}$ states are visible. This can be seen in more detail in Figure C.5 in the appendix. For bond lengths greater than 3.1 Å, the signal again changes drastically and two constant signals at 47.3 eV and 48.8 eV arise. They can be attributed to the spectroscopic signature of the I$^+$ ($^3P_2$) cation [228]. Summarizing, the delayed signal at 47.3 eV can be explained by the CT from fluorine to iodine, that coincides with the drastic change in the spectroscopic features.
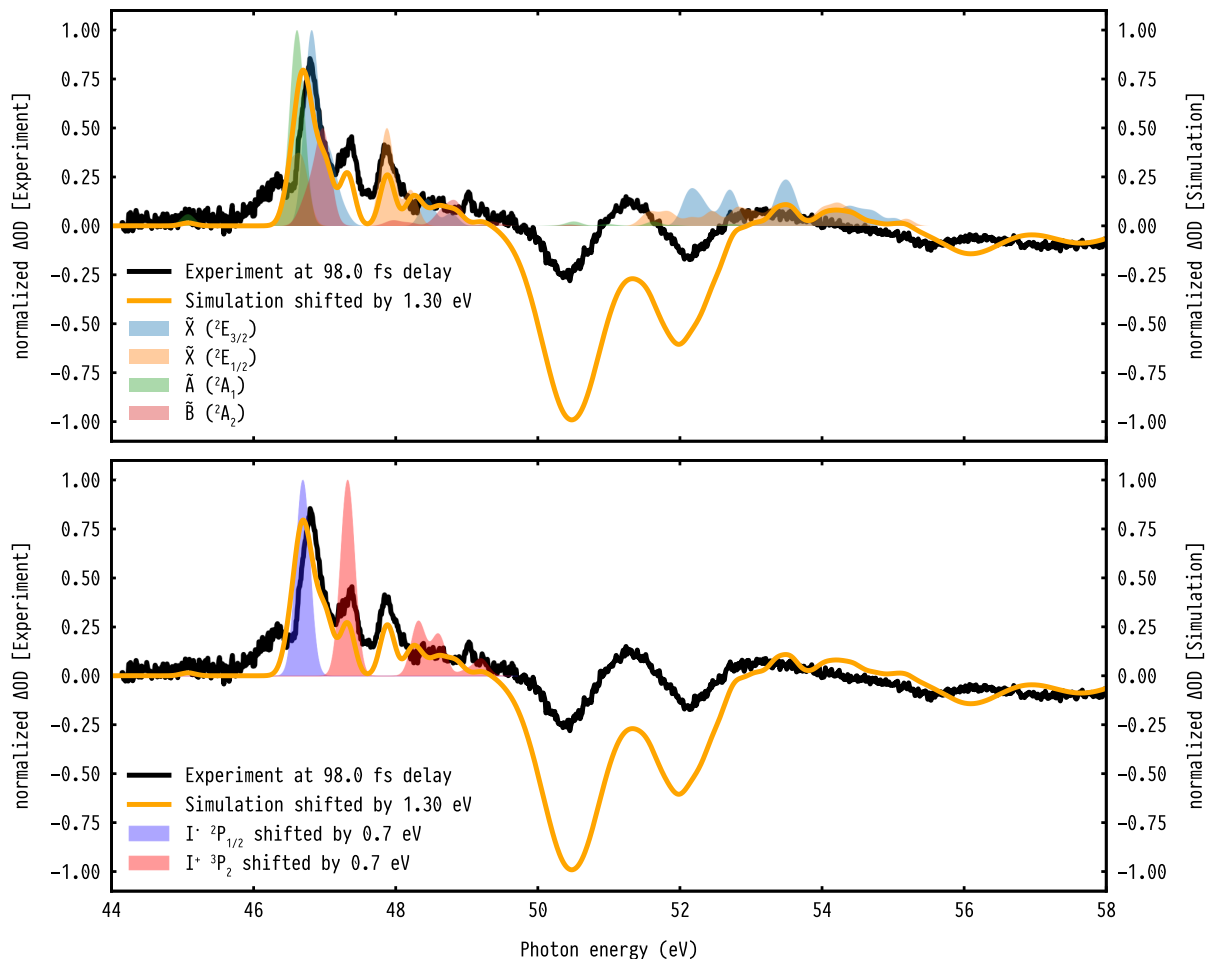
Figure 2.12 – (Top) The simulated spectrum of cationic CF$_3$I$^+$ based on the final geometry in the relaxed scan is shown in orange, shifted by 1.30 eV. It is calculated as the sum of the individual spectra for the first four states $\tilde{X}$ ($^2E_{3/2}$, $^2E_{1/2}$), $\tilde{A}$, $\tilde{B}$ and contributions form the I$^\bullet$ radical and I$^+$ cation. The separate contribution of the different states is indicated in blue, orange, green and red, respectively. The contribution of the I radical and cation are shown in the bottom part of the Figure. Additionally, the GS spectrum of CF$_3$I was subtracted, to approximate the GS bleach present in the experiment. The calculated peaks for the cationic states, the iodine cation and radical were broadened by applying a Gaussian with $\sigma = 0.1$ eV. The experimental signal is shown in black for a delay of 98.0 fs. (Bottom) Simulated spectra of I$^\bullet$ ($^3P_{3/2}$) radical and the I$^+$ ($^3P_2$) cation. The calculations were performed using a RAS$(15, 0, 1; 5, 3, 0)$ and RAS$(14, 0, 1; 5, 3, 0)$ respectively. The RAS2 subspace included the three $5p$ orbitals and the five $4d$ orbitals were included in the RAS1 subspace. For all calculations, the uncontracted ANO-RCC basis set was utilized. By comparing to experimental values taken from the work of O'Sullivan and coworkers [228], the necessary shift of 0.7 eV was determined. The calculated peaks were broadened by applying a Gaussian with $\sigma = 0.1$ eV.
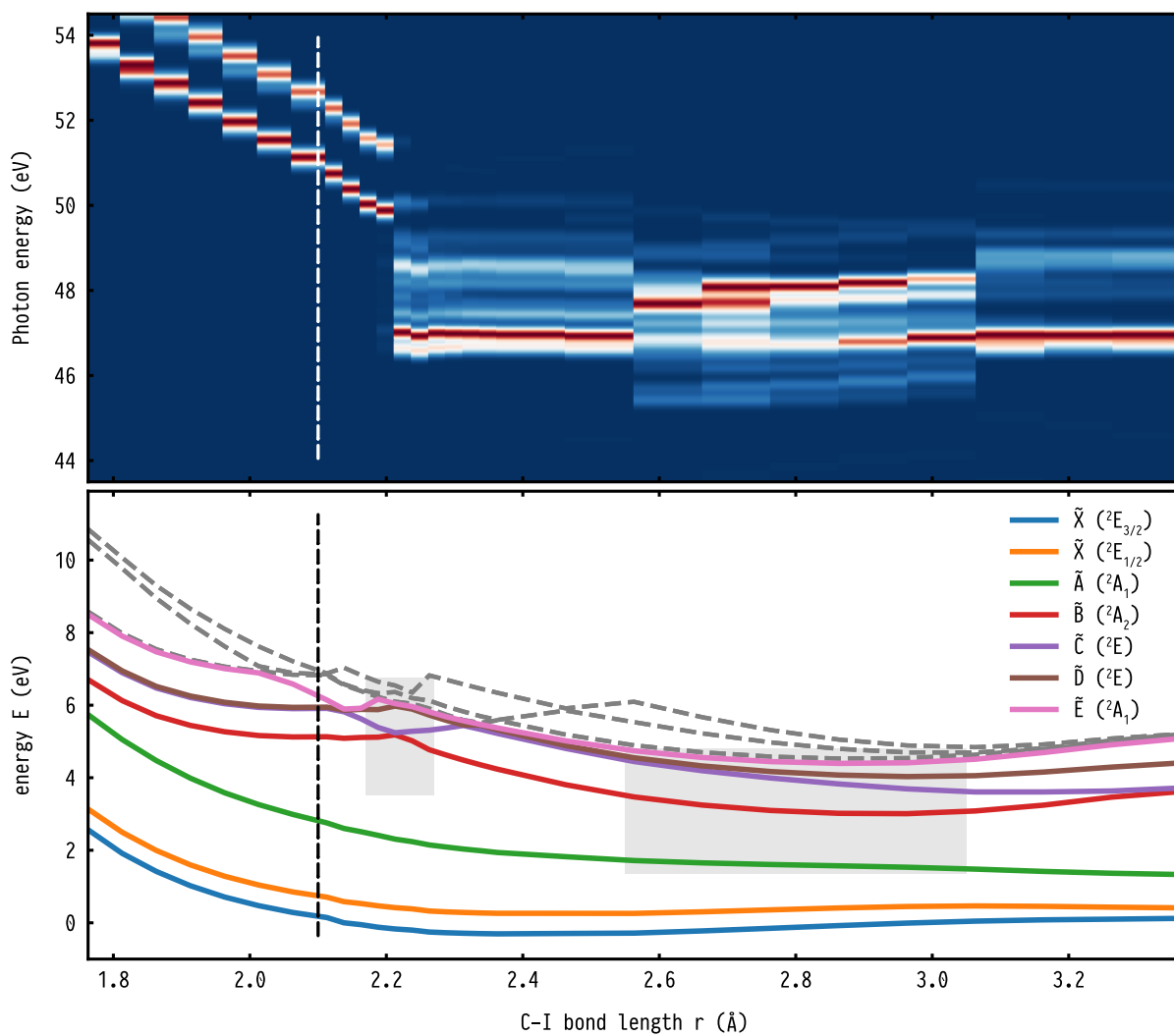
Figure 2.13 – (Top) Simulated TAS of the $\tilde{B}$ state along the C−I bond, shifted by $1.30\,\mathrm{eV}$ in energy. (Bottom) Relaxed scan of the C−I bond. The states are color-coded corresponding to their electronic character at the FC region indicated by the black dotted line. Additionally, the region of the CoIn at about $2.20\,\text{Å}$ and the second region of strong coupling between $2.55\,\text{Å}$ to $3.10\,\text{Å}$ are highlighted in gray.

THREE

Summary & Outlook

Within this thesis, different light-induced reactions in small and large molecules were studied with quantum chemistry (QC) and NAMD methods. In the first part of this work, the relaxation pathways after photoexcitation of the photoswitch HTI and the two artificial molecular motors, *motor-1* and *motor-2*, based on the HTI motive, were studied by high quality *ab initio* calculations of their PESs. The second part mainly focused on the theoretical simulation of transient XAS. Here, a versatile framework based on the RASSCF method to calculate core-excitations and subsequently the XAS was introduced. It was then applied in studying the ultrafast processes after laser excitation in vinyl bromide (C_2H_3Br) and trifluoroiodomethane (CF_3I).

For the photoswitch HTI, a comprehensive reaction model of its *cis*/*trans* photoisomerization is introduced by the presented study [17]. Further, the effects of different solvents as well as substitutions on its switching speed and photophysical properties was discussed. The combination of time-resolved absorption and emission measurements allowed for the identification of different timescales for the relaxation from the excited electronic state to the ground state, which are influenced by the different solvents and substitutions. Here, a strong interaction with the polarity of the solvent was found. For the different substituents, it was shown that electron donating groups accelerate the isomerization, whereas electron withdrawing groups slowed it down. This trend was already discussed by März *et al.* in an earlier study [109], and it is also present in different solvents. These experimental observations suggested a relaxation via a barrier whose height depends on the solvent and substitution effects. This was supported by high-level calculation of the ground and first excited state PES and through further analysis of the electronic wavefunction at critical optimized points. Here, the different effects on the switching speed could be explained by the change in magnitude and direction of the dipole moment throughout the isomerization process. The detailed understanding of the relaxation pathway of HTI and how it can be influenced opens up new possibilities in the systematic design and tuning of molecular switches in general. For both molecular motors, *motor-1* and *motor-2*, the detailed calculations of the ground and excited state PESs presented in the studies [22, 32] elucidated the mechanism of their unidirectional rotation. The molecular motor, *motor-1*, was designed and synthesized in the lab of Prof. Henry Dube based on the photoswitch HTI. The inclusion of two additional stereocenters resulted in four distinct isomers **A-1**, **B-1**, **C-1** and **D-1**. Here, they proposed a four-step process for the rotation, consisting of two thermal and two light-induced steps [31]. Due to the fast rotation speed of about $1\,kHz$ at ambient temperatures, a complete experimental proof via time resolved NMR spectroscopy was not possible. Here, the combination of multiscale broadband transient absorption measurements with a high-level description of

the involved excited states could confirm the proposed mechanism of the unidirectional rotation. For both photo isomerizations, the calculations revealed an energetically accessible CoIn that allowed the ultrafast relaxation to the GS of the next isomer by rotating around the central double bond. Additionally, an unproductive pathway via ISC back to the GS of the initial isomer could also be identified. Finally, a rate model calculation including both photoreactions forming the thermodynamically metastable states, **B-1** and **D-1**, revealed the constant population of isomer **D-1** as rate limiting and not the thermal step itself. From these findings, three pathways to improve the rotation speeds and efficiency of light-driven molecular motors were derived. First, enhance the quantum yields of the photoreactions. Second, lower the barriers of the thermal steps, thus effectively removing the metastable isomers from the reaction pathway. Third, enhance the extinction coefficients and absorption range to increase the probability of a photon absorption. Following the second pathway led to the improved design of *motor-2* [32]. By introducing a nitrogen heteroatom into the stilbene ring, the barrier for the second thermal step could be reduced to such an extent that the metastable isomer **D-1** was removed from the rotation pathway, resulting in a three-step process for the rotation. Here, a similar mechanism and CoIns as described for *motor-1* could be identified, making *motor-2* capable of ultrafast rotation upon irradiation with visible light. This confirms the possibility to improve the efficiency of molecular motors by removing one of the thermal steps. However, one must keep in mind that, for both molecular motors, only static calculations of the PES were performed. As a next step, one could perform *ab initio* NAMD simulations to refine the understanding of the reaction pathways. Elucidating the relation between the productive and unproductive pathways, could especially open up new possibilities for improving the efficiency of the HTI based motors, as well as light-powered molecular motors in general. However, due to the molecular size of *motor-1* and *motor-2* and the quite large AS necessary to describe their electronic structures adequately, the NAMD simulations are computationally very expensive. The efficient implementation of the CASSCF method and its analytical gradients in the electronic-structure program BAGLE [229] and computation time on SuperMUC-NG, the supercomputer at the Leibniz-Rechenzentrum (LRZ), could make those simulations feasible.

The second part of this work introduced a comprehensive framework to simulate time-dependent XUV/X-ray transient absorption spectra. The framework combines the changes in the electronic structure as well as the nuclear motion accessible by *ab initio* NAMD with the high quality description of the core-excited states with the multi-reference method RASSCF. This framework was then applied to study the ultrafast dynamics of laser excited C_2H_3Br and CF_3I. The presented study on C_2H_3Br [55] demonstrated the strength of the combined experimental and theoretical approach to follow in real time the electronic structure change in molecules via ATAS. In particular, this pump-probe experiment investigated the simultaneously strong-field initiated processes of the neutral and ionized state dynamics. Experimentally, C_2H_3Br gets exposed to a few-cycle near-infrared (NIR) pulse capable of exciting a valence electron or even ionizing the molecule. To follow the competing dynamics of both species, a state-of-the-art ATAS setup, which probes at the bromide $M_{4,5}$ edge, was utilized. The excellent time and spectroscopic resolution of this setup made it possible to distinguish sub 100 fs features characteristic of electronic and nuclear coupling. In order to explain the complete transient absorption spectrogram and disentangle the involvement of the two species, the transient XAS spectra for both neutral and ionic vinyl bromide was simulated. Using *ab initio* NAMD, we were able to simulate the neutral and cationic dynamics resulting from the initial interaction of the molecule with the strong-field. Based on these results, the corresponding time-dependent XUV/X-ray transient absorption spectra were calculated with the presented RASSCF/RASPT2 procedure. This allowed for detailed and quantitative comparison with the experimental data. Here, we were able to assess the strong-field ionization as the main outcome of the interaction with the few-cycle NIR pulse. In particular, the dynamics of the first three electronic states of the cation, D_1, D_2 and D_3, could be unambiguously assigned to distinct features in the experimentally observed spectrum. The first two states remain bound, which allowed us to time-resolve the ensuing mul-

tidimensional vibrational dynamics with high sensitivity. The second excited cationic state D_3 instead presents richer dynamics. In addition to pure vibrational motion, fast and slow dissociation channels appear, leading to ultrafast rupture of the carbon-bromide bond. The excellent agreement of the simulated spectrum with the experimental results established the combined experimental and theoretical approach as a spectroscopic technique capable of resolving coupled non-adiabatic electronic-nuclear dynamics in photoexcited molecules with sub-femtosecond resolution. The framework was also applied to study the ultrafast dynamics of ionized trifluoroiodomethane (CF_3I). In the experiment, CF_3I gets exposed to a strong-field pump pulse, ionizing the molecule. The onsetting dynamics are probed by ATAS on the $N_{4,5}$ edge of iodine, combined with strong-field-ionization mass spectrometry. This setup takes advantage of the excellent time and spectral resolution of ATAS, while also supporting the electronic state assignment with the measured fragmentation patterns. The recorded transient spectra showed a delayed appearance of an absorption feature at $47.3\,eV$, known to be the spectroscopic signature of the GS of the I^+ cation [228]. Simulating the transient XAS spectra allowed for the explanation of this feature with an ultrafast CT, mediated by a CoIn in the vicinity of the FC point. Initially the $\tilde{B}$ state, an ionization from the F lone-pair orbitals, gets populated by the strong-field. In the FC region, it does not exhibit hole-density on the I atom, leading to a lack of absorption below $53\,eV$. The hole can be transferred to the I via passage through the CoIn with the $\tilde{E}$ state, giving rise to the signal at $47.3\,eV$ and ultimately resulting in the fragmentation of CF_3I^+ into a CF_3 radical and the I^+ cation.

As a next step, the RASSCF/RASPT2 framework could be applied to investigate the early stages of electron motion in biologically relevant systems like the deoxyribonucleic acid (DNA) nucleobases or even photosynthetic complexes. Multiple possibilities are conceivable for extending the presented framework. First, one could also include the simulation of the initial excitation by the pump laser. This would allow for a better understanding of the involved species and their different relaxation and fragmentation channels. On the experimental side, this understanding could be further enhanced by the combination of the attosecond absorption with charged-particle-based spectroscopies, such as time-of-flight, or even velocity-map-imaging spectroscopy. Second, with only minor modifications to the RASSCF/RASPT2 procedure, the presented protocol would make the simulation of other spectroscopic techniques like resonant inelastic X-ray scattering (RIXS) and attosecond stimulated Raman spectroscopy (ASRS) possible. Finally, a tighter integration of the RASSCF/RASPT2 procedure, necessary for the core- and valence-excited states, with the NAMD program, could drastically reduce the time needed for the manual setup and the post-processing of the results.

Input Files for the Simulation of Transient XUV/X-ray Absorption Spectrograms

In the following, all necessary input files for the OPENMOLCAS program package[1] are listed in order to perform the simulation of a XUV/X-ray absorption spectra with the RASSCF protocol introduced in section 2.1. To help with the understanding of the utilized keywords and their values, we will use the calculations for vinyl bromide, presented in section 2.2, as an example. Here for the neutral species, an AS of $\text{RAS}(18, 1, 0; 5, 7, 0)$, illustrated in Figure A.1, was used. As a reminder, in the labeling $\text{RAS}(n, l, m; i, j, k)$, i, j and k correspond to the number of orbitals in the RAS1, RAS2, and RAS3 sub spaces, respectively, n is the total number of electrons in all active spaces, l the maximum number of holes allowed in the RAS1, and m the maximum number of electrons allowed in RAS3. All values supplied in the input files will be in reference to a neutral vinyl bromide molecule utilizing this $\text{RAS}(18, 1, 0; 5, 7, 0)$. Finally, in the illustration in figure A.2 the interconnection of the different calculated states with the RASSCF protocol is summarized.

Listing A.1 – General HF calculation for the initial set of orbitals.

```
1   &GATEWAY
2    TITLE= hf
3    COORD= geom.xyz
4    BASIS= ANO-RCC-VTZP
5    GROUP= NOSYM
6    AMFI
7    RICD
8
9   &SEWARD
10
11  &SCF
12   SPIN= 1
13   CHARGE= 0
```

---

[1] At the time of writing this thesis, the version v21.02 of OPENMOLCAS was used.
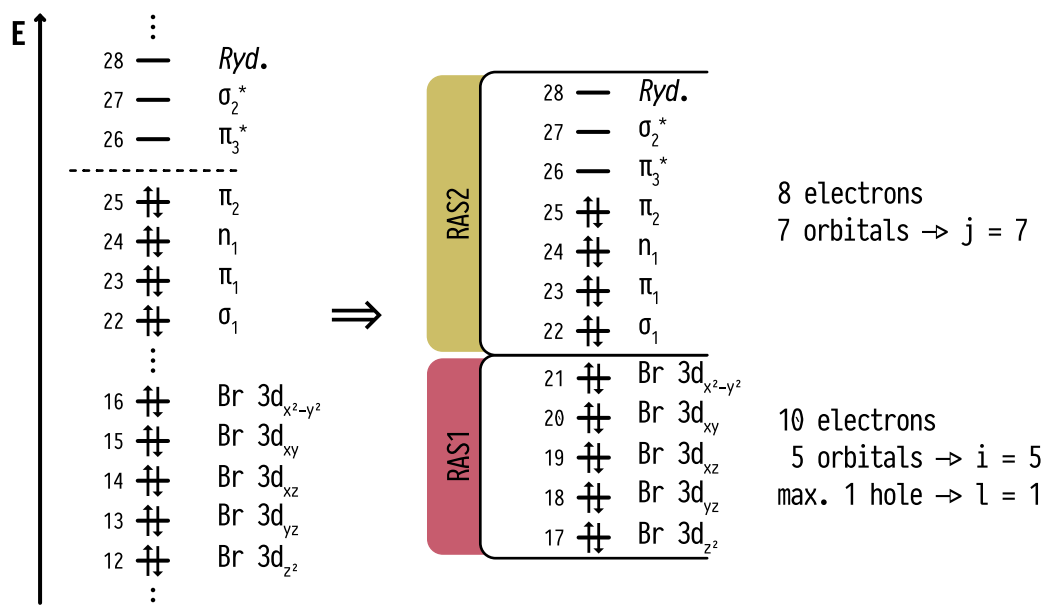
Figure A.1 – (Left) The orbital scheme of the relevant orbitals for vinyl bromide. The orbitals are numbered and listed according to increasing energy. (Right) Definition of the RAS subspaces for all RASSCF calculations. The shown variables correspond to the introduced labeling $RAS(n, l, m; i, j, k)$. As the RAS3 subspace is not utilized, it follows that $k = 0$ and $m = 0$. In the RAS2 subspace, 7 orbitals $(j = 7)$ and 8 electrons are included. The RAS1 subspace is built up of 10 electrons in five orbitals $(i = 5)$ and one hole is allowed $(l = 0)$. As the AS needs to be continuous, the core orbitals (12-16, in the orbital scheme) are rotated to the end of the RAS2 block (17-21). Therefore, the shown example the complete AS is labeled as $RAS(18, 1, 0; 5, 7, 0)$.

Listing A.2 – Initial RASSCF calculation utilizing the HF orbitals as the starting guess in the self-consistend field (SCF) procedure. If just the RAS2 subspace is utilized, the calculation is analogous to a standard CASSCF calculation.

```
1   &GATEWAY
2     TITLE= casscf
3     COORD= geom.xyz
4     BASIS= ANO-RCC-VTZP
5     GROUP= NOSYM
6     AMFI
7     RICD
8
9   &SEWARD
10
11  &RASSCF
12    FILEORB= hf.Orb
13    SPIN= 1
14    CHARGE= 0
15    NACTEL= 8 0 0 (n l m)
16    RAS2= 7 (j)
17    CIROOT= 7 7 1 (n_valence_states, size of the CI matrix, relative weights)
```

Listing A.3 – RASSCF and MS-CASPT2 calculation for the valence-excited states. As the AS needs to be continuous, the core orbitals (12-16) are rotated by the **ALTER** keyword to the end of the RAS2 subspace (17-21). Saving the JobMix file at the end of the calculation is vital, as it is needed in the final RASSI calculation.

```
1   &GATEWAY
2    TITLE= rasscf_valence
3    COORD= geom.xyz
4    BASIS= ANO-RCC-VTZP
5    GROUP= NOSYM
6    AMFI
7    RICD
8
9   &SEWARD
10
11  &RASSCF
12   FILEORB= casscf.RasOrb
13   ALTER= 5
14   1 16 21
15   1 15 20
16   1 14 19
17   1 13 18
18   1 12 17
19   SPIN= 1
20   CHARGE= 0
21   NACTEL= 18 1 0 (n l m)
22   RAS3= 0 (k)
23   RAS2= 7 (j)
24   RAS1= 5 (i)
25   CIROOT= 7 7 1 (n_valence_states, size of the CI matrix, relative weights)
26   CIONLY
27
28  &CASPT2
29   IPEAshift= 0.25
30   IMAGinary= 0.2
31   MULTistate
32   ALL
33
34  >>>> COPY $Project.JobMix rasscf_valence_m1.JobMix
```

Listing A.4 – RASSCF and MS-CASPT2 calculation for the core-excited states. As the AS needs to be continuous, the core orbitals (12-16) are rotated by the **ALTER** keyword to the end of the RAS2 subspace (17-21). Then using the **HEXS** keyword one hole is forced in the RAS1. Again, the JobMix file is saved at the end of the calculation.

```
1   &GATEWAY
2    TITLE= rasscf_core
3    COORD= geom.xyz
4    BASIS= ANO-RCC-VTZP
5    GROUP= NOSYM
6    AMFI
7    RICD
8
9   &SEWARD
10
11  &RASSCF
12   FILEORB= casscf.RasOrb
13   ALTER= 5
14   1 16 21
15   1 15 20
16   1 14 19
17   1 13 18
18   1 12 17
19   SPIN= 1
20   CHARGE= 0
21   NACTEL= 18 1 0 (n l m)
22   RAS3= 0 (k)
23   RAS2= 7 (j)
24   RAS1= 5 (i)
25   HEXS
26   1
27   1
28   CIROOT= 40 40 1 (n_core_states, size of the CI matrix, relative weights)
29   CIONly
30
31  &CASPT2
32   IPEAshift= 0.25
33   IMAGinary= 0.2
34   MULTistate
35   ALL
36
37  >>>> COPY $Project.JobMix rasscf_core_m1.JobMix
```

Listing A.5 – RASSI calculation for the final oscillator strengths and vertical transition energies necessary to simulate an XAS spectrum. The calculation of the valence- and core-excited states needs to be performed for both multiplicities, M_1 and M_2, in order to include the SOC effects via the `SPIN` keyword in the `RASSI` programm.

```
1   &GATEWAY
2    TITLE= rassi
3    COORD= geom.xyz
4    BASIS= ANO-RCC-VTZP
5    GROUP= NOSYM
6    AMFI
7    RICD
8
9   &SEWARD
10
11  >>>> COPY rasscf_valence_m1.JobMix   JOB001
12  >>>> COPY rasscf_core_m1.JobMix      JOB002
13  >>>> COPY rasscf_valence_m2.JobMix   JOB003
14  >>>> COPY rasscf_core_m2.JobMix      JOB004
15
16  &RASSI
17   NROFJOBIPHS= 4 7 40 8 40
18   1 2 3 ... 7 (n_valence_states_m1)
19   1 2 3 ... 40 (n_core_states_m1)
20   1 2 3 ... 8 (n_valence_states_m2)
21   1 2 3 ... 40 (n_core_states_m2)
22   SPIN
23   HDIAG
24   -7448.13807556
25   -7448.13750127
26   ... (all MS-CASPT2 energies in the same order
27       as the wave functions supplied with the
28       JOB001, JOB002, JOB003 and JOB004 files)
```
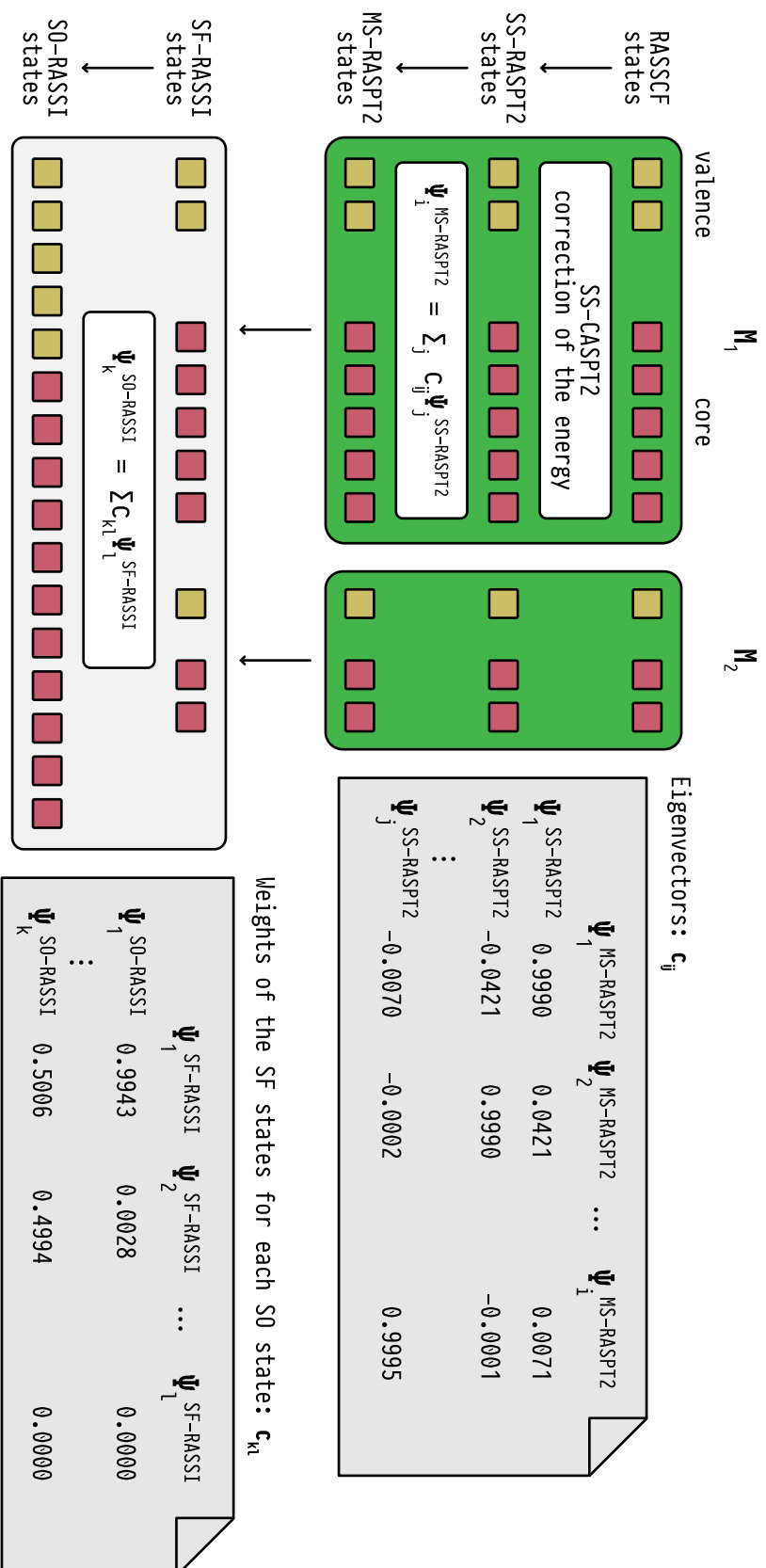
RASSCF states

SS-RASPT2 states

MS-RASPT2 states

SF-RASSI states

SO-RASSI states

valence   core

M_1 M_2

SS-CASPT2 correction of the energy

$$\Psi_i^{\text{MS-RASPT2}} = \sum_j c_{ij}\,\Psi_j^{\text{SS-RASPT2}}$$

$$\Psi_k^{\text{SO-RASSI}} = \sum_l C_{kl}\,\Psi_l^{\text{SF-RASSI}}$$

Eigenvectors: c_{ij}

	$\Psi_1^{\text{MS-RASPT2}}$	$\Psi_2^{\text{MS-RASPT2}}$	...	$\Psi_i^{\text{MS-RASPT2}}$
$\Psi_1^{\text{SS-RASPT2}}$	0.9990	0.0421		0.0071
$\Psi_2^{\text{SS-RASPT2}}$	−0.0421	0.9990		−0.0001
...				
$\Psi_j^{\text{SS-RASPT2}}$	−0.0070	−0.0002		0.9995

Weights of the SF states for each SO state: c_{kl}

	$\Psi_1^{\text{SF-RASSI}}$	$\Psi_2^{\text{SF-RASSI}}$	...	$\Psi_l^{\text{SF-RASSI}}$
$\Psi_1^{\text{SO-RASSI}}$	0.9943	0.0028		0.0000
...				
$\Psi_k^{\text{SO-RASSI}}$	0.5006	0.4994		0.0000

Figure A.2 – Illustration of the interconnections between the different states calculated within the RASSCF framework to simulate an XAS spectrum. In a first step, starting with the RASSCF states, valence- and core-excited of both multiplicities M_1 and M_2 (e.g. singlet and triplet), the dynamic electron correlation is included by a single-state CASPT2 (SS-CASPT2) calculation. Afterwards, these SS-RASPT2 states are used as the basis in the MS-CASPT2 calculation, which results in a set of MS-RASPT2 states. These states, in turn, are represented as a linear combination of the initial SS-RASPT2 states. The corresponding coefficients c_{ij} are listed as "Eigenvectors" within the **CASPT2** section of the OpenMolcas output/log file (see sample output on the right). The sets of MS-RASPT2 states of both multiplicities are used as the basis in the RASSI method, where all state interactions, including the SOC, are calculated. In the RASSI formalism, these input states are referred to as SF states (SF-RASSI). From the RASSI calculation, one arrives at a set of SO states (SO-RASSI), that are represented as a linear combination of all SF states. In the OpenMolcas the coefficients c_{kl} are listed in a table titled "Weights of the five most important spin-orbit-free states for each spin-orbit state." in the **RASSI** section of the output/log file.

Formulas

In the following, the three functions commonly used in broadening calculated peaks are listed. The **Gaussian function** is defined by

$$G(x; x_0, \sigma) = \frac{1}{\sigma\sqrt{2\pi}} \exp\left(\frac{-\left(x - x_0\right)^2}{2\sigma^2}\right) \tag{B.1}$$

with x_0 the peak position and σ the standard deviation, which can be calculated from Γ_G, it's FWHM, by

$$\sigma = \frac{\text{FWHM}}{2\sqrt{2\ln 2}} = \frac{\Gamma_G}{2\sqrt{2\ln 2}}. \tag{B.2}$$

The **Lorentz function** in turn is defined by

$$L(x; x_0, \gamma) = \frac{1}{\pi} \frac{\gamma}{\left(x - x_0\right)^2 + \gamma^2} \tag{B.3}$$

with γ the so called half width at half maximum (HWHM) so that

$$\gamma = \text{HWHM} = \frac{\Gamma_L}{2}. \tag{B.4}$$

Finally, the **Voigt profile**, a convolution of both a Gaussian and a Lorentz function, is defined by:

$$V(x; x_0, \sigma, \gamma) = \int_{-\infty}^{\infty} G(x'; x_0, \sigma) L(x - x'; x_0, \gamma) dx'. \tag{B.5}$$

Solving this integral analytically is impossible, but there are a number of efficient algorithms to calculate Voigt profile numerically [230, 231]. However, for the simulation of spectral line shapes, the Voigt profile is often approximated by just the linear combination of the two functions. This so called **pseudo-Voigt profile** is defined by

$$V_p(x; x_0, \eta, \sigma, \gamma) = \eta G(x; x_0, \sigma) + (1 - \eta)L(x; x_0, \gamma), \text{ with } 0 < \eta < 1. \tag{B.6}$$

For different mixing parameters η, the pseudo-Voigt profile becomes more Gaussian or Lorentz like. If this approximation should be accurate to within about 1 % of the exact Voigt profile [232, 233], the mixing parameter η, itself a function of the total FWHM Γ, can be calculated by

$$\eta = 1.36603 \frac{\Gamma_L}{\Gamma} - 0.47719\left(\frac{\Gamma_L}{\Gamma}\right)^2 + 0.11116\left(\frac{\Gamma_L}{\Gamma}\right)^3, \tag{B.7}$$

were Γ is described by

$$\Gamma = \left(\Gamma_G^5 + 2.69269\Gamma_G^4\Gamma_L + 2.42843\Gamma_G^3\Gamma_L^2 + 4.47163\Gamma_G^2\Gamma_L^3 + 0.07842\Gamma_G\Gamma_L^4 + \Gamma_L^5\right)^{\frac{1}{5}}. \qquad \text{(B.8)}$$

All three functions are plotted in figure B.1, the utilized values for the parameters are also listed in the figure.
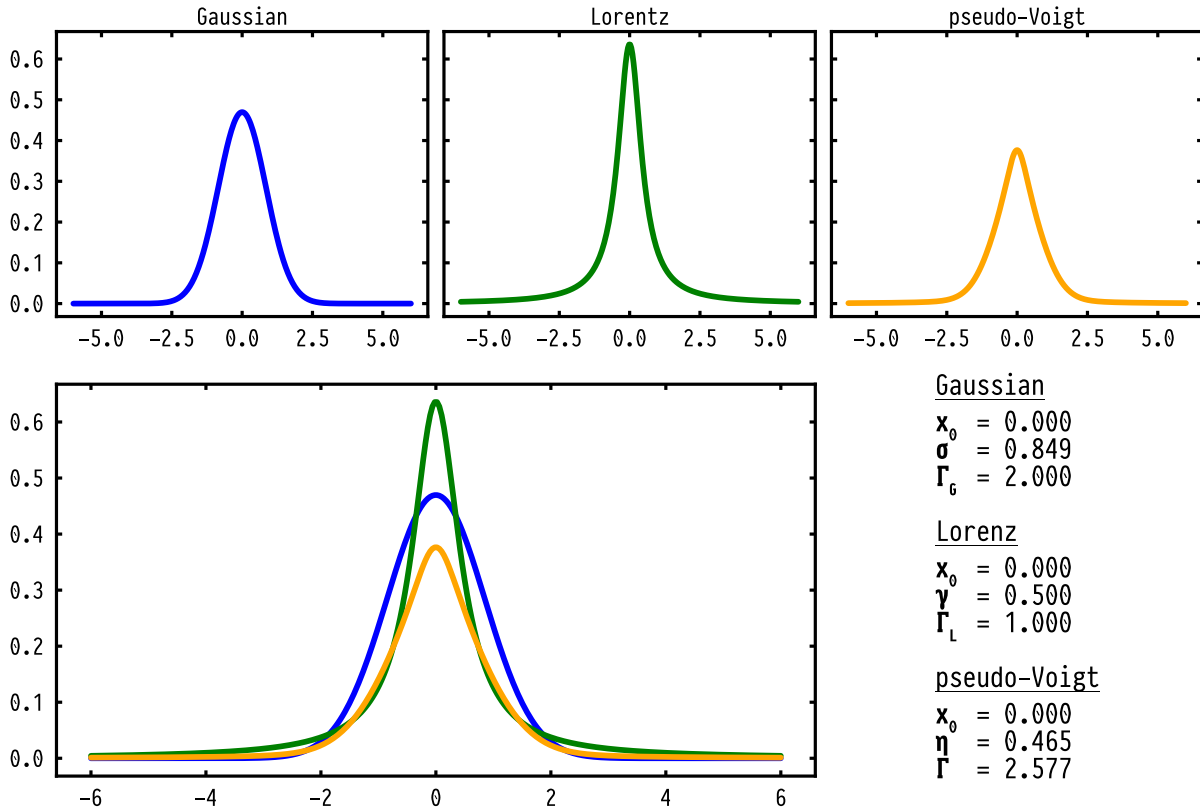

Figure B.1 – Plots of the three functions/profiles, Gaussian, Lorentz and pseudo-Voigt. The pseudo-Voigt profile is calculated from the shown Gaussian and Lorentz functions. All utilized parameters are listed on the right.

Supporting Information for the Study on Trifluoroiodomethane

C.1 Geometry of the Optimized Ground State Minimum

All benchmark calculations were performed at the GS minimum geometry of trifluoroiodomethane CF_3I. It was optimized with GAUSSIAN 16 [234] at the DFT level of theory using the ωB79X-D functional [235] and the basis set 6-311G [236, 237] (ωB79X-D/6-311G). The basis set was taken from the Basis Set Exchange (BSE) [238–240]. Table C.1 shows the xyz coordinates of the optimized geometry.

Table C.1 – Geometry of the ωB79X-D/6-311G optimized ground state minimum.

Number	Element	x (Å)	y (Å)	z (Å)
1	C	0.000 000	0.000 000	−0.004 017
2	I	0.000 000	0.000 000	2.158 913
3	F	1.242 440	0.000 000	−0.467 045
4	F	−0.621 220	1.075 985	−0.467 045
5	F	−0.621 220	−1.075 985	−0.467 045

C.2 Benchmark of the Computational Setup

In the following, the benchmark calculations of the computational setup for the simulation of the XUV TAS for trifluoroiodomethane (CF_3I) are presented.

Validation of the Active Space

Choosing a suitable AS is vital for CASSCF and RASSCF calculations. In order to sufficiently describe the valence excited states of CF_3I and CF_3I^+, three different ASs where tested. All calculations were carried out with the OPENMOLCAS [197, 198] program package using the ANO-RCC [210–214] basis set, contracted to VDZP quality (ANO-RCC-VDZP). The smallest AS, forming the common basis for the two larger ASs, included 12 electrons in 10 orbitals [AS(12,10)]. It was comprised of the carbon-iodine bond (σ_4, σ_4^*), both iodine lone-pair orbitals lp_1 and lp_2 as well as the three carbon-fluorine bonds (σ_1, σ_6^*, σ_2, σ_7^* and σ_3, σ_8^*). Subsequently, the medium AS was extended by three fluorine lone-pair orbitals lp_3, lp_4 and lp_5 resulting in 18

electrons in 13 orbitals [AS(18,13)]. The large AS was extended by an additional three orbitals (lp_6, lp_7 and lp_8), including all six fluorine lone-pair orbitals [AS(24,16)]. The orbitals included in the ASs are shown in Figure C.1. For the calculation of the cation, the same orbitals are included but with one electron removed, resulting in the set AS(11,10), AS(17,13) and AS(23,16).
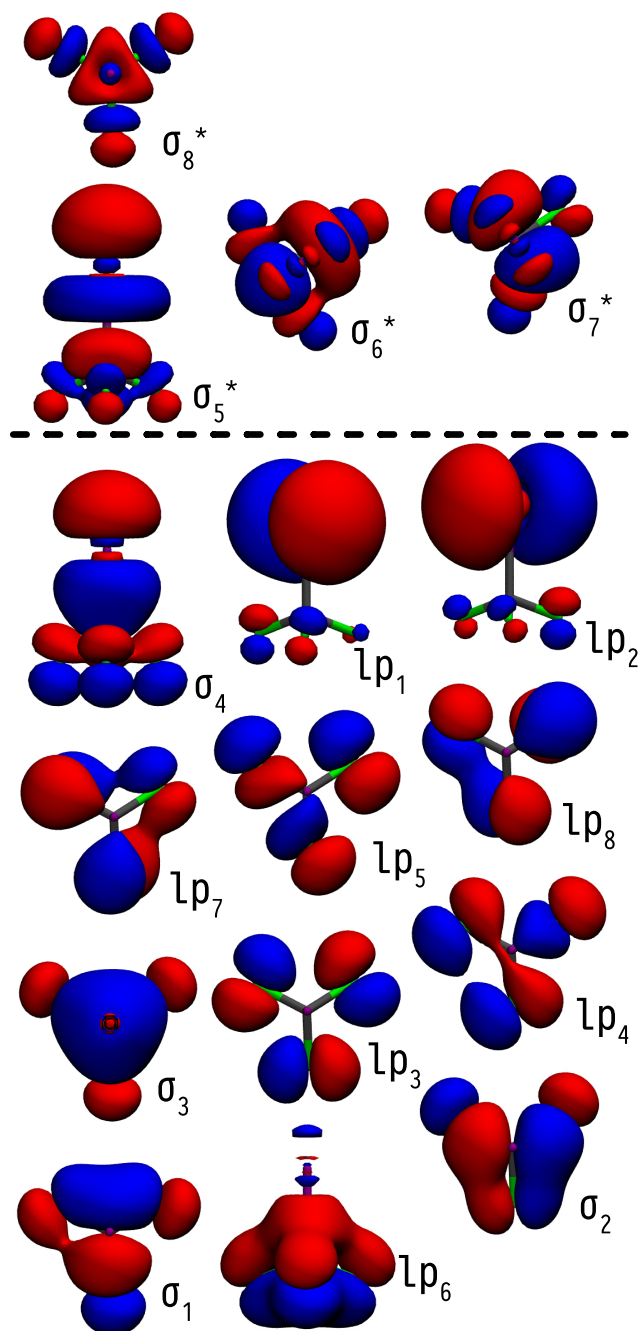

Figure C.1 – CASSCF molecular orbitals included in AS(12,10), AS(18,13) and AS(24,16) of trifluoroiodomethane, obtained using the ANO-RCC-VDZP basis set at the ωB79X-D/6-311G optimized ground state minimum geometry. The orbitals are rendered with an isovalue of 0.04.

As a first validation step for the three ASs, the ionization energies were compared to the experimental values taken from the study of Yates and coworkers [227]. The ionization energies listed in Table C.2 were calculated at the MS-CASPT2 level of theory, including SO effects, as the difference between the GS of the neutral CF_3I and the excited states of the cation. Further we compared the electronic character of the excited states to calculated charge distributions taken from the same publication as listed in Table C.3. The first two states, $\tilde{X}$ ($^2E_{3/2}$) and $\tilde{X}$ ($^2E_{1/2}$), describe an ionization from either of the I lone pair orbitals lp_1 and lp_2. Their ionization energies are described quite well by all three ASs. The third state, $\tilde{B}$ ($^2A_1$), an

Table C.2 – Ionization energies for the first seven states of the CF_3I^+ cation in eV at the MS-CASPT2 level of theory, including spin-orbit couplings. The energies were calculated as the difference of the GS energy of neutral species and the energies of the cationic states $\tilde{X}$-$\tilde{F}$. For the electronic character of the states, the partially occupied orbitals of the dominant CI vector based on the calculation with the AS(23,16) are listed.

State	Character	Ionization energies (eV)			
		AS(11,10)	AS(17,13)	AS(23,16)	Exp. [227]
$\tilde{X}$ $(^2E_{3/2})$	lp_1	10.74	10.49	10.54	10.45
$\tilde{X}$ $(^2E_{1/2})$	lp_2	11.36	11.11	11.12	11.18
$\tilde{A}$ $(^2A_1)$	σ_4	14.07	13.74	13.30	13.25
$\tilde{B}$ $(^2A_2)$	lp_3	-	15.15	15.22	15.56
$\tilde{C}$ (^2E)	lp_4	-	17.01	15.92	16.32
$\tilde{D}$ (^2E)	lp_5	-	17.02	16.27	17.28
$\tilde{E}$ $(^2A_1)$	$lp_{1,2}$, σ_5^*	16.33	16.18	16.80	19.25

Table C.3 – Calculated charge distribution of the first seven cationic states of CF_3I^+ taken from the work of Yates and coworkers [227]. 'Out' and 'In' are the percentage charge of the outersphere and intersphere regions, respectively. The column 'Sum' is not taken from the reference, but is an interpretation of the data. For our calculations the partially occupied orbitals of the transition with the largest CI weight are shown as an approximation for the charge distribution.

State	Charge distribution [%] [227]						Partially occupied orbitals		
	Out	C	F	I	In	Sum	AS(11,10)	AS(17,13)	AS(23,16)
$\tilde{X}$ $(^2E_{3/2})$	4.2	0.1	1.1	77.6	17.0	I^+	lp_1	lp_1	lp_1
$\tilde{X}$ $(^2E_{1/2})$	4.2	0.1	1.1	77.6	17.0	I^+	lp_2	lp_2	lp_2
$\tilde{A}$ $(^2A_1)$	1.9	27.9	18.0	44.2	8.0	Non-local	σ_4	σ_4	σ_4
$\tilde{B}$ $(^2A_2)$	0.6	0.0	80.5	0.0	18.9	F^+	$lp_{1,2}$, σ_5^*	lp_3	lp_3
$\tilde{C}$ (^2E)	0.7	0.3	78.4	0.3	20.3	F^+	$lp_{1,2}$, σ_5^*	$lp_{1,2}$, σ_5^*	lp_4
$\tilde{D}$ (^2E)	2.2	0.7	76.9	0.1	20.2	F^+	$lp_{1,2}$, σ_5^*	lp_4	lp_5
$\tilde{E}$ $(^2A_1)$	1.9	1.0	36.2	49.7	11.2	Non-local	-	lp_5	$lp_{1,2}$, σ_5^*

ionization from the $C-I$ bonding σ_4 orbital, is correctly described by the AS(23,16), with the other two overestimating the ionization energy. For the next three states, the electron hole is generated in the three F lone-pair orbitals lp_3, lp_4 and lp_5. These states cannot be described by the AS(11,10), as the necessary orbitals are not included. The other two ASs correctly describe their electronic character and more or less capture the range of the ionization energy. However, the AS(17,13) fails to describe the correct order of the states, as, energetically, the last state $\tilde{E}$ appears between the states $\tilde{B}$ and $\tilde{C}$. For the $\tilde{E}$ state, the hole is again located mainly on the I with the lp_1, lp_2 and σ_5^* orbitals partially occupied. Here, only the AS(23,16) is able to correctly describe the order of the electronic states. It does fall short in matching the ionization energies of the highest states, but as all three ASs struggle in this regard, we suspect the limiting factor to be the moderate size of the basis set ANO-RCC-VDZP, as it is, for example, unable to sufficiently describe possible Rydberg-type contributions to the orbitals.

Finally, the GS spectrum of neutral CF_3I was simulated for all three ASs and compared to the experimental signal, as shown in Figure C.2. Here all three spectra show the pronounced double-peak structures of the experiment at 50.4 eV and 52.1 eV and at 55.4 eV and 57.1 eV. But depending on the size of the AS, a different shift of the excitation energies needed to be applied. Shifting to the biggest peak in the experiment at 50.4 eV, resulted in values of 2.00 eV, 1.60 eV and 1.30 eV for the spectra of AS(12,10), AS(18,13), and AS(24,16), receptively. In general, the prominent doublet at 50.4 eV and 52.1 eV is described quite well by all three ASs. With the AS(24,16) it was even possible to reproduce the correct intensity distribution of said

doublet. For the second doublet at $55.4\,\text{eV}$ and $57.1\,\text{eV}$, all three spectra are energetically off by about $0.7\,\text{eV}$ to $0.8\,\text{eV}$. Here, it is again possible that the size of the basis set ANO-RCC-VDZP is prohibiting a perfect match of this feature. But considering the fact that calculations with a larger basis set were computationally infeasible and the otherwise excellent agreement with the experimental spectrum, we are convinced that the ASs (24,16) and (23,16) are adequate to describe the valence space and core-excited states of neutral and ionic CF_3I.
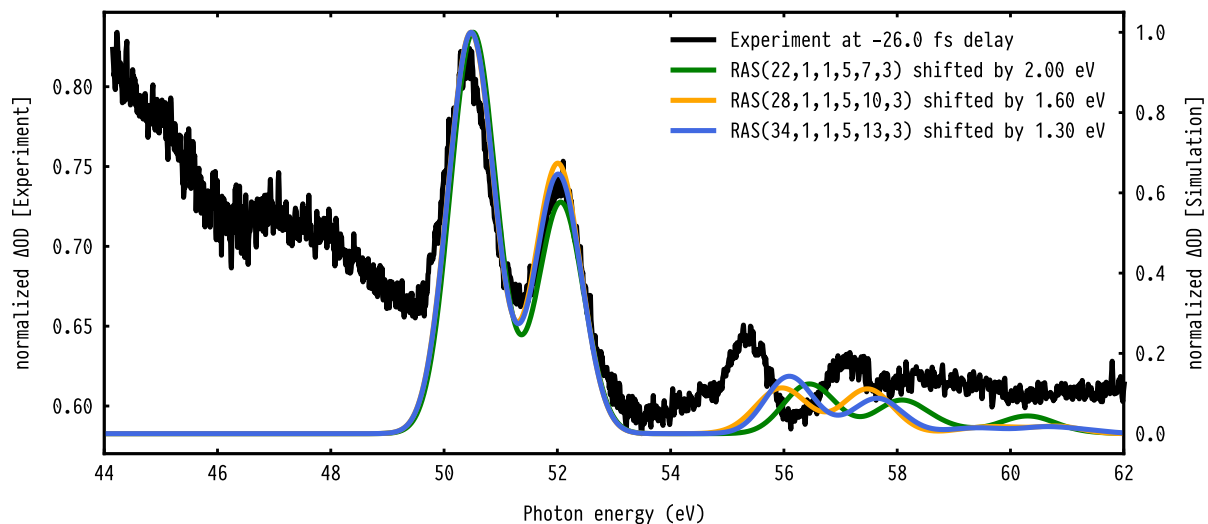

Figure C.2 – GS spectra of neutral CF_3I, simulated for the three different ASs. The calculated peaks are broadened by applying a Gaussian with $\sigma = 0.4\,\text{eV}$. In order to match the experimental signal shown in black, the excitation energies needed to be shifted by different amounts.

Validation for Utilizing the RAS3 Subspace

To reduce the computational time of the necessary RASSCF calculations, the AS for the valence space was split up into the RAS2 and RAS3 subspaces, and only a single excitation was allowed into the RAS3 subspace. Here the three virtual orbitals of the carbon-fluorine bonds (σ_6^*, σ_7^* and σ_8^*) were relocated to the RAS3 subspace, leaving the rest of the orbitals in the RAS2 subspace. To judge whether this affected the simulated spectrum, we compared the GS spectrum of the "full" AS with the approximation of splitting the AS. As this benchmark was performed for the AS(12,10), the resulting RAS are RAS(22, 1, 0; 5, 10, 0) and RAS(22, 1, 1; 5, 7, 3). Both calculated spectra, shifted by $2.00\,\text{eV}$ to match the experimental signal, are shown in Figure C.3. The spectra are nearly identical, with the only difference appearing in the intensity of the second peak of the doublet at $50.4\,\text{eV}$ and $52.1\,\text{eV}$, which is a bit lower, when the AS is split up between the two RAS subspaces. So, in summary, the splitting of the AS does not change the simulated spectrum in a meaningfull way and one can safely utilize this approximation, at least in the case of trifluoroiodomethane. The total calculation time necessary to arrive at the final spectrum, could be cut down drastically in this way. The initial calculation time of over eight days for RAS(22, 1, 0; 5, 10, 0) could be reduced to about four and a half hours by utilizing the RAS3 subspace. This speedup made simulations with the AS(24,16) possible, as they could be completed in about three days. For the original setup of just using the RAS2 subspaces, these calculations were not feasible as a total calculation time of about three months was estimated.

C.3 Relaxed Scan of Cationic Trifluoroiodomethane

In a first step, we generated PESs for each cationic state by performing a relaxed scan of the C–I bond. The relaxed scan was calculated with OPENMOLCAS utilizing the state tracking feature (keyword `TRACK`) of the `SLAPAF` program, where one is able to follow the character of a specific state throughout a geometry optimization. In our case we choose to follow the character
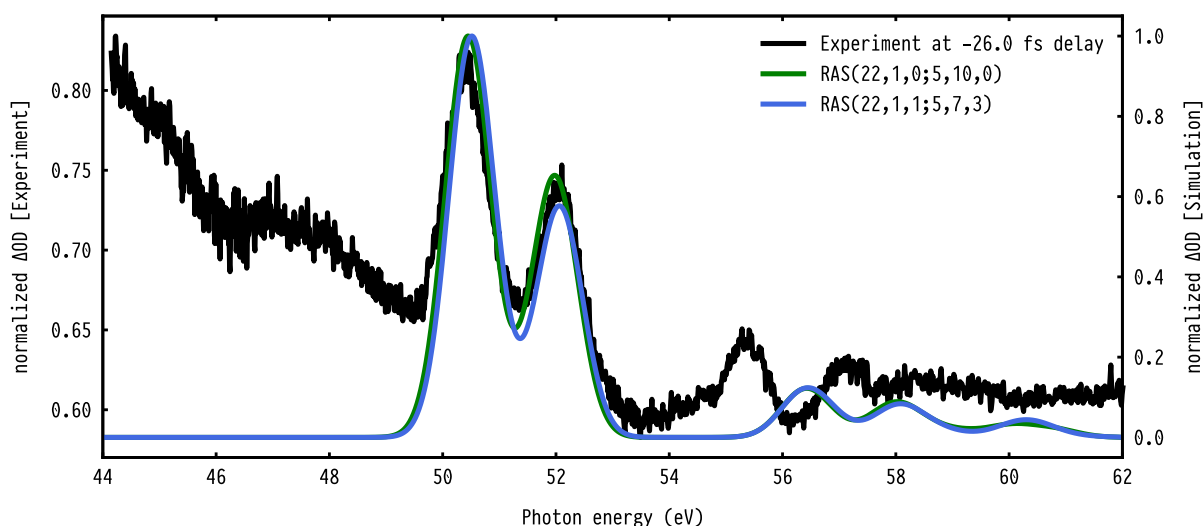
Figure C.3 – GS spectra of neutral CF_3I, simulated for the AS(12,10). In both cases, the excitation energies were shifted by $2.00\,eV$ to match the experimental signal shown in black and broadened by applying a Gaussian with $\sigma = 0.4\,eV$. The spectrum where all orbitals are included in the RAS2 is shown in green. And the one where the AS is split up between the RAS3 and RAS2 subspaces is shown in blue.

of the first state, $\tilde{X}$, at the FC region. At each step in the scan, the geometry was optimized at the SA11-CASSCF(17,13)/ANO-RCC-VDZP level of theory. The C−I bond length was scanned from $1.6\,\text{Å}$ to $3.4\,\text{Å}$ with an initial step size of $0.05\,\text{Å}$. The step size was increased to $0.1\,\text{Å}$ at a bond length of $2.3\,\text{Å}$. In the FC region between $2.0\,\text{Å}$ to $2.3\,\text{Å}$, the steps size was reduced to $0.025\,\text{Å}$. Building on top of the optimized geometries, we further performed single point MS-CASPT2 calculations, including SO effects, utilizing the full AS(23,16). To reduce the computational costs of these calculations, we again included the three highest virtual orbitals (σ_6^*, σ_7^* and σ_8^*) into the RAS3 space and allowed for a single excitation [RAS(23, 0, 1; 0, 13, 3)]. The resulting PESs are plotted in Figure C.4.
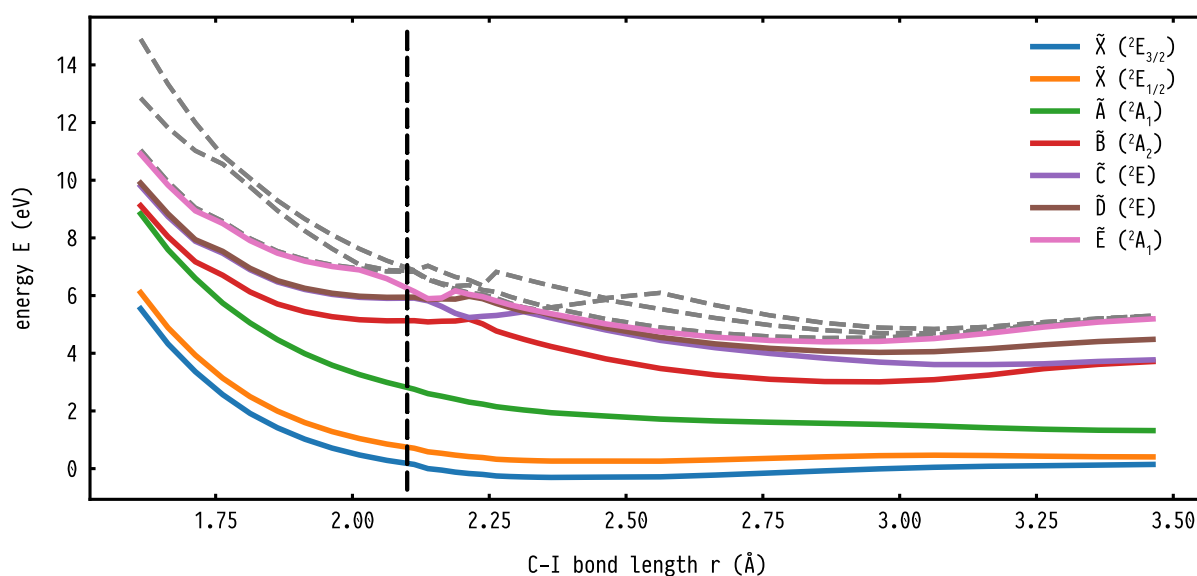

Figure C.4 – Relaxed scan of the C−I bond. The states are color-coded corresponding to their electronic character in the FC region indicated by the black dotted line.

C.4 Transient Absorption Spectra based on the Relaxed Scan

Based on the relaxed scan, the TAS of the first five states, $\tilde{X}$ ($^2E_{3/2}$), $\tilde{X}$ ($^2E_{1/2}$), $\tilde{A}$, $\tilde{B}$ and $\tilde{C}$ were calculated. They are plotted over the corresponding C–I bond length in Figure C.5.
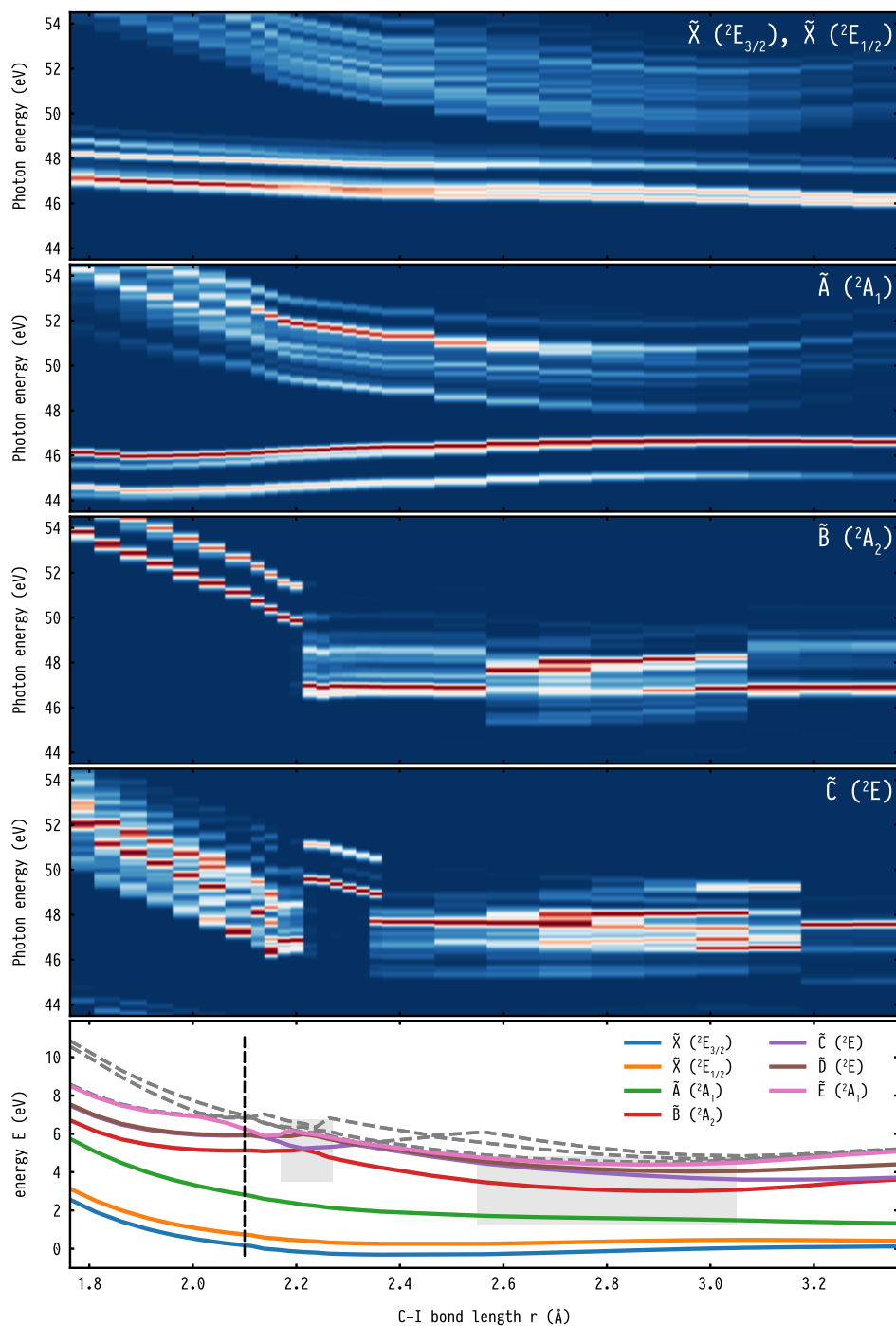

Figure C.5 – Simulated TAS along the C–I bond of the $\tilde{X}$, $\tilde{A}$, $\tilde{B}$ and $\tilde{C}$ states respectively. The spectra of the SO split states $\tilde{X}$ ($^2E_{3/2}$) and $\tilde{X}$ ($^2E_{1/2}$) are combined in the first plot.

C.5 Dissociation Dynamics of Cationic Trifluoroiodomethane

In order to analyze the dissociation dynamics of cationic trifluoroiodomethane, a QD simulation based on PESs generated from a relaxed scan of the C–I bond was performed. The QD simulations for the nuclear dynamics were performed by solving the TDSE for each relevant cationic state

$$i\hbar\frac{\partial}{\partial t}\chi(R,t) \quad = \quad \hat{H}\chi(R,t), \tag{C.1}$$

$$\text{with } \hat{H} \quad = \quad \frac{1}{2m_R}\frac{\partial^2}{\partial R^2} + \hat{V}_X(R). \tag{C.2}$$

with the reduced mass m_R along the dissociation coordinate R and the potential energy operator $\hat{V}_X(R)$. The numerical propagation on the adiabatic PESs is performed by integration of the TDSE according to

$$\chi(t+dt) = \exp\left(-i\hat{H}dt\right)\chi(t) = \hat{U}\chi(t). \tag{C.3}$$

The evolution operator $\hat{U}$ is expanded in a Chebyshev series [241]. The PESs are represented on a one-dimensional spatial grid with 256 grid points obtained by interpolating the results of the relaxed scan of cationic trifluoroiodomethane. The limits of the used grid are $1.6\,\text{Å}$ and $3.4\,\text{Å}$, respectively, and a Butterworth filter [242] was employed, which absorbs the parts of the wave packet that reach the dissociation area. The filter was of "left-pass" type (absorbing all parts on the right side of the grid), and placed at $3.3\,\text{Å}$ with an order of 100. The total simulation time was $250\,\text{fs}$ with a time step of $2\,\text{a.u.}$. All propagations are started by setting the first vibrational eigenfunction of the S_0 potential to the particular cationic potential, assuming delta-pulse ionization. All the quantum dynamical simulations are conducted with a program developed in-house.

Figure C.6 shows the change in population of the first four states $\tilde{X}$ ($^2E_{3/2}$, $^2E_{1/2}$), $\tilde{A}$ and $\tilde{B}$ over the $250\,\text{fs}$ of simulation time. The $\tilde{X}$ ($^2E_{3/2}$) state does not show any dissociation, and its SO split counterpart $\tilde{X}$ ($^2E_{1/2}$) only shows a marginal decrease in population of about $10\,\%$ within the simulation time. The $\tilde{A}$ state completely dissociates within about $60\,\text{fs}$. The population of the $\tilde{B}$ state shows a sharp decrease at $40\,\text{fs}$, but only to about $20\,\%$. Parts of the wave packet are reflected at the barrier in the region of the CoIn visible in Figure C.4, resulting in the further stepwise decrease over the subsequent simulation time.
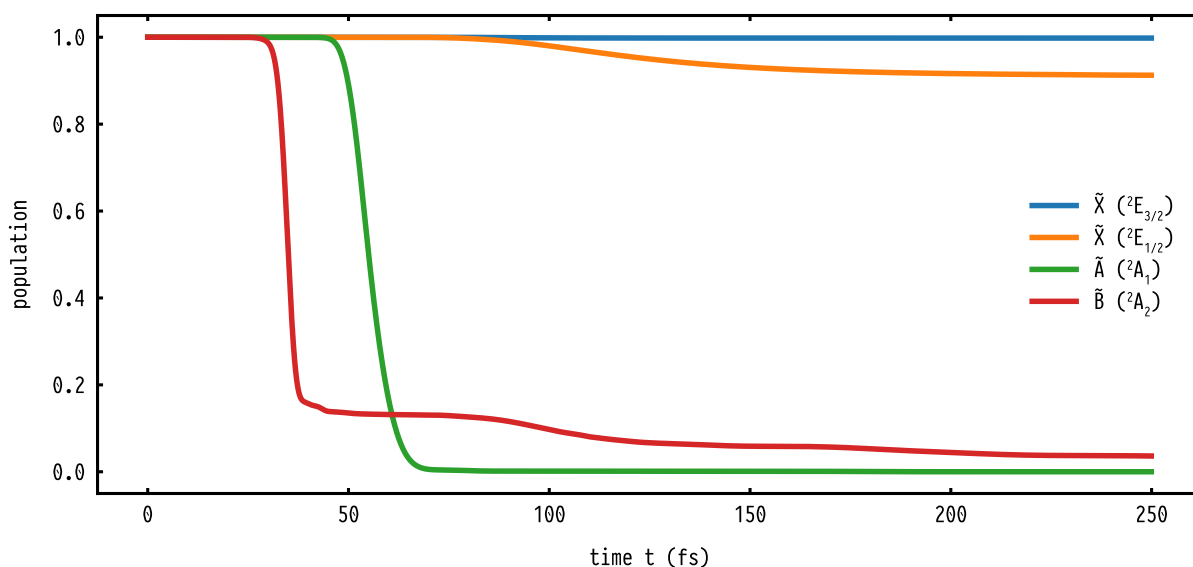

Figure C.6 – Population of the first four states of the CF_3I^+ cation for the $250\,\text{fs}$ of simulation time.

Supporting Information of the Presented Publications

In the following sections, the supporting information of the publications "Complete Mechanism of Hemithioindigo Motor Rotation", "A Prospective Ultrafast Hemithioindigo Molecular Motor" and "Ultrafast strong-field dissociation of vinyl bromide: an attosecond transient absorption spectroscopy and non-adiabatic molecular dynamics study" presented in the chapters 1 and 2 are reprinted.

D.1 Supporting Information for "The Complete Mechanism of the Hemithioindigo Motor Rotation"

In the following, the chapter "Quantum Mechanical calculations" (pages 33–35) of the supporting information for the publication "Complete Mechanism of Hemithioindigo Motor Rotation" published in the *Journal of the American Chemical Society* is reprinted with permission from *J. Am. Chem. Soc.* **140**, 15, 5311–5318 (2018). Copyright 2018 American Chemical Society. It details the quantum mechanical calculations performed for the publication. In particular, all orbitals of the AS utilized in the CASSCF calculations are shown. Also, the relative ground and excited states energies and geometric coordinates of important points on the unidirectional rotation pathway are listed. Lastly the results (excited state electronic character, vertical excitation energy and oscillator strength) of the benchmark calculations rationalizing the chosen AS are summarized. The optimized geometries of all the relevant points, as well as detailed information on the experimental setup for the transient absorption measurements and their evaluation, can be found in the complete SI, accessible at: https://pubs.acs.org/doi/abs/10.1021/jacs.8b02349.

Quantum Mechanical calculations
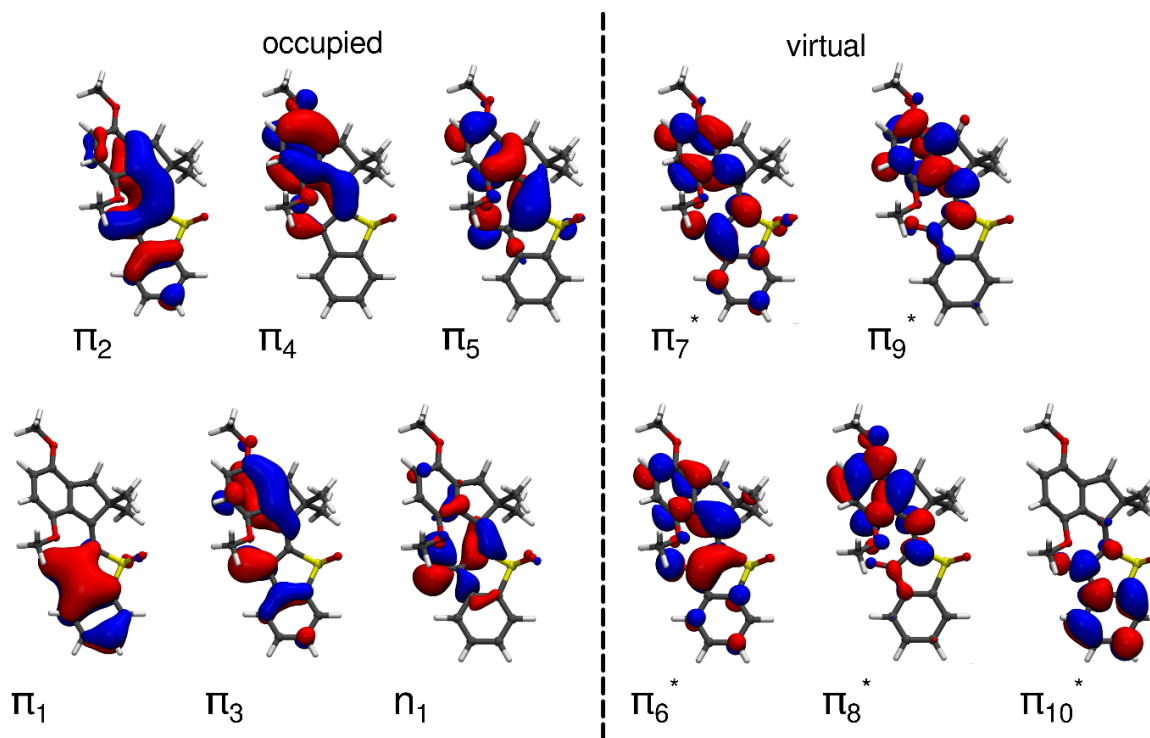
Active space for motor **1**

Figure S25:   The (12,11) active space of motor-**1**. The orbitals are shown for the *E*-(*S*)-(*P*) isomer (**A-1**) with an isovalue of 0.02, ordered from left to right with increasing energy.

Theoretical description of the excited state pathways shown in Figure 2

Table S1: Relative ground/excited state energies with respect to the FC_{A-1} point for path ways ①, ② and FC_{C-1} for ③, ④ at CASSCF(12/11)/6-31G* state average over five singlet and three triplet states (SA S5T3) level and important coordinates for all points of relevance for the four pathways depicted in Figure 2 in the manuscript.

path	structure	ΔS_0 (eV)	ΔS_1 (eV)	ΔS_2 (eV)	ΔS_3 (eV)	ΔS_4 (eV)	ΔT_1 (eV)	ΔT_2 (eV)	ΔT_3 (eV)	C=C[a] (Å)	Torsion[b] (°)
①	FC_{A-1}	0.00	3.83	5.40	5.94	6.35	3.16	3.66	4.39	1.35	16.3
	S_1 Min1	1.70	2.81	4.63	5.50	5.70	2.27	2.78	5.02	1.47	55.3
	TS2 int.pol.	2.27	3.07	4.86	5.53	5.85	2.41	3.04	5.32	1.47	75.7
	S_2/S_1 CoIn1[c]	1.93	3.08	3.93	5.14	5.39	1.91	3.05	5.12	1.45	90.7
	S_1 Min2	2.19	2.85	4.69	5.12	5.63	2.17	2.83	5.12	1.47	91.1
	FC_{B-1}	0.10	4.04	5.72	6.34	6.55	3.42	3.84	4.50	1.35	175.7
②	FC_{A-1}	0.00	3.83	5.40	5.94	6.35	3.16	3.66	4.39	1.35	16.3
	S_1 Min1	1.70	2.81	4.63	5.50	5.70	2.27	2.78	5.02	1.47	55.3
	TS1 int.pol.	1.48	3.00	5.03	5.74	5.96	2.69	2.95	4.96	1.44	37.5
	S_1/T_2 ISC	0.91	2.81	5.19	5.48	6.04	2.69	2.77	4.56	1.41	19.8
	T_2/T_1 CoIn	0.79	2.84	5.25	5.44	6.01	2.73	2.74	4.47	1.41	23.7
	T_1 Min1	1.63	3.56	4.21	5.00	5.58	1.61	3.66	4.98	1.46	86.7
	T_1/S_0 ISC	1.61	3.57	4.26	4.84	5.59	1.60	3.70	4.81	1.46	82.2
③	FC_{C-1}	0.00	3.82	5.57	6.02	6.37	3.17	3.64	4.42	1.35	189.0
	S_1 Min3	2.16	2.83	4.67	5.17	5.60	2.16	2.81	5.10	1.47	269.0
	S_2/S_1 Coin2[c]	1.90	3.07	3.93	5.13	5.34	1.88	3.04	5.10	1.45	277.4
	FC_{D-1}	0.14	4.03	5.63	6.22	6.55	3.44	3.83	4.58	1.35	348.4
④	FC_{C-1}	0.00	3.82	5.57	6.02	6.37	3.17	3.64	4.42	1.35	189.0
	S_1/T_1 ISC	0.99	2.85	5.23	5.50	6.13	2.77	2.79	4.62	1.41	195.8
	T_1 Min2	1.87	3.71	4.36	5.21	5.61	1.83	3.80	5.19	1.46	279.1
	T_1/S_0 ISC2	1.61	3.55	4.24	4.99	5.58	1.61	3.66	4.96	1.46	271.4

[a] Central CC double bond linking the stilbene and thioindigo part.
[b] Dihedral angle of the central CC double bond as depicted in Figure 2 in the manuscript.
[c] For both conical intersections the mean value of ΔS_1 and ΔS_2 was used in Figure 2. The splitting in the energy values stems from the different number of states used in the calculations for the geometry optimization and for the here presented data. E.g. for S_2/S_1 CoIn1 the energy splitting with the same number of states as in the optimization (CASSCF(12/11) /6-31G* SA S3) was only 0.0023 eV.

Vertical excitation energies at different levels of theory

For the three levels of theory scrutinized in this work, the character as well as the order of states did not change. Upon irradiation with 460 nm (2.80 eV, see experimental part) the S_1 state which is of $n_1p_6^*$ character, is populated. Although the oscillator strength is quite small it is still nonzero and there is simply not enough energy to reach the other bright states (see Table S2).

Table S2: Excited state electronic character, vertical excitation energy ΔE and oscillator strength f at the FC points of the **A-1** and **C-1** isomer. The approximated maxima (Max) of the corresponding electronic spectra depicted in Figure 1 in the manuscript are also given.

			CASSCF[a]		CCSD[b]		TDDFT[c]		Max
			ΔE	f	ΔE	f	ΔE	f	ΔE
		character	**(eV)**	(a.u.)	(eV)	(a.u.)	(eV)	(a.u.)	(eV)
A-1	S_1	$n_1\pi_6^*$	3.83	0.001	3.55	0.029	3.37	0.056	2.88
	S_2	$\pi_4\pi_6^*$	5.40	0.148	3.89	0.114	3.64	0.093	3.64
	S_3	$\pi_5\pi_6^*$	5.94	0.507	4.34	0.148	4.07	0.159	-
	T_1	$\pi_5\pi_6^*$	3.16	-	-	-	2.39	-	-
	T_2	$n_1\pi_6^*$	3.66	-	-	-	3.05	-	-
C-1	S_1	$n_1\pi_6^*$	3.82	0.0002	3.58	0.011	3.40	0.023	3.10
	S_2	$\pi_4\pi_6^*$	5.57	0.061	3.94	0.159	3.71	0.182	3.44
	S_3	$\pi_5\pi_6^*$	6.02	0.756	4.13	0.129	3.88	0.094	-
	T_1	$\pi_5\pi_6^*$	3.17	-	-	-	2.36	-	-
	T_2	$n_1\pi_6^*$	3.64	-	-	-	3.03	-	-

[a] CASSCF(12/11)/6-31G* state average over five singlet and three triplet states (SA S5T3) level of theory.

[b] EOM-CCSD/6-31G* with five singlet states.

[c] TDDFT CAM-B3LYP/6-31G* with five singlet and five triplet states.

D.2 Supporting Information for "A Prospective Ultrafast Hemi-thioindigo Molecular Motor"

Here, the chapter "Excited state calculations" (pages 43–45) of the supporting information from the article "A Prospective Ultrafast Hemithioindigo Molecular Motor" published in *ChemPhotoChem* is reprinted with permission from *ChemPhotoChem* **3**, 6, 365–371 (2019). Copyright 2019 John Wiley and Sons. The complete AS utilized in the CASSCF calculations, as well as all relative ground and excited state energies of the important points on the excited state reaction pathways are shown. Further, the results (excited state electronic character, vertical excitation energy and oscillator strength) of the benchmark calculations rationalizing the chosen AS are summarized. For all optimized structures and for detailed information on the synthesis and the physical and photophysical properties of the HTI molecular motor, refer to the complete supporting information available at: https://doi.org/10.1002/cptc.201900074.

Excited state calculations

The benchmark calculations for the active space are carried out at the TDDFT level of theory with the Gaussian09 Revision A.02 program package[6] using the CAM-B3LYP functional and the 6-31G(d) basis set. All complete active space SCF (CASSCF) calculations were done with the MOLPRO 2015 program package[8-9] again using the 6-31G(d) basis set. The used active space depicted in Fig. SI 39, includes the central CC double bond (π_5), the CO double bond (π_2), two sets of bonding and antibonding orbitals on the stilbene fragment (π_3, π_4) and one set on the thioindigo fragment (π_1) as well as the oxygen lone-pair (n_1) of the CO double bond.

Active space for HTI 1

π_2 π_4 π_5 π_7^* π_9^*

π_1 π_3 n_1 π_6^* π_8^* π_{10}^*
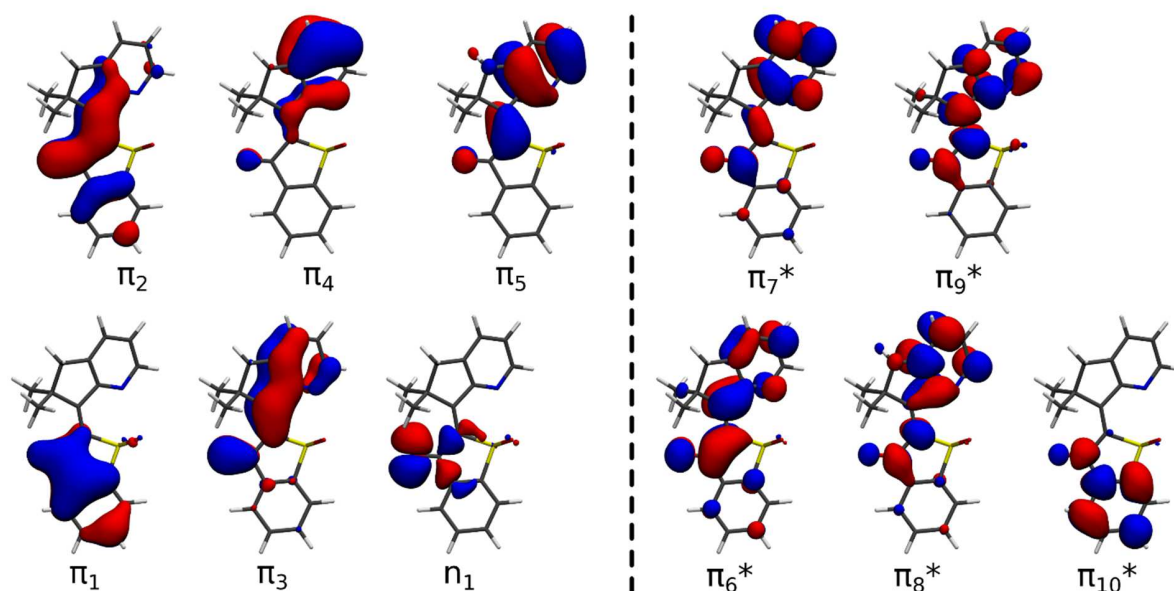
Figure SI 39   The (12,11) active space of HTI **1**. The orbitals are shown for the *Z*-(*S*)-(*P*) isomer (**A-1**) with an isovalue of 0.02, ordered from left to right with increasing energy.

Theoretical description of the excited state pathways shown in Figure 2

Table SI 5 Relative ground/excited state energies with respect to the FC$_{A-1}$ point for path way ①, and FC$_{C-1}$ for ② at CASSCF(12/11)/6-31G(d) state average over four singlet states (SA S4) level of theory and important coordinates for all points of relevance for the two pathways depicted in Figure 2 in the manuscript.

path	structure	ΔS_0 [eV]	ΔS_1 [eV]	ΔS_2 [eV]	ΔS_3 [eV]	C=C[a] [Å]	Torsional[b] [°]
①	FC$_{A-1}$	0.00	3.86	5.67	6.09	1.36	190.8
	S$_1$ Min1	0.82	2.62	4.95	5.22	1.42	196.5
	TS1 interpol.	1.96	3.12	4.75	5.70	1.45	243.7
	S$_1$ Min2	2.24	2.95	4.48	5.16	1.47	275.2
	S$_2$/S$_1$ CoIn1	2.10	3.72	3.73	5.33	1.44	276.0
	FC$_{B-1}$	0.20	3.91	5.89	6.26	1.35	345.7
②	FC$_{C-1}$	0.00	3.72	5.72	5.41	1.35	13.8
	S$_1$ Min 3	0.97	2.60	5.17	5.41	1.41	7.8
	TS2 interpol.	2.36	3.13	4.67	5.37	1.46	84.0
	S$_1$ Min 4	2.30	3.02	4.55	5.23	1.47	92.5
	S$_2$/S$_1$ Coin2	2.17	3.69	3.69	5.62	1.45	84.3
	FC$_{A-1}$	-0.06	3.80	5.62	6.03	1.36	190.8
	FC$_{B-1}$	0.14	3.85	5.84	6.21	1.35	345.7

[a] Central CC double bond linking the stilbene and thioindigo part.

[b] Dihedral angle of the central CC double bond as depicted in Figure 2 in the manuscript.

Vertical excitation energies at different levels of theory

For the two levels of theory scrutinized in this work, the character as well as the order of states did not change. Upon irradiation with 450 nm (2.80 eV, see experimental part) the S_1 state which is of $n_1\pi_6^*$ character, is populated. Although the oscillator strength is quite small it is still nonzero and there is simply not enough energy to reach the other bright states (see Table S6).

Table SI 6 Excited state electronic character, vertical excitation energy ΔE and oscillator strength f at the FC points of the **A-1** and **C-1** isomer of HTI **1**. The approximated maxima (Max) of the corresponding electronic spectra depicted in Figure 1 in the manuscript are also given.

			CASSCF[a]		TDDFT[b]		Max
			ΔE [eV]	f [a.u.]	ΔE [eV]	f [a.u.]	ΔE [eV]
		character					
A-1	S_1	$n_1\pi_6^*$	3.85	0.0001	3.11	0.009	2.82
	S_2	$\pi_5\pi_6^*$	5.67	0.334	3.71	0.050	3.54
	S_3	$\pi_4\pi_6^*$	6.09	0.268	4.02	0.514	-
C-1	S_1	$n_1\pi_6^*$	3.72	0.0001	3.28	0.005	3.02
	S_2	$\pi_5\pi_6^*$	5.72	0.241	4.02	0.242	3.65
	S_3	$\pi_4\pi_6^*$	6.20	0.017	4.21	0.013	-

[a] CASSCF(12/11)/6-31G(d) state average over four singlet states (SA S4) level of theory.

[b] TDDFT CAM-B3LYP/6-31G(d) with ten singlet states.

D.3 Supporting Information for "The Ultrafast Strong-Field Dissociation of Vinyl Bromide"

In the following, the supporting information for the article "Ultrafast strong-field dissociation of vinyl bromide: an attosecond transient absorption spectroscopy and non-adiabatic molecular dynamics study" published in *Structural Dynamics* under the terms of the Creative Commons Attribution 4.0 International License (CC BY 4.0, URL: https://creativecommons.org/licenses/by/4.0/) is reprinted. It contains the post-processing protocol and evaluation of the recorded datasets from the ATAS experiment. Also, the optimized geometries of the ground state minimum S_0, the excited state minima D_{1-3} and the minimum energy conical intersection between the D_3 and D_4 states are listed. Further, the computational details including the validation of the level of theory as well as the modified basis set utilized in the NAMD simulation are presented. Also, a comprehensive flowchart summarizing the complete procedure for the simulation of the XAS spectra is shown. To aid the analysis of the calculated trajectories as well as the experimental transient absorption spectrum, all excited state population, along with the temporal evolution of the C–C bond and the C=Br double bond for both neutral and cationic vinyl bromide and their resulting transient absorption spectra, are shown. The modified basis set is provided in the OPENMOLCAS and MOLPRO format and can be downloaded at: https://www.scitation.org/doi/suppl/10.1063/4.0000102.

Supplemental Material: Ultrafast strong-field dissociation of vinyl bromide: an attosecond transient absorption spectroscopy and non-adiabatic molecular dynamics study

Florian Rott,[1, a)] Maurizio Reduzzi,[2, a)] Thomas Schnappinger,[1] Yuki Kobayashi,[2] Kristina F. Chang,[2] Henry Timmers,[2] Daniel M. Neumark,[2, 3] Regina de Vivie-Riedle,[1, b)] and Stephen R. Leone[2, 3, 4, b)]

[1)]*Department of Chemistry, LMU Munich, 81377 Munich, Germany*

[2)]*Department of Chemistry, University of California, Berkeley, CA 94720, USA*

[3)]*Chemical Sciences Division, Lawrence Berkeley National Laboratory, CA 94720, USA*

[4)]*Department of Physics, University of California, Berkeley, CA 94720, USA*

(Dated: 25 May 2021)

[a)]These authors contributed equally to this work

[b)]Authors to whom correspondence should be addressed: regina.de_vivie@cup.uni-muenchen.de, srl@berkeley.edu

CONTENTS

I.   EXPERIMENTAL DETAILS

A.   Post-processing of the Experimental Data

The transient absorption spectrum is averaged over 150 frames, in order to improve statistics. Furthermore, the raw experimental data have been processed with a low-pass Gaussian filter with a standard deviation of 1.6 fs in the time axis and 20 meV in the energy axis. The procedure allows to filter out high frequency noise fluctuations due to the residual intensity noise of the light source. Both in the time and energy axis, the procedure is very unlikely to mask relevant information: in the time axis, because the selected standard deviation is smaller than the step size used (2.3 fs); in the energy axis, because it is smaller than the spectral resolution provided by the spectrograph ($E/dE = 1000$, translating into a resolution of 70 meV at 70 eV). Raw and post-processed transient absorption traces are shown in FIG. S1 and FIG. S2, respectively. The calculations performed in I B, the results of which are reported in the main text, have been performed on the post-processed data.
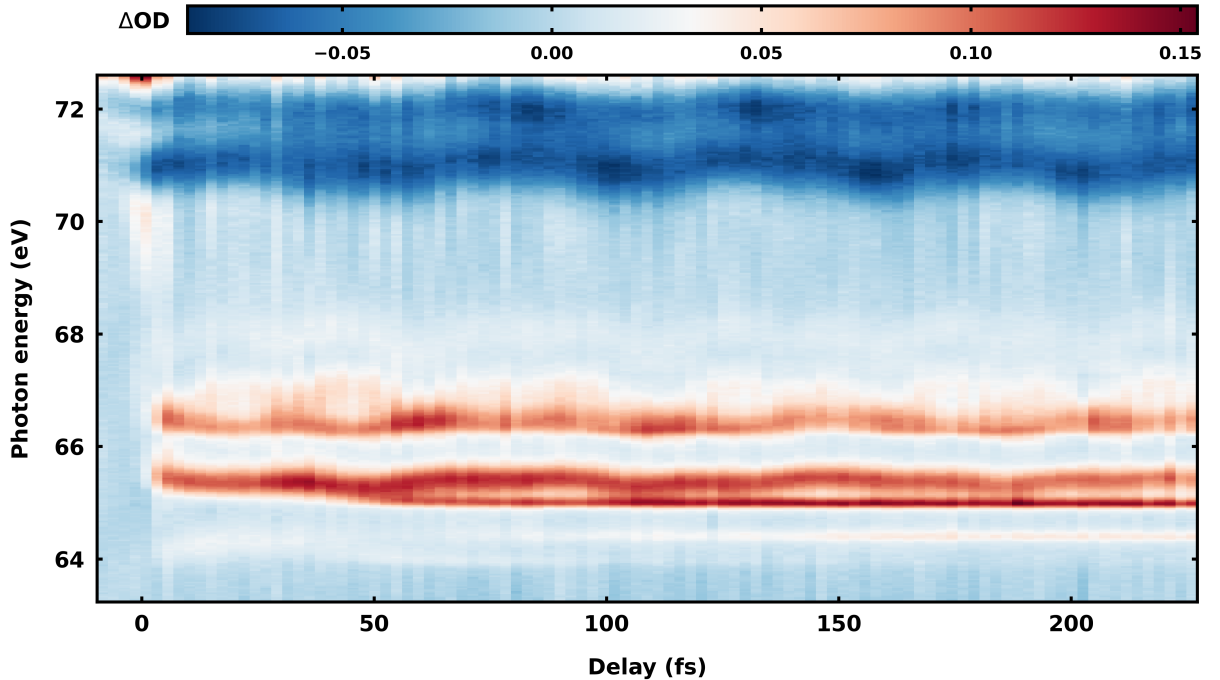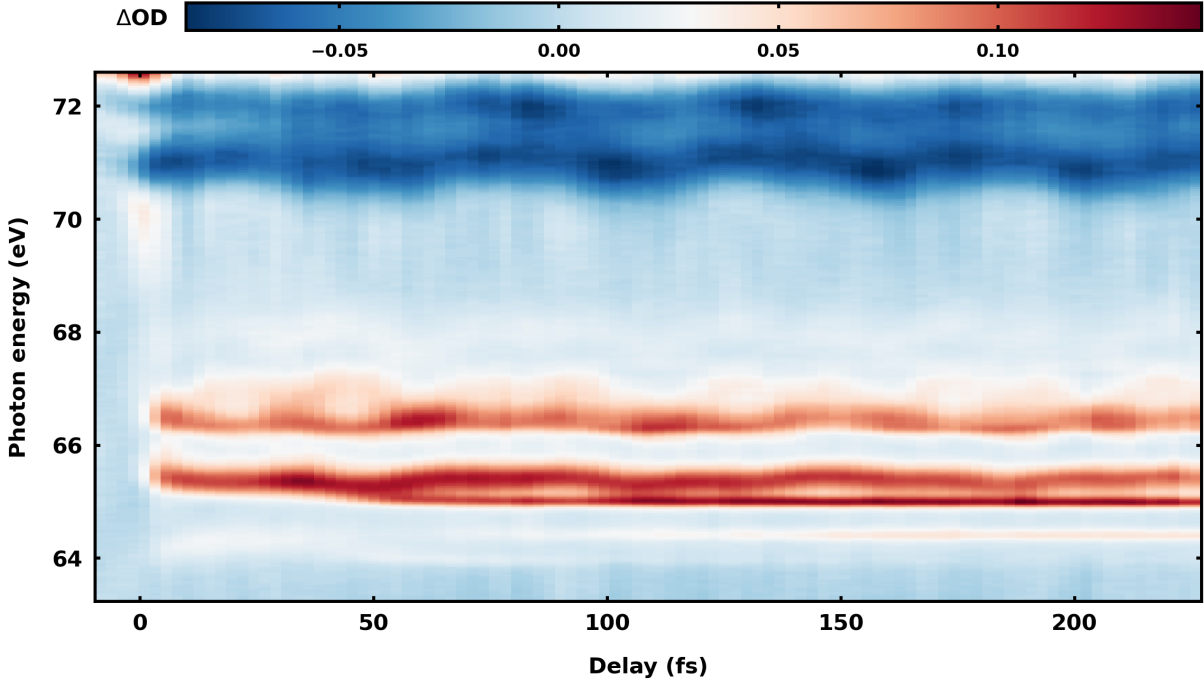

FIG. S1. Raw experimental ATAS trace.

3

FIG. S2. Post-processed experimental ATAS trace.

B. Vibrational Dynamics

The vibrational dynamics of the neutral ground state of vinyl bromide, as well as the first excited cationic state D_2 can be experimentally evaluated by computing the spectral first moment (i.e. center of mass) of the ATAS trace in the windows of interest. The experimental points have been fitted with a single cosinusoidal function for the ground state and the sum of two cosinusoidals for the D_2 state:

$$cm_{gr}(t) = A_{gr_0} + B_{gr_1}cos(2\pi\nu_{CBr_{gr}}t + \phi_{CBr_{gr}}) \tag{S1}$$

$$cm_{D2}(t) = A_{D2_0} + B_{D2_1}cos(2\pi\nu_{CBr_{D2}}t + \phi_{CBr_{D2}}) + C_{D2_2}cos(2\pi\nu_{CC_{D2}}t + \phi_{CC_{D2}}). \tag{S2}$$

The results are shown in FIG. S3 and FIG. S4, for the ground state and the D_2 state, respectively. The results of the fit yield

$$\nu_{CBr_{gr}} = 635\,\text{cm}^{-1}, \ \phi_{CBr_{gr}} = -\pi,$$

$$\nu_{CBr_{D2}} = 480\,\text{cm}^{-1}, \ \phi_{CBr_{D2}} = -0.5\pi,$$

$$\nu_{CC_{D2}} = 1220\,\text{cm}^{-1} \text{ and } \phi_{CC_{D2}} = -0.7\pi.$$

4

The extracted value for $\nu_{CBr_{gr}}$ is in good agreement with the calculated value for ν_3, while $\nu_{CBr_{D2}}$ and $\nu_{CC_{D2}}$ are in good agreement with the calculated values for ν_3 and ν_7, respectively (see TABLE S7).
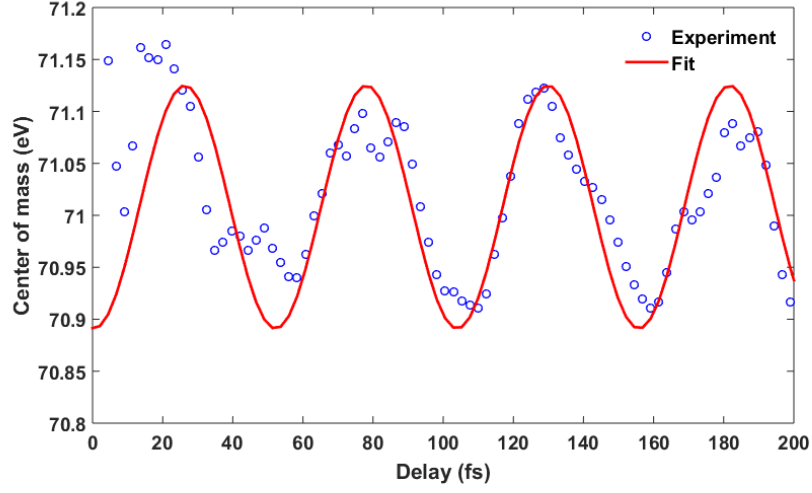

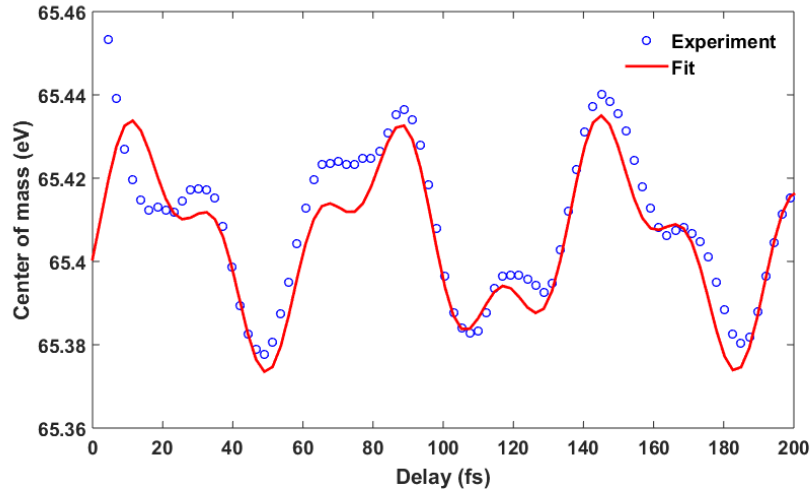FIG. S3. Experimental center of mass of the ATAS trace in the range $70.3\,\text{eV}$ to $71.5\,\text{eV}$ (blue circles) and its fit (red line).

FIG. S4. Experimental center of mass of the ATAS trace in the range $65.2\,\text{eV}$ to $65.7\,\text{eV}$ (blue circles) and its fit (red line).

5

II. COMPUTATIONAL DETAILS

A. Geometry of the Optimized Minimum

The minimum geometry of vinyl bromide was optimized with MOLPRO2012.1[S1,S2] at the closed-shell coupled-cluster level of theory, including singles, double and perturbative contributions of triples using the aug-cc-pVTZ basis set[S3–S7] (CCSD(T)/aug-cc-pVTZ). TABLE S1 shows the xyz coordinates of the optimized geometry.

TABLE S1. Geometry of the CCSD(T)/aug-cc-pVTZ optimized ground state minimum.

Number	Element	x [Å]	y [Å]	z [Å]
1	C	0.000 000	0.000 000	0.000 000
2	C	0.000 000	0.000 000	1.332 924
3	H	0.000 000	0.916 808	−0.574 890
4	H	−0.003 204	−0.944 947	−0.530 277
5	H	−0.001 234	−0.895 278	1.938 618
6	Br	0.003 811	1.593 998	2.361 016

B. Validation of the Level of Theory

In order to describe the electronic states sufficiently within the context of the dynamical simulations, we performed benchmark calculations at different levels of theory with the following computational setup. For the closed-shell coupled-cluster calculations, including singles, doubles (CCSD)[S8], we treated seven excited states within the equation-of-motion (EOM)[S9] approach. For the CASSCF and CASPT2 calculations we included five states in the state-averaging procedure. An active space (AS) including eight electrons in six orbitals (AS(8,6)) (see FIG. S6) was employed. It includes the carbon-carbon double bond (π_1, π_3^*), the carbon-bromine single bond (σ_1, σ_2^*) as well as both remaining bromine $4p$ orbitals. One is part of a second π orbital (π_2) the other one is the lone-pair n_1. In case of the m-ATZP basis set one additional virtual orbital (π_4^*) which has significant Rydberg contributions was added to stabilize the active space. Resulting in the AS shown in FIG. S7 with eight electrons in seven orbitals (AS(8,7)). The dynamic correlation was included perturbatively via the extended multi-state CASPT2 method (XMS-CASPT2)[S10], using an ionization-potential electron-affinity shift (IPEA)[S11] of 0.2 hartree. All calculations were performed using the

6

MOLPRO 2012.1 program package using the cc-pVTZ[S3–S7] basis set. TABLE S2 shows the character, the vertical excitation energy ΔE and the oscillator strength f of the first four singlet excited states.

In the literature[S12–S14] there are two bands described below 10 eV. A first small one at 5.70 eV is assigned to a $\pi \rightarrow \sigma^*$ transition, the second intense one at 6.50 eV to a bright $\pi \rightarrow \pi^*$ transition. Looking at the EOM-CCSD results, the first excited state S_1 is a weak $\pi_2 \rightarrow \sigma_2^*$ transition. The S_2 state is again a transition to the σ_2^* orbital but from the n_1 lone pair orbital of the bromine. It is located energetically close to the S_3 state, a bright $\pi_2 \rightarrow \pi_2^*$ transition with an oscillator strength of 0.2571 a.u.. For slightly higher energies you can find the S_4 state, a weak $n_1 \rightarrow \pi_3^*$ transition. For the result of the CASSCF(8,6) calculation, we see with the exception of the S_1 state, higher excitation energies. In general this is expected as the CASSCF method is known to overestimate excitation energies. But in this case the bright $\pi_2\pi_3^*$ state is described particularly poorly compared to the S_2 and S_3 states switching the order of the states and making it the highest excited state. Adding dynamic correlation with XMS-CASPT2 recovers the correct order of the excited states, as well as giving better excitation energies in general. But one has to keep in mind that XMS-CASPT2 is considerably more computationally expensive compared to CASSCF. But with the combination of the m-ATZP basis set and the slightly larger AS(8,7) we can archive a balanced description of all excited states, resulting in the same order of states. One has to mention that the excitation energies are about 1 eV higher compared to the experimental values. But as already mentioned this is a known drawback of the CASSCF method in general, and specifically in case of vinyl bromide, which was already reported in the literature by[S14].

As a second validation, we compared the gradient of the bright $\pi_2\pi_3^*$ state at the minimum geometry for the different levels of theory. FIG. S5 shows the most prominent components as color coded arrows. As the gradient components at the hydrogen atoms are quite small, they are not shown for sake of clarity. For the complete gradient vectors see Section II C. In general it can be noted that the vector at the C1 carbon atoms is described nearly identically at all levels of theory, slightly varying only in their absolute value. For both the high-level methods CCSD (green) and CASPT2 (red), this is also true for the rest of the shown vectors. But for the C2 carbon and the Br bromine atom, the direction of the vector significantly changes for the CASSCF/cc-pVTZ (blue) method. Again using the m-ATZP basis set

(magenta) one can recover sufficient description of the excited state gradient. In order to simulate the dissociation process of vinyl bromine a multi-reference method is needed. Since CASPT2 trajectories are not feasible, we are convinced that the CASSCF level of theory in conjunction with the m-ATZP basis set is adequate to describe the dynamics of vinyl bromide.

TABLE S2. Excited state electronic character, vertical excitation energy ΔE and oscillator strength f at the minimum geometry at different levels of theory. Also show are experimental values for the excitation energies of the bright states.

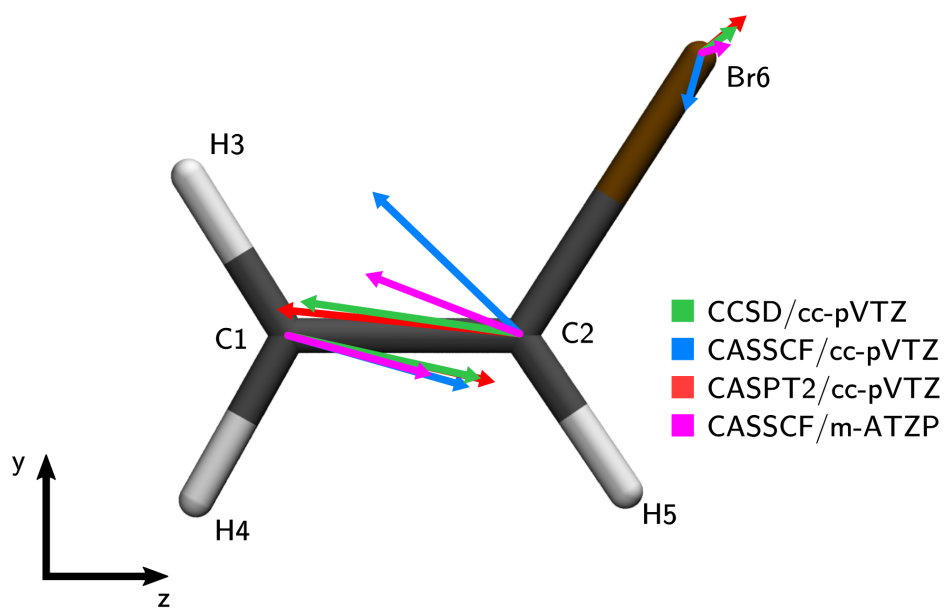|		character	ΔE [eV]	f [a.u.]
EOM-CCSD/cc-pVTZ	S_1	$\pi_2 \to \sigma_2^*$	6.62	0.0001
	S_2	$n_1 \to \sigma_2^*$	7.01	0.0033
	S_3	$\pi_2 \to \pi_3^*$	7.11	0.2571
	S_4	$n_1 \to \pi_3^*$	7.37	0.0002
CASSCF(8,6)/cc-pVTZ	S_1	$\pi_2 \to \sigma_2^*$	6.55	0.0045
	S_2	$n_1 \to \sigma_2^*$	7.38	0.0068
	S_3	$n_1 \to \pi_3^*$	7.74	0.0001
	S_4	$\pi_2 \to \pi_3^*$	7.80	0.2391
XMS-CASPT2(8,6)/cc-pVTZ	S_1	$\pi_2 \to \sigma_2^*$	6.12	–
	S_2	$\pi_2 \to \pi_3^*$	6.99	–
	S_3	$n_1 \to \sigma_2^*$	7.03	–
	S_4	$n_1 \to \pi_3^*$	7.20	–
CASSCF(8,7)/m-ATZP	S_1	$\pi_2 \to \sigma_2^*$	6.67	0.0041
	S_2	$\pi_2 \to \pi_3^*$	7.35	0.2797
	S_3	$n_1 \to \sigma_2^*$	7.50	0.0095
	S_4	$n_1 \to \pi_3^*$	7.77	0.0010
Exp./Lit.[S12,S13]	S_1	$\pi \to \sigma^*$	5.70	–
	S_2	$\pi \to \pi^*$	6.50	–

FIG. S5. Comparison between the gradients of the bright excited state ($\pi\pi^*$) at the CCSD(T)/aug-cc-pVTZ optimized ground state minimum geometry. The gradients are shown with color coded arrows corresponding to their level of theory. For sake of clarity only the vectors with a significant absolute value are shown.

9

C. Gradient Vectors for Different Level of Theories

We calculated the gradient vectors of the bright $\pi\pi^*$ state at the optimized ground state minimum geometry for different levels of theory. Tables S3 to S6 show the complete vectors for all atoms. FIG. S5 shows these gradients as color coded arrows overlaid on top of the vinyl bromide geometry.

TABLE S3. Gradient vectors of the bright $\pi\pi^*$ state for CCSD/cc-pVTZ level of theory.

Number	Element	x [Å]	y [Å]	z [Å]
1	C	$-0.000\,003$	$-0.011\,188$	$0.050\,582$
2	C	$-0.000\,017$	$0.008\,668$	$-0.057\,432$
3	H	$-0.000\,006$	$0.001\,265$	$0.000\,805$
4	H	$0.000\,000$	$-0.001\,270$	$-0.000\,763$
5	H	$0.000\,000$	$-0.004\,453$	$-0.002\,823$
6	Br	$0.000\,026$	$0.006\,977$	$0.009\,632$

TABLE S4. Gradient vectors of the bright $\pi\pi^*$ state for CASSCF(8,6)/cc-pVTZ level of theory

Number	Element	x [Å]	y [Å]	z [Å]
1	C	$-0.000\,023$	$-0.025\,389$	$0.089\,491$
2	C	$0.000\,176$	$0.069\,680$	$-0.072\,472$
3	H	$-0.000\,003$	$0.009\,221$	$-0.000\,821$
4	H	$-0.000\,031$	$-0.008\,831$	$-0.005\,179$
5	H	$-0.000\,043$	$-0.017\,210$	$-0.002\,998$
6	Br	$-0.000\,076$	$-0.027\,470$	$-0.008\,021$

10

TABLE S5. Gradient vectors of the bright $\pi\pi^*$ state for XMS-CASPT2(8,6)/cc-pVTZ level of theory

Number	Element	x [Å]	y [Å]	z [Å]
1	C	0.000 179	−0.022 850	0.101 923
2	C	−0.000 627	0.011 974	−0.119 615
3	H	−0.000 165	0.002 091	0.001 194
4	H	0.000 196	−0.001 523	−0.001 764
5	H	0.000 098	−0.007 732	−0.004 539
6	Br	0.000 319	0.018 040	0.022 801

TABLE S6. Gradient vectors of the bright $\pi\pi^*$ state for CASSCF(8,7)/m-ATZP level of theory

Number	Element	x [Å]	y [Å]	z [Å]
1	C	0.000 151	−0.019 516	0.071 072
2	C	−0.000 140	0.029 484	−0.076 147
3	H	−0.000 081	0.008 399	−0.001 738
4	H	−0.000 007	−0.007 988	−0.004 530
5	H	0.000 003	−0.013 027	0.000 420
6	Br	0.000 075	0.002 648	0.010 923

D. Modified ATZP Basis Set

The used m-ATZP basis set is based on the jorge-ATZP[S15,S16]. It was taken from the Basis Set Exchange (BSE)[S17–S19] and shrunken so its size lies between the ATZP and ADZP basis set. The basis set is provided in the Molpro (*basisset_molpro.txt*) as well as the OpenMolcas (*basisset_molcas.txt*) format.

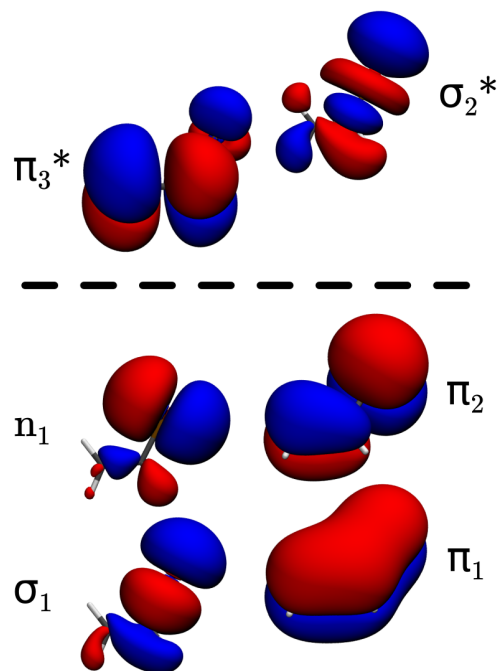**E.   Active Spaces for the Different Computational Setups**

FIG. S6. SA5-CASSCF molecular orbitals included in the active space AS(8/6) of vinyl bromine, obtained using the cc-pVTZ basis set at the CCSD(T)/aug-cc-pVTZ optimized ground state minimum geometry. The orbitals are rendered with an isovalue of 0.02.
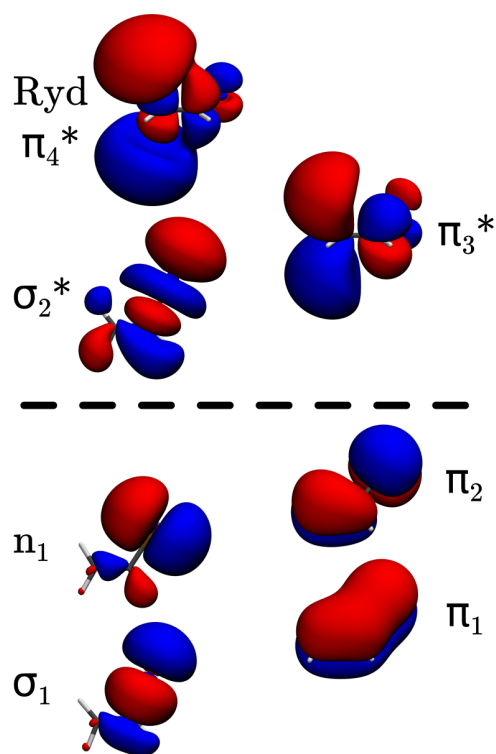
FIG. S7. SA5-CASSCF molecular orbitals included in the active space AS(8/7) of vinyl bromine, obtained using the m-ATZP basis set at the CCSD(T)/aug-cc-pVTZ optimized ground state minimum geometry. The orbitals are rendered with an isovalue of 0.02.

F.   Vibrational Frequencies of Vinyl Bromide

The vibrational frequencies of neutral and cationic vinyl bromide were calculated at the density functional theory (DFT) and time dependent DFT (TDDFT) level of theory using the Gaussian 16[S20] program package. All calculations where performed with the hybrid meta exchange-correlation functional M06-2X[S21] in conjunction with the aug-cc-pVTZ[S6,S7,S22] basis set.

TABLE S7. Vibrational frequencies of vinyl bromide at the S_0, D_1 and D_2 state minima.

Mode	Type/Description	Frequency [cm^{-1}]		
		S_0	D_1	D_2
ν_1	CCBr, bending	355	282	211
ν_2	CHHH, twisting	608	586	215
ν_3	C−Br, stretching	625	515	454
ν_4	CH$_2$, wagging	958	931	783
ν_5	CHHH, twisting	990	1034	992
ν_6	CCH, bending	1026	946	963
ν_7	CCH, bending	1288	1255	1252
ν_8	HCH, bending	1408	1425	1449
ν_9	C=C,stretching	1689	2017	14161
ν_{10}	C−H, sym. stretching	3175	3158	3121
ν_{11}	C−H, stretching	3245	3209	3174
ν_{12}	C−H, asym. stretching	3273	3268	3244

G.   XAS Procedure and Molcas Input Files

FIG. S8 presents a flowchart of the complete procedure for the simulation of the XAS spectra. Starting from the information of the NAMD simulation, at every time step t the vinyl bromide geometry defined by the nuclear coordinates $R(t)$ and the active state k can be extracted. Both quantities are used in the simulation of the XAS spectrum at each time step t. For the geometry $R(t)$ an initial HF/CASSCF calculation is performed and the obtained orbitals are used to set up two separate RASSCF/RASPT2 calculations for each multiplicity. The input for the calculations of the core excited states is show in LISTING S1 and for the valence excited states in LISTING S2. All four RASPT2 wave functions are then combined in one final RASSI calculation, see LISTING S3 for its input. As mentioned in the manuscript the four wave functions are not inevitably orthogonal. This can be addressed
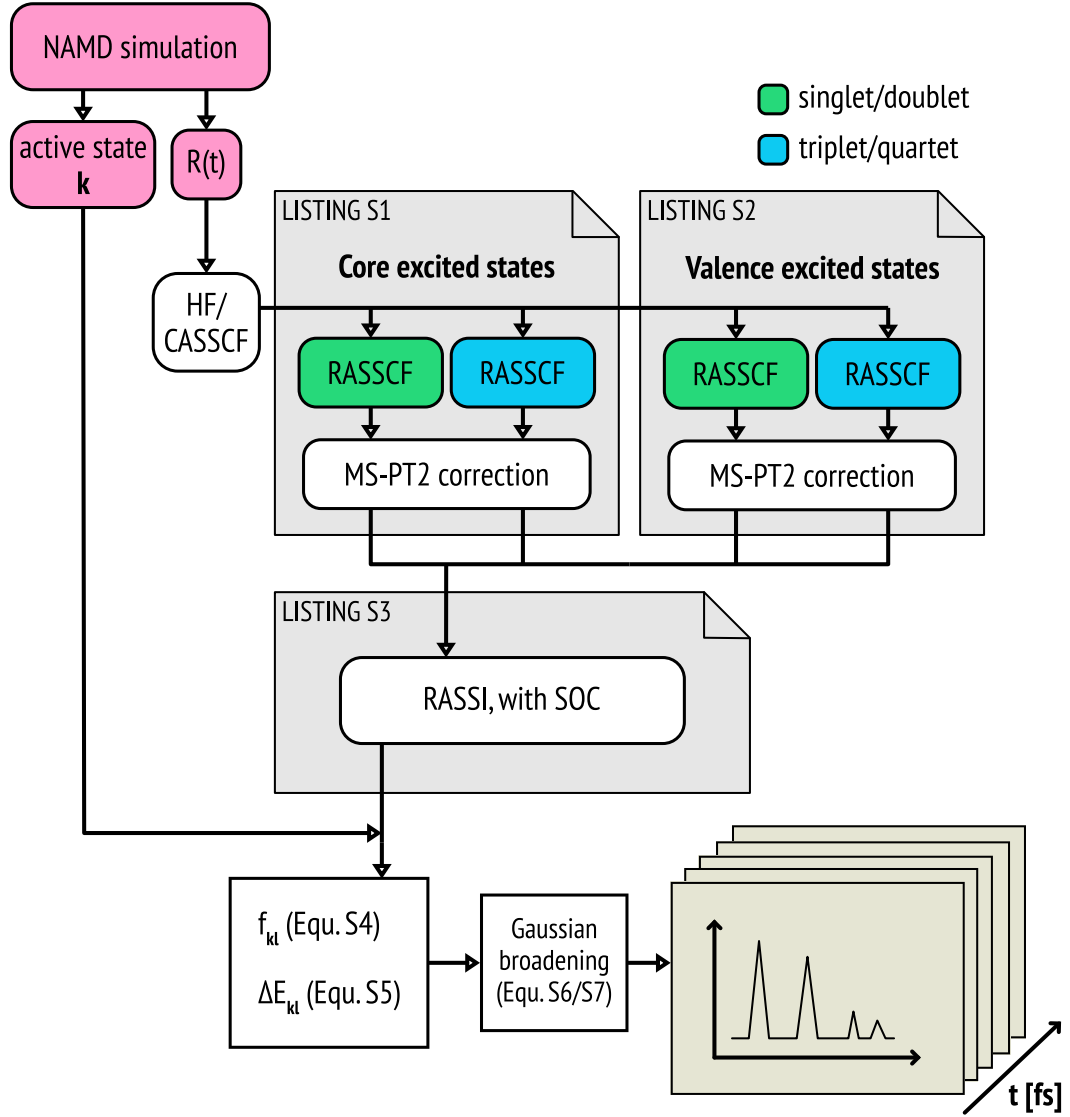
14

FIG. S8. Flowchart illustrating the complete procedure for the simulation of the XAS spectra.

by applying the following correction to the overall Hamiltonian[S23,S24]. The Hamilton matrix element H_{kl} is shifted by:

$$\Delta H_{kl} = \frac{1}{2}\big(\Delta E_k + \Delta E_l\big)S_{kl}, \tag{S3}$$

with ΔE_k and ΔE_l being, the energy shifts of the kth and lth RASSCF roots and S_{kl} the overlap matrix element. This can be achieved by using the the keyword HDIAG in the RASSI module. From this RASSI calculation two values, the oscillator strengths f_{kl} and the excitation energies ΔE_{kl} , are used in the simulation of the spectrum for the current time

15

step. Focusing on a specific core valence transition $k \to l$ the initial state k with the wave function $\psi_k(r; R(t))$ is the ground state or any other valence excited state. The final state l with $\psi_l(r; R(t))$ is a core excited state with a hole in the core space (RAS1 sub space). The oscillator strength f_{kl} for this transition is calculated by

$$f_{kl} = \frac{2}{3} \frac{m_e}{\hbar^2} (E_l - E_k) \sum_{x,y,z} \left\langle \psi_l(r; R(t)) \left| \hat{\mu}_{x,y,z} \right| \psi_k(r; R(t)) \right\rangle^2 \tag{S4}$$

with the electron mass m_e, the energy E of the states and $\hat{\mu}$ the dipole moment operator. The excitation energy is given by the difference

$$\Delta E_{kl} = E_k - E_l. \tag{S5}$$

To broaden the signal for the transition $k \to l$ a Gaussian function g_{kl} with the width σ is defined according to equation S6 using the the two quantities ΔE_{kl} and f_{kl}. In this work a width of $\sigma = 0.1\,\text{eV}$ is used.

$$g_{kl}(E) = f_{kl} \cdot \frac{1}{\sigma\sqrt{2\pi}} \cdot e^{-\frac{1}{2}\left(\frac{E - \Delta E_{kl}}{\sigma}\right)^2} \tag{S6}$$

The complete spectrum $g_k(E)$ for given initial state k is obtained by the summation over all relevant broaden signals $g_{kl}(E)$ and subsequent normalization.

$$g_k(E) = \frac{1}{N} \sum_l g_{kl}(E) \tag{S7}$$

For simulating the complete spectrum the $g_k(E)$ of each trajectory are summed up. Repeating this procedure for every time step t one arrives at the complete transient XAS shown in the manuscript.

LISTING S 1. RASSCF calculation for the core excited states. As the active space needs to be continuous, the core orbitals (23-27) are rotated to the end of the RAS2. Then using the HEXS keyword one hole is forced in the RAS1.

```
&GATEWAY
    Title= d_core
    Coord= geom.xyz
    Basis= ANO-RCC-VTZP
    ANGMOM
        0.0 0.0 0.0
    AMFI
    RICD

&SEWARD

&RASSCF
    FILEorb= cas_d.RasOrb
    ALTER= 5
    1 27 34
    1 26 33
    1 25 32
    1 24 31
    1 23 30
    SPIN= 2
    NACTEL= 27 0 0
    INACTIVE= 29
    RAS2= 10
    RAS1= 5
    HEXS
    1
    1
    CIROOT= 40 40 1
    CIONly

&CASPT2
    IPEAshift= 0.25
    IMAGinary= 0.2
    MULTistate
    ALL
```

17

LISTING S 2. RASSCF calculation for the valence excited states. As the active space needs to be continuous, the core orbitals (23-27) are rotated to the end of the RAS2.

```
&GATEWAY
    Title= d_vale
    Coord= geom.xyz
    Basis= ANO-RCC-VTZP
    ANGMOM
        0.0 0.0 0.0
    AMFI
    RICD

&SEWARD

&RASSCF
    FILEorb= cas_d.RasOrb
    ALTER= 5
    1 27 34
    1 26 33
    1 25 32
    1 24 31
    1 23 30
    SPIN= 2
    NACTEL= 27 0 0
    INACTIVE= 29
    RAS2= 10
    RAS1= 5
    CIROOT= 12 12 1
    CIONly

&CASPT2
    IPEAshift= 0.25
    IMAGinary= 0.2
    MULTistate
    ALL
```

18

LISTING S 3. RASSI calculation for the final oscillator strengths and vertical transition energies necessary to simulate a XAS spectrum.

```
&GATEWAY
    Title= xas
    Coord= geom.xyz
    Basis= ANO-RCC-VTZP
    ANGMOM
        0.0 0.0 0.0
    AMFI
    RICD

&SEWARD

>>> COPY raspt2_d_vale.JobMix JOB001
>>> COPY raspt2_d_core.JobMix JOB002
>>> COPY raspt2_q_vale.JobMix JOB003
>>> COPY raspt2_q_core.JobMix JOB004

&RASSI
    Nrofjobiphs= 4 12 40 12 40
    1 2 3 4 5 ... 12
    1 2 3 4 5 6 7 8 ... 40
    1 2 3 4 5 ... 12
    1 2 3 4 5 6 7 8 ... 40
    SPIN
    HDIAG
-7448.13807556
-7448.13750127
... <all MS-CASPT2 engergies>
```

19

III. DYNAMIC SIMULATIONS

Following the excited state population as well as the temporal evolution of the C=C bond and the C–Br bond for both the neutral (FIG. S9 and S10) as well as cationic (FIG. S11 - S17) vinyl bromide dynamics simulations are shown.

A. Neutral Dynamics
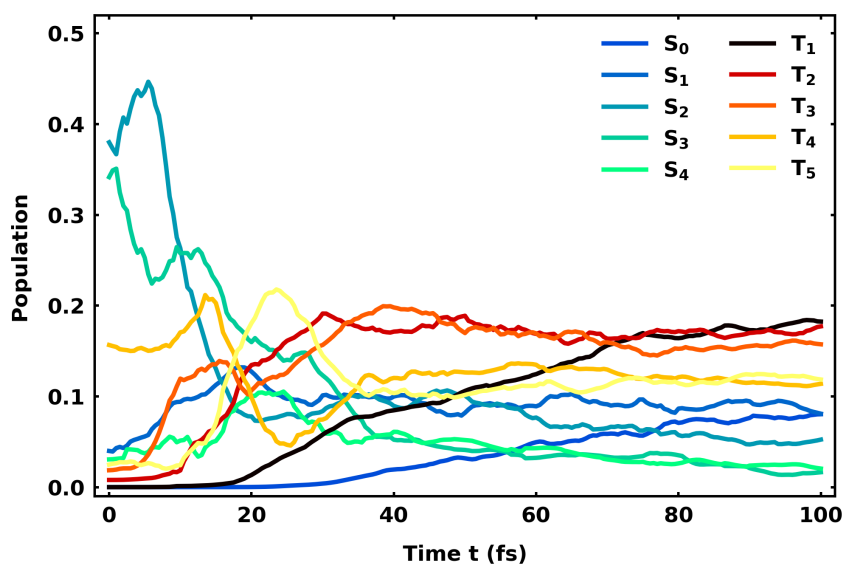
FIG. S9. Excited state population of neutral vinyl bromide based on all 189 analyzed trajectories for the 100 fs of simulation time.
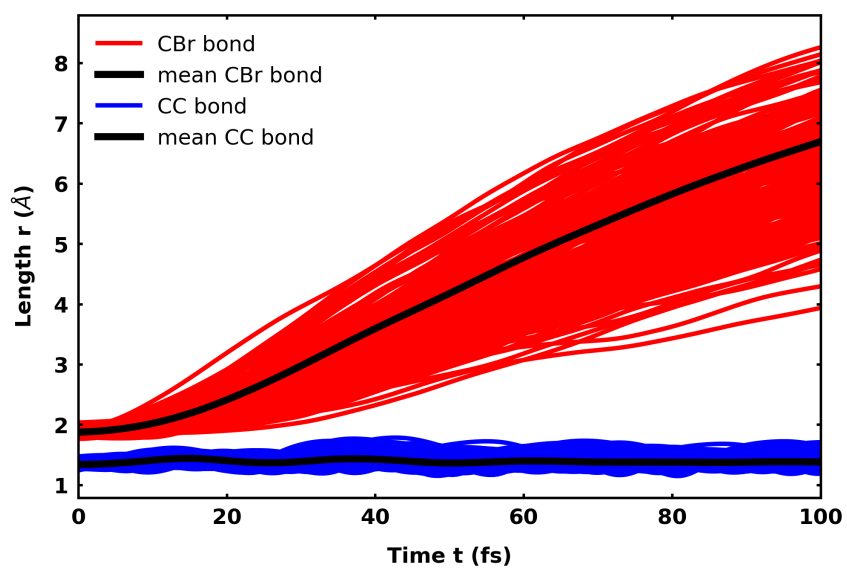
FIG. S10. Temporal evolution of the CC double bond and the CBr bond for the 189 analyzed trajectories of neutral vinyl bromide.

B. Cation Dynamics
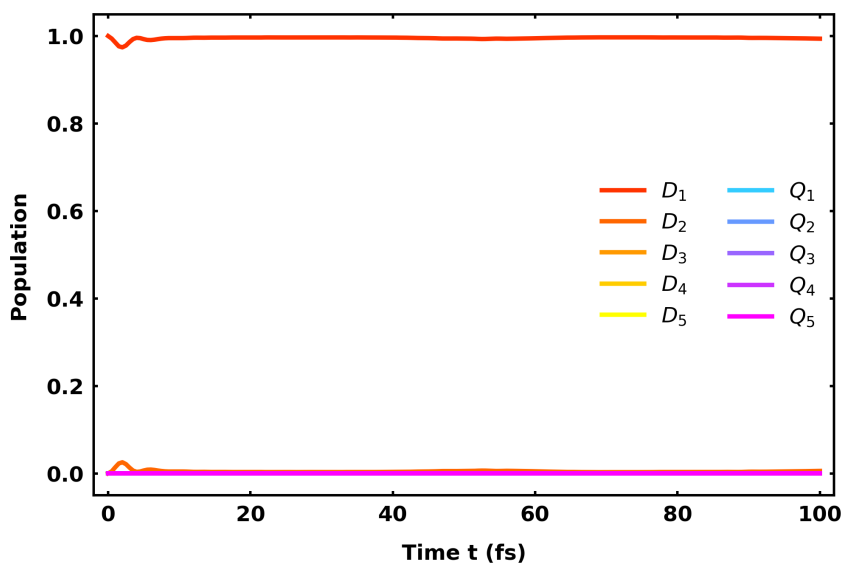
FIG. S11. Excited state population of cationic vinyl bromide based on the 11 analyzed trajectories starting in the D_1 state.
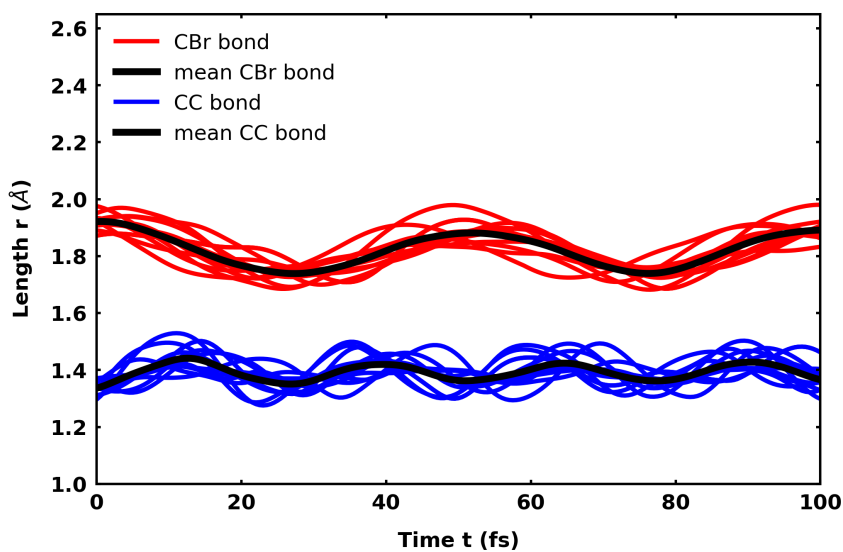
FIG. S12. Temporal evolution of the CC double bond and the CBr bond for the 11 analyzed trajectories that started in the D_1 stat of cationic vinyl bromide.
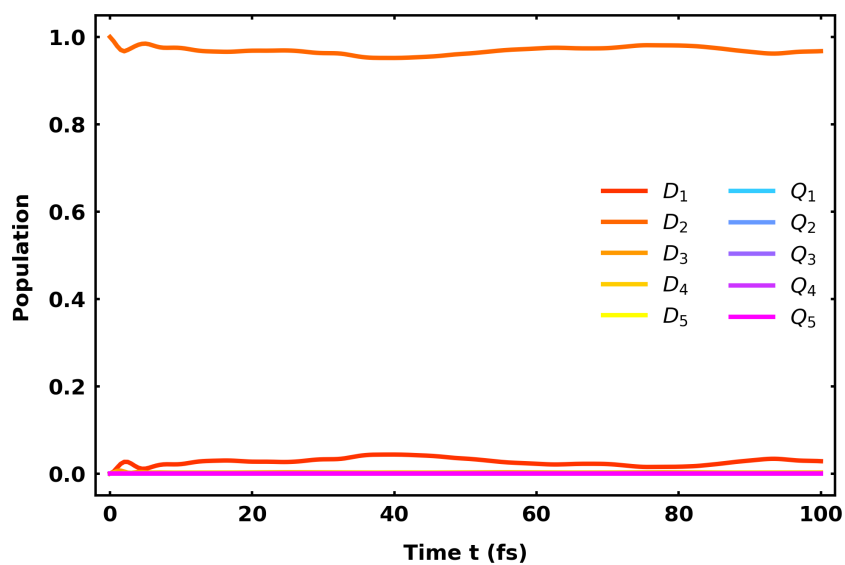
FIG. S13. Excited state population of cationic vinyl bromide based on the 26 analyzed trajectories starting in the D_2 state.
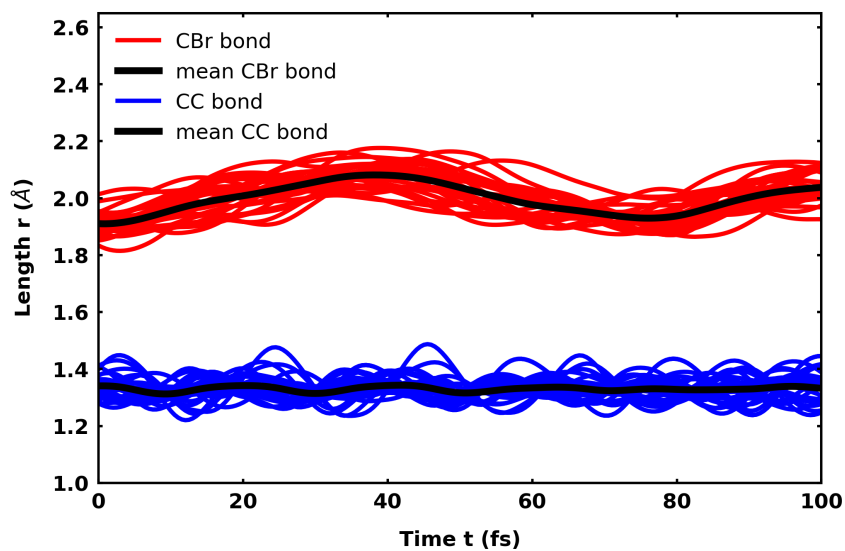

FIG. S14. Temporal evolution of the CC double bond and the CBr bond for the 26 analyzed trajectories that started in the D_2 stat of cationic vinyl bromide.
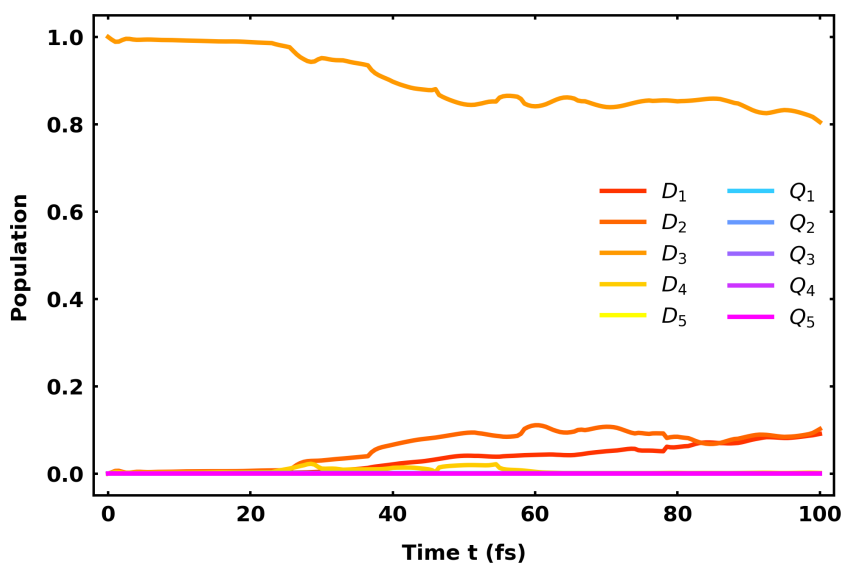
FIG. S15. Excited state population of cationic vinyl bromide based on all 45 analyzed trajectories starting in the D_3 state.
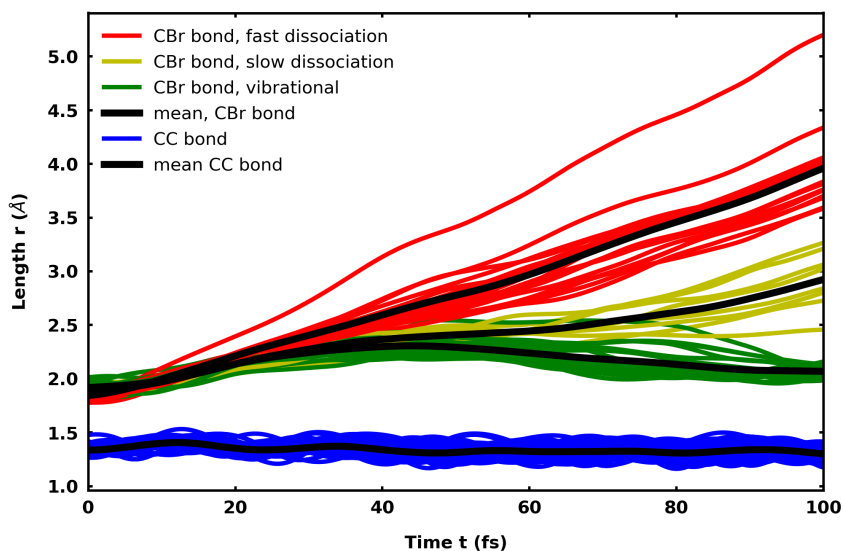

FIG. S16. Temporal evolution of the CC double bond and the CBr bond for the 45 analyzed trajectories that started in the D_3 stat of cationic vinyl bromide.
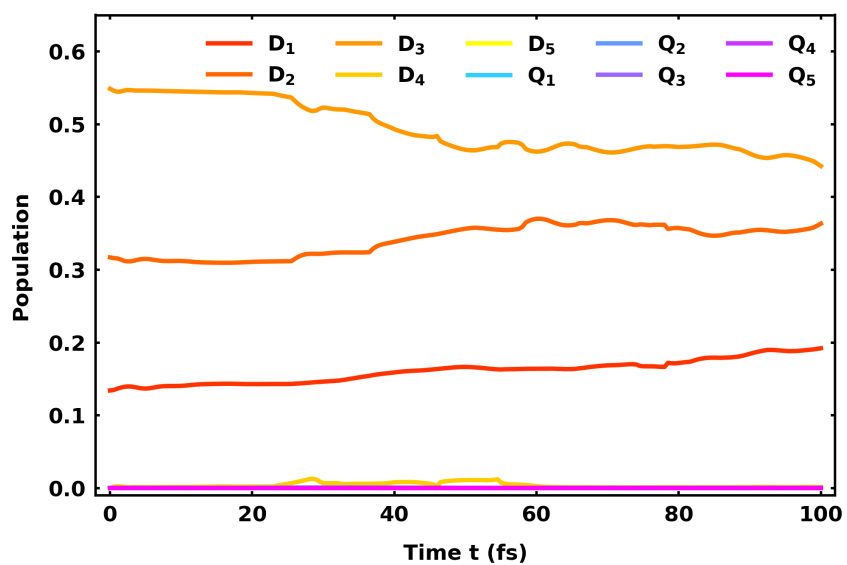
FIG. S17. Excited state population of cationic vinyl bromide based on all 82 analyzed trajectories for the 100 fs of simulation time.

IV.   SIMULATED TRANSIENT X-RAY ABSORPTION SPECTRA

In order to better visualize and analyze the contribution of the different cationic states D_1, D_2 and D_3 to the complete transient XAS (see FIG. S19) we also simulated the spectra only using the trajectories with each corresponding initial state (FIG. S21 - S23). In case of the trajectories starting from the D_3 state we also separated the XAS into the three different observed dynamics, fast dissociation (FIG. S26), slow dissociation (FIG. S25) and vibrational (FIG. S24). The underlying data sets for each of the XAS were normalized relative to just the corresponding data set and not the whole data set, as that was done for the complete XAS. For the convenience of the reader, we have also reprinted here the overall XAS for neutral and cationic vinyl bromide from the manuscript (see FIG. S18 and S19). For the cationic transient XAS we show additional overlays of the experimental spectra with the simulated ones at times $t = 0, 24, 48, 72, 99$ fs (see FIG. S20).

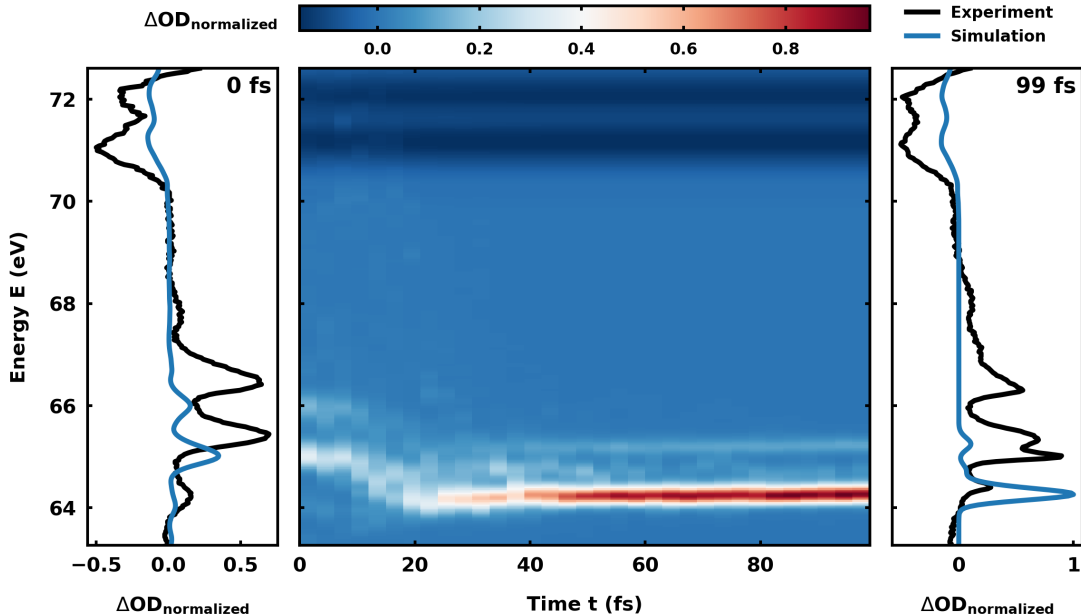### A.   Overall Spectra of Neutral and Cationic Vinyl Bromide

FIG. S18. Simulated transient XAS of the neutral trajectories starting in the bright $\pi\pi^*$ state. On the left and right the spectrum for time $t = 0$ fs and $t = 99$ fs, respectively, is shown in blue overlaid with the experimental transient absorption spectrogram in black at delays $d = 6.8$ fs and $d = 107.6$ fs.

FIG. S19. Simulated transient XAS of the cationic trajectories starting in the D_1, D_2 and D_3 states. On the left and right the spectrum for time $t = 0$ fs and $t = 99$ fs, respectively, is shown in blue overlaid with the experimental transient absorption spectrogram in black at delays $d = 6.8$ fs and $d = 107.6$ fs.
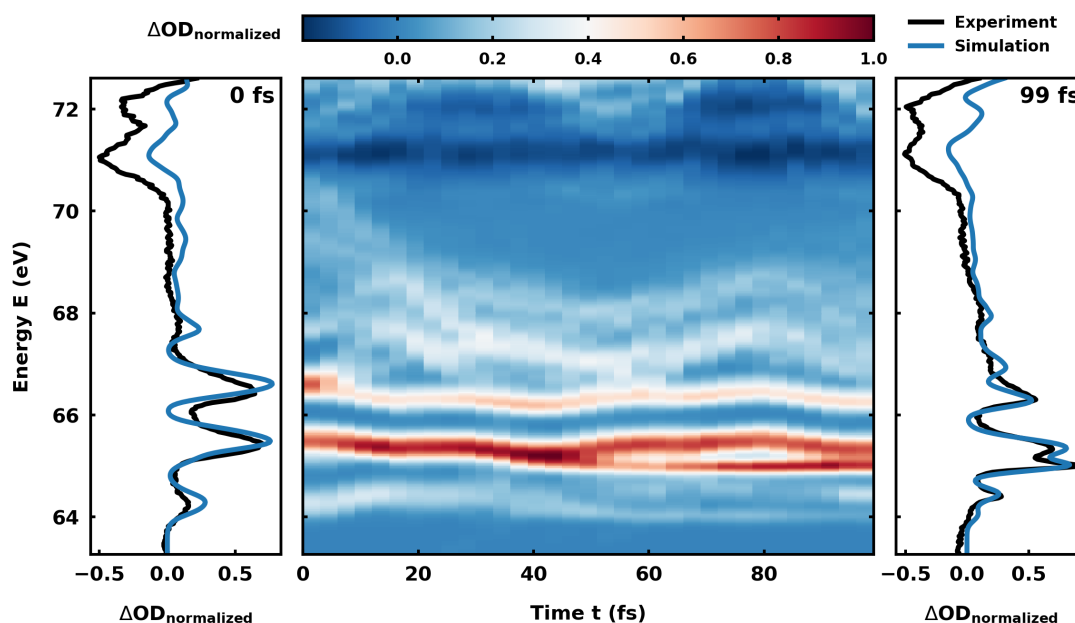

FIG. S20. Overlays of the simulated transient XAS of the cationic trajectories starting in the D_1, D_2 and D_3 states in blue with the experimental transient absorption spectra in black. The times 0 fs, 24 fs, 48 fs, 72 fs and 99 fs correspond to experimental delays of 6.8 fs, 23.2 fs, 49.0 fs, 72.4 fs and 107.6 fs.

B. Spectra of the Different Initial States for Cationic Vinyl Bromide

FIG. S21. Simulated transient XAS of the 11 cationic trajectories starting in the D_1 state. On the left and right the spectrum for time $t = 0$ fs and $t = 99$ fs, respectively, is shown in blue overlaid with the experimental transient absorption spectrogram in black at delays $d = 6.8$ fs and $d = 107.6$ fs.
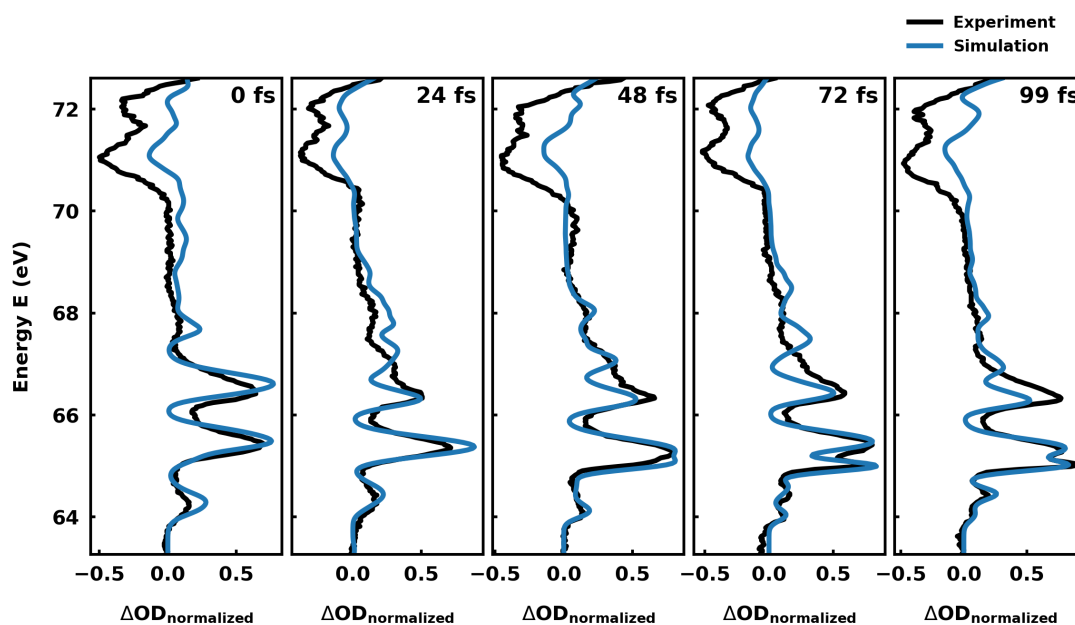
FIG. S22. Simulated transient XAS of the 26 cationic trajectories starting in the D_2 state. On the left and right the spectrum for time $t = 0$ fs and $t = 99$ fs, respectively, is shown in blue overlaid with the experimental transient absorption spectrogram in black at delays $d = 6.8$ fs and $d = 107.6$ fs.
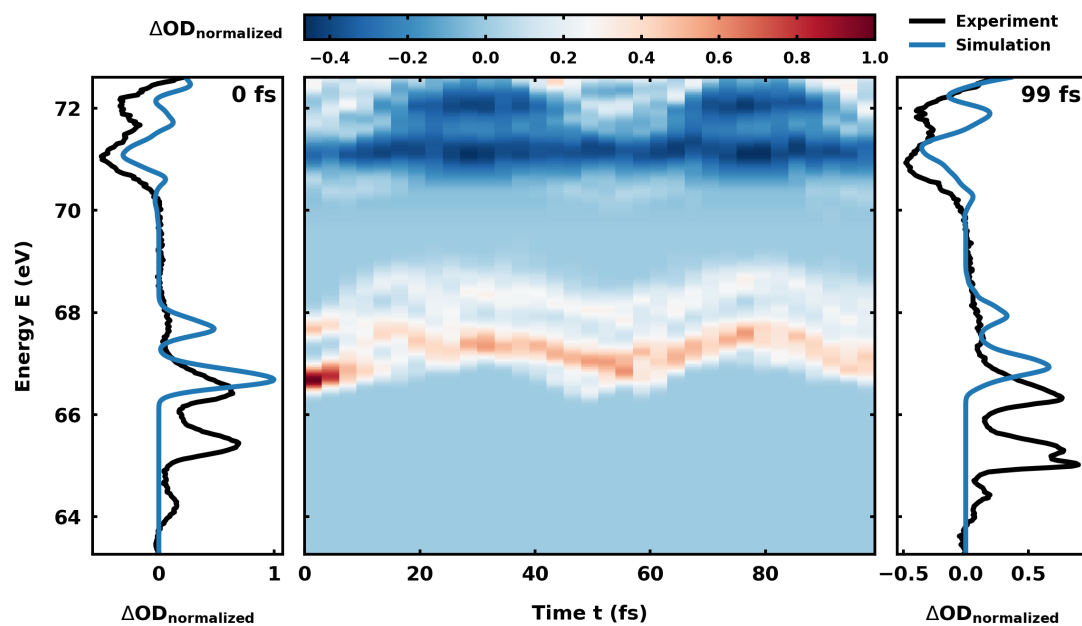

FIG. S23. Simulated transient XAS of the 45 cationic trajectories starting in the D_3 state. On the left and right the spectrum for time $t = 0$ fs and $t = 99$ fs, respectively, is shown in blue overlaid with the experimental transient absorption spectrogram in black at delays $d = 6.8$ fs and $d = 107.6$ fs.

29

C. Spectra of the Different Observed Dynamics for the D_3 Trajectories
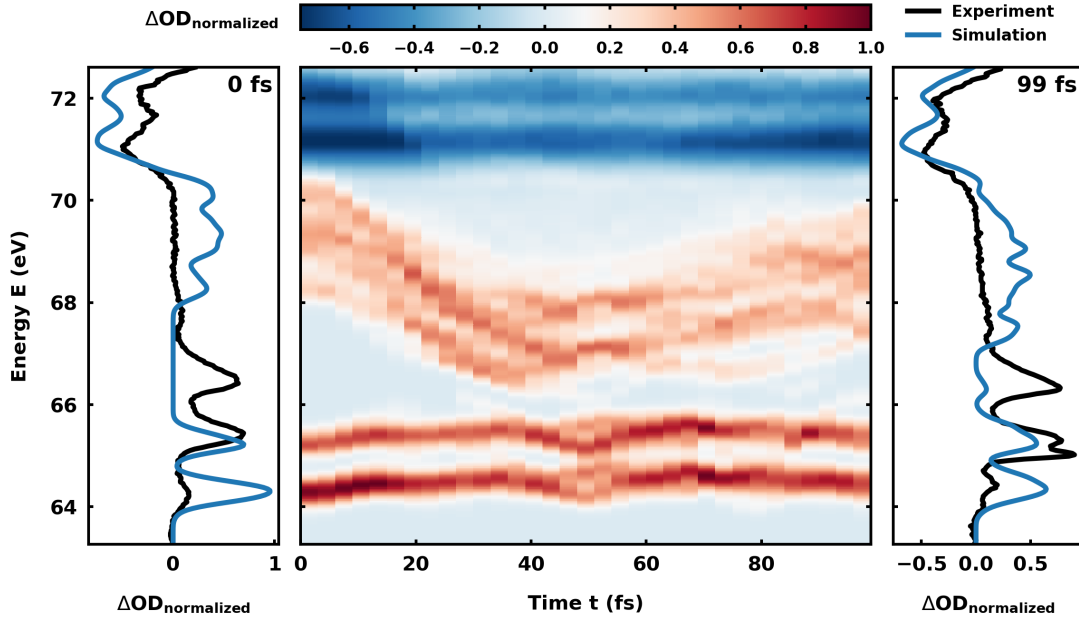
FIG. S24. Simulated transient XAS of the 21 trajectories, showing only vibrational dynamics. On the left and right the spectrum for time $t = 0$ fs and $t = 99$ fs, respectively, is shown in blue overlaid with the experimental transient absorption spectrogram in black at delays $d = 6.8$ fs and $d = 107.6$ fs.
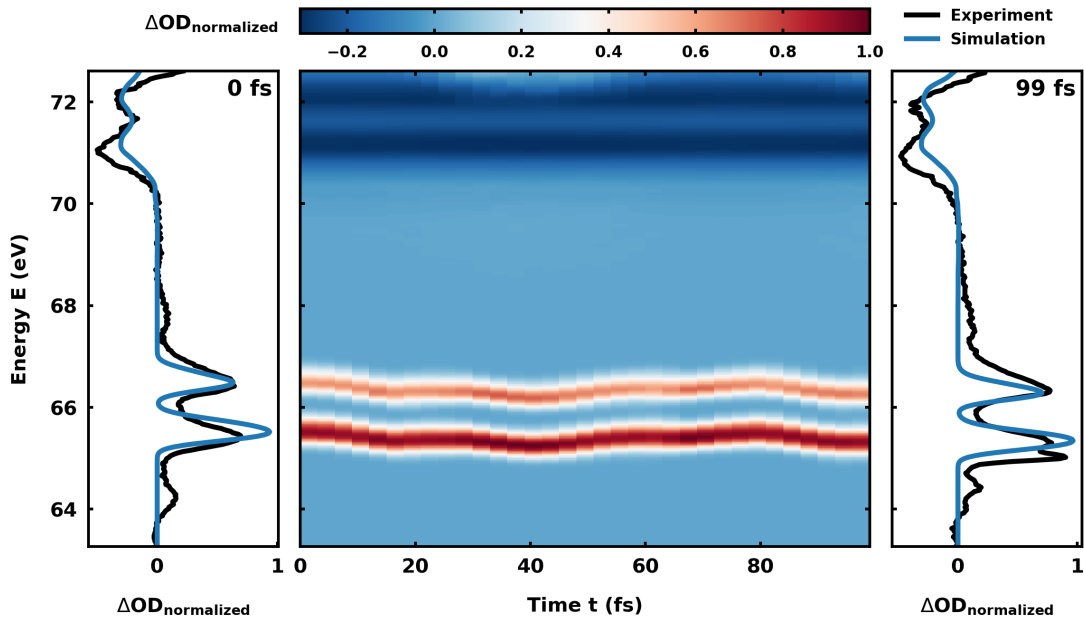
FIG. S25. Simulated transient XAS of the eight slow dissociating trajectories. On the left and right the spectrum for time $t = 0$ fs and $t = 99$ fs, respectively, is shown in blue overlaid with the experimental transient absorption spectrogram in black at delays $d = 6.8$ fs and $d = 107.6$ fs.
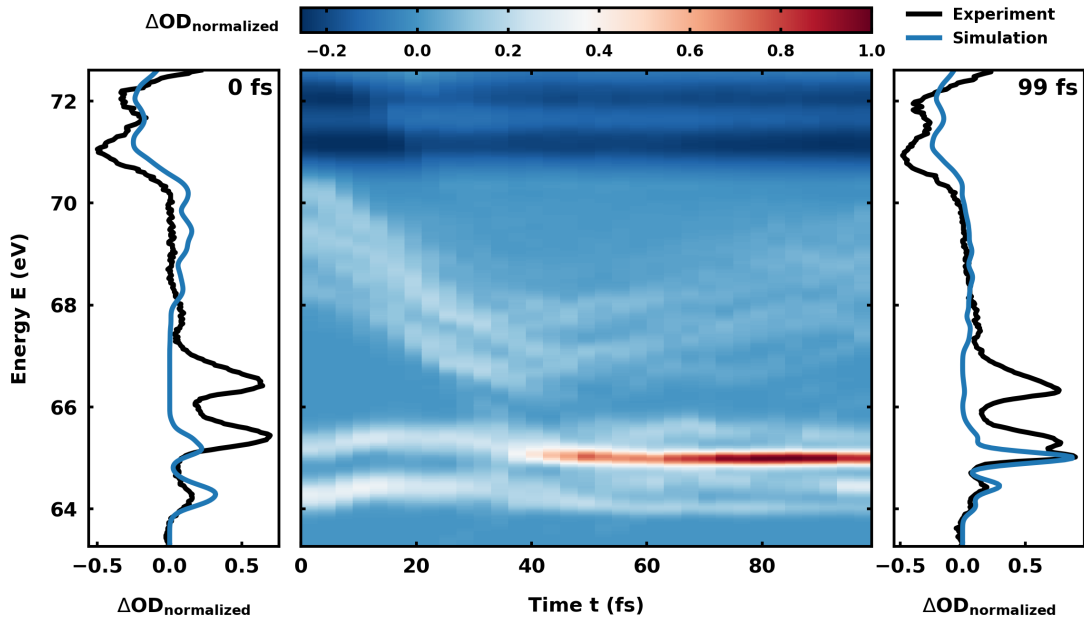

FIG. S26. Simulated transient XAS of the 16 fast dissociating trajectories . On the left and right the spectrum for time $t = 0$ fs and $t = 99$ fs, respectively, is shown in blue overlaid with the experimental transient absorption spectrogram in black at delays $d = 6.8$ fs and $d = 107.6$ fs.
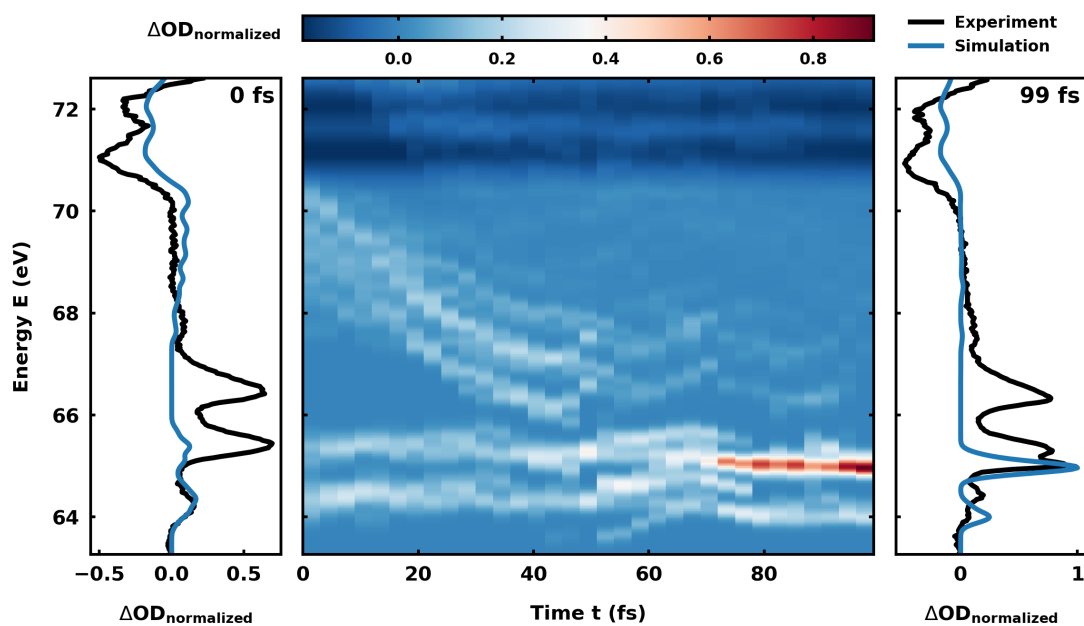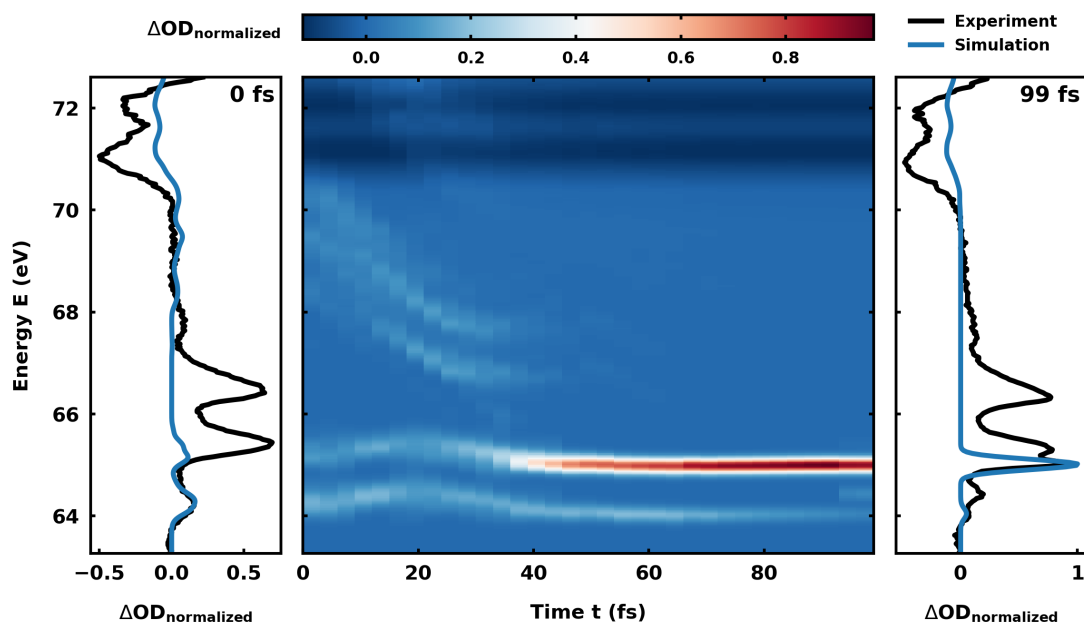
V. CONICAL INTERSECTION AND EXCITED STATE MINIMA

A. Geometry of the Optimized D_3/D_4 Conical Intersection

The conical Intersection between the D_3 and D_4 state was optimized with OpenMolcas at the CASSCF level of theory using the AS(8,7) shown in FIG. S7 and the ANO-RCC-VTZP basis set. TABLE S8 shows the xyz coordinates of the optimized geometry depicted in FIG. S27. As one can see the geometry of the conical intersection is characterized by an elongated C–Br bond. Here the bond length is 2.339 Å compared to the 2.10 Å at the ground state minimum. Furthermore the H–C=C bond angle is increased form 115° to 151°.

TABLE S8. Geometry of the SA5-CASSCF(8,7)/ANO-RCC-VTZP optimized conical intersection between the D_3 and D_4 state of cationic vinyl bromide.

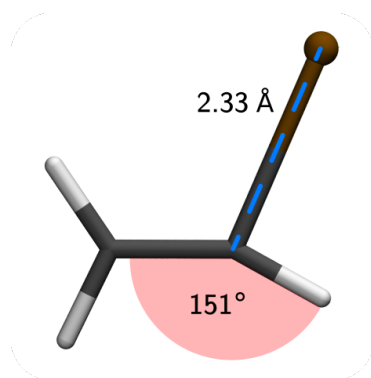| Number	Element	x [Å]	y [Å]	z [Å]
1	C	0.000 000	0.000 000	0.000 000
2	C	0.000 000	0.000 000	1.332 924
3	H	0.000 000	0.916 808	−0.574 890
4	H	−0.003 204	−0.944 947	−0.530 277
5	H	−0.001 234	−0.895 278	1.938 618
6	Br	0.003 811	1.593 998	2.361 016

FIG. S27. Geometry of the SA5-CASSCF(8,7)/ANO-RCC-VTZP optimized conical intersection between the D_3 and D_4 state of cationic vinyl bromide.

B. Relaxed Scan of Cationic Vinyl Bromide

To further analyze the dissociation dynamics of the cation after excitation to D_3 state, we also performed a relaxed scan of the C–Br bond. The relaxed scan was done with Open-Molcas utilizing the tracking feature (keyword *TRACk*) of the *SLAPAF* program, where one is able to follow the character of a specific state throughout a geometry optimization. In our case we choose to follow the character of the D_3 state at the Frank-Condon region. At each step in the scan the geometry was optimized at the SA5-CASSCF(8,7)/ANO-RCC-VTZP level of theory. The resulting potential energy surfaces (PES) of the first four states are shown in FIG. S28. Their color corresponds to the electronic character of the state at the Frank-Condon region. The D_1 state, an ionization from the π_2 orbital is shown in blue. In green the D_2 state, an ionization from the lone pair orbital n_1 of the bromine. In yellow the D_3 state, an ionization from the π_1 orbital and in magenta the D_4 an ionization from the σ_1 orbitals of the C–Br bond.
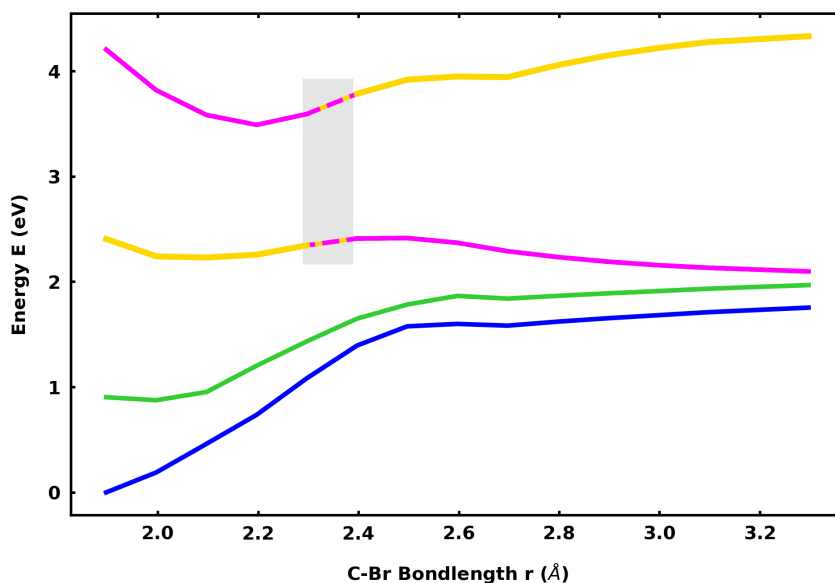

FIG. S28. Relaxed scan of the the C–Br bond. The color of the potential energy surfaces corresponds to the character of the state at the Frank-Condon region. The D_1 state is shown in blue, the D_2 in green, the D_3 in yellow and the D_4 in magenta. The region of the conical intersection is highlighted in grey.

C.   Geometries of the Optimized Excited State Minima

We also optimized the geometries for the first three doublet states of the cationic vinyl bromide. All calculations were done in OpenMolcas at the CASSCF level of theory using the AS(8,7) shown in FIG. S7 and the ANO-RCC-VTZP basis set. Table S9 lists the same geometrical parameters, $r(C-Br)$ and $a(H-C=C)$ of the optimized minima, that were discussed for the conical intersection between the D_3 and D_4 state. Tables S10 to S12 show the complete xyz coordinates of the optimized geometries. For comparison we also show the CASSCF optimized structure and relevant geometrical parameters of the S_0 minimum of neutral vinyl bromide S13.

TABLE S9. Relevant geometry parameters of the SA5-CASSCF(8,7)/ANO-RCC-VTZP optimized D_1 to D_3 minima of cationic vinyl bromide and S_0 minimum of neutral vinyl bromide. The geometry parameters are the same as the ones discussed for the D_3/D_4 conical intersection.

State	$r(C-Br)[\text{Å}]$	$a(H-C=C)[°]$
D_1	1.831	124.2
D_2	1.986	132.8
D_3	2.054	127.4
S_0	1.925	123.7

TABLE S10. Geometry of the SA5-CASSCF(8,7)/ANO-RCC-VTZP optimized D_1 minimum of cationic vinyl bromide.

Number	Element	x [Å]	y [Å]	z [Å]
1	C	0.005 700	0.000 783	−0.007 271
2	C	−0.005 194	−0.000 624	1.368 825
3	H	0.921 675	−0.001 144	−0.562 672
4	H	−0.924 191	0.003 927	−0.540 602
5	H	−0.894 950	0.000 654	1.962 577
6	Br	1.567 545	−0.002 967	2.306 523

34

TABLE S11. Geometry of the SA5-CASSCF(8,7)/ANO-RCC-VTZP optimized D_2 minimum of cationic vinyl bromide.

Number	Element	x [Å]	y [Å]	z [Å]
1	C	0.003 837	0.000 924	−0.011 473
2	C	−0.066 556	−0.000 548	1.311 030
3	H	0.919 151	0.000 160	−0.567 069
4	H	−0.920 003	0.002 427	−0.556 157
5	H	−0.887 536	0.001 749	1.993 988
6	Br	1.621 693	−0.004 084	2.357 061

TABLE S12. Geometry of the SA5-CASSCF(8,7)/ANO-RCC-VTZP optimized D_3 minimum of cationic vinyl bromide.

Number	Element	x [Å]	y [Å]	z [Å]
1	C	−0.014 304	−0.000 047	−0.046 037
2	C	−0.040 495	0.000 549	1.328 755
3	H	0.900 531	−0.001 117	−0.602 497
4	H	−0.950 652	0.004 499	−0.569 772
5	H	−0.902 086	0.000 077	1.962 333
6	Br	1.677 593	−0.003 331	2.454 598

TABLE S13. Geometry of the SA5-CASSCF(8,7)/ANO-RCC-VTZP optimized S_0 minimum of neutral vinyl bromide.

Number	Element	x [Å]	y [Å]	z [Å]
1	C	−0.003 056	0.001 021	−0.005 306
2	C	−0.001 250	0.000 048	1.329 286
3	H	0.897 925	−0.000 570	−0.582 734
4	H	−0.940 094	0.002 997	−0.527 094
5	H	−0.888 749	0.000 924	1.923 509
6	Br	1.605 811	−0.003 791	2.389 719

REFERENCES

[S1] H.-J. Werner, P. J. Knowles, G. Knizia, F. R. Manby, M. Schütz, P. Celani, T. Korona, R. Lindh, A. Mitrushenkov, G. Rauhut, K. R. Shamasundar, T. B. Adler, R. D. Amos, A. Bernhardsson, A. Berning, D. L. Cooper, M. J. O. Deegan, A. J. Dobbyn, F. Eckert, E. Goll, C. Hampel, A. Hesselmann, G. Hetzer, T. Hrenar, G. Jansen, C. Köppl, Y. Liu, A. W. Lloyd, R. A. Mata, A. J. May, S. J. McNicholas, W. Meyer, M. E. Mura, A. Nicklass, D. P. O'Neill, P. Palmieri, D. Peng, K. Pflüger, R. Pitzer, M. Reiher, T. Shiozaki, H. Stoll, A. J. Stone, R. Tarroni, T. Thorsteinsson, and M. Wang, "MOLPRO, version 2012.1, a package of ab initio programs," (2012).

[S2] H.-J. Werner, P. J. Knowles, G. Knizia, F. R. Manby, and M. Schütz, "Molpro: a general-purpose quantum chemistry program package: Molpro," WIREs Comput Mol Sci **2**, 242–253 (2012).

[S3] A. K. Wilson, T. van Mourik, and T. H. Dunning, "Gaussian basis sets for use in correlated molecular calculations. VI. sextuple zeta correlation consistent basis sets for boron through neon," Journal of Molecular Structure: THEOCHEM **388**, 339–349 (1996).

[S4] K. A. Peterson, D. E. Woon, and T. H. Dunning, "Benchmark calculations with correlated molecular wave functions. IV. the classical barrier height of the H+H2→H2+H reaction," J. Chem. Phys. **100**, 7410–7415 (1994).

[S5] D. E. Woon and T. H. Dunning, "Gaussian basis sets for use in correlated molecular calculations. III. the atoms aluminum through argon," J. Chem. Phys. **98**, 1358–1371 (1993).

[S6] R. A. Kendall, T. H. Dunning, and R. J. Harrison, "Electron affinities of the first-row atoms revisited. systematic basis sets and wave functions," J. Chem. Phys. **96**, 6796–6806 (1992).

[S7] T. H. Dunning, "Gaussian basis sets for use in correlated molecular calculations. i. the atoms boron through neon and hydrogen," J. Chem. Phys. **90**, 1007–1023 (1989).

[S8] C. Hampel, K. A. Peterson, and H.-J. Werner, "A comparison of the efficiency and accuracy of the quadratic configuration interaction (QCISD), coupled cluster (CCSD), and brueckner coupled cluster (BCCD) methods," Chem. Phys. Lett. **190**, 1–12 (1992).

36

[S9]T. Korona and H.-J. Werner, "Local treatment of electron excitations in the EOM-CCSD method," J. Chem. Phys. **118**, 3006–3019 (2003).

[S10]T. Shiozaki, W. Gyorffy, P. Celani, and H.-J. Werner, "Communication: extended multi-state complete active space second-order perturbation theory: energy and nuclear gradients," J. Chem. Phys. **135**, 081106 (2011).

[S11]G. Ghigo, B. O. Roos, and P.-Å. Malmqvist, "A modified definition of the zeroth-order hamiltonian in multiconfigurational perturbation theory (CASPT2)," Chem. Phys. Lett. **396**, 142–149 (2004).

[S12]K. H. Sze, C. E. Brion, A. Katrib, and B. El-Issa, "Excitation and ionization of the monohaloethylenes (C2H3X, X = f, cl, br, i). II. photoionization by He(I) and He(II) photoelectron spectroscopy and valence-shell excitation by electron energy loss spectroscopy," Chem. Phys. **137**, 369–390 (1989).

[S13]J. Schander and B. R. Russell, "Vacuum ultraviolet spectra of bromoethylene and dibromoethylenes," J. Am. Chem. Soc. **98**, 6900–6904 (1976).

[S14]A. Hoxha, R. Locht, B. Leyh, D. Dehareng, K. Hottmann, H. W. Jochims, and H. Baumgärtel, "The photoabsorption and constant ionic state spectroscopy of vinylbromide," Chem. Phys. **260**, 237–247 (2000).

[S15]P. A. Fantin, P. L. Barbieri, A. Canal Neto, and F. E. Jorge, "Augmented gaussian basis sets of triple and quadruple zeta valence quality for the atoms H and from li to ar: Applications in HF, MP2, and DFT calculations of molecular dipole moment and dipole (hyper)polarizability," Journal of Molecular Structure: THEOCHEM **810**, 103–111 (2007).

[S16]G. G. Camiletti, A. Canal Neto, F. E. Jorge, and S. F. Machado, "Augmented gaussian basis sets of double and triple zeta valence qualities for the atoms K and Sc–Kr: Applications in HF, MP2, and DFT calculations of molecular electric properties," Journal of Molecular Structure: THEOCHEM **910**, 122–125 (2009).

[S17]B. P. Pritchard, D. Altarawy, B. Didier, T. D. Gibson, and T. L. Windus, "New basis set exchange: An open, Up-to-Date resource for the molecular sciences community," J. Chem. Inf. Model. **59**, 4814–4820 (2019).

[S18]K. L. Schuchardt, B. T. Didier, T. Elsethagen, L. Sun, V. Gurumoorthi, J. Chase, J. Li, and T. L. Windus, "Basis set exchange: a community database for computational sciences," J. Chem. Inf. Model. **47**, 1045–1052 (2007).

[S19] D. Feller, "The role of databases in support of computational chemistry calculations," J. Comput. Chem. **17**, 1571–1586 (1996).

[S20] M. J. Frisch, G. W. Trucks, H. B. Schlegel, G. E. Scuseria, M. A. Robb, J. R. Cheeseman, G. Scalmani, V. Barone, G. A. Petersson, H. Nakatsuji, X. Li, M. Caricato, A. V. Marenich, J. Bloino, B. G. Janesko, R. Gomperts, B. Mennucci, H. P. Hratchian, J. V. Ortiz, A. F. Izmaylov, J. L. Sonnenberg, D. Williams-Young, F. Ding, F. Lipparini, F. Egidi, J. Goings, B. Peng, A. Petrone, T. Henderson, D. Ranasinghe, V. G. Zakrzewski, J. Gao, N. Rega, G. Zheng, W. Liang, M. Hada, M. Ehara, K. Toyota, R. Fukuda, J. Hasegawa, M. Ishida, T. Nakajima, Y. Honda, O. Kitao, H. Nakai, T. Vreven, K. Throssell, J. A. Montgomery, Jr., J. E. Peralta, F. Ogliaro, M. J. Bearpark, J. J. Heyd, E. N. Brothers, K. N. Kudin, V. N. Staroverov, T. A. Keith, R. Kobayashi, J. Normand, K. Raghavachari, A. P. Rendell, J. C. Burant, S. S. Iyengar, J. Tomasi, M. Cossi, J. M. Millam, M. Klene, C. Adamo, R. Cammi, J. W. Ochterski, R. L. Martin, K. Morokuma, O. Farkas, J. B. Foresman, and D. J. Fox, "Gaussian 16 Revision A.03," (2016), Gaussian Inc. Wallingford CT.

[S21] Y. Zhao and D. G. Truhlar, "The M06 suite of density functionals for main group thermochemistry, thermochemical kinetics, noncovalent interactions, excited states, and transition elements: two new functionals and systematic testing of four m06-class functionals and 12 other functionals," Theor. Chem. Acc. **120**, 215–241 (2008).

[S22] A. K. Wilson, D. E. Woon, K. A. Peterson, and T. H. Dunning, "Gaussian basis sets for use in correlated molecular calculations. IX. the atoms gallium through krypton," J. Chem. Phys. **110**, 7667–7676 (1999).

[S23] H. Wang, M. Odelius, and D. Prendergast, "A combined multi-reference pump-probe simulation method with application to XUV signatures of ultrafast methyl iodide photodissociation," J. Chem. Phys. **151**, 124106 (2019).

[S24] P. Å. Malmqvist, B. O. Roos, and B. Schimmelpfennig, "The restricted active space (RAS) state interaction approach with spin–orbit coupling," Chem. Phys. Lett. **357**, 230–240 (2002).

Bibliography

[1] R. Croce and H. van Amerongen, "Light-harvesting in photosystem I", Photosynth. Res. **116**, 153 (2013).

[2] H. van Amerongen and R. Croce, "Light harvesting in photosystem II", Photosynth. Res. **116**, 251 (2013).

[3] T. Yoshizawa and G. Wald, "Pre-Lumirhodopsin and the bleaching of visual pigments", Nature **197**, 1279 (1963).

[4] G. Wald, "The receptors of human color vision", Science **145**, 1007 (1964).

[5] H. G. Khorana, "Rhodopsin, photoreceptor of the rod cell. an emerging pattern for structure and function", J. Biol. Chem. **267**, 1 (1992).

[6] R. Send and D. Sundholm, "Stairway to the conical intersection: a computational study of the retinal isomerization", J. Phys. Chem. A **111**, 8766 (2007).

[7] D. Polli, P. Altoè, O. Weingart, K. M. Spillane, C. Manzoni, D. Brida, G. Tomasello, G. Orlandi, P. Kukura, R. A. Mathies, M. Garavelli, and G. Cerullo, "Conical intersection dynamics of the primary photoisomerization event in vision", Nature **467**, 440 (2010).

[8] M. Barbatti, A. J. A. Aquino, J. J. Szymczak, D. Nachtigallova, P. Hobza, and H. Lischka, "Relaxation mechanisms of UV-photoexcited DNA and RNA nucleobases", Proceedings of the National Academy of Sciences **107**, 21453 (2010).

[9] M. Barbatti, A. C. Borin, and S. Ullrich, "Photoinduced processes in nucleic acids", Top. Curr. Chem. **355**, 1 (2015).

[10] M. Barbatti, A. C. Borin, and S. Ullrich, *Photoinduced phenomena in nucleic acids II: DNA fragments and phenomenological aspects*, edited by M. Barbatti, A. C. Borin, and S. Ullrich, 2015th ed., Topics in current chemistry (Springer International Publishing, Cham, Switzerland, Jan. 2015).

[11] W. J. Schreier, P. Gilch, and W. Zinth, "Early events of DNA photodamage", Annu. Rev. Phys. Chem. **66**, 497 (2015).

[12] R. Improta, F. Santoro, and L. Blancafort, "Quantum mechanical studies on the photophysics and the photochemistry of nucleic acids and nucleobases", Chem. Rev. **116**, 3540 (2016).

[13] L. Martinez-Fernandez and R. Improta, "Photoactivated proton coupled electron transfer in DNA: insights from quantum mechanical calculations", Faraday Discuss. **207**, 199 (2018).

[14] A. A. Ismail and D. W. Bahnemann, "Photochemical splitting of water for hydrogen production by photocatalysis: a review", Sol. Energy Mater. Sol. Cells **128**, 85 (2014).

[15] K. Wenderich and G. Mul, "Methods, mechanism, and applications of photodeposition in photocatalysis: a review", Chem. Rev. **116**, 14587 (2016).

[16] A. Nenov, T. Cordes, T. T. Herzog, W. Zinth, and R. de Vivie-Riedle, "Molecular driving forces for Z/E isomerization mediated by heteroatoms: the example hemithioindigo", J. Phys. Chem. A **114**, 13016 (2010).

[17] F. F. Graupner, T. T. Herzog, F. Rott, S. Oesterling, R. de Vivie-Riedle, T. Cordes, and W. Zinth, "Photoisomerization of hemithioindigo compounds: combining solvent- and substituent- effects into an advanced reaction model", Chem. Phys. **515**, 614 (2018).

[18] H. M. D. Bandara and S. C. Burdette, "Photoisomerization in different classes of azobenzene", Chem. Soc. Rev. **41**, 1809 (2012).

[19] J. D. Harris, M. J. Moran, and I. Aprahamian, "New molecular switch architectures", Proc. Natl. Acad. Sci. U. S. A. **115**, 9414 (2018).

[20] B. L. Feringa, "The art of building small: from molecular switches to molecular motors", J. Org. Chem. **72**, 6635 (2007).

[21] S. Erbas-Cakmak, D. A. Leigh, C. T. McTernan, and A. L. Nussbaumer, "Artificial molecular machines", Chem. Rev. **115**, 10081 (2015).

[22] R. Wilcken, M. Schildhauer, F. Rott, L. A. Huber, M. Guentner, S. Thumser, K. Hoffmann, S. Oesterling, R. de Vivie-Riedle, E. Riedle, and H. Dube, "Complete mechanism of hemithioindigo motor rotation", J. Am. Chem. Soc. **140**, 5311 (2018).

[23] D. R. Yarkony, "Diabolical conical intersections", Rev. Mod. Phys. **68**, 985 (1996).

[24] W. Domcke, D. Yarkony, and H. Köppel, *Conical intersections: electronic structure, dynamics & spectroscopy* (World Scientific, 2004).

[25] W. Domcke and D. R. Yarkony, "Role of conical intersections in molecular spectroscopy and photoinduced chemical dynamics", Annual Review of Physical Chemistry **63**, 325 (2012).

[26] G. A. Worth and L. S. Cederbaum, "Beyond Born-Oppenheimer: molecular dynamics through a conical intersection", Annu. Rev. Phys. Chem. **55**, 127 (2004).

[27] S. Herre, T. Schadendorf, I. Ivanov, C. Herrberger, W. Steinle, K. Rück-Braun, R. Preissner, and H. Kuhn, "Photoactivation of an inhibitor of the 12/15-lipoxygenase pathway", Chembiochem **7**, 1089 (2006).

[28] S. Wiedbrauk and H. Dube, "Hemithioindigo—an emerging photoswitch", Tetrahedron Lett. **56**, 4266 (2015).

[29] A. Sailer, F. Ermer, Y. Kraus, F. H. Lutter, C. Donau, M. Bremerich, J. Ahlfeld, and O. Thorn-Seshold, "Hemithioindigos for cellular photopharmacology: desymmetrised molecular switch scaffolds enabling design control over the Isomer-Dependency of potent antimitotic bioactivity", Chembiochem **20**, 1305 (2019).

[30] A. Sailer, J. C. M. Meiring, C. Heise, L. N. Pettersson, A. Akhmanova, J. Thorn-Seshold, and O. Thorn-Seshold, "Pyrrole hemithioindigo antimitotics with Near-Quantitative bidirectional photoswitching that photocontrol cellular microtubule dynamics with Single-Cell precision", Angew. Chem. Int. Ed Engl. **60**, 23695 (2021).

[31] M. Guentner, M. Schildhauer, S. Thumser, P. Mayer, D. Stephenson, P. J. Mayer, and H. Dube, "Sunlight-powered khz rotation of a hemithioindigo-based molecular motor", Nat. Commun. **6**, 8406 (2015).

[32] M. Schildhauer, F. Rott, S. Thumser, P. Mayer, R. de Vivie-Riedle, and H. Dube, "A prospective ultrafast hemithioindigo molecular motor", ChemPhotoChem **3**, 365 (2019).

[33] G. Cerullo, M. Nisoli, and S. De Silvestri, "Generation of 11 fs pulses tunable across the visible by optical parametric amplification", Appl. Phys. Lett. **71**, 3616 (1997).

[34] E. Riedle, M. Beutter, S. Lochbrunner, J. Piel, S. Schenkl, S. Spörlein, and W. Zinth, "Generation of 10 to 50 fs pulses tunable through all of the visible and the NIR", Appl. Phys. B **71**, 457 (2000).

[35] M. Hentschel, R. Kienberger, C. Spielmann, G. A. Reider, N. Milosevic, T. Brabec, P. Corkum, U. Heinzmann, M. Drescher, and F. Krausz, "Attosecond metrology", Nature **414**, 509 (2001).

[36] J. Itatani, F. Quéré, G. L. Yudin, M. Y. Ivanov, F. Krausz, and P. B. Corkum, "Attosecond streak camera", Phys. Rev. Lett. **88**, 173903 (2002).

[37] A. Baltuska, T. Udem, M. Uiberacker, M. Hentschel, E. Goulielmakis, C. Gohle, R. Holzwarth, V. S. Yakovlev, A. Scrinzi, T. W. Hänsch, and F. Krausz, "Attosecond control of electronic processes by intense light fields", Nature **421**, 611 (2003).

[38] P. Baum, S. Lochbrunner, and E. Riedle, "Generation of tunable 7-fs ultraviolet pulses: achromatic phase matching and chirp management", Appl. Phys. B **79**, 1027 (2004).

[39] C. Manzoni, D. Polli, and G. Cerullo, "Two-color pump-probe system broadly tunable over the visible and the near infrared with sub-30fs temporal resolution", Rev. Sci. Instrum. **77**, 023103 (2006).

[40] D. Polli, M. R. Antognazza, D. Brida, G. Lanzani, G. Cerullo, and S. De Silvestri, "Broadband pump-probe spectroscopy with sub-10-fs resolution for probing ultrafast internal conversion and coherent phonons in carotenoids", Chem. Phys. **350**, 45 (2008).

[41] F. Krausz and M. Ivanov, "Attosecond physics", Rev. Mod. Phys. **81**, 163 (2009).

[42] A. H. Zewail, "Femtochemistry: Atomic-Scale dynamics of the chemical bond", J. Phys. Chem. A **104**, 5660 (2000).

[43] M. Fushitani, "Applications of pump-probe spectroscopy", Annu. Rep. Prog. Chem. Sect. C: Phys. Chem. **104**, 272 (2008).

[44] S. R. Leone and D. M. Neumark, "Attosecond science in atomic, molecular, and condensed matter physics", Faraday Discuss. **194**, 15 (2016).

[45] M. Nisoli, P. Decleva, F. Calegari, A. Palacios, and F. Martín, "Attosecond electron dynamics in molecules", Chem. Rev. **117**, 10760 (2017).

[46] E. Goulielmakis, Z.-H. Loh, A. Wirth, R. Santra, N. Rohringer, V. S. Yakovlev, S. Zherebtsov, T. Pfeifer, A. M. Azzeer, M. F. Kling, S. R. Leone, and F. Krausz, "Real-time observation of valence electron motion", Nature **466**, 739 (2010).

[47] K. F. Chang, H. Wang, S. M. Poullain, D. Prendergast, D. M. Neumark, and S. R. Leone, "Mapping wave packet bifurcation at a conical intersection in CH3I by attosecond XUV transient absorption spectroscopy", J. Chem. Phys. **154**, 234301 (2021).

[48] T. A. A. Oliver and G. R. Fleming, "Following coupled Electronic-Nuclear motion through conical intersections in the ultrafast relaxation of β-Apo-8'-carotenal", J. Phys. Chem. B **119**, 11428 (2015).

[49] A. Bhattacherjee and S. R. Leone, "Ultrafast x-ray transient absorption spectroscopy of Gas-Phase photochemical reactions: a new universal probe of photoinduced molecular dynamics", Acc. Chem. Res. **51**, 3203 (2018).

[50] Y. Kobayashi, K. F. Chang, T. Zeng, D. M. Neumark, and S. R. Leone, "Direct mapping of curve-crossing dynamics in IBr by attosecond transient absorption spectroscopy", Science **365**, 79 (2019).

[51] H. Timmers, X. Zhu, Z. Li, Y. Kobayashi, M. Sabbar, M. Hollstein, M. Reduzzi, T. J. Martínez, D. M. Neumark, and S. R. Leone, "Disentangling conical intersection and coherent molecular dynamics in methyl bromide with attosecond transient absorption spectroscopy", Nat. Commun. **10**, 3133 (2019).

[52] B. W. Toulson, M. Borgwardt, H. Wang, F. Lackner, A. S. Chatterley, C. D. Pemmaraju, D. M. Neumark, S. R. Leone, D. Prendergast, and O. Gessner, "Probing ultrafast C-Br bond fission in the UV photochemistry of bromoform with core-to-valence transient absorption spectroscopy", Struct Dyn **6**, 054304 (2019).

[53] K. F. Chang, M. Reduzzi, H. Wang, S. M. Poullain, Y. Kobayashi, L. Barreau, D. Prendergast, D. M. Neumark, and S. R. Leone, "Revealing electronic state-switching at conical intersections in alkyl iodides by ultrafast XUV transient absorption spectroscopy", Nat. Commun. **11**, 4042 (2020).

[54] K. S. Zinchenko, F. Ardana-Lamas, I. Seidu, S. P. Neville, J. van der Veen, V. U. Lanfaloni, M. S. Schuurman, and H. J. Wörner, "Sub-7-femtosecond conical-intersection dynamics probed at the carbon k-edge", Science **371**, 489 (2021).

[55] F. Rott, M. Reduzzi, T. Schnappinger, Y. Kobayashi, K. F. Chang, H. Timmers, D. M. Neumark, R. d. Vivie-Riedle, and S. R. Leone, "Ultrafast strong-field dissociation of vinyl bromide: an attosecond transient absorption spectroscopy and non-adiabatic molecular dynamics study", Structural Dynamics **8**, 034104 (2021).

[56] V. Balzani V, A. Credi, F. M. Raymo, and J. F. Stoddart, "Artificial molecular machines", Angew. Chem. Int. Ed Engl. **39**, 3348 (2000).

[57] B. P. Jena, *Cellular nanomachines: from discovery to Structure-Function and therapeutic applications* (Springer International Publishing, Apr. 2020).

[58] K. D. Ridge, N. G. Abdulaev, M. Sousa, and K. Palczewski, "Phototransduction: crystal clear", Trends Biochem. Sci. **28**, 479 (2003).

[59] K. Palczewski, "Chemistry and biology of vision", J. Biol. Chem. **287**, 1612 (2012).

[60] P. D. Kiser, M. Golczak, and K. Palczewski, "Chemistry of the retinoid (visual) cycle", Chem. Rev. **114**, 194 (2014).

[61] M. A. Geeves and K. C. Holmes, "Structural mechanism of muscle contraction", Annu. Rev. Biochem. **68**, 687 (1999).

[62] T. A. Duke, "Molecular model of muscle contraction", Proc. Natl. Acad. Sci. U. S. A. **96**, 2770 (1999).

[63] H. L. Sweeney and D. W. Hammers, "Muscle contraction", Cold Spring Harb. Perspect. Biol. **10**, 10.1101/cshperspect.a023200 (2018).

[64] H. L. Sweeney and E. L. F. Holzbaur, "Motor proteins", Cold Spring Harb. Perspect. Biol. **10**, 10.1101/cshperspect.a021931 (2018).

[65] B. P. Jena, in *Cellular nanomachines: from discovery to Structure-Function and therapeutic applications*, edited by B. P. Jena (Springer International Publishing, Cham, 2020), pp. 79–89.

[66] R. D. Vale and R. A. Milligan, "The way things move: looking under the hood of molecular motor proteins", Science **288**, 88 (2000).

[67] J. A. Spudich, "The myosin swinging cross-bridge model", Nat. Rev. Mol. Cell Biol. **2**, 387 (2001).

[68] R. H. Fitts, "The cross-bridge cycle and skeletal muscle fatigue", J. Appl. Physiol. **104**, 551 (2008).

[69] B. P. Jena, in *Cellular nanomachines: from discovery to Structure-Function and therapeutic applications*, edited by B. P. Jena (Springer International Publishing, Cham, 2020), pp. 57–62.

[70] P. D. Boyer, "The ATP synthase–a splendid molecular machine", Annu. Rev. Biochem. **66**, 717 (1997).

[71] S. Mukherjee and A. Warshel, "Realistic simulations of the coupling between the protomotive force and the mechanical rotation of the F0-ATPase", National Academy of Sciences (2012).

[72] S. Mukherjee and A. Warshel, "Dissecting the role of the γ-subunit in the rotary-chemical coupling and torque generation of F1-ATPase", Proc. Natl. Acad. Sci. U. S. A. **112**, 2746 (2015).

[73] S. Mukherjee, R. P. Bora, and A. Warshel, "Torque, chemistry and efficiency in molecular motors: a study of the rotary-chemical coupling in F1-ATPase", Q. Rev. Biophys. **48**, 395 (2015).

[74] C. Bai and A. Warshel, "Revisiting the protomotive vectorial motion of F0-ATPase", Proc. Natl. Acad. Sci. U. S. A. **116**, 19484 (2019).

[75] S. Shinkai and O. Manabe, "Photocontrol of ion extraction and ion transport by photo-functional crown ethers", in Host guest complex chemistry III (1984), pp. 67–104.

[76] Y. Feng, M. Ovalle, J. S. W. Seale, C. K. Lee, D. J. Kim, R. D. Astumian, and J. F. Stoddart, "Molecular pumps and motors", J. Am. Chem. Soc. **143**, 5569 (2021).

[77] A. Perrot, E. Moulin, and N. Giuseppone, "Extraction of mechanical work from stimuli-responsive molecular systems and materials", TRECHEM **3**, 926 (2021).

[78] M.-M. Russew and S. Hecht, "Photoswitches: from molecules to materials", Adv. Mater. **22**, 3348 (2010).

[79] L. Zhang, V. Marcos, and D. A. Leigh, "Molecular machines with bio-inspired mechanisms", Proc. Natl. Acad. Sci. U. S. A. **115**, 9397 (2018).

[80] D. Dattler, G. Fuks, J. Heiser, E. Moulin, A. Perrot, X. Yao, and N. Giuseppone, "Design of collective motions from synthetic molecular switches, rotors, and motors", Chem. Rev. **120**, 310 (2020).

[81] A. Goulet-Hanssens, F. Eisenreich, and S. Hecht, "Enlightening materials with photoswitches", Adv. Mater. **32**, e1905966 (2020).

[82] F. Nicoli, E. Paltrinieri, M. Tranfić Bakić, M. Baroncini, S. Silvi, and A. Credi, "Binary logic operations with artificial molecular machines", Coord. Chem. Rev. **428**, 213589 (2021).

[83] J. C. M. Kistemaker, A. S. Lubbe, and B. L. Feringa, "Exploring molecular motors", Mater. Chem. Front. **5**, 2900 (2021).

[84] J.-P. Sauvage, "From chemical topology to molecular machines (nobel lecture)", Angew. Chem. Int. Ed Engl. **56**, 11080 (2017).

[85] J. F. Stoddart, "Mechanically interlocked molecules (MIMs)-Molecular shuttles, switches, and machines (nobel lecture)", Angew. Chem. Int. Ed Engl. **56**, 11094 (2017).

[86] B. L. Feringa, "The art of building small: from molecular switches to motors (nobel lecture)", Angew. Chem. Int. Ed Engl. **56**, 11060 (2017).

[87] S. Kawata and Y. Kawata, "Three-Dimensional optical data storage using photochromic materials", Chem. Rev. **100**, 1777 (2000).

[88] Y. Yokoyama, "Fulgides for memories and switches", Chem. Rev. **100**, 1717 (2000).

[89] H. Tian and S. Yang, "Recent progresses on diarylethene based photochromic switches", Chem. Soc. Rev. **33**, 85 (2004).

[90] M. Irie, T. Fukaminato, K. Matsuda, and S. Kobatake, "Photochromism of diarylethene molecules and crystals: memories, switches, and actuators", Chem. Rev. **114**, 12174 (2014).

[91] W. A. Velema, W. Szymanski, and B. L. Feringa, "Photopharmacology: beyond proof of principle", J. Am. Chem. Soc. **136**, 2178 (2014).

[92] M. Borowiak, W. Nahaboo, M. Reynders, K. Nekolla, P. Jalinot, J. Hasserodt, M. Rehberg, M. Delattre, S. Zahler, A. Vollmar, D. Trauner, and O. Thorn-Seshold, "Photoswitchable inhibitors of microtubule dynamics optically control mitosis and cell death", Cell **162**, 403 (2015).

[93] J. Broichhagen, J. A. Frank, and D. Trauner, "A roadmap to success in photopharmacology", Acc. Chem. Res. **48**, 1947 (2015).

[94] K. Hüll, J. Morstein, and D. Trauner, "In vivo photopharmacology", Chem. Rev. **118**, 10710 (2018).

[95] P. D. Bregestovski and G. V. Maleeva, "Photopharmacology: a brief review using the control of potassium channels as an example", Neurosci. Behav. Physiol. **49**, 184 (2019).

[96] S. Lakshmanan, G. K. Gupta, P. Avci, R. Chandran, M. Sadasivam, A. E. S. Jorge, and M. R. Hamblin, "Physical energy for drug delivery; poration, concentration and activation", Adv. Drug Deliv. Rev. **71**, 98 (2014).

[97] M. A. Watson and S. L. Cockroft, "Man-made molecular machines: membrane bound", Chem. Soc. Rev. **45**, 6118 (2016).

[98] V. García-López, F. Chen, L. G. Nilewski, G. Duret, A. Aliyan, A. B. Kolomeisky, J. T. Robinson, G. Wang, R. Pal, and J. M. Tour, "Molecular machines open cell membranes", Nature **548**, 567 (2017).

[99] D. Sluysmans and J. F. Stoddart, "Growing community of artificial molecular machinists", Proc. Natl. Acad. Sci. U. S. A. **115**, 9359 (2018).

[100] P. Friedländer, "Über schwefelhaltige Analoga der Indigogruppe", Ber. Dtsch. Chem. Ges. **39**, 1060 (1906).

[101] T. Yamaguchi, T. Seki, T. Tamaki, and K. Ichimura, "Photochromism of hemithioindigo derivatives. i. preparation and photochromic properties in organic solvents", BCSJ **65**, 649 (1992).

[102] T. Seki, T. Tamaki, T. Yamaguchi, and K. Ichimura, "Photochromism of hemithioindigo derivatives. II. photochromic behaviors in bilayer membranes and related systems", BCSJ **65**, 657 (1992).

[103] D. H. Waldeck, "Photoisomerization dynamics of stilbenes in polar solvents", J. Mol. Liq. **57**, 127 (1993).

[104] D. H. Waldeck, "Photoisomerization dynamics of stilbenes", Chem. Rev. **91**, 415 (1991).

[105] J. Saltiel, E. D. Megarity, and K. G. Kneipp, "The mechanism of direct cis-trans photoisomerization of the stilbenes", J. Am. Chem. Soc. **88**, 2336 (1966).

[106] T. Cordes, T. Schadendorf, B. Priewisch, K. Rück-Braun, and W. Zinth, "The hammett relationship and reactions in the excited electronic state: hemithioindigo Z/E-photoisomerization", J. Phys. Chem. A **112**, 581 (2008).

[107] T. Cordes, T. Schadendorf, K. Rück-Braun, and W. Zinth, "Chemical control of hemithioindigo photoisomerization – substituent-effects on different molecular parts", Chem. Phys. Lett. **455**, 197 (2008).

[108] T. Cordes, T. Schadendorf, M. Lipp, K. Rück-Braun, and W. Zinth, "Substitution- and Temperature-Effects on hemithioindigo photoisomerization – the relevance of energy barriers", in Ultrafast phenomena XVI (2009), pp. 319–321.

[109] B. Maerz, S. Wiedbrauk, S. Oesterling, E. Samoylova, A. Nenov, P. Mayer, R. de Vivie-Riedle, W. Zinth, and H. Dube, "Making fast photoswitches faster–using hammett analysis to understand the limit of donor-acceptor approaches for faster hemithioindigo photoswitches", Chemistry **20**, 13984 (2014).

[110] S. Wiedbrauk, B. Maerz, E. Samoylova, P. Mayer, W. Zinth, and H. Dube, "Ingredients to TICT formation in donor substituted hemithioindigo", J. Phys. Chem. Lett. **8**, 1585 (2017).

[111] K. Stallhofer, M. Nuber, F. Schüppel, S. Thumser, H. Iglev, R. de Vivie-Riedle, W. Zinth, and H. Dube, "Electronic and geometric characterization of TICT formation in hemithioindigo photoswitches by picosecond infrared spectroscopy", J. Phys. Chem. A **125**, 4390 (2021).

[112] S. Wiedbrauk, B. Maerz, E. Samoylova, A. Reiner, F. Trommer, P. Mayer, W. Zinth, and H. Dube, "Twisted hemithioindigo photoswitches: solvent polarity determines the type of Light-Induced rotations", J. Am. Chem. Soc. **138**, 12219 (2016).

[113] R. Navrátil, S. Wiedbrauk, J. Jašík, H. Dube, and J. Roithová, "Transforming hemithio-indigo from a two-way to a one-way molecular photoswitch by isolation in the gas phase", Phys. Chem. Chem. Phys. **20**, 6868 (2018).

[114] L. Köttner, M. Schildhauer, S. Wiedbrauk, P. Mayer, and H. Dube, "Oxidized hemithio-indigo Photoswitches-Influence of oxidation state on (photo)physical and photochemical properties", Chemistry **26**, 10712 (2020).

[115] L. A. Huber, K. Hoffmann, S. Thumser, N. Böcher, P. Mayer, and H. Dube, "Direct observation of Hemithioindigo-Motor unidirectionality", Angew. Chem. Int. Ed Engl. **56**, 14536 (2017).

[116] M. Dantus, M. J. Rosker, and A. H. Zewail, "Real-time femtosecond probing of "transition states" in chemical reactions", J. Chem. Phys. **87**, 2395 (1987).

[117] V. Engel, H. Metiu, R. Almeida, R. A. Marcus, and A. H. Zewail, "Molecular state evolution after excitation with an ultra-short laser pulse: a quantum analysis of NaI and NaBr dissociation", Chem. Phys. Lett. **152**, 1 (1988).

[118] A. H. Zewail, "Femtochemistry: Atomic-Scale dynamics of the chemical bond using ultrafast lasers (Nobel Lecture)", Angew. Chem. Int. Ed Engl. **39**, 2586 (2000).

[119] T. Elsaesser, "Introduction: ultrafast processes in chemistry", Chem. Rev. **117**, 10621 (2017).

[120] M. Maiuri, M. Garavelli, and G. Cerullo, "Ultrafast spectroscopy: state of the art and open challenges", J. Am. Chem. Soc. **142**, 3 (2020).

[121] M. Chini, K. Zhao, and Z. Chang, "The generation, characterization and applications of broadband isolated attosecond pulses", Nat. Photonics **8**, 178 (2014).

[122] I. Conti, G. Cerullo, A. Nenov, and M. Garavelli, "Ultrafast spectroscopy of photoactive molecular systems from first principles: where we stand today and where we are going", J. Am. Chem. Soc. **142**, 16117 (2020).

[123] L. V. Keldysh, "Ionization in the field of a strong electromagnetic wave", Sov. Phys. JETP **20**, 1307 (1965).

[124] T. Brabec and F. Krausz, "Intense few-cycle laser fields: frontiers of nonlinear optics", Rev. Mod. Phys. **72**, 545 (2000).

[125] L. R. Moore, M. A. Lysaght, L. A. A. Nikolopoulos, J. S. Parker, H. W. van der Hart, and K. T. Taylor, "The RMT method for many-electron atomic systems in intense short-pulse laser light", J. Mod. Opt. **58**, 1132 (2011).

[126] A. G. Harvey, D. S. Brambila, F. Morales, and O. Smirnova, "An R-matrix approach to electron–photon–molecule collisions: photoelectron angular distributions from aligned molecules", J. Phys. B At. Mol. Opt. Phys. **47**, 215005 (2014).

[127] D. D. A. Clarke, G. S. J. Armstrong, A. C. Brown, and H. W. van der Hart, "R-matrix-with-time-dependence theory for ultrafast atomic processes in arbitrary light fields", Phys. Rev. A **98**, 053442 (2018).

[128] Z. Mašín, J. Benda, J. D. Gorfinkiel, A. G. Harvey, and J. Tennyson, "UKRmol : a suite for modelling electronic processes in molecules interacting with electrons, positrons and photons using the R-matrix method", Computer Physics Communications **249**, 107092 (2020).

[129] A. C. Brown, G. S. J. Armstrong, J. Benda, D. D. A. Clarke, J. Wragg, K. R. Hamilton, Z. Mašín, J. D. Gorfinkiel, and H. W. van der Hart, "RMT: R-matrix with time-dependence. solving the semi-relativistic, time-dependent schrödinger equation for general, multielectron atoms and molecules in intense, ultrashort, arbitrarily polarized laser pulses", Comput. Phys. Commun. **250**, 107062 (2020).

[130] J. Tennyson, D. B. Brown, J. J. Munro, I. Rozum, H. N. Varambhia, and N. Vinci, "Quantemol-N: an expert system for performing electron molecule collision calculations using the R-matrix method", J. Phys. Conf. Ser. **86**, 012001 (2007).

[131] M. Ruberti, V. Averbukh, and P. Decleva, "B-spline algebraic diagrammatic construction: application to photoionization cross-sections and high-order harmonic generation", J. Chem. Phys. **141**, 164126 (2014).

[132] V. Averbukh and M. Ruberti, "First-principles many-electron dynamics using the b-spline algebraic diagrammatic construction approach", in *Attosecond molecular dynamics* (Aug. 2018), pp. 68–102.

[133] M. Ruberti, P. Decleva, and V. Averbukh, "Multi-channel dynamics in high harmonic generation of aligned CO_2: ab initio analysis with time-dependent b-spline algebraic diagrammatic construction", Phys. Chem. Chem. Phys. **20**, 8311 (2018).

[134] M. Ruberti, P. Decleva, and V. Averbukh, "Full ab initio many-electron simulation of attosecond molecular pump-probe spectroscopy", J. Chem. Theory Comput. **14**, 4991 (2018).

[135] M. Ruberti, "Restricted correlation space B-Spline ADC approach to molecular ionization: theory and applications to total photoionization Cross-Sections", J. Chem. Theory Comput. **15**, 3635 (2019).

[136] J. Benda, Z. Mašín, G. S. J. Armstrong, D. D. A. Clarke, A. C. Brown, J. D. Gorfinkiel, and H. van der Hart, "Photoionization of H_2 using the molecular r-matrix with time approach", J. Phys. Conf. Ser. **1412**, 152066 (2020).

[137] J. Benda, J. D. Gorfinkiel, Z. Mašín, G. S. J. Armstrong, A. C. Brown, D. D. A. Clarke, H. W. van der Hart, and J. Wragg, "Perturbative and nonperturbative photoionization of H_2 and H_2O using the molecular r-matrix-with-time method", Phys. Rev. A **102**, 052826 (2020).

[138] K. Wang, J. Liu, H. Zhang, and Y. Liu, "Photoionization cross sections of the ground and first excited states of the OH radical", Phys. Rev. A **103**, 063101 (2021).

[139] J. Benda and Z. Mašín, "Multi-photon above threshold ionization of multi-electron atoms and molecules using the R-matrix approach", Sci. Rep. **11**, 11686 (2021).

[140] K. L. Ishikawa and T. Sato, "A review on ab initio approaches for multielectron dynamics", 1 (2015).

[141] G. S. J. Armstrong, M. A. Khokhlova, M. Labeye, A. S. Maxwell, E. Pisanty, and M. Ruberti, "Dialogue on analytical and ab initio methods in attoscience", Eur. Phys. J. D **75**, 209 (2021).

[142] H. B. Schlegel, "A comparison of geometry optimization with internal, cartesian, and mixed coordinates", Int. J. Quantum Chem. **44**, 243 (1992).

[143] A. Hofmann and R. de Vivie-Riedle, "Quantum dynamics of photoexcited cyclohexadiene introducing reactive coordinates", J. Chem. Phys. **112**, 5054 (2000).

[144] M. Kowalewski, J. Mikosch, R. Wester, and R. de Vivie-Riedle, "Nucleophilic substitution dynamics: comparing wave packet calculations with experiment", J. Phys. Chem. A **118**, 4661 (2014).

[145] S. Thallmair, M. K. Roos, and R. de Vivie-Riedle, "Design of specially adapted reactive coordinates to economically compute potential and kinetic energy operators including geometry relaxation", J. Chem. Phys. **144**, 234104 (2016).

[146] J. P. P. Zauleck, S. Thallmair, M. Loipersberger, and R. de Vivie-Riedle, "Two new methods to generate internal coordinates for molecular wave packet dynamics in reduced dimensions", J. Chem. Theory Comput. **12**, 5698 (2016).

[147] J. P. P. Zauleck and R. de Vivie-Riedle, "Constructing grids for molecular quantum dynamics using an autoencoder", J. Chem. Theory Comput. **14**, 55 (2018).

[148] S. Reiter, T. Schnappinger, and R. de Vivie-Riedle, "Using an autoencoder for dimension-ality reduction in quantum dynamics", in *Artificial neural networks and machine learning – ICANN 2019: workshop and special sessions* (2019), pp. 783–787.

[149] R. Crespo-Otero and M. Barbatti, "Recent advances and perspectives on nonadiabatic mixed Quantum-Classical dynamics", Chem. Rev. **118**, 7026 (2018).

[150] T. R. Nelson, A. J. White, J. A. Bjorgaard, A. E. Sifain, Y. Zhang, B. Nebgen, S. Fernandez-Alberti, D. Mozyrsky, A. E. Roitberg, and S. Tretiak, "Non-adiabatic Excited-State molecular dynamics: theory and applications for modeling photophysics in extended molecular materials", Chem. Rev. **120**, 2215 (2020).

[151] M. Richter, P. Marquetand, J. González-Vázquez, I. Sola, and L. González, "SHARC: ab initio molecular dynamics with surface hopping in the adiabatic representation including arbitrary couplings", J. Chem. Theory Comput. **7**, 1253 (2011).

[152] S. Mai, P. Marquetand, and L. González, "Nonadiabatic dynamics: the SHARC approach", Wiley Interdiscip. Rev. Comput. Mol. Sci. **8**, e1370 (2018).

[153] S. Mai, M. Richter, M. Heindl, M. F. S. J. Menger, A. Atkins, M. Ruckenbauer, F. Plasser, L. M. Ibele, S. Kropf, M. Oppel, P. Marquetand, and L. González, *SHARC2.1: surface hopping including arbitrary couplings — program package for Non-Adiabatic dynamics*, https://sharc-md.org, 2019.

[154] T. B. Schnappinger, "Coupled nuclear and electron dynamics in molecules", PhD thesis (July 2021).

[155] E. R. Davidson, "The iterative calculation of a few of the lowest eigenvalues and corre-sponding eigenvectors of large real-symmetric matrices", J. Comput. Phys. **17**, 87 (1975).

[156] L. S. Cederbaum, W. Domcke, and J. Schirmer, "Many-body theory of core holes", Phys. Rev. A **22**, 206 (1980).

[157] A. Barth and L. S. Cederbaum, "Many-body theory of core-valence excitations", Phys. Rev. A **23**, 1038 (1981).

[158] M. Stener, G. Fronzoni, and M. de Simone, "Time dependent density functional theory of core electrons excitations", Chem. Phys. Lett. **373**, 115 (2003).

[159] K. Lopata, B. E. Van Kuiken, M. Khalil, and N. Govind, "Linear-Response and Real-Time Time-Dependent density functional theory studies of Core-Level Near-Edge X-Ray absorption", J. Chem. Theory Comput. **8**, 3284 (2012).

[160] N. A. Besley and A. Noble, "Time-Dependent density functional theory study of the x-ray absorption spectroscopy of acetylene, ethylene, and benzene on si(100)", J. Phys. Chem. C **111**, 3333 (2007).

[161] S. DeBeer George, T. Petrenko, and F. Neese, "Time-dependent density functional cal-culations of ligand k-edge x-ray absorption spectra", Inorganica Chim. Acta **361**, 965 (2008).

[162] Y. Zhang, J. D. Biggs, D. Healion, N. Govind, and S. Mukamel, "Core and valence exci-tations in resonant x-ray spectroscopy using restricted excitation window time-dependent density functional theory", J. Chem. Phys. **137**, 194306 (2012).

[163] F. Lackner, A. S. Chatterley, C. D. Pemmaraju, K. D. Closser, D. Prendergast, D. M. Neumark, S. R. Leone, and O. Gessner, "Direct observation of ring-opening dynamics in strong-field ionized selenophene using femtosecond inner-shell absorption spectroscopy", J. Chem. Phys. **145**, 234313 (2016).

[164] A. R. Attar, A. Bhattacherjee, C. D. Pemmaraju, K. Schnorr, K. D. Closser, D. Prender-gast, and S. R. Leone, "Femtosecond x-ray spectroscopy of an electrocyclic ring-opening reaction", Science **356**, 54 (2017).

[165]   J. Wenzel, M. Wormit, and A. Dreuw, "Calculating core-level excitations and x-ray absorption spectra of medium-sized closed-shell molecules with the algebraic-diagrammatic construction scheme for the polarization propagator", J. Comput. Chem. **35**, 1900 (2014).

[166]   J. Wenzel, M. Wormit, and A. Dreuw, "Calculating x-ray absorption spectra of Open-Shell molecules with the unrestricted Algebraic-Diagrammatic construction scheme for the polarization propagator", J. Chem. Theory Comput. **10**, 4583 (2014).

[167]   J. Wenzel, A. Holzer, M. Wormit, and A. Dreuw, "Analysis and comparison of CVS-ADC approaches up to third order for the calculation of core-excited states", J. Chem. Phys. **142**, 214104 (2015).

[168]   J. Wenzel and A. Dreuw, "Physical properties, exciton analysis, and visualization of Core-Excited states: an intermediate state representation approach", J. Chem. Theory Comput. **12**, 1314 (2016).

[169]   T. Fransson and A. Dreuw, "Simulating x-ray emission spectroscopy with algebraic diagrammatic construction schemes for the polarization propagator", J. Chem. Theory Comput. **15**, 546 (2019).

[170]   S. Coriani and H. Koch, "Communication: x-ray absorption spectra and core-ionization potentials within a core-valence separated coupled cluster framework", J. Chem. Phys. **143**, 181103 (2015).

[171]   M. L. Vidal, X. Feng, E. Epifanovsky, A. I. Krylov, and S. Coriani, "New and efficient Equation-of-Motion Coupled-Cluster framework for Core-Excited and Core-Ionized states", J. Chem. Theory Comput. **15**, 3117 (2019).

[172]   B. N. C. Tenorio, T. Moitra, M. A. C. Nascimento, A. B. Rocha, and S. Coriani, "Molecular inner-shell photoabsorption/photoionization cross sections at core-valence-separated coupled cluster level: theory and examples", J. Chem. Phys. **150**, 224104 (2019).

[173]   R. Faber and S. Coriani, "Core-valence-separated ccsd complex-polarization-propagator approach to x-ray spectroscopies", Phys. Chem. Chem. Phys. **22**, 2642 (2020).

[174]   L. Halbert, M. L. Vidal, A. Shee, S. Coriani, and A. Severo Pereira Gomes, "Relativistic EOM-CCSD for Core-Excited and Core-Ionized state energies based on the Four-Component Dirac-Coulomb(-Gaunt) hamiltonian", J. Chem. Theory Comput. **17**, 3583 (2021).

[175]   I. Josefsson, K. Kunnus, S. Schreck, A. Föhlisch, F. de Groot, P. Wernet, and M. Odelius, "Ab initio calculations of x-ray spectra: atomic multiplet and molecular orbital effects in a multiconfigurational SCF approach to the L-Edge spectra of transition metal complexes", J. Phys. Chem. Lett. **3**, 3565 (2012).

[176]   P. Wernet, K. Kunnus, S. Schreck, W. Quevedo, R. Kurian, S. Techert, F. M. F. de Groot, M. Odelius, and A. Föhlisch, "Dissecting local atomic and intermolecular interactions of Transition-Metal ions in solution with selective x-ray spectroscopy", J. Phys. Chem. Lett. **3**, 3448 (2012).

[177]   S. I. Bokarev, M. Khan, M. K. Abdel-Latif, J. Xiao, R. Hilal, S. G. Aziz, E. F. Aziz, and O. Kühn, "Unraveling the electronic structure of photocatalytic manganese complexes by L-Edge x-ray spectroscopy", J. Phys. Chem. C **119**, 19192 (2015).

[178]   L. Weinhardt, E. Ertan, M. Iannuzzi, M. Weigand, O. Fuchs, M. Bär, M. Blum, J. D. Denlinger, W. Yang, E. Umbach, M. Odelius, and C. Heske, "Probing hydrogen bonding orbitals: resonant inelastic soft x-ray scattering of aqueous NH_3", Phys. Chem. Chem. Phys. **17**, 27145 (2015).

[179]   M. Guo, L. K. Sørensen, M. G. Delcey, R. V. Pinjari, and M. Lundberg, "Simulations of iron K pre-edge x-ray absorption spectra using the restricted active space method", Phys. Chem. Chem. Phys. **18**, 3250 (2016).

[180] M. Preuße, S. I. Bokarev, S. G. Aziz, and O. Kühn, "Towards an ab initio theory for metal l-edge soft x-ray spectroscopy of molecular aggregates", Struct Dyn **3**, 062601 (2016).

[181] M. Guo, E. Källman, R. V. Pinjari, R. C. Couto, L. Kragh Sørensen, R. Lindh, K. Pierloot, and M. Lundberg, "Fingerprinting electronic structure of heme iron by ab initio modeling of metal L-Edge x-ray absorption spectra", J. Chem. Theory Comput. **15**, 477 (2019).

[182] H. Wang, M. Odelius, and D. Prendergast, "A combined multi-reference pump-probe simulation method with application to XUV signatures of ultrafast methyl iodide photodissociation", J. Chem. Phys. **151**, 124106 (2019).

[183] N. H. List, A. L. Dempwolff, A. Dreuw, P. Norman, and T. J. Martínez, "Probing competing relaxation pathways in malonaldehyde with transient x-ray absorption spectroscopy", Chem. Sci. **11**, 4180 (2020).

[184] S. I. Bokarev, M. Dantz, E. Suljoti, O. Kühn, and E. F. Aziz, "State-dependent electron delocalization dynamics at the solute-solvent interface: soft-x-ray absorption spectroscopy and ab initio calculations", Phys. Rev. Lett. **111**, 083002 (2013).

[185] E. Suljoti, R. Garcia-Diez, S. I. Bokarev, K. M. Lange, R. Schoch, B. Dierker, M. Dantz, K. Yamamoto, N. Engel, K. Atak, O. Kühn, M. Bauer, J.-E. Rubensson, and E. F. Aziz, "Direct observation of molecular orbital mixing in a solvated organometallic complex", Angew. Chem. Int. Ed Engl. **52**, 9841 (2013).

[186] K. Atak, S. I. Bokarev, M. Gotz, R. Golnak, K. M. Lange, N. Engel, M. Dantz, E. Suljoti, O. Kühn, and E. F. Aziz, "Nature of the chemical bond of aqueous Fe^{2+} probed by soft x-ray spectroscopies and ab initio calculations", J. Phys. Chem. B **117**, 12613 (2013).

[187] K. Kunnus, I. Josefsson, S. Schreck, W. Quevedo, P. S. Miedema, S. Techert, F. M. F. de Groot, M. Odelius, P. Wernet, and A. Föhlisch, "From ligand fields to molecular orbitals: probing the local valence electronic structure of ni(2+) in aqueous solution with resonant inelastic x-ray scattering", J. Phys. Chem. B **117**, 16512 (2013).

[188] N. Engel, S. I. Bokarev, E. Suljoti, R. Garcia-Diez, K. M. Lange, K. Atak, R. Golnak, A. Kothe, M. Dantz, O. Kühn, and E. F. Aziz, "Chemical bonding in aqueous ferrocyanide: experimental and theoretical x-ray spectroscopic study", J. Phys. Chem. B **118**, 1555 (2014).

[189] D. Maganas, P. Kristiansen, L.-C. Duda, A. Knop-Gericke, S. DeBeer, R. Schlögl, and F. Neese, "Combined experimental and ab initio multireference configuration interaction study of the resonant inelastic x-ray scattering spectrum of CO_2", J. Phys. Chem. C **118**, 20163 (2014).

[190] R. V. Pinjari, M. G. Delcey, M. Guo, M. Odelius, and M. Lundberg, "Restricted active space calculations of l-edge x-ray absorption spectra: from molecular orbitals to multiplet states", J. Chem. Phys. **141**, 124116 (2014).

[191] P. Wernet, K. Kunnus, I. Josefsson, I. Rajkovic, W. Quevedo, M. Beye, S. Schreck, S. Grübel, M. Scholz, D. Nordlund, W. Zhang, R. W. Hartsock, W. F. Schlotter, J. J. Turner, B. Kennedy, F. Hennies, F. M. F. de Groot, K. J. Gaffney, S. Techert, M. Odelius, and A. Föhlisch, "Orbital-specific mapping of the ligand exchange dynamics of $Fe(CO)_5$ in solution", Nature **520**, 78 (2015).

[192] Y. Zhang, W. Hua, K. Bennett, and S. Mukamel, "Nonlinear spectroscopy of core and valence excitations using short X-Ray pulses: simulation challenges", Top. Curr. Chem. **368**, 273 (2016).

[193] P. Norman and A. Dreuw, "Simulating x-ray spectroscopies and calculating Core-Excited states of molecules", Chem. Rev. **118**, 7208 (2018).

[194] M. Lundberg and M. G. Delcey, in *Transition metals in coordination environments: computational chemistry and catalysis viewpoints*, edited by E. Broclawik, T. Borowski, and M. Radoń (Springer International Publishing, Cham, 2019), pp. 185–217.

[195] C. D. Rankine and T. J. Penfold, "Progress in the theory of x-ray spectroscopy: from quantum chemistry to machine learning and ultrafast dynamics", J. Phys. Chem. A **125**, 4276 (2021).

[196] X. Li, N. Govind, C. Isborn, A. E. DePrince 3rd, and K. Lopata, "Real-Time Time-Dependent electronic structure theory", Chem. Rev. **120**, 9951 (2020).

[197] I. Fdez Galván, M. Vacher, A. Alavi, C. Angeli, F. Aquilante, J. Autschbach, J. J. Bao, S. I. Bokarev, N. A. Bogdanov, R. K. Carlson, L. F. Chibotaru, J. Creutzberg, N. Dattani, M. G. Delcey, S. S. Dong, A. Dreuw, L. Freitag, L. M. Frutos, L. Gagliardi, F. Gendron, A. Giussani, L. González, G. Grell, M. Guo, C. E. Hoyer, M. Johansson, S. Keller, S. Knecht, G. Kovačević, E. Källman, G. Li Manni, M. Lundberg, Y. Ma, S. Mai, J. P. Malhado, P. Å. Malmqvist, P. Marquetand, S. A. Mewes, J. Norell, M. Olivucci, M. Oppel, Q. M. Phung, K. Pierloot, F. Plasser, M. Reiher, A. M. Sand, I. Schapiro, P. Sharma, C. J. Stein, L. K. Sørensen, D. G. Truhlar, M. Ugandi, L. Ungur, A. Valentini, S. Vancoillie, V. Veryazov, O. Weser, T. A. Wesołowski, P.-O. Widmark, S. Wouters, A. Zech, J. P. Zobel, and R. Lindh, "OpenMolcas: from source code to insight", J. Chem. Theory Comput. **15**, 5925 (2019).

[198] F. Aquilante, J. Autschbach, A. Baiardi, S. Battaglia, V. A. Borin, L. F. Chibotaru, I. Conti, L. De Vico, M. Delcey, I. Fdez Galván, N. Ferré, L. Freitag, M. Garavelli, X. Gong, S. Knecht, E. D. Larsson, R. Lindh, M. Lundberg, P. Å. Malmqvist, A. Nenov, J. Norell, M. Odelius, M. Olivucci, T. B. Pedersen, L. Pedraza-González, Q. M. Phung, K. Pierloot, M. Reiher, I. Schapiro, J. Segarra-Martí, F. Segatta, L. Seijo, S. Sen, D.-C. Sergentu, C. J. Stein, L. Ungur, M. Vacher, A. Valentini, and V. Veryazov, "Modern quantum chemistry with [Open]Molcas", J. Chem. Phys. **152**, 214117 (2020).

[199] H.-J. Werner, P. J. Knowles, G. Knizia, F. R. Manby, and M. Schütz, "Molpro: a general-purpose quantum chemistry program package", Wiley Interdiscip. Rev. Comput. Mol. Sci. **2**, 242 (2012).

[200] H.-J. Werner, P. J. Knowles, F. R. Manby, J. A. Black, K. Doll, A. Heßelmann, D. Kats, A. Köhn, T. Korona, D. A. Kreplin, Q. Ma, T. F. Miller 3rd, A. Mitrushchenkov, K. A. Peterson, I. Polyak, G. Rauhut, and M. Sibaev, "The Molpro quantum chemistry package", J. Chem. Phys. **152**, 144107 (2020).

[201] Q. Sun, X. Zhang, S. Banerjee, P. Bao, M. Barbry, N. S. Blunt, N. A. Bogdanov, G. H. Booth, J. Chen, Z.-H. Cui, J. J. Eriksen, Y. Gao, S. Guo, J. Hermann, M. R. Hermes, K. Koh, P. Koval, S. Lehtola, Z. Li, J. Liu, N. Mardirossian, J. D. McClain, M. Motta, B. Mussard, H. Q. Pham, A. Pulkin, W. Purwanto, P. J. Robinson, E. Ronca, E. R. Sayfutyarova, M. Scheurer, H. F. Schurkus, J. E. T. Smith, C. Sun, S.-N. Sun, S. Upadhyay, L. K. Wagner, X. Wang, A. White, J. D. Whitfield, M. J. Williamson, S. Wouters, J. Yang, J. M. Yu, T. Zhu, T. C. Berkelbach, S. Sharma, A. Y. Sokolov, and G. K.-L. Chan, "Recent developments in the PySCF program package", J. Chem. Phys. **153**, 024109 (2020).

[202] Q. Sun, T. C. Berkelbach, N. S. Blunt, G. H. Booth, S. Guo, Z. Li, J. Liu, J. D. McClain, E. R. Sayfutyarova, S. Sharma, S. Wouters, and G. K.-L. Chan, "PySCF: the python-based simulations of chemistry framework", Wiley Interdiscip. Rev. Comput. Mol. Sci. **8**, e1340 (2018).

[203] Q. Sun, "Libcint: an efficient general integral library for gaussian basis functions", J. Comput. Chem. **36**, 1664 (2015).

[204] B. O. Roos, "The complete active space SCF method in a fock-matrix-based super-CI formulation", Int. J. Quantum Chem. **18**, 175 (2009).

[205] P. A. Malmqvist, A. Rendell, and B. O. Roos, "The restricted active space self-consistent-field method, implemented with a split graph unitary group approach", J. Phys. Chem. **94**, 5477 (1990).

[206] M. W. Schmidt and M. S. Gordon, "The construction and interpretation of MCSCF wavefunctions", Annu. Rev. Phys. Chem. **49**, 233 (1998).

[207] V. Veryazov, P. Å. Malmqvist, and B. O. Roos, "How to select active space for multiconfigurational quantum chemistry?", Int. J. Quantum Chem. **111**, 3329 (2011).

[208] M. Douglas and N. M. Kroll, "Quantum electrodynamical corrections to the fine structure of helium", Ann. Phys. **82**, 89 (1974).

[209] B. A. Hess, "Relativistic electronic-structure calculations employing a two-component no-pair formalism with external-field projection operators", Phys. Rev. A Gen. Phys. **33**, 3742 (1986).

[210] B. O. Roos, V. Veryazov, and P.-O. Widmark, "Relativistic atomic natural orbital type basis sets for the alkaline and alkaline-earth atoms applied to the ground-state potentials for the corresponding dimers", Theor. Chem. Acc. **111**, 345 (2004).

[211] B. O. Roos, R. Lindh, P.-Å. Malmqvist, V. Veryazov, and P.-O. Widmark, "Main group atoms and dimers studied with a new relativistic ANO basis set", J. Phys. Chem. A **108**, 2851 (2004).

[212] B. O. Roos, R. Lindh, P.-Å. Malmqvist, V. Veryazov, and P.-O. Widmark, "New relativistic ANO basis sets for actinide atoms", Chem. Phys. Lett. **409**, 295 (2005).

[213] B. O. Roos, R. Lindh, P.-A. Malmqvist, V. Veryazov, and P.-O. Widmark, "New relativistic ANO basis sets for transition metal atoms", J. Phys. Chem. A **109**, 6575 (2005).

[214] B. O. Roos, R. Lindh, P.-A. Malmqvist, V. Veryazov, P.-O. Widmark, and A. C. Borin, "New relativistic atomic natural orbital basis sets for lanthanide atoms with applications to the ce diatom and LuF3", J. Phys. Chem. A **112**, 11431 (2008).

[215] M. G. Delcey, L. K. Sørensen, M. Vacher, R. C. Couto, and M. Lundberg, "Efficient calculations of a large number of highly excited states for multiconfigurational wavefunctions", J. Comput. Chem. **40**, 1789 (2019).

[216] J. Finley, P.-Å. Malmqvist, B. O. Roos, and L. Serrano-Andrés, "The multi-state CASPT2 method", Chem. Phys. Lett. **288**, 299 (1998).

[217] A. A. Granovsky, "Extended multi-configuration quasi-degenerate perturbation theory: the new approach to multi-state multi-reference perturbation theory", J. Chem. Phys. **134**, 214113 (2011).

[218] T. Shiozaki, W. Gyorffy, P. Celani, and H.-J. Werner, "Communication: extended multi-state complete active space second-order perturbation theory: energy and nuclear gradients", J. Chem. Phys. **135**, 081106 (2011).

[219] G. Ghigo, B. O. Roos, and P.-Å. Malmqvist, "A modified definition of the zeroth-order hamiltonian in multiconfigurational perturbation theory (CASPT2)", Chem. Phys. Lett. **396**, 142 (2004).

[220] N. Forsberg and P.-Å. Malmqvist, "Multiconfiguration perturbation theory with imaginary level shift", Chem. Phys. Lett. **274**, 196 (1997).

[221] P. Å. Malmqvist, "Calculation of transition density matrices by nonunitary orbital transformations", Int. J. Quantum Chem., Lecture Notes **30**, 479 (1986).

[222] P. Å. Malmqvist and B. O. Roos, "The CASSCF state interaction method", Chem. Phys. Lett. **155**, 189 (1989).

[223] P. Å. Malmqvist, B. O. Roos, and B. Schimmelpfennig, "The restricted active space (RAS) state interaction approach with spin–orbit coupling", Chem. Phys. Lett. **357**, 230 (2002).

[224] B. Schimmelpfennig, L. Maron, U. Wahlgren, C. Teichteil, H. Fagerli, and O. Gropen, "On the efficiency of an effective hamiltonian in spin-orbit CI calculations", Chem. Phys. Lett. **286**, 261 (1998).

[225] M.-F. Lin, D. M. Neumark, O. Gessner, and S. R. Leone, "Ionization and dissociation dynamics of vinyl bromide probed by femtosecond extreme ultraviolet transient absorption spectroscopy", J. Chem. Phys. **140**, 064311 (2014).

[226] P. Downie and I. Powis, "An angle resolved electron–ion recoil vector correlation study of alternate ion dissociation channels in ã CF3I+", Faraday Discuss. **115**, 103 (2000).

[227] B. W. Yates, K. H. Tan, G. M. Bancroft, and J. S. Tse, "A variable energy photoelectron study of the valence levels and I 4d core levels of CF3I", J. Chem. Phys. **85**, 3840 (1986).

[228] G. O'Sullivan, C. McGuinness, J. T. Costello, E. T. Kennedy, and B. Weinmann, "Trends in 4d-subshell photoabsorption along the iodine isonuclear sequence: i, I^+, and I^{2+}", Phys. Rev. A **53**, 3211 (1996).

[229] T. Shiozaki, "BAGEL: brilliantly advanced general electronic-structure library", Wiley Interdiscip. Rev. Comput. Mol. Sci. **8**, e1331 (2018).

[230] W. J. Thompson, "Numerous neat algorithms for the voigt profile function", Computers in Physics **7**, 627 (1993).

[231] S. M. Abrarov and B. M. Quine, "Efficient algorithmic implementation of the voigt/complex error function based on exponential series approximation", Appl. Math. Comput. **218**, 1894 (2011).

[232] P. Thompson, D. E. Cox, and J. B. Hastings, "Rietveld refinement of Debye–Scherrer synchrotron x-ray data from Al_2O_3", J. Appl. Crystallogr. **20**, 79 (1987).

[233] T. Ida, M. Ando, and H. Toraya, "Extended pseudo-voigt function for approximating the voigt profile", J. Appl. Crystallogr. **33**, 1311 (2000).

[234] M. J. Frisch, G. W. Trucks, H. B. Schlegel, G. E. Scuseria, M. A. Robb, J. R. Cheeseman, G. Scalmani, V. Barone, G. A. Petersson, H. Nakatsuji, X. Li, M. Caricato, A. V. Marenich, J. Bloino, B. G. Janesko, R. Gomperts, B. Mennucci, H. P. Hratchian, J. V. Ortiz, A. F. Izmaylov, J. L. Sonnenberg, Williams, F. Ding, F. Lipparini, F. Egidi, J. Goings, B. Peng, A. Petrone, T. Henderson, D. Ranasinghe, V. G. Zakrzewski, J. Gao, N. Rega, G. Zheng, W. Liang, M. Hada, M. Ehara, K. Toyota, R. Fukuda, J. Hasegawa, M. Ishida, T. Nakajima, Y. Honda, O. Kitao, H. Nakai, T. Vreven, K. Throssell, J. A. Montgomery Jr., J. E. Peralta, F. Ogliaro, M. J. Bearpark, J. J. Heyd, E. N. Brothers, K. N. Kudin, V. N. Staroverov, T. A. Keith, R. Kobayashi, J. Normand, K. Raghavachari, A. P. Rendell, J. C. Burant, S. S. Iyengar, J. Tomasi, M. Cossi, J. M. Millam, M. Klene, C. Adamo, R. Cammi, J. W. Ochterski, R. L. Martin, K. Morokuma, O. Farkas, J. B. Foresman, and D. J. Fox, *Gaussian 16 rev. a.03*, Wallingford, CT, 2016.

[235] J.-D. Chai and M. Head-Gordon, "Long-range corrected hybrid density functionals with damped atom-atom dispersion corrections", Phys. Chem. Chem. Phys. **10**, 6615 (2008).

[236] M. N. Glukhovtsev, A. Pross, M. P. McGrath, and L. Radom, "Extension of gaussian-2 (g2) theory to bromine- and iodine-containing molecules: use of effective core potentials", J. Chem. Phys. **103**, 1878 (1995).

[237] R. Krishnan, J. S. Binkley, R. Seeger, and J. A. Pople, "Self-consistent molecular orbital methods. XX. a basis set for correlated wave functions", J. Chem. Phys. **72**, 650 (1980).

[238] B. P. Pritchard, D. Altarawy, B. Didier, T. D. Gibson, and T. L. Windus, "New basis set exchange: an open, Up-to-Date resource for the molecular sciences community", J. Chem. Inf. Model. **59**, 4814 (2019).

[239] K. L. Schuchardt, B. T. Didier, T. Elsethagen, L. Sun, V. Gurumoorthi, J. Chase, J. Li, and T. L. Windus, "Basis set exchange: a community database for computational sciences", J. Chem. Inf. Model. **47**, 1045 (2007).

[240] D. Feller, "The role of databases in support of computational chemistry calculations", J. Comput. Chem. **17**, 1571 (1996).

[241]   H. Tal-Ezer and R. Kosloff, "An accurate and efficient scheme for propagating the time dependent schrödinger equation", J. Chem. Phys. **81**, 3967 (1984).

[242]   S. Butterworth, "On the theory of filter amplifiers", Wireless Engineer **7**, 536 (1930).

List of Abbreviations

ADC algebraic diagrammatic construction. 37

ADP adenosine diphosphate. 3

AMFI atomic mean field integrals. 42

ANO-RCC relativistic atomic natural orbital. 39, 42, 61, 64, 77

AS active space. 16, 26, 38–40, 60, 61, 63, 67, 69–72, 77–81, 84, 88

ASRS attosecond stimulated Raman spectroscopy. 68

ATAS attosecond transient absorption spectroscopy. 2, 35, 36, 43–45, 59, 60, 67, 68, 92

ATI above-threshold ionization. 36

ATP adenosine triphosphate. 3

CASPT2 complete active space perturbation theory. 40, 41, 59, 60, 63, 71, 72, 74, 78, 81, 147, 148

CASSCF complete active space self-consistend field. 6, 16, 26, 38–40, 67, 70, 77, 78, 84, 88

CC coupled cluster. 37

CCSD coupled-cluster, including singles and doubles. 16

CoIn conical intersection. 1, 2, 6, 16, 26, 27, 60, 63, 65, 67, 68, 83

CT charge transfer. 6, 60, 63, 64, 68

CVS core-valence separation. 37, 38, 40

DCM dichloromethane. 5

DFT density functional theory. 37, 38, 77

DK Douglas–Kroll. 41

DKH Douglas–Kroll Hamiltonian. 39

DMSO dimethyl sulfoxide. 5

DNA deoxyribonucleic acid. 68

FC Franck–Condon. 5, 16, 26, 27, 60–63, 65, 68, 81

FCI full configuration interaction. 39

FWHM full width at half maximum. 43, 75

GS ground state. 1, 60, 62–64, 67, 68, 77–81

HF Hartee-Fock. 39, 40, 69, 70

HHG high-harmonic generation. 35, 36

HOMO highest occupied molecular orbital. 59

HTI hemithioindigo. 1, 4, 5, 15, 16, 26, 27, 66, 67, 88

HWHM half width at half maximum. 75

IC internal conversion. 1

IPEA ionization-potential electron-affinity. 40

IR infrared. 2, 35

ISC intersystem crossing. 1, 16, 67

MS-CASPT2 multi-state CASPT2. 40, 41, 59, 60, 63, 71, 72, 74, 78, 81

NAMD non-adiabatic molecular dynamics. 2, 37, 38, 41–45, 66–68, 92

NIR near-infrared. 67

NMR nuclear magnetic resonance. 15, 26, 66

OD optical density. 59

PES potential energy surface. 1, 6, 15, 26, 27, 60, 63, 66, 67, 80, 81, 83

QC quantum chemistry. 66

QD quantum dynamics. 37, 63, 83

RAS restricted active space. 38, 61, 80

RASPT2 restricted active space perturbation theory. 2, 38–42, 45, 59, 60, 63, 67, 68

RASSCF restricted active space self-consistend field. 2, 37–42, 59, 60, 63, 66–72, 74, 77, 80

RASSI restricted active space state interaction. 42, 71, 74

REW-TDDFT restricted excitation window time dependent density functional theory. 37

RIXS resonant inelastic X-ray scattering. 68

RMT *R*-matrix with time dependence. 36

RS relaxed structure. 5, 6

RT real-time. 38

SCF self-consistend field. 70

SF spin-free. 42, 74

SHARC surface hopping including arbitrary couplings. 37

SO spin-orbit. 42, 59, 60, 62, 74, 78, 81–83

SOC spin-orbit coupling. 39, 40, 42, 59, 73, 74

SS-CASPT2 single-state CASPT2. 74

TAS transient absorption spectrum. 41, 63, 65, 77, 82

TD B-spline ADC time-dependent B-spline algebraic diagrammatic construction. 36

TDDFT time-dependent density functional theory. 16, 26, 37

TDSE time-dependent Schrödinger equation. 37, 83

TISE time-independent Schrödinger equation. 37, 41

TS transition state. 6, 26, 27

UV ultraviolet. 2, 4

Vis visible. 2

X-ray X-ray. 2, 35, 37, 38, 41, 45, 67, 69

XAS XUV/X-ray absorption spectrum. 39, 45, 60–63, 66–68, 73, 74, 92

XMS-CASPT2 extended multi-state CASPT2. 40, 41

XUV extreme ultraviolet. 2, 35, 37, 38, 41, 43, 45, 67, 69, 77

Danksagung

Zu guter Letzt möchte ich all denjenigen danken, die mich über die Jahre unterstützt haben und so diese Arbeit überhaupt erst möglich gemacht haben.

Hier gilt zuallererst mein Dank meiner Doktormutter und Chefin Frau Prof. Regina de Vivie-Riedle, die mich nicht nur für die Quantenchemie begeistern konnte, sondern auch in ihre Arbeitsgruppe aufgenommen hat und mir die Möglichkeit und Zeit gegeben hat diese Doktorarbeit zu verfassen. Vielen Dank auch für ihr Vertrauen in mich, meine Ergebnisse auf diversen Konferenzen in Vorträgen oder Postern zu präsentieren. Die übertragene Verantwortung für die Betreuung des Computerkurses und der Verwaltung des Rechenclusters unterstreicht dieses Vertrauen. Herzlichen Dank!

Ein großer Dank gilt allen ehemaligen und momentanen Kollegen im Arbeitskreis. Hierbei möchte ich mich vor allem bei Sven, Julius und Thali für ihre Betreuung und Unterstützung während meiner Bachelor- und Masterarbeit bedankten. Aber auch bei Patrick, Matthias, Robert, Daniel, Thomas, Martin, Franziska, Sebastian, Lena, und Ferdinand für die freundliche Umgebung und die Bereitschaft bei jedem Problem gemeinsam nach einer Lösung zu suchen. Patrick und Sven, gerne blicke ich auf unsere gemeinsame Zeit im Bergbüro zurück, die eventuell nicht die produktivste aber sicherlich die lustigste war. Sven und Matthias danke für eure Erfahrung und Zusammenarbeit bei der Administration unseres Cluster. Thomas, vielen Dank für deine Unterstützung und Diskussionen gerade in den letzten Monaten. Ich werde die Zeit im Arbeitskreis und dem "Gasthaus zur fs" vermissen. Bei meinen Kooperationspartnern möchte ich mich vor allem bei Roland Wilcken, Henry Dube, Herrn Zinth, Herrn Riedle, Maurizio Reduzzi, Steve Leone, Danylo Matselyukh und Herrn Wörner für die freundlichen und kollegialen Diskussionen auf dem Weg zu unseren gemeinsamen Veröffentlichungen danken.

Aber bevor eine Promotion und Kooperationen überhaupt möglich sind, muss natürlich erst mal das Studium geschafft sein. Und an meinem Erfolg im Studium seid ihr Kilian, Max, René und Travis sicherlich nicht ganz unbeteiligt gewesen. Vielen Dank dafür, ich habe mit euch nicht nur gute Kommilitonen sondern auch Freunde gefunden. Mein Studium ebenso wie diese Arbeit wäre ohne die Unterstützung meiner Freunde, besonders Alex, Rabia, Raphael, Viola, Jon, Liz, Gregor, Thomas, Marina, Johannes, Matthias, Großer Flori, Markus, Alf, Schw4rz, Benni, Joey, Lino, Vitalij, Vasi, Chris, Philipp und Eckhard niemals fertig geworden. Vielen Dank für euere Unterstützung und gemeinsame Gaudi der letzten Jahre und Jahrzehnte.

Bei meinen Eltern und meinen Brüdern, Stephan und Matthias möchte ich mich für ihre unermüdliche Unterstützung über all die Jahre bedanken. Zuletzt, Tabea, Danke für alles!

Hiermit möchte ich mich auch bei Fabrizio Schiavi dem Designer der Schriftart PragmataPro™ für die Erlaubnis zur Verwendung dieser im Rahmen meiner Dissertation bedanken.

Und ganz zum Schluss noch ein kleines Schmankerl:

```
.#################.
.# Happy landing! #.
.#################.
```